Digital Holographic Microscopy for Three-Dimensional Studies of Bacteria

James L. Flewellen

Lincoln College

University of Oxford

A thesis submitted for the degree of

Doctor of Philosophy

Trinity Term 2012

Digital Holographic Microscopy for Three-Dimensional Studies of Bacteria

James L. Flewellen
Lincoln College

A thesis submitted for the degree of
Doctor of Philosophy
at the University of Oxford, Trinity Term 2012

Abstract

Holography has the ability to render three-dimensional information of a recorded scene by capturing both the amplitude and phase of light incident on the recording medium. The application of digital camera technology and high-speed computing means digital holograms can be analysed numerically and novel applications can be found for this technology. This thesis explores the potential for both inline and off-axis digital holographic microscopy to study the three-dimensional swimming behaviour of bacteria.

A high-magnification (225×) digital holographic microscope was designed and constructed with the ability to switch easily between inline and off-axis imaging modalities. Hardware aspects, in particular the illumination source, the choice of camera and data transfer rates, were considered. Novel strategies for off-axis holography combining dark field microscopy were designed and implemented.

The localisation accuracy of the inline imaging modality was assessed by studying samples of polystyrene microspheres. The microscope is sensitive to stage drift on the order of angstroms per second and can successfully localise microspheres in dilute suspensions at least 100μm from the objective specimen plane. As a simple test of the capabilities of the microscope, the diffusion coefficient of a 0.5μm microsphere was found to be isotropic and consistent with the theoretical value.

Amplitude and phase image reconstructions from the off-axis modality are demonstrated. High-magnification dark field off-axis holographic microscopy is shown to be superior to inline microscopy in localising 100nm gold nanoparticles. An artifact from our method of dark-field imaging, however, restricts the depth range to 15μm.

A lower-magnification (45×) configuration of the microscope was used to study the 3D swimming behaviour of wild type *Escherichia coli* as a qualitative demonstration of the potential for this instrument in microbiological applications.

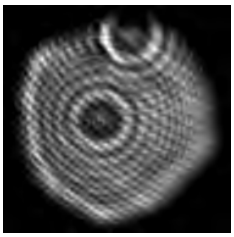

omnium rerum principia parva sunt

Acknowledgements

There are many people who deserve credit and my thanks for helping me along this journey. Firstly to Richard, my supervisor. I suspect very few supervisors give their students such *carte blanche* to create their own projects, yet still provide the necessary support and direction. Thank you for your faith in me, for inviting me to study under you and for everything (and it is a great deal) I have learned from you.

The more I learn about the wider academic environment, the more pleased I am to have 'landed' in the Berry group, with its relaxed approach to doing science primarily for the fun of it. The Berry group members exemplify this spirit along with a sense of quiet community and generous support. From all members − post-docs past and present, students senior and junior − I have learned a lot about science, a lot about being a scientist, and a lot about the world in our *ex laboratorio* conversations.

This project really is a two-man effort: a true synthesis of skills and ideas toward a common goal. 'Team DHM' has not been around all that long and we find ourselves in the company of bigger and better-funded groups that have been doing this a lot longer than we have. It is great to be able to work with someone on a project, to contribute with our own individual strengths, and ultimately to celebrate the achievements and to puzzle over the failures. Thank you Irwin for being my lab partner on this endeavour: this thesis would look a lot different without you.

I am beholden to the staff that keep the Oxford Physics Department ticking over. In particular, the biophysics technical staff and the Clarendon workshop guys have all helped me to conduct my experiments and to build my microscope.

The wider Oxford community has been a source of support, inspiration and sanity. I appreciate immensely all the friendships made and time spent with the members of the Common Rooms of Lincoln College and the Oxford Blind Tasting Society in particular, and the sense of being at home these communities have fostered over the past four years.

Such is the reality of being an international student, I would not be here without the generous support of a number of funding bodies. Particular thanks go to the

EPSRC, the University of Oxford, the benefaction of Arthur and Agnes Marion Sims via my *alma mater* the University of Canterbury, and Christ's College (NZ).

Many have encouraged and inspired me to take the first steps along this path. I am indebted to the support of my whanau, friends, teachers and professors in Christchurch and to the late, great, Sir Paul Callaghan, who took the time to reply to an undergraduate's email about the future of biophysics.

Finally and most significantly, Latoya has been at my side throughout this entire journey. She has tolerated the late nights, the frantic schedules, and even being uprooted from the call of the tui and the rattle of quakes to the drizzle and hum of these crowded, mountainless isles. We have shared joy and sorrow, stress and silliness. For all that there are no words great enough to thank you. This is for you.

Contents

List of Figures

List of Tables

List of Abbreviations

1D, **2D**, **3D**	one-, two-, three-dimensional
CCD	charge-coupled device
CMOS	complementary metal-oxide semiconductor
CoM	centre of mass
CPU	central processing unit
DHM	digital holographic microscope
EDTA	ethylenediaminetetraacetic acid
flops	floating point operations per second
FoV	field of view
fps	frames per second
GPU	graphics processing unit
GUI	graphical user interface
HDF5 or **h5**	hierarchical data format
HeNe	helium-neon (gas laser)
LB	lysogeny broth
LED	light emitting diode
MB	motility buffer
MKS	metre, kilogram, second − used as fundamental units of measurement
MSD	mean squared displacement
NA	numerical aperture
ND	neutral density
PDMS	polydimethylsiloxane
PIV	particle image velocimetry
px	pixel
RAM	random-access memory
RoI	region of interest
ROYGBIV	red to violet colour scale
SLM	spatial light modulator
SSD	solid-state hard drive
TB	tryptone broth
tif or **tiff**	tagged image file format

Chapter 1

Three-Dimensional Microscopy

1.1 Contextual Remarks

I was attracted to the field of microorganism motility for the dynamic opportunites it offers to blend physics and biology, science and technology. Despite its relatively long history, the vastness of the microworld and the complexity of the biological problems found there mean there are myriad chances to develop new technologies to readdress old problems, and to pioneer the use of established technologies in entirely new fields. Digital holographic microscopy certainly fits this bill, adapting long-established holography theory to the recently emergent digital camera and graphics processing technologies. And then taking the ensemble to bear on an entirely biological problem: that of how bacteria behave in their three-dimensional (3D) environment.

However, this was not my initial doctoral research project. The original project was a Research Council-funded 'Basic Technology' grant, in collaboration with the University of Glasgow, to develop a remote sensing technology for measuring dynamic mechanical signals of biological and man-made aqueous microsystems. The rotary motor found in many species of bacteria was be to one such test system. We aimed to detect the presence of a bacterium through high-speed analysis of the motion of

an array of microspheres held in optical tweezers.

For a number of reasons, not least of all the difficulty of what we were trying to achieve, this project foundered and 18 months into my doctorate I began to consider other methods of 'remotely' detecting the motion of a swimming bacterium. One approach that came to mind was the use of tracer particles to probe the surrounding fluid as a cell swims. It was a step away from picking up mechanical signals towards optically-observed hydrodynamics. It became clear that there was little point in restricting this study to only two dimensions as bacteria simply do not inhabit a two-dimensional 'flatland'. Thus the scene was set for a foray into the world of three-dimensional microscopy.

A chance meeting with Irwin Zaid, a theoretical physics student who was working on the behaviour of microswimmers, led to our collaboration on digital holographic microscopy. We began with me designing the optics and conducting the experiments and Irwin developing the code to reconstruct our holograms. Although, it has recently become apparent to me that to be truly effective in this field, you need a thorough understanding of the entirety of the process, from microscope to microchip. Thus, I foresee a slow and frustrating journey ahead, outside my comfort zone, deeper into the world of computer and graphics card programming.

As is the nature of doctoral projects the focus shifted several times; the microscope underwent numerous reimaginings, redesigns and rebuilds. As well as the question of remotely sensing bacterial motion through hydrodynamic observations we have added to our focus directly tracking the organisms themselves.

I predict a strong future in three-dimensional microscopy in general and in digital holography specifically with its ability to record single-shot high-speed 3D video at a large range of magnifications. There are many applications to be explored in both the biological and purely physical fields and I believe we stand at the cusp of a new technological drive.

This chapter continues with an overview of microorganism motility and three-dimensional imaging in general. A survey of the theory of holography as it applies to digital holographic microscopy follows in chapter 2. Chapter 3 represents the bulk of my time spent over the last two years in designing and building the digital holographic microscope. Chapters 4 and 5 divulge the experiments to calibrate this microscope and to discern its capabilities in both inline and off-axis holography. A brief look at a microbiological application is presented in chapter 6: that of tracking swimming *Escherichia coli* cells in three dimensions. Finally, conclusions and considerations for the future of this project are to be found in chapter 7.

I am pleased that such a positive piece of technology has grown out of the original remote sensing project, even if it took almost two years to commence. As is often the case in life, the destination is not always apparent at the start, nor even halfway through the journey. The image that serves as a frontispiece to this thesis is one of the first holograms acquired on my microscope, dated 4$^{\text{th}}$ August 2010. I certainly could not have foreseen then what form the descendant of that image would take today, nor even where it will go tomorrow. To requote Cicero: "Everything has a small beginning."

1.2 Introduction

The invention of the compound light microscope around the turn of the 17th century, and Antonie van Leeuwenhoek's later discovery (using a simple microscope) of microorganisms [1], revolutionised our understanding of the world.

Over the centuries, numerous technological developments in lens manufacture and illumination sources have given us greater insight into the structure and motion of cells and inorganic matter. Such innovations have been the bedrock upon which our experimental investigations into the microworld have been founded. In terms of

optical microscopy, the 20th century saw us go beyond the optical diffraction limit, using techniques such as structured illumination [2] or fluorophore localisation [3–5], imaging increasingly smaller objects and unlocking some of the secrets of dynamic processes within cells.

However, these now-conventional microscopy techniques are fundamentally limited to investigating a two-dimensional plane. For many dynamic microscopic processes, this gives us only a slice of the whole story as cells and microorganisms, in general, inhabit a three-dimensional world.

This thesis seeks a technological solution to obtaining a high-speed, three-dimensional view of the dynamics of motile microorganisms. At the extreme end, to investigate the fluid flow around microorganisms by, say, imaging tracer nanoparticles, one might wish to record data over a field of view several tens of microns across at framerates of many hundred frames per second (fps). The spatial and temporal resolution criteria are relaxed slightly for investigating the motion of, say, a 2μm bacterium capable of swimming at $30\mu\text{m.s}^{-1}$. In this case we might wish for a field of view several hundred microns across and a recording framerate of at least 50fps. Although, $30\mu\text{m.s}^{-1}$ is by no means the fastest recorded speed for a microorganism and recording at higher framerates would allow for more detailed study of transient motility processes. While some novel techniques are starting to yield three-dimensional information of biologically relevant objects, these techniques are typically too slow to aid an investigation into cell motility [6], operate on either a smaller [7] or larger [8] length scale than is desirable for this thesis, or are best suited to examining the topology of cells or membranes [9].

It is hoped that the development of an instrument that affords us a truly 3D and high-speed view of the microworld will be a foundation upon which an even greater understanding of the behaviour of microorganisms can be established.

1.3 Bacterial Motility

While an instrument designed to probe the dynamic three-dimensional nature of the microworld should be able to investigate any number of the creatures that inhabit it, we need an initial test pilot. Thus, drawing on the experience and resources of the Berry Laboratory, at the hub of this study is the bacterium.

Escherichia coli has long been considered a 'model organism', studied the world over. A rod-shaped bacterium typically 2μm in length, *E. coli* has a number of long helical filaments (four, on average) attached to rotary molecular motors embedded in its cell envelope [10–13]. Counter-clockwise rotation of these motors drives the filaments, known as flagella, to form a super-coiled bundle behind the cell and propels the organism in a forward direction in a fluid environment. This forward propulsion is termed a 'run'. Clockwise rotation of even one of the motors breaks the bundle and the forward motion of the organism, casting it into a random reorientation known as a 'tumble' [14]. While it is generally acknowledged that hydrodynamic forces must play an important role in the formation and disruption of the flagellar bundle, the exact nature of the flows these forces generate has not yet been observed nor completely explained, although some investigators have attempted models [15–18].

The organism actively navigates its environment through randomly switching from counter-clockwise to clockwise rotation of the motors [19], resulting in a series of runs and tumbles. This process is biased through a process known as 'chemotaxis', whereby chemical attractants or repellents in the external medium affect the binding of the chemotactic signalling protein CheY to the motor inside the cell [20–22]. This in turn affects the likelihood of a motor 'switching' directions.

During a run, *E. coli* can swim at speeds of around 30μm.s^{-1} [23]; other species of bacteria have been observed at speeds up to 147μm.s^{-1} [24]. The length scale of a bacterium means that it operates in a low Reynolds number environment [25]. The Reynolds number (Re) is a dimensionless quantity relating the inertial and viscous

forces in a fluid environment:

$$\mathrm{Re} = \frac{\rho_{\mathrm{med}} v_{\mathrm{obj}} L}{\mu_{\mathrm{med}}} \tag{1.1}$$

where ρ_{med} and μ_{med} are the density and dynamic viscosity of the fluid medium respectively, v_{obj} is the velocity of the object (a swimming bacterium in this case), and L is the characteristic length scale (1μm for a bacterium). In a low Reynolds regime ($\mathrm{Re} \approx 10^{-4}$), the viscous forces of fluid shear movement dominate the inertial forces of accelerating particles, meaning that when an object ceases to propel itself it comes to an instant stop with no inertial 'coasting' [26].

E. coli is only one of many species of motile bacteria, though perhaps the most studied. These species represent an astonishing collection of morphologies with a huge array of techniques for navigating their environment. Motile bacteria may have one, many or no flagella [27–30]; these may be located randomly on the cell body or in specific locations; the cells may employ chemotaxis or they may be sensitive to light, oxygen levels, temperature or magnetic fields [31–33]. Despite substantial work having been done on the nature of bacterial motility, many of the questions as to why these organisms have evolved in this manner remain unanswered.

Experimental parameters of interest when studying the motility of bacteria include: run length, run speed, tumble time and reorientation angle. To obtain an understanding of the swimming strategies of different organisms and different strains in different biochemical environments, many records of swimming paths would need to be acquired and analysed. The benchmark experiments for three-dimensional observations of bacterial motility, performed by Howard Berg and colleagues, used a microscope that tracks an individual cell by physically moving the microscope stage such that the identified cell remained constant to an array of photomultiplier detectors [34]. Position data were acquired at 12 points per second [35]. Needless to say, many experiments would need to be performed to gather data in the quantities required for a meaningful statistical analysis.

A further interesting question around bacterial motility is the mechanism through which individual, planktonic cells come together to form symbiotic relationships as a precursor to the formation of a biofilm [36]. Biofilms have been implicated in a large number of human infections and are difficult to treat [37], yet we still do not have a complete picture of how these aggregates of cells come to form. Looking at a single cell moving in three dimensions over time is not sufficient to understand the cell-to-cell interactions and population behaviour involved in biofilm formation. Meanwhile, conventional microscopy techniques give us only a two-dimensional snapshot of the positions of cells at any given time, from which we need to infer the full 3D nature of their movement [38]: again, not a satisfactory solution.

1.4 Probing the Third Dimension

As well as increasing our understanding of bacterial motility, there is a host of applications where it is clear that a three-dimensional understanding of the microworld is necessary to make further inroads. The field of microbial hydrodynamics, initiated by experimental observations, has for a while now been the domain of theoreticians [39–42], with experimentalists having all but exhausted the available 2D microscopy techniques for generating new information. Groups are interested in the motility and hydrodynamic interactions of sperm [43, 44], algae [45–47], crustaceans [48], and protozoae [27], all of which have different environment-navigation and swimming strategies [49], as well as the possibilities of designing bespoke, autonomous microswimmers [50, 51]. It is increasingly clear that a three-dimensional understanding of the way in which these organisms move, of how they interact with each other and the rest of their environment, and of the forces generated when swimming, would be of great benefit.

Along with other methods, microorganisms are being used in the burgeoning field

of microfluidics to provide pumps or mixers for novel devices [52–55]. A 3D model of the flows generated in such devices would lead to more exact characterisation of the instruments and improve the efficiency of future designs. There is also interest in 3D anomalous diffusion processes and being able to experimentally verify established theoretical models [56, 57].

In a fluid environment, there are two main approaches to experimentally studying the motility and fluid dynamics of microorganisms. One method is to study directly the organism or cell, identifying it in each subsequent frame of a video recording and inferring its motion by studying the 'tracks' made in space over the course of the recording. This is the method of Berg's microscope seen in [34] and in numerous two-dimensional studies of microorganisms, such as [58, 59]. The second approach is to seed the fluid with a suspension of tracer particles, which are localised in each frame as a proxy for the fluid environment. In this case the tracks of the tracers are used to inform on the motion of the fluid around a swimming microorganism of interest. Attention must be given to the size and concentration of the particles (as discussed in, for instance, [60–62]) so that they do not impede upon the natural behaviour of the organism but still give as complete an understanding as possible of the surrounding fluid. Such a technique is called 'particle image velocimetry' (PIV) and has long been a feature of both macro- and microscopic studies in fluid environments [62–65]. Some researchers have combined these two methods and have, at least in two dimensions, tracked both a microorganism and a field of tracer particles [47].

Of course, a number of techniques have been developed over recent years to explore the three-dimensional microworld. Confocal microscopes and similar techniques employ either a scanning stage or scanning objective to move the sample relative to the imaging focus [6]. While spinning disk confocal microscopy techniques can record two-dimensional images at many thousands of frames per second, the best 3D tracking technique is limited to an acquisition rate of 30Hz with an isotropic localisation

resolution of around 5μm [66]. Two cameras set orthogonally to one another can be effective at imaging larger organisms in three dimensions as exhibited by the Goldstein group [8]. Defocusing techniques have also been used for the 3D localisation of both fluorescent and bright field samples. Analysis of the size of the image of a defocused particle by Toprak *et al.* [67] gives the depth location in a split-view defocusing (bifocal) setup. Two groups have used a mask of three pinholes arranged as a triangle that separates each object of interest into a triangle of three images [68, 69]. Measuring the dimensions of the triangle gives a direct relation to the displacement along the optical axis from the focus. Cylindrical (anamorphic) lenses have also been used to assess the depth of spherical samples through measurement of the eccentricity of the ellipse image [70]. Stereoscopic techniques [71] can determine the axial displacement of an object through viewing (and possibly illuminating) an object from two different angles and analysing the in-plane displacement between the stereo image pair. Finally, optical models of the Mie scattering behaviour of spherical objects, such as polystyrene microspheres, can be applied to recorded digital micrographs in order to localise the objects in three dimensions [72].

The brief for this project was to be able to study motile bacteria in an environment as natural as possible. The chosen imaging modality had to provide sufficiently high magnification to resolve the organisms, as well as any tracer particles with which we may wish to seed the fluid. It had to be able to resolve odd-shaped samples and not be restricted to spherical microbeads or fluorescent particles. It needed to record images fast enough to capture the dynamic processes of bacterial reorientation. This criterion precluded any form of scanning stage technique, which are inherently too slow to observe bacterial swimming. Additionally, the effect the presence of a surface has on the swimming behaviour of bacteria has been well-documented [76–78]. It is desirable to be able to study the free-swimming behaviour of bacteria, away from walls and surfaces. This requires the ability to detect cells and tracer particles at

least 20μm away from a surface. The original brief also anticipated combining optical trapping [79] techniques with the microscopy, thus the ability to use a 100$\times$ objective was considered critical.

Table 1.1 shows a summary of the various methods considered when embarking on this three-dimensional microscopy project. Given the pros and cons of the various approaches considered, it was decided that digital holographic microscopy was the only option that satisfied these criteria. Use of an anamorphic lens, for instance, as found in [70] is primarily restricted to studying spherical particles, which precluded its use for imaging non-spherical bacteria. Both the bifocal imaging [67] and stereoscopic microscopy techniques [71] have an observational range that is too limited along the imaging axis; thus, these methods could not recover position information from sufficiently deep into the sample to be clear of surface interactions. Spinning disk confocal microscopy such as that found in [6], while an impressive microscopy technique, can still only capture three-dimensional data at a few tens of frames per second, which was deemed too slow for our applications. Additionally, fluorescent tracer particles are required preventing the tracking of individual (non-fluorescent) cells, and the equipment itself was prohibitively expensive. The orthogonal objective technique described in [8] was appealing due to the quality of results obtained for tracking protists such as *Chlamydomonas reinhardtii* and *Volvox carteri* as well as measuring the flow field around *Volvox* using particle image velocimetry techniques. Regrettably, these specimens are several times larger than the bacteria we wished to investigate; the technique requires the specimen to be studied in a cuvette and is thus not scaleable to the high magnifications required to study bacteria on a microscope slide. While the pinhole defocusing techniques presented in [68] and [69] were appealing for the simplicity in the apparatus design, concerns were raised over the potential for the technique to successfully analyse densely-seeded samples.

Ultimately digital holographic microscopy [73,80] was settled on as the option that

best addressed our needs; it is capable of being customised to a range of magnifications, is optically robust, interfaceable with other optical techniques such as optical trapping and fluorescence microscopy and is economically competitive. Samples can be studied sufficiently far from surfaces to neglect surface interactions and samples need not be restricted to spherical or fluorescent tracers. Additionally, the acquisition rate of the technique is limited only by the digital camera hardware and the stage requires no actively moving parts, increasing the stability of the system.

The expansion in popularity of holographic microscopy techniques in a range of different applications found in the literature since 2010 (see [44,81–90] for instance) is an indication of both the robustness of the technology and its promise for the future.

1.5 Recent Developments in Holography

The field of holography is most certainly mature: it is now over 60 years since Dennis Gabor's Nobel Prize-winning invention of "a new microscopic principle" [91]. The term 'hologram' has since entered the vernacular, and 'classical' (that is, film-based) holography has been used in myriad applications over the decades. The principles of holography are well-understood and details of these and of classical applications may be found in the following references: [92–95].

The developments of affordable, high-resolution and high-speed digital cameras, along with increased computer processing abilities, have seen holography enter a new phase over the last two decades. While the first digital processing of a hologram was performed in 1967 [96], it was not until the early 2000s that digital holographic microscopy started to supersede film-based techniques. Meng *et al.* chart the developments from film- to digital chip-based holography for micro-PIV experiments [97]. In short, digital camera pixels needed to be sufficiently small to resolve micron-scale objects; these cameras needed to have sufficiently fast framerates for video imaging;

and computers needed to be powerful enough to reconstruct three-dimensional electromagnetic fields in a timescale that was deemed useful. These developments drew researchers away from expensive and highly technical film-based microscopes and opened holographic microscopy to a much wider audience. The advantages gained in cost, ease of implementation and versatility are seen by most to outweigh the loss of resolution in moving from holographic film to digital pixels [97].

Digital holographic microscopy has since been used for metrology applications, achieving sub-nanometer precision along the optical axis[1] [98], to characterise micro-electromechanical systems [99] and to image the birefringence of optical fibres [100]. It has been applied to micro-PIV applications examining the time-averaged fluid flow in microtubes [101] and microfluidic channels [102], and to track a variety of individual micro-objects in fluid environments [73, 103, 104].

It was recognised at the start of the 2000s that digital holographic microscopy could play a large role in biological imaging [105] and we have seen DHMs used to study algae [81, 103], copepods [48], dinoflagellates [106] and mammalian cells [107]. Digital holographic microscopy has been combined with optical tweezers [108] and fluorescence imaging [107]. Holographic microscopy has even been used to localise gold nanoparticles inside live murine fibroblasts [86]. Two recent reviews [82, 85] and a textbook [95] dedicated to digital holographic microscopy highlight the importance of this burgeoning and rapidly maturing field.

However, despite the enormous promise shown by digital holographic microscopy over the last decade in a diverse range of applications, it is yet to be realised in a meaningful way in the fields of 3D transient flow analysis and 3D microorganism motility. While the aforementioned references show the promise of applying DHMs to understanding the three-dimensional swimming behaviour of microorganisms, what has been lacking so far is a way in which to do this quickly and for large populations.

[1] That is, measuring the height variation of a sample.

The same can be said for transient micro-PIV, which relies on tracking many particles over individual frames to obtain individual particle velocities rather than a time-averaged flow profile. It seems that despite advances in computing, we still lack the processing power and memory storage to efficiently process the huge arrays of often high-resolution digital holograms required for these applications.

It is here where the even more recent development of graphics processing units (GPU) for the scientific community promises to unlock holographic microscopy in a way that has not yet been seen. Digital holographic processing is ideally suited to the parallel processing capabilities of GPUs, which could see an increase in computation speeds of several orders of magnitude over current CPUs. However, NVIDIA, the leading manufacturer of scientific GPUs, only released a software language to allow consumers to program these devices in 2006; thus, the technology is only now leaving its infancy.

From movies to displays [109] and now to microscopy, it is clear that we are embarking on a revolution in three-dimensional imaging. The Grier group is one of the early adopters of GPUs for holographic reconstruction [104] and others are now following. As GPU technology itself matures and as more groups adopt to more efficient processing techniques, I believe we will see an explosion in high-throughput, high-speed 3D holographic imaging.

Technique	Method	Pros	Cons	Reference
Anamorphic Lens Imaging	Cylindrical lens element placed in front of image-forming lens. z-displacement calculated by analysis of eccentricity of resulting ellipse.	Optically simple to implement.	Densely-seeded samples would be difficult, as would non-spherical objects.	Chen *et al.* 2009 [70]
Bifocal Imaging	Imaging path is split into two arms. One arm forms a focused image on a CCD, the other is deliberately defocused. z values determined by defocused spot size and diffraction rings.	Dual-imaging cassette is commerically available.	Relatively limited depth range. Camera resolution reduced.	Toprak *et al.* 2007 [67]
Confocal Microscopy	Spinning disk confocal allows for 1000s of full-frame (2D) images per second. z sectioning occurs by scanning objective with piezo actuator.	High spatial resolution and high magnification.	Expensive equipment. Fluorescent sample required. z scanning too slow for motility data.	Lima *et al.* 2006 [6] **Klein *et al.* 2012** [66]
Digital Holography	Coherent light scatters off particles interfering with unscattered light to form holograms. Use of diffraction theory reconstructs original light field that generated hologram pattern, or optical models used to fit data to theory.	Scaleable to high magnifications while retaining large depth of field. Acquisition is single shot and single image.	Computationally intensive. Effective analysis is potentially complex.	Ovryn *et al.* 2000 [72], Sheng *et al.* 2006 [73] **Su *et al.* 2012** [44]
Orthogonal Objectives	Two objectives (and cameras) are set orthogonally to the sample, which is contained in a cuvette. z analysis by comparing orthogonal images along the common axis.	Good for large microoorganisms.	Not scaleable to high magnifications on slides.	Drescher *et al.* 2009 [8] **Mochizuki *et al.* 2012** [74]
Pinhole Defocusing	Mask with three pinholes arranged as a triangle is set between the objective and image plane. Distances between vertices of triangles indicates z displacement.	Relatively simple analysis.	A lot of light lost due to the mask. Particle triplets overlap making dense samples difficult.	Pereira *et al.* 2007 [68]
Pinhole Colour Defocusing	Similar to above but each pinhole mask has a colour filter that aids in identifiying particle triplets in the image.	More robust than standard pinhole method.	Requires colour camera. Scaleability to high magnifications not obvious.	Tien *et al.* 2008 [69]
Stereo-microscopy	Sample illuminated by two fibres angularly displaced. Stereoimages separated by wedge prisms in Fourier plane. z determined by comparing relative x displacement in image pairs.	High magnification achievable.	Limited axial range.	Bowman *et al.* 2010 [71] **Bowman *et al.* 2011** [75]

Table 1.1: Summary of three-dimensional microscopy techniques circa 2010. Where the techniques have progressed since 2010, a reference to the most recent technology is given in bold.

Chapter 2

Theory of Digital Holographic Microscopy

This chapter provides an outline of the theory behind holography, especially as it pertains to digital holographic microscopy. Some relevant mathematical preliminaries and physical concepts relating to the nature of light are discussed initially.

2.1 Mathematical and Physical Preliminaries

2.1.1 The Wave Nature of Light

Light can be thought of as an electromagnetic wave whose behaviour is governed by a set of four differential equations, which appeared in James Clerk Maxwell's 1861 paper *On Physical Lines of Force* [110]. In modern MKS[1] units, and in their differential

[1] That is: 'metre', 'kilogram', 'second'.

form, these equations are:

$$\begin{aligned} \nabla \times \mathbf{E} &= -\mu \frac{\partial \mathbf{H}}{\partial t} \\ \nabla \times \mathbf{H} &= \epsilon \frac{\partial \mathbf{E}}{\partial t} \\ \nabla \cdot \mathbf{E} &= 0 \\ \nabla \cdot \mu\mathbf{H} &= 0 \end{aligned} \tag{2.1}$$

where $\mathbf{E}$ and $\mathbf{H}$ are, respectively, the vectorial electric and magnetic fields of the wave, which are functions of position (x, y, z) and time t. Expressed in Cartesian coordinates these fields are: $\mathbf{E} = (E_x(t), E_y(t), E_z(t))$ and $\mathbf{H} = (H_x(t), H_y(t), H_z(t))$. μ and ϵ are, respectively, the permeability and permittivity of the medium of propagation. The ∇ operator is $\hat{\mathbf{x}}\frac{\partial}{\partial x} + \hat{\mathbf{y}}\frac{\partial}{\partial y} + \hat{\mathbf{z}}\frac{\partial}{\partial z}$, and $\times$ and $\cdot$ are the vector cross and dot products, respectively [92]. This thesis will adopt the convention of $\hat{\mathbf{z}}$ as the axis of propagation of the wave, or the 'optical axis'[2].

With the assumptions that the medium of propagation is linear, isotropic (independent of polarisation orientation), homogeneous (constant permittivity), non-dispersive (permittivity independent of wavelength) and non-magnetic ($\mu = \mu_0$, the permeability of the vacuum), the individual components of the electric and magnetic fields behave identically. Thus, the four Maxwell equations presented in equation 2.1 reduce to a single, scalar, wave equation:

$$\nabla^2 \mathrm{U}(x, y, z, t) - \frac{n^2}{c^2} \frac{\partial^2 \mathrm{U}(x, y, z, t)}{\partial t^2} = 0 \tag{2.2}$$

where $\mathrm{U}(x, y, z, t)$ represents any of the scalar field components. The Laplacian ∇^2 is defined as: $\hat{\mathbf{x}}\frac{\partial^2}{\partial x^2} + \hat{\mathbf{y}}\frac{\partial^2}{\partial y^2} + \hat{\mathbf{z}}\frac{\partial^2}{\partial z^2}$. n is termed the 'refractive index' of the medium and

[2]The ˆ symbol indicates the unit vector.

is defined:

$$n = \sqrt{\frac{\epsilon}{\epsilon_0}} \tag{2.3}$$

with ϵ_0 the permittivity of the vacuum. c is the speed of the electromagnetic wave in the vacuum and is given by:

$$c = \frac{1}{\sqrt{\mu_0 \epsilon_0}} \tag{2.4}$$

In the case of a monochromatic wave, the scalar field may be represented explicitly as:

$$\mathrm{U}(x, y, z, t) = \mathbb{R}\{\tilde{U}(x, y, z)\mathrm{e}^{-i\omega t}\} \tag{2.5}$$

or, in other words, the real part[3] of a complex function of position $\tilde{U}(x, y, z)$ and an oscillatory function of time. $i = \sqrt{-1}$, the usual imaginary unit. ω is the angular frequency of the wave and is related to its wavelength λ and velocity v by:

$$\omega = \frac{2\pi v}{\lambda} \tag{2.6}$$

$\tilde{U}(x, y, z)$ represents the amplitude $|U(x, y, z)|$ and phase $\alpha(x, y, z)$ of the wave at a given position coordinate and can be written explicitly as:

$$\tilde{U}(x, y, z) = |U(x, y, z)|\mathrm{e}^{i\alpha(x,y,z)} \tag{2.7}$$

By substituting the expression for the scalar field in equation 2.5 into the scalar wave equation (2.2), we arrive at the time-independent equation:

$$(\nabla^2 + k^2)\tilde{U}(x, y, z) = 0 \tag{2.8}$$

where k is known as the 'wavenumber' and relates to the angular frequency, the

[3]Signified by $\mathbb{R}$.

wavelength, the vacuum speed of light and the refractive index such that:

$$k = \frac{n\omega}{c} = \frac{2\pi n}{\lambda} \tag{2.9}$$

Equation 2.8 is known as the 'Helmholtz equation' after the 19th-century Prussian physicist Hermann von Helmholtz and is an adequate description of the electromagnetic field in monochromatic applications.

2.1.2 Scalar Diffraction Theory

The description in section 2.1.1 lays the foundation for what is known as 'scalar diffraction theory'. This theory was formulated in an effort to understand the phenomenon of 'diffraction', which is the apparent bending of waves at boundary interfaces. The concept of diffraction through an aperture is of crucial importance to holographic imaging.

Diffraction can be thought of using 'Huygens' principle' [111], which treats every point on a wave front as a source of secondary spherical wavelets. The sum of these secondary wave fronts gives the form of the diffracted wave at any given time. Implicit in Huygens' idea is that the secondary waves only travel in the initial direction of propagation. Figure 2.1 illustrates the diffraction of a spherical wave through an aperture using Huygens' principle to qualitatively describe the shape of the diffracted wave front.

A number of mathematical formulations exist to treat the problem of diffraction through an aperture [92,93,112]. These formulations are approximations in that they ignore the vectorial nature of the electromagnetic field, which results in a coupling of electric and magnetic field components at boundaries, and assume the scalar theory of light holds; this is to say that there exists a complex function of position that satisfies equation 2.8. Experimental research [113, 114] has shown that the scalar

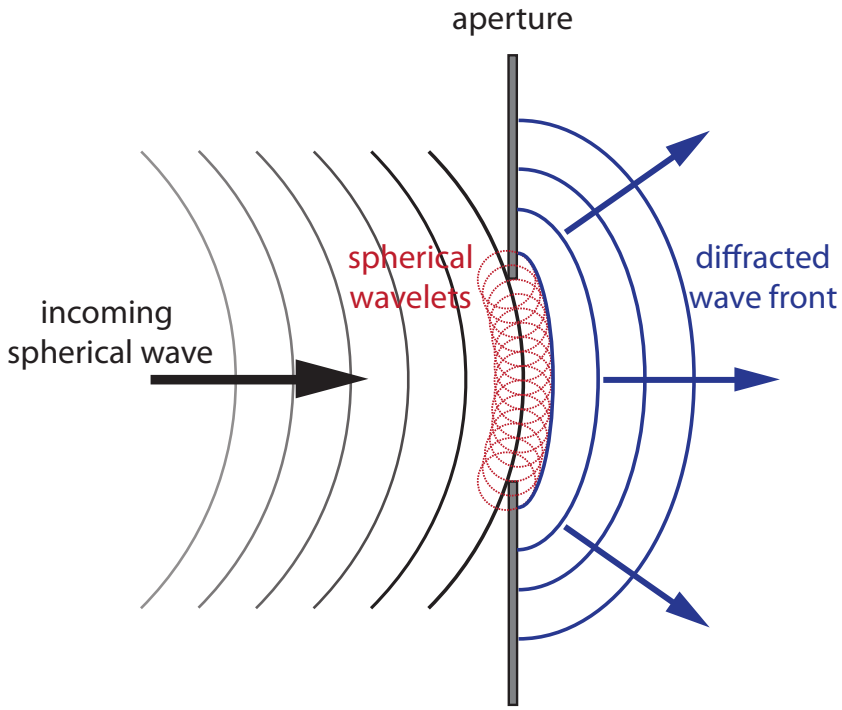

Figure 2.1: A spherical wave diffracts through an aperture. The shape of the diffracted wave front can be arrived at using Huygens' principle. The incident spherical wave front at the aperture is considered to be a source of secondary spherical wavelets (in red). These wavelets are summed over on the right hand side of the aperture to give the shape of the diffracted wave.

theory of diffraction through an aperture yields very good results as long as one observes sufficiently far from the aperture and providing the aperture is large when compared to the wavelength [92].

The problem we wish to solve is that of finding the complex position function $\tilde{U}(x,y,z) = |U(x,y,z)|\mathrm{e}^{i\alpha(x,y,z)}$ of the scalar field at a particular point in space after the wave has diffracted through an aperture. To do this, we need initially to invoke Green's theorem, the derivation of which can be found in [115]:

$$\iiint_V \left(\tilde{U}\nabla^2\tilde{G} - \tilde{G}\nabla^2\tilde{U}\right)\mathrm{d}v = \iint_S \left(\tilde{U}\frac{\partial\tilde{G}}{\partial n} - \tilde{G}\frac{\partial\tilde{U}}{\partial n}\right)\mathrm{d}s \tag{2.10}$$

where $\tilde{U}$ and $\tilde{G}$ are complex functions of position. V is a volume surrounded by a

closed surface S and $\frac{\partial}{\partial n}$ represents a partial derivative in the outward normal direction of the surface. Green's theorem holds providing $\tilde{U}$, $\tilde{G}$ and their first and second derivatives are continuous within and on the surface S.

To find the value of the field $\tilde{U}$ at a position $\boldsymbol{\rho}_0 = (x_0, y_0, z_0)$, we make a judicious selection of a 'Green's function' $\tilde{G}$ as well as the geometry of the surface S over which to integrate. One method commonly employed is that of Gustav Kirchhoff [116], who, drawing on the intuition of Huygens, chose as his Green's function an expanding spherical wave of unit amplitude and radius ϱ:

$$\tilde{G}(\varrho) = \frac{\mathrm{e}^{ik\varrho}}{\varrho} \tag{2.11}$$

For the problem of diffraction through an aperture in an opaque screen, Kirchhoff then applied boundary conditions that assume the field $\tilde{U}$ and its derivative $\frac{\partial \tilde{U}}{\partial n}$ are zero along the opaque screen and that, in the region of the aperture, they are unaffected by the presence of the aperture. Figure 2.2 describes the geometry of the situation.

To find $\tilde{U}(\boldsymbol{\rho}_0)$ we need to solve the surface integral on the right hand side of equation 2.10, with Kirchhoff's boundary conditions. As can be seen in figure 2.2, the surface S consists of two components: S_1, a planar surface lying directly behind the aperture; and S_2, a large spherical cap of radius ϱ centred on the point of observation. The Green's function for S_2 remains as in equation 2.11; however, on surface S_1 it must be modified to:

$$\tilde{G}(\boldsymbol{\rho}_1) = \frac{\mathrm{e}^{ik|\boldsymbol{\rho}_1 - \boldsymbol{\rho}_0|}}{|\boldsymbol{\rho}_1 - \boldsymbol{\rho}_0|} \tag{2.12}$$

Solving these surface integrals assuming illumination of the aperture is a spherical wave emanating from a point source yields what is known as the 'Fresnel-Kirchhoff diffraction formula'. Chapter 3 in [92] completes the details of the derivation.

Kirchhoff's approach is commonly employed in digital holographic applications

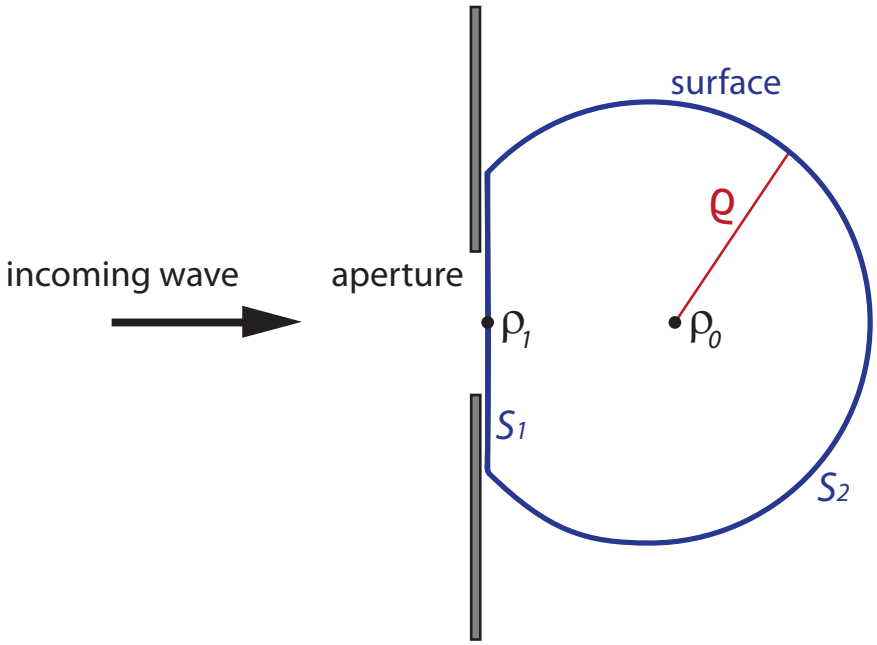

Figure 2.2: The geometry of Kirchhoff's approach to diffraction through an aperture. The surface of integration is shown in blue and centred on the arbitrary point $\boldsymbol{\rho}_0$. $\boldsymbol{\rho}_1$ is a point in the plane immediately behind the aperture.

[88, 105, 117]. However, there is an inconsistency in the approach that can be overcome: that of requiring both the field and its normal derivative to disappear at the opaque plane boundary. The 'Rayleigh-Sommerfeld' formulation removes this mathematical inconsistency by using an alternative Green's function for the S_1 surface. This assumes illumination at the aperture by simultaneous spherical waves generated at point $\boldsymbol{\rho}_0$ and at a mirror image of this point $\boldsymbol{\rho'}_0$ the other side of the aperture, illustrated in figure 2.3.

These point sources can oscillate either in phase or with a phase difference of π, thus leading to two Green's functions:

$$\begin{aligned}\tilde{G}_0(\boldsymbol{\rho}_1) &= \frac{\mathrm{e}^{ik|\boldsymbol{\rho}_1-\boldsymbol{\rho}_0|}}{|\boldsymbol{\rho}_1-\boldsymbol{\rho}_0|} - \frac{\mathrm{e}^{ik|\boldsymbol{\rho}_1-\boldsymbol{\rho'}_0|}}{|\boldsymbol{\rho}_1-\boldsymbol{\rho'}_0|} \\ \tilde{G}_\pi(\boldsymbol{\rho}_1) &= \frac{\mathrm{e}^{ik|\boldsymbol{\rho}_1-\boldsymbol{\rho}_0|}}{|\boldsymbol{\rho}_1-\boldsymbol{\rho}_0|} + \frac{\mathrm{e}^{ik|\boldsymbol{\rho}_1-\boldsymbol{\rho'}_0|}}{|\boldsymbol{\rho}_1-\boldsymbol{\rho'}_0|}\end{aligned} \tag{2.13}$$

where the subscript on $\tilde{G}$ indicates the initial phase difference of the sources. Although

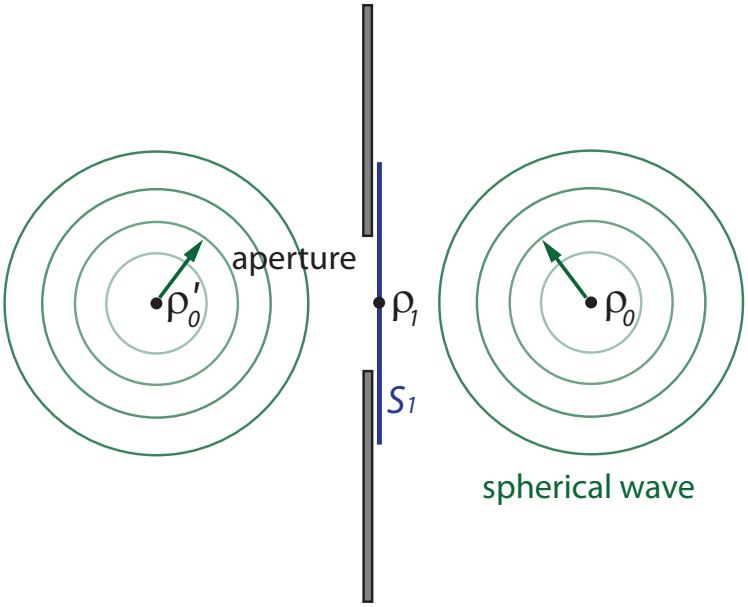

Figure 2.3: The Rayleigh-Sommerfeld solution to the inconsistencies in the Kirchhoff boundary conditions is to assume the aperture is illuminated by mirror image sources of spherical waves at $\boldsymbol{\rho}_0$ and $\boldsymbol{\rho'}_0$. 'True' illumination is still incident on the aperture from the left. Only the S_1 surface of integration over the aperture is shown.

not representative of the actual physical situation, in the context of digital holography, this approach to scalar diffraction theory generates more accurate results and requires only a minor increase in computing operations [90, 118].

The Green's functions in equation 2.13 can now be used to solve for $\tilde{U}(\boldsymbol{\rho}_0)$, resulting in the Rayleigh-Sommerfeld integral:

$$\tilde{U}_0(\boldsymbol{\rho}_0) = -\frac{i}{\lambda} \iint\limits_{Aperture} \tilde{U}_1(\boldsymbol{\rho}_1) \left(1 - \frac{1}{ik\varrho}\right) \cos\alpha \frac{\mathrm{e}^{ik\varrho}}{\varrho} \mathrm{d}^2\mathbf{r}_1 \tag{2.14}$$

where $\tilde{U}_1(\boldsymbol{\rho}_1)$ is any scalar field at the aperture, an inclusion that will become useful in the application to holographic reconstruction in section 2.6. Note that $\boldsymbol{\rho}_1 \equiv (\mathbf{r}_1, z_1) \equiv (x_1, y_1, z_1)$ and similarly for $\boldsymbol{\rho}_0$. Here, ϱ is the distance from a point in the aperture plane $\boldsymbol{\rho}_1$ to an arbitrary point in space $\boldsymbol{\rho}_0$ at which we wish to evaluate the field (on

a screen, for instance). Explicitly, in Cartesian coordinates:

$$\varrho = \sqrt{(x_1 - x_0)^2 + (y_1 - y_0)^2 + d^2} \tag{2.15}$$

where d is the distance along $\hat{\mathbf{z}}$ between the aperture and the point of observation. α is the angle ϱ makes with the optical axis, thus:

$$\cos\alpha = \frac{d}{\varrho}. \tag{2.16}$$

This geometry is displayed in figure 2.4.

Physically, equation 2.14 can be interpreted through Huygens' principle. The $\cos\alpha$ term is required to preserve the forward-directionality of the propagation, and $-i$ arrives from the nature of considering the wave fronts as secondary sources as opposed to primary sources[4] [93]. The superposition of many secondary sources lying in the aperture plane is arrived at by integrating over the entire aperture area. This yields the resultant field $\tilde{U}_1(\boldsymbol{\rho}_1)$ in the object plane.

For a derivation of the Rayleigh-Sommerfeld integral in equation 2.14 that demonstrates the integration explicitly see [92, 119]. These references also contain a direct comparison between the Kirchhoff and Rayleigh-Sommerfeld formulations. Pritchett and Trubatch [112] also offer an interesting alternative approach to deriving the scalar diffraction theory based on solving partial differential equations, as opposed to the integral methods shown above.

It is of interest to note that through the judicious choice of limits, two classic diffraction results can be arrived at using the Rayleigh-Sommerfeld integral in equation 2.14. Firstly, we apply what is known as the 'radiation approximation' [93], which assumes a radiative, as opposed to an evansecent, field. This is made by assuming

[4]This phase difference has no physical origin but is required for the Huygens model to 'work' mathematically.

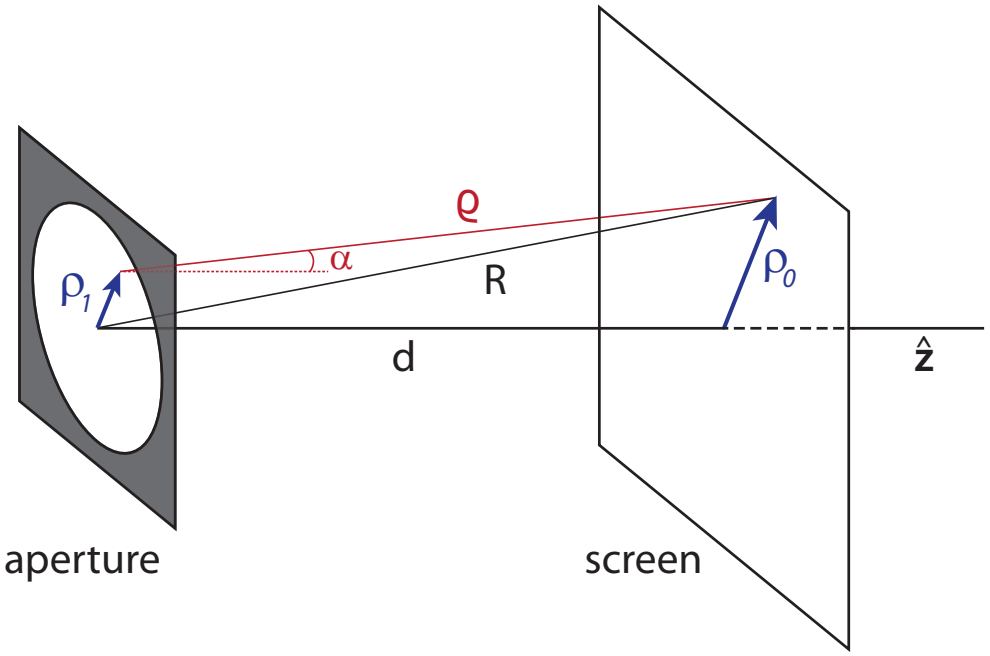

Figure 2.4: The geometry used in a generalised treatment of the diffraction of a wave through an aperture as described in the text. d is the distance from the aperture to the screen.

the wavelength of light is small compared to the observation distance [120]. That is, $\lambda \ll \varrho$ or $\frac{1}{k\varrho} \ll 1$. Thus, equation 2.14 becomes:

$$\tilde{U}_0(\boldsymbol{\rho}_0) = -\frac{i}{\lambda} \iint_{Aperture} \tilde{U}_1(\boldsymbol{\rho}_1) \cos\alpha \frac{\mathrm{e}^{ik\varrho}}{\varrho} \mathrm{d}^2\mathbf{r}_1 \tag{2.17}$$

Fraunhofer Diffraction

What is termed the 'Fraunhofer approximation' describes the behaviour of diffracting light in the far-field. That is, when the plane of observation is sufficiently far from the aperture that the diffracting light can be assumed to be parallel. Given the wavelength dependence of diffraction, this is tantamount to a small aperture approximation:

$$(\boldsymbol{\rho}_1^{\max})^2 \ll \frac{\varrho}{k} \tag{2.18}$$

where $\boldsymbol{\rho}_1^{\max}$ is the radius of the aperture, and thus the maximum coordinate of the field. In this case, ϱ can be expressed as a Taylor series [93], which to first order becomes:

$$\varrho \sim R - \frac{\boldsymbol{\rho}_1 \cdot \boldsymbol{\rho}_0}{R} \tag{2.19}$$

Making this substitution, equation 2.17 becomes:

$$\tilde{U}_0(\boldsymbol{\rho}_0) = -\frac{i}{\lambda}\frac{\cos\alpha}{R}\mathrm{e}^{ikR}\iint\limits_{Aperture}\tilde{U}_1(\boldsymbol{\rho}_1)\mathrm{e}^{-i\frac{k}{R}\boldsymbol{\rho}_1\cdot\boldsymbol{\rho}_1}\mathrm{d}^2\mathbf{r}_1 \tag{2.20}$$

which is the Fraunhofer diffraction integral.

In the case of a plane wave illuminating a circular aperture, Fraunhofer diffraction results in a radially symmetric diffraction pattern known as an 'Airy pattern' after the 19th-century English astronomer, George Airy. An Airy pattern is shown in figure 2.5. For diffraction through an aperture of area A and radius a, the observed intensity of an Airy pattern as a function of radius r can be represented mathematically by:

$$I(r) = \left(\frac{A}{\lambda d}\right)^2\left(2\frac{J_1(rka/d)}{rka/d}\right)^2 \tag{2.21}$$

where d is the distance of observation from the aperture and $J_1(rka/d)$ is the cylindrical Bessel function of order 1 [93]. It can also be shown[5] that the expression:

$$\mathcal{F}(r) = \frac{J_1(2\pi r)}{r} \tag{2.22}$$

is related to the circular aperture function, $\mathrm{circ}(\rho)$, by the Fourier transform operation with radial symmetry, $\mathscr{F}$:

$$\mathscr{F}\{\mathrm{circ}(\rho)\} = \frac{J_1(2\pi r)}{r} \tag{2.23}$$

[5]See [92] or [93] for instance.

ρ is the radius of the circular aperture, which is described by:

$$\text{circ}(\rho) = \begin{cases} 1 & \rho < 1 \\ \frac{1}{2} & \rho = 1 \\ 0 & \text{otherwise} \end{cases}$$

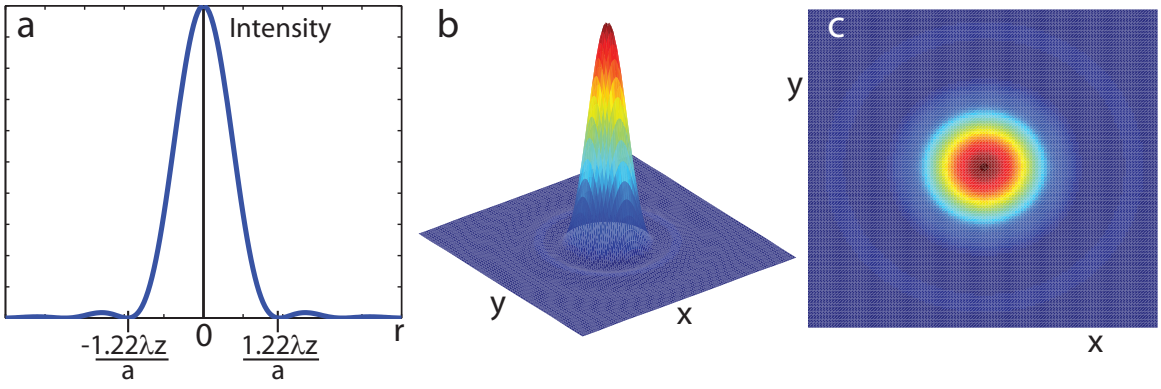

Figure 2.5: Diffraction through a circular aperture results in an Airy pattern, displayed in these images. *a*) shows a plot of the intensity in arbitrary units as a function of radius r. The first minimum of the pattern occurs at $\pm\frac{1.22\lambda z}{a}$, where a is the radius of the aperture, z is the distance from the aperture to the viewing screen and λ is the wavelength of light. *b*) shows a three-dimensional surface plot of an Airy pattern and *c*) illustrates the intensity of the pattern.

Fresnel Diffraction

The 'Fresnel approximation' describes the behaviour of diffracting light close to the aperture, in the near-field. Still assuming the radiative field condition in equation 2.17, Fresnel diffraction then holds that the path of light deviates only slightly from the axial propagation direction. This is known as the 'paraxial approximation' and allows us to adopt the small angle approximation: $\cos\alpha \sim 1$; as well as $\varrho \sim d$ in the denominator of equation 2.17. The Rayleigh-Sommerfeld integral becomes:

$$\tilde{U}_0(\boldsymbol{\rho}_0) = -\frac{i}{\lambda d} \iint_{Aperture} \tilde{U}_1(\boldsymbol{\rho}_1) \mathrm{e}^{ik\varrho} \mathrm{d}^2\mathbf{r}_1 \tag{2.24}$$

ϱ is then expanded as a Taylor series in $|\boldsymbol{\rho}_1 - \boldsymbol{\rho}_0|^2$, which to first order is:

$$\varrho \sim d + \frac{|\boldsymbol{\rho}_1 - \boldsymbol{\rho}_0|^2}{2d} \tag{2.25}$$

The Fresnel diffraction integral is arrived at by substituting the Taylor series expansion into equation 2.24:

$$\tilde{U}_0(\boldsymbol{\rho}_0) = -\frac{i}{\lambda d} \mathrm{e}^{ikd} \iint\limits_{Aperture} \tilde{U}_1(\boldsymbol{\rho}_1) \mathrm{e}^{\frac{ik}{2d}|\boldsymbol{\rho}_1 - \boldsymbol{\rho}_0|^2} \mathrm{d}^2\mathbf{r}_1 \tag{2.26}$$

This equation is valid in the near-field [93], which is to say:

$$|\boldsymbol{\rho}_1 - \boldsymbol{\rho}_0|^4 \ll \lambda d^3 \tag{2.27}$$

and which applies for most optical microscopy applications.

Significantly, the Fresnel approximation can be used to show that a lens produces a Fourier transform of an image at its back focal plane. See, for instance, chapter 5 in [92] for details.

2.1.3 Interference of Light

One of the properties of waves is their ability to interfere. This phenomenon is most easily observed when two waves of the same wavelength superimpose to form a resultant wave of either larger or smaller amplitude, respectively termed 'constructive' or 'destructive' interference.

A classic experiment demonstrating interference in light is to use a Michelson interferometer, which separates a beam of light into two through a half-silvered mirror, or beam-splitter. The two beams reflect off additional mirrors and recombine at the beam-splitter. The distance of at least one of these mirrors from the beam-splitter can be adjusted. The resulting interference pattern is then displayed on a screen or

recorded on a camera. Figure 2.6*a* shows a schematic of a Michelson interferometer.

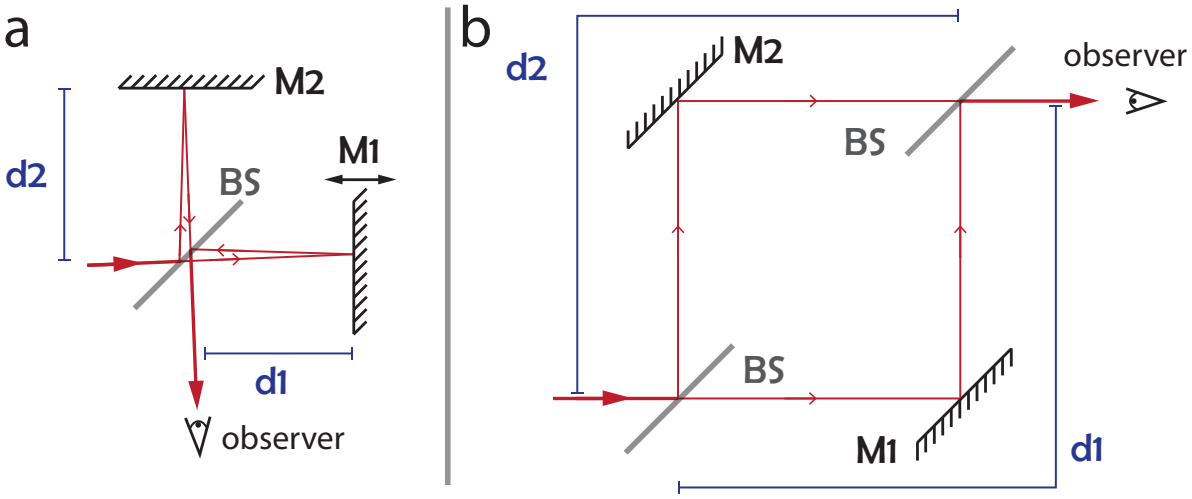

Figure 2.6: *a*) Schematic of a Michelson interferometer. An incoming beam is split into two by a beam-splitter (BS). The two beams then reflect off mirror M1 or M2 before recombining at the beam-splitter and passing to an observer (or a camera or screen). The angles of reflection have been exaggerated for clarity. Interference will be observed as long as the difference between $d1$ and $d2$ is no greater than half the coherence length of the light source. *b*) Schematic of a Mach-Zender interferometer. Two beam-splitters are used in this case, which allows for greater flexibility in inserting additional optical elements in the beam path. Similarly, interference will only be observed if the difference between $d1$ and $d2$ is not greater than the coherence length of the source.

All sources of light come with an associated 'coherence length' L related to its spectral width (that is, its range of frequencies) Δf:

$$L = \frac{c}{\Delta f} \tag{2.28}$$

where c is the speed of light. White light from, say, filament bulbs has a very large range of frequencies and thus a very short coherence length (on the order of several microns) [94]. Lasers are nominally monochromatic and thus have potentially very long coherence lengths. When a beam of light is split and then recombined as in the Michelson interferometer, for any interference pattern to be observed, the path difference between the two beams must be less than the coherence length. For light, maximum interference is observed when the two interfering beams are polarised along

the same direction.

Another configuration of an interferometer is that of Mach and Zender, shown in figure 2.6*b*. It is this geometry on which the off-axis holographic microscope described in section 3.8 is based.

2.1.4 Spatial Frequencies

Any signal can be represented as a sum of sinusoids of different frequencies and can thus be decomposed into its composite frequencies by taking the Fourier transform of the signal. A two-dimensional Fourier transform can be taken of an image leading to a 2D representation of the 'spatial frequencies' of the image. Mathematically, a two-dimensional Fourier transform of a function $f(x, y)$ can be represented as:

$$\mathcal{F}(k_x, k_y) = \int_{-\infty}^{\infty} \int_{-\infty}^{\infty} f(x, y) \mathrm{e}^{-i2\pi(k_x x + k_y y)} \mathrm{d}x \mathrm{d}y \tag{2.29}$$

where $\mathcal{F}$ is the Fourier-transformed function with k_x and k_y the coordinates in the Fourier domain.

High spatial frequencies correspond to sharp changes in intensities in the image or in other words, edges of objects. Low spatial frequencies correspond to bulk areas of similar intensity in the image.

Images can be analysed and manipulated in the Fourier domain, which is also known as 'frequency-space', and this is a critical technique for off-axis holography described in section 2.6.2.

The ability of an optical system to capture spatial frequencies is dependent on its 'numerical aperture' (NA). This value refers to the maximum angle at which a lens can capture light from a specimen and is conventionally defined:

$$\mathrm{NA} = n \sin \theta \tag{2.30}$$

where n is the index of refraction of the medium and θ is the half-angular width of the maximum cone of light captured by the lens. In most cases we can take the paraxial limit, assuming small angles; thus, $\sin\theta \sim \theta$.

In considering monochromatic imaging with a circular lens of finite radius, the 'coherent transfer function' describes the resolution of the optical system [121]. This is a function of Fourier coordinates k_x and k_y, more easily represented in two dimensions as: $\mathbf{k}_T = (k_x, k_y)$. Note that $k_T = |\mathbf{k}_T| = \sqrt{k_x^2 + k_y^2}$. Δk_T is termed the 'spatial bandwidth', and $\Delta r = \frac{2\pi}{\Delta k_T}$ is termed the 'spatial resolution'. $r = |\mathbf{r}| = \sqrt{x^2 + y^2}$, where $\mathbf{r} = (x, y)$, the spatial coordinates of the system. See chapter 3 in [93] for a complete derivation of the coherent transfer function.

For an ideal microscope imaging system with no aberrations, Δk_T is found to be:

$$\Delta k_T = k\Theta \tag{2.31}$$

where k is the total wavenumber of the wave and Θ is the full angular width of the lens; that is, $\Theta = 2\theta$.

By applying the paraxial approximation to equation 2.30 and recalling the definition for k in equation 2.9, we can express the numerical aperture in terms of spatial bandwidth:

$$\mathrm{NA} = \frac{\lambda}{2}\frac{\Delta k_T}{2\pi} \tag{2.32}$$

Making a substitution for Δk_T, the spatial resolution of an imaging system can be seen to depend on numerical aperture thus:

$$\Delta r = \frac{\lambda}{2\mathrm{NA}} \tag{2.33}$$

Equation 2.33 expresses what is known as diffraction-limited resolution. As seen in section 2.1.2 diffraction causes light incident on a circular aperture to form an Airy

pattern. Lord Rayleigh invented a criterion for resolving two point sources which considers the sources just resolved when the principal maximum of one Airy pattern lies over the first minimum of the second. This is demonstrated in figure 2.7.

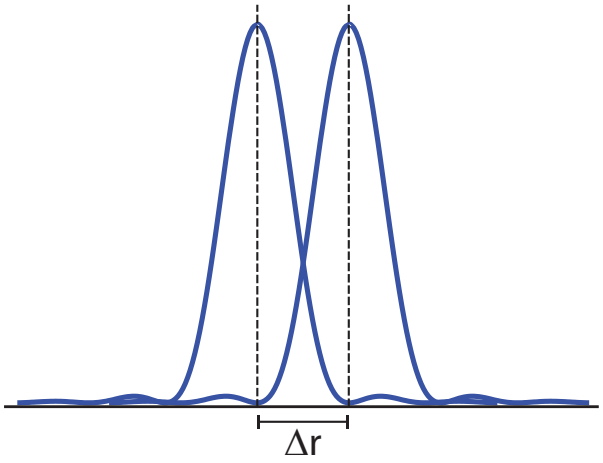

Figure 2.7: A point source diffracting through a circular aperture produces an Airy pattern; the form of the pattern's intensity is shown here. Rayleigh's resolution criterion states that two point sources are 'just resolved' if the maximum of one Airy pattern lies over the first minimum of the second. This is the case here, where Δr is the spatial resolution of the system.

Rayleigh's (angular) resolution criterion can be stated as:

$$\sin\theta = 1.220\frac{\lambda}{D} \tag{2.34}$$

where D is the diameter of the aperture and the 1.220 factor comes from the mathematical description of an Airy pattern (seen in figure 2.5). Related to the numerical aperture, the spatial resolution becomes:

$$\Delta r = \frac{0.610\lambda}{\mathrm{NA}} \tag{2.35}$$

which is approximately equal to the expression in equation 2.33, which made use of the paraxial approximation.

Increasing the spread of available angles incident on a lens (the numerical aperture

of the system) has the effect of producing a smaller Airy pattern from a point source. Thus a system with a higher NA can resolve smaller distances.

2.1.5 The Convolution Theorem

The 'convolution theorem' is a useful mathematical tool found in digital holographic reconstruction as described in section 2.6.

The two-dimensional convolution of two functions $f(x, y)$ and $g(x, y)$ can be defined as [92]:

$$(f * g)(x, y) = \int_{-\infty}^{\infty} \int_{-\infty}^{\infty} f(x', y')g(x - x', y - y')\mathrm{d}x'\mathrm{d}y' \tag{2.36}$$

with $*$ indicating the convolution. The convolution theorem then states that the product of the Fourier transforms of the two functions is equivalent to the Fourier transform of the convolution of the two functions:

$$\mathscr{F}\{f(x, y) * g(x, y)\} = \mathcal{F}(k_x, k_y)\mathcal{G}(k_x, k_y) \tag{2.37}$$

where $\mathscr{F}$ indicates the Fourier transform operator and $\mathcal{F}$ and $\mathcal{G}$ are the Fourier-transformed functions with k_x and k_y the coordinates in Fourier space.

2.1.6 The Nyquist-Shannon Sampling Condition

The digitisation of analogue signals is crucial for all applications that involve computational analysis. 'Sampling' is the term used to describe the conversion of an analogue, that is, continuous, signal into a discrete, digital signal. This occurs in digital holography through use of a charge-coupled device (CCD) or complementary metal-oxide semiconductor (CMOS) chip made up of an array of discrete pixels[6].

[6] A 'pixel' in this analogy is approximated by a point sampler. In reality, light incident on a pixel is averaged over the pixel area to produce the electronic signal. Neverless, a single, discrete

The Nyquist-Shannon sampling condition[7] states that in order for a signal to be successfully sampled, the sampling frequency must be at least twice that of the highest frequency in the signal [122]. If a signal is undersampled 'aliasing' occurs, leading to a false, lower-frequency component represented in the digital output.

Figure 2.8 demonstrates the effect of sampling and undersampling a simple one-dimensional sinusoid.

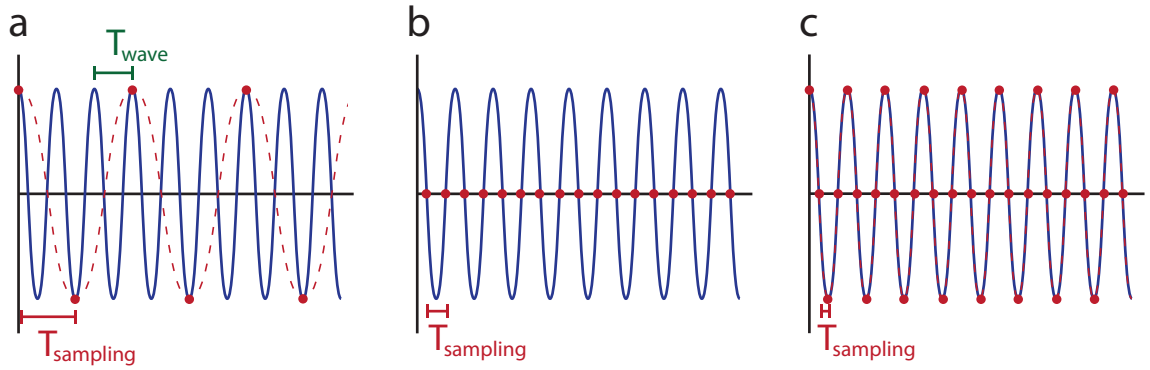

Figure 2.8: The effect of sampling frequency (f) on a simple one-dimensional sinusoid. The period ($T = 1/f$) of the analogue wave to be sampled is indicated in green. *a*) has a sampling period greater than that of the analogue signal, resulting in undersampling – the lower-frequency sampled wave is shown in red, with the red dots indicating each sampled value. *b*) is also an example of undersampling, which can occur when the sampling frequency is exactly double that of the analogue signal. For the signal to be sampled successfully, the sampling frequency must be strictly greater than twice the signal frequency. This is known as the Nyquist-Shannon sampling condition and is demonstrated in *c*), where the sampled signal (red) successfully overlays the original analogue signal (blue).

In digital holography, the spatial sampling is determined by the pixel spacing of the camera chip. This imposes a limit on the spatial frequencies able to be successfully captured in such applications. The practical implications of this are discussed in section 2.5.

'sampled' value for that area is returned.

[7]Often simply called the 'Nyquist condition'.

2.2 Principles of Holography

In general terms, holography is a two-part process. The first procedure is to record both the amplitude and phase of an electromagnetic wave scattered off (in reflection mode), or diffracted by (in transmission mode), an object. This is in contrast to conventional photography, which records the intensity (amplitude-squared) of the incident electromagnetic wave. In practice, this is achieved by illuminating an object with a coherent light source, interfering the resulting scattered light (the 'object beam') with a mutually coherent 'reference beam', and recording the resulting interference pattern on either analogue[8] or digital media. This process is sometimes called 'writing' the hologram.

The image of the object may also be magnified before recording. The reference beam may interfere with the object beam before magnification or the beam could be expanded in size in order to interfere with a conjugate image of the object further down the optical path.

There are two mainstream recording geometries used in holography: 'inline' as employed in Gabor's original technique [91], and 'off-axis', first developed by Emmett Leith and Juris Upatnieks [123]. The differences between these will be discussed below in sections 2.3 and 2.4.

Generally, we can consider the light emanating from the object and the reference source to obey the scalar theory of light, and thus to satisfy the time-independent Helmholtz equation (equation 2.8).

The object and reference waves can be defined, respectively, as:

$$\begin{aligned} \tilde{O}(\mathbf{r}, z) &= |O(\mathbf{r}, z)|\mathrm{e}^{i\phi(\mathbf{r},z)} \\ \tilde{R}(\mathbf{r}, z) &= |R(\mathbf{r}, z)|\mathrm{e}^{i\psi(\mathbf{r},z)} \end{aligned} \tag{2.38}$$

[8] Typically silver-halide film.

where ϕ and ψ are the respective phase factors and $\mathbf{r} = (x, y)$.

The intensity of the superposition of these two waves is recorded by the imaging device:

$$\begin{aligned} I_H(\mathbf{r}_H, z_H) &= |\tilde{R}(\mathbf{r}_H, z_H) + \tilde{O}(\mathbf{r}_H, z_H)|^2 \\ &= |R(\mathbf{r}_H, z_H)|^2 + |O(\mathbf{r}_H, z_H)|^2 \\ &\quad + \tilde{R}(\mathbf{r}_H, z_H)\tilde{O}^*(\mathbf{r}_H, z_H) + \tilde{R}^*(\mathbf{r}_H, z_H)\tilde{O}(\mathbf{r}_H, z_H) \end{aligned} \tag{2.39}$$

$I_H(\mathbf{r}_H, z_H)$ is the recorded hologram, where the subscript $_H$ signifies the hologram plane. The asterisk indicates the complex conjugate.

For transmission-mode holography, we assume a high average transmittance of the object [92, 108]. That is to say:

$$t(x_0, y_0) = t_0 + \Delta t(x_0, y_0); \quad \Delta t \ll |t_0| \tag{2.40}$$

where $t(x_0, y_0)$ is the transmittance of the sample written in terms of a constant base transmittance t_0 modified by a small variation Δt. Reflection-mode holography has not been used in this work, thus the specific details of reflection holography will not be discussed here.

The second component of the holography process is to 'reconstruct' this recorded hologram into a complex image by extracting the object term $\tilde{O}(\mathbf{r}_H, z_H)$. This procedure is also known as 'reading' the hologram. As the recorded interference pattern has encoded both amplitude and phase information of the object, the reconstruction process recovers the three-dimensional nature of the object. Classical holography records the interference pattern on high-resolution holographic film[9] [94]. After the

[9]Currently-available holographic film has a typical resolution of about 3000 lines/mm, corresponding to a grain size of around 330nm, although film for specialised reflection-mode holography can be found with resolution greater than 5000 lines/mm. As a comparison, conventional photographic film has a resolution of around 300 lines/mm.

film has been developed, the same light source is used to illuminate the film from the opposite side in order to optically reconstruct the object beam. Mathematically, this equates to multiplying $I_H(\mathbf{r}_H, z_H)$ by $\tilde{R}^*(\mathbf{r}_H, z_H)$ and equation 2.39 becomes:

$$\begin{aligned} I_H(\mathbf{r}_H, z_H)\tilde{R}^*(\mathbf{r}_H, z_H) &= |R(\mathbf{r}_H, z_H)|^2\tilde{R}^*(\mathbf{r}_H, z_H) \\ &\quad +|O(\mathbf{r}_H, z_H)|^2\tilde{R}^*(\mathbf{r}_H, z_H) \\ &\quad +|R(\mathbf{r}_H, z_H)|^2\tilde{O}^*(\mathbf{r}_H, z_H) \\ &\quad +\tilde{R}^{*2}(\mathbf{r}_H, z_H)\tilde{O}(\mathbf{r}_H, z_H) \end{aligned} \tag{2.41}$$

We are left with four individual terms; the third term is simply a purely real function multiplied by the conjugate of the desired object term, thus preserving the phase of the object term. The geometry of the reconstruction (see figures 2.9 and 2.12) means that this term forms a real image in the position of the original object that the viewer can observe. The subtleties in different holographic imaging approaches arise in separating these four terms in order to isolate this object term. The two major approaches to this problem are discussed in sections 2.3 and 2.4.

Digital holography differs from classical holography in that the recording medium is a charge-coupled device (CCD) or complementary metal-oxide semiconductor (CMOS) chip instead of film. The reconstruction procedure takes place in a numerical environment rather than optically. The optical reconstruction approach expressed in equation 2.41 can be performed numerically and can be a useful analogy. In practice, however, multiplication by the reference beam is not required. Numerical techniques instead focus on isolating the object beam term $\tilde{O}(\mathbf{r}_H, z_H)$ from the intensity recorded in equation 2.39, treating the hologram as an aperture and applying scalar diffraction theory in a numerical environment. This technique is called 'back-propagation' and is looked at in context in section 2.6.

2.3 Inline Holography

With inline holography the illumination beam doubles as the reference beam. Scattered light from the object interferes with unscattered light, creating an interference pattern that is directly incident on the recording medium. Figure 2.9 illustrates the geometry used in recording and reconstructing inline holograms. If magnification is used, the interference pattern is generated at the specimen plane of the magnifying lens. An image of this plane is then focused onto the recording medium. Figure 2.10 illustrates the formation of an inline hologram at the specimen plane.

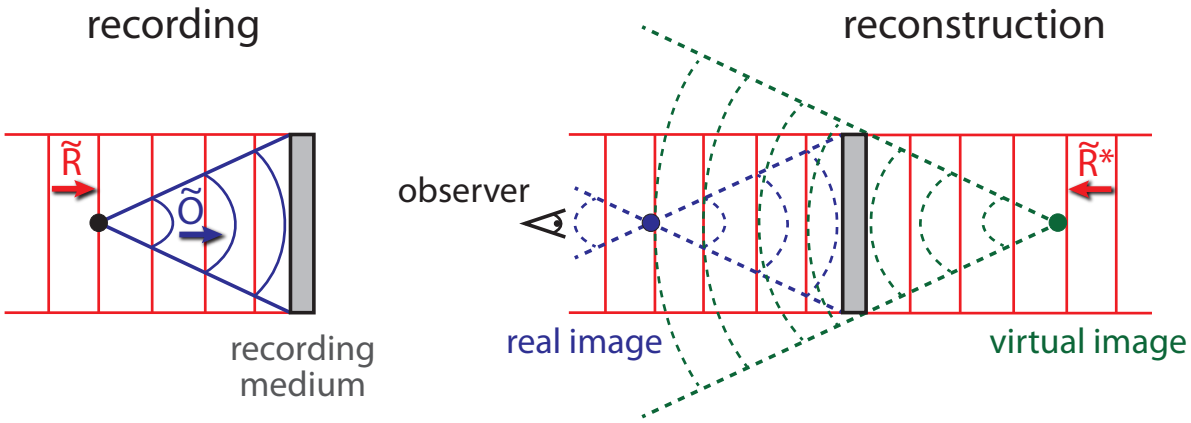

Figure 2.9: The geometry employed in recording and reconstructing an inline hologram. Note that from the point of view of the observer, the real and virtual images are overlaid: the so-called twin image problem. Additionally, the through-term from the reconstruction beam also reaches the observer, a feature that could also adversely affect the quality of the reconstructed image.

From equation 2.39, we may identify the four terms relative to the geometry of the reconstructed light field. The first term $|R(\mathbf{r}_H, z_H)|^2$ corresponds to a background related to the profile of the undiffracted illumination beam. Ideally, this is a uniform background across the whole image; although in practice, uneven illumination and artifacts in the imaging path from light scattering off dust on optical elements result in a background of non-uniform intensity. For a digital video holographic apparatus with a moving sample, a mean of an image stack over a particular time interval can be

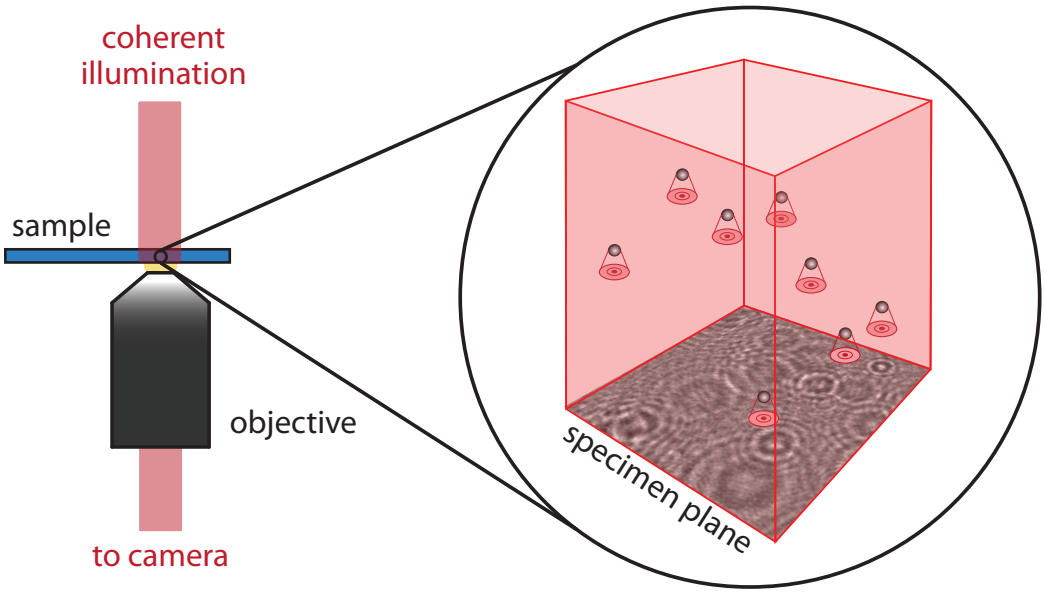

Figure 2.10: Schematic of hologram formation at the specimen plane of a microscope objective. The coherent illumination generates a diffraction pattern as light scattered off each object in the sample interferes with non-scattered light. The summation of all diffraction patterns at the objective specimen plane is captured by the imaging optics to form a focused image on the hologram recording device. Spherical particles, such as polystyrene microbeads, are represented here.

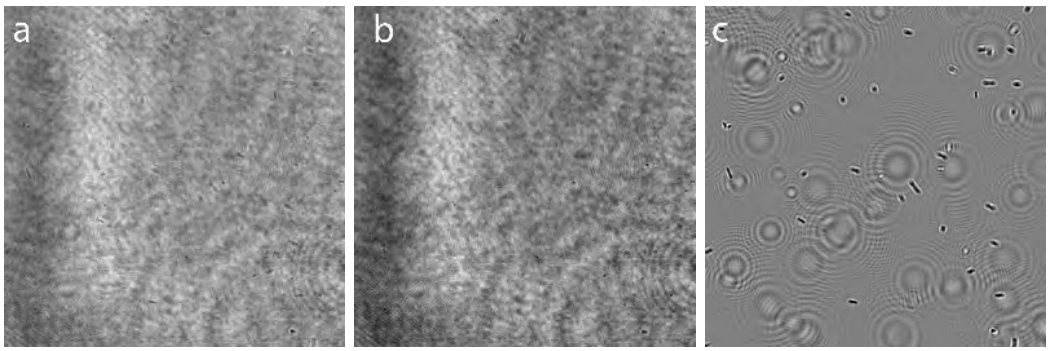

Figure 2.11: The efficacy of normalising an inline hologram can be seen in this set of three images. *a*) An inline hologram captured at a total magnification of 45× of motile *E. coli*. *b*) A reference image generated by taking the mean of an image stack recorded over 40 seconds. *c*) The hologram is normalised by dividing by the reference image. Note that the diffraction rings, representing the positions of bacteria, are clearly visible, whereas they are rather more difficult to see in the original hologram.

used to estimate and thus remove the background in a process called 'normalisation'. This involves dividing each hologram by a background reference image. For static samples, the sample can be moved out of the way and a separate reference image can be recorded. Figure 2.11 demonstrates the effect of normalising an inline hologram by a reference image generated by a time-averaged mean through an image stack and the effect of the procedure is shown mathematically in section 2.6.2.

The second term $|O(\mathbf{r}_H, z_H)|^2$ in equation 2.39 is termed the 'object halo' [85]. In transmission holography, given a high average transmittance of the sample, this term is negligible: $|O(\mathbf{r}_H, z_H)| \ll |R(\mathbf{r}_H, z_H)|$. At worst, it simply contibutes to noise.

The final two terms result in a focused real image and an out-of-focus virtual image. These two images are directly overlaid and are not separable with conventional inline techniques. This issue is termed the 'twin image problem' in holography [95, 124–126]. The result is that the phase of the object cannot be unambiguously recovered due to an unwanted artifact term from the virtual image. This could potentially lead to greater error in localising objects along the direction of the optical axis [127, 128].

Phase-stepping is one approach that retains the inline geometry, yet unambiguously recovers phase by using a stepper motor mirror to adjust the beam by a fraction of a wavelength [84, 129]. The downside to this technique, for use with dynamic samples, is that multiple images must be recorded, reducing the available maximum framerate. Spatial light modulators (SLM) have also been used to adjust the phase of the reference beam [130]. While SLMs give greater control over the shape and phase of the reference beam, they suffer from relatively slow refresh rates, similarly reducing the maximum framerate. Xu *et al.* [131] ignore the effects of the defocused virtual image by reasoning that if the source-to-sample distance is several thousand times the wavelength, the defocused twin image is an equivalent distance on the other side of the hologram. Thus, its signal is sufficiently spread over the available area of

the reconstruction that the observer sees to render it below the noise floor. Elements of this idea are discussed in a practical context in section 4.5.3.

In the 1940s Gabor was restricted to inline applications only due to the inferior coherence properties of light sources available at the time − the laser was not to be invented for another decade − and he acknowledged the limitations of the technique [132]. Yet, despite the drawback of the twin image problem, the advantages of inline holography are clear: it is easier to implement optically than off-axis holography; simple microscopes can be made very cheaply [133]; the apparatus can be miniaturised more readily − suitable for *in vivo* [83] and submersible applications [134]; arguably it allows for higher x-y resolution in digital applications as the off-axis reconstruction approach can require a clipping of the recorded hologram in Fourier space [125] (see section 2.4). The lack of unambiguous phase information and potential imprecision in localisation along the optical axis due to the twin image problem, when compared to off-axis holography, has seemingly not impeded the development of inline holography for myriad applications.

2.4 Off-Axis Holography

The critical difference between inline and off-axis approaches to holography is that the reference beam is set at an angle to the object beam in off-axis holography. This angle offset adds a carrier frequency to the signal and as long as this is sufficiently high, the twin image problem of inline holography can be avoided and the amplitude and phase of the light from the original object can be unambiguously reconstructed from the hologram.

For microscopy applications, off-axis holography necessitates splitting the illumination beam upstream of the object and recombining the reference wave with an image of the object captured at the objective specimen plane in front of the recording me-

dium. The most common approach is to use a Mach-Zender interferometer geometry, as in figure 2.6*b* [99, 117, 135], although other methods have been used [136–138]. Needless to say, in order for interference to be observed, the two beam paths need to have optical path lengths that are identical within the coherence length of the light source. An off-axis apparatus is generally more sensitive to noise from mechanical vibrations and air movement than an inline setup. This is because vibrations can affect the object and reference beams separately, and thus introduce relative, and transient, phase shifts.

The illumination of the object can be either direct (as per the inline case) or oblique. Two points for consideration are: firstly, that of the scattering profile of the object along the imaging axis in relation to the angle of incident illumination; secondly, that the illumination beam can be suitably blocked, deflected, or oriented such that it is not incident on the recording medium, otherwise an unwanted artifact will result. With digital holography, should the illumination beam end up incident on the camera, this term can be negated somewhat through numerical means. However, as the amplitude of the resulting object beam is generally a lot smaller than that of the illumination beam, a stronger signal will result if the illumination can be removed after the object, yet before the camera.

In the simplest and ideal case, the reference beam is a plane wave with a phase factor due to the angle δ it makes relative to the object beam:

$$\tilde{R}(\mathbf{r}_H, z_H) = |R(\mathbf{r}_H, z_H)|\mathrm{e}^{-ikx\sin\delta} \tag{2.42}$$

In this example, only an angle along $\hat{\mathbf{x}}$ is considered.

The interference pattern incident on the recording medium can now be seen to be:

$$\begin{aligned} I_H(\mathbf{r}_H, z_H) &= |R(\mathbf{r}_H, z_H)|^2 + |O(\mathbf{r}_H, z_H)|^2 + |R(\mathbf{r}_H, z_H)|\tilde{O}^*(\mathbf{r}_H, z_H)\mathrm{e}^{-ikx\sin\delta} \\ &\quad + |R(\mathbf{r}_H, z_H)|\tilde{O}(\mathbf{r}_H, z_H)\mathrm{e}^{ikx\sin\delta} \end{aligned} \tag{2.43}$$

The effect of the angled reference beam is to apply a linear phase shift along the x-axis of the recording plane.

Optical reconstruction involves illuminating the developed film at the same angle in order to separate the real and virtual images in the viewed image [92]. Figure 2.12 shows the geometry of off-axis recording and classical reconstruction.

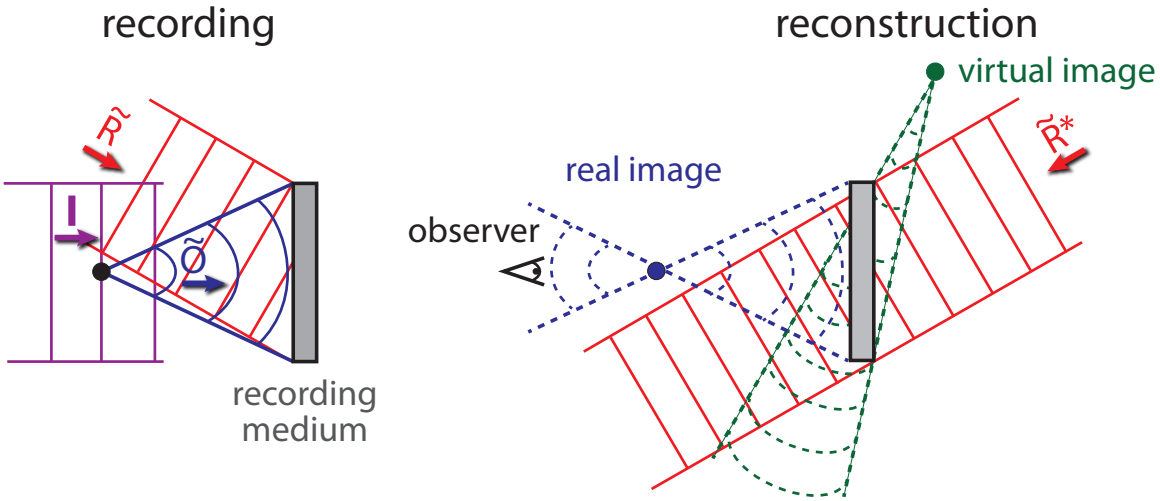

Figure 2.12: Classical recording and reconstruction geometry for off-axis holography. Note that, compared to the inline geometry in figure 2.9, the undiffracted reconstruction beam and the real and virtual images are now spatially separated from one another and that the observer only sees the real image.

In high-magnification digital applications it can be difficult to measure the exact angle between the reference and object beams. Fortunately, separation of the individual terms in equation 2.43 can be achieved numerically by taking a Fourier transform of the hologram and isolating the desired quadrant containing the spatial frequencies of the real image. This procedure is illustrated in section 2.6.2.

These individual terms are only separable if the angle offset δ between the object

and reference beams is above some minimum angle δ_{min}. The criterion for δ_{min} is that it must be sufficiently large so that the spatial frequency spectra of the phase-shifted twin images do not overlap each other nor overlap the spectra of the two direct terms $|R(\mathbf{r}_H, z_H)|^2$ and $|O(\mathbf{r}_H, z_H)|^2$.

The extent of the spatial frequency spectra, or spatial bandwidth Δk, of each of these terms is directly related to the numerical aperture of the system and the wavelength of illumination, as seen in equation 2.32. Considering the example of an angle between the reference and object beams applied along $\hat{\mathbf{x}}$ only, let us say the highest spatial frequency term in the object wave is k_x^{max}, noting that $\Delta k = 2|k_x^{\text{max}}|$. A schematic of the 2D Fourier transform of the intensity of a recorded hologram in equation 2.43 is shown in figure 2.13.

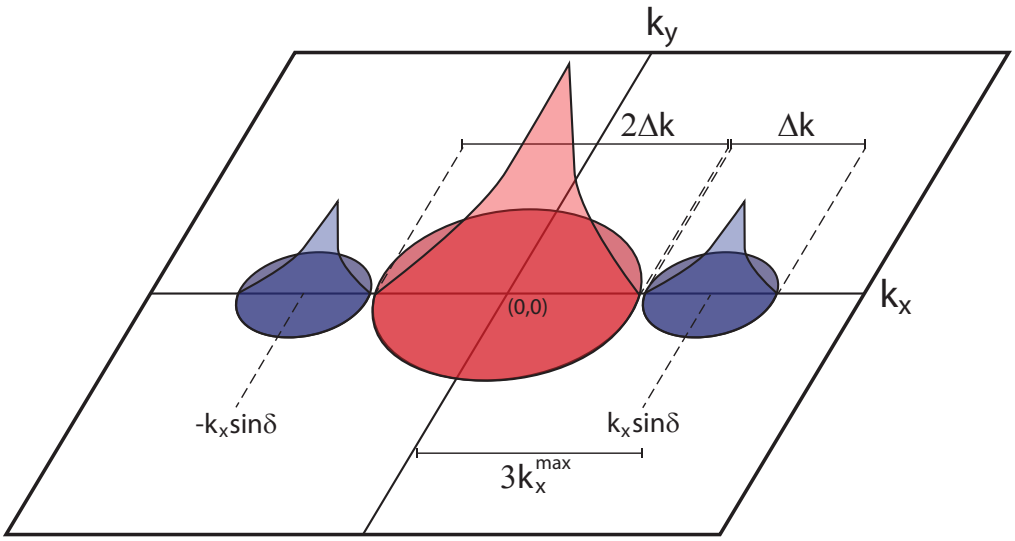

Figure 2.13: The spatial frequency, or Fourier, domain of an off-axis hologram, with a separation angle between the object and reference beams applied along $\hat{\mathbf{x}}$. k_x and k_y are coordinates in Fourier space. The spatial frequency spectra of the reference beam and object halo are represented in red, while those of the phase-shifted twin images are shown in blue. The centre of each twin image spectrum has been shifted from the centre by $\pm k_x \sin\delta$, where δ is the angle between the object and reference beams. To avoid overlap of frequency spectra, $k \sin\delta_{\text{min}} \geq 3k_x^{\text{max}}$.

The Fourier transform of the $|R(\mathbf{r}_H, z_H)|^2$ term is a delta function[10] centred on $(0, 0)$ in the spatial frequency plane, while the object halo term $|O(\mathbf{r}_H, z_H)|^2$ has a range of frequencies up to $2k_x^{\max}$. Thus, for the spatial bandwidth of an image term to be just clear of that of the object halo:

$$k \sin \delta_{\min} \geq 3k_x^{\max} \tag{2.44}$$

or, using the definition of numerical aperture and the relation in equation 2.32:

$$\sin \delta_{\min} \geq 3\mathrm{NA} \tag{2.45}$$

For high-magnification microscopic applications this condition is difficult to meet in the specimen plane. Instead, the two beams usually interfere at a conjugate image plane before the recording medium.

An additional constraint is found in digital holography with the relatively low-resolution digital recording media of CCD or CMOS sensors. In this case a maximum condition is imposed on δ to ensure aliasing does not occur if the twin images move beyond the limits imposed by the Nyquist-Shannon sampling theorem [139]. This is discussed further in section 2.5.

Off-axis holography shows advantages over inline holography in that the phase of the object beam can be unambiguously determined in a single image. Off-axis holography for phase imaging thus has a higher temporal resolution than comparable inline techniques, which rely on recording several phases per image. There are specific phase-contrast applications where this is of benefit − live-cell imaging in particular [80, 117]. Off-axis holography also has a higher tolerance of speckle noise [127] − a crucial factor when imaging densely-seeded samples − although Pu and Meng show the technique has its limits [128]. In addition, as the desired object beam is also

[10] For an ideal, infinite aperture.

separable from the reference beam, as well as from the virtual image in the reconstruction process, there is no need to normalise the hologram by an additional background image. This can also improve temporal resolution, and for samples that cannot be physically moved without disrupting the reference beam, off-axis holography is thus a requirement.

What off-axis holography gains in temporal resolution, it loses in spatial resolution, due to the physical separation of twin images in the Fourier plane [140] (demonstrated in figure 2.15 in section 2.6.2). This is of greater concern with digital media, which are comparatively low-resolution, than it was for holographic film. The optical implementation of an off-axis microscope is also less trivial; it is susceptible to mechanical noise and unable to be miniaturised to the extent that has been shown for inline holography. For digital applications, there is an additional computational expense (two fast Fourier transforms) per image, although with current computing power, this is not a significant obstacle.

Theoretical work over the last decade has focused on developing improved numerical reconstruction techniques for digital holography in order to achieve the phase imaging advantages of off-axis holography combined with increased area usage of the imaging chip. Some examples can be found in the following: [88, 126, 141, 142]; although this thesis adopts the conservative approach to off-axis reconstruction described above.

Off-axis holography has been most successfully implemented in phase-contrast applications, for imaging densely-seeded samples and in reflection-mode metrology applications [98,99,135]. Perhaps the largest impediment to its use in high-magnification transmission microscopy is the difficulty with which the illumination beam can be steered away from the camera. One group has recently demonstrated a principle that could help overcome this limitation [87] and this thesis also offers some solutions to this problem.

2.5 Considerations for Digital Holographic Microscopy

Holographic silver-halide emulsion consists of grains several hundreds of nanometers in size [94]. As CMOS and CCD technology will not allow for pixels of this size (typical pixel scale is 6.5μm or greater) digital holography is necessarily of a much lower resolution. The advantage of digital holography is that it does away with expensive, time-consuming chemical processing and the necessary digitisation to perform numerical analysis [97]. In theory, the entire process from recording to reconstruction and data analysis could be automated on computers.

Although not strictly true due to the area integration over a pixel, a digital hologram can be approximated as a two-dimensional spatial sampling of the incident interference pattern [95]:

$$I'_H(k,l) = I_H(x,y,z_H) \sum_{k}^{M} \sum_{l}^{N} \delta(x - k\Delta x, y - l\Delta y) \tag{2.46}$$

where the prime indicates the sampled hologram ($M \times N$). k and l are pixel indices along orthogonal directions on the CCD or CMOS chip and Δx and Δy are the dimensions of the pixels.

The chip size and pixel spacing influence the choice of holography and magnification of the image able to be implemented. Applications using off-axis holography in particular must pay attention to the maximum angular separation between the object and reference beams, which is determined by the pixel spacing. Consider the interference pattern generated by two plane waves meeting at angle δ. The fringe spacing is given by:

$$d = \frac{\lambda}{2 \sin \frac{\delta}{2}} \tag{2.47}$$

To avoid aliasing, the Nyquist condition outlined in section 2.1.6 results in a minimum

fringe spacing on a digital sensor of $2\Delta x$, thus the maximum resolvable angle between the two beams is:

$$\delta = 2\sin^{-1}\frac{\lambda}{4\Delta x} \tag{2.48}$$

to go along with the minimum angle separation for off-axis holography described in equation 2.44. In practice, both these conditions may not be met in high magnification digital holographic microscopy. Given a high average transmittance of the object, the effect of the object halo is argued to be negligible, as it is in processing of digital inline holograms [108]. Thus a recording geometry may be considered acceptable as long as the frequency spectra of the twin images are separated from each other. There also exist non-linear approaches to suppressing the object halo term through Fourier filtering [139].

Ultimately, a camera with smaller pixels is thus more desirable in this context. Section 3.3.1 discusses the practical implementation of this.

2.6 Numerical Reconstruction

2.6.1 The Hologram as an Aperture

Section 2.1.2 outlines the procedural approach to finding the complex position function of an electromagnetic wave having diffracted through an aperture. The matter of reading, or 'reconstructing', a hologram to inform us of the position function of the wave that originally generated the hologram is akin to the aperture diffraction problem. In this case, however, the aperture is the hologram with a non-zero intensity distribution that modifies the diffracting beam. Additionally, we wish to reverse the direction of the propagating wave, that is, to 'back-propagate' towards the original illumination source. The geometry of the reconstruction problem is shown in figure 2.14, which is a slight variation on the general case in figure 2.4.

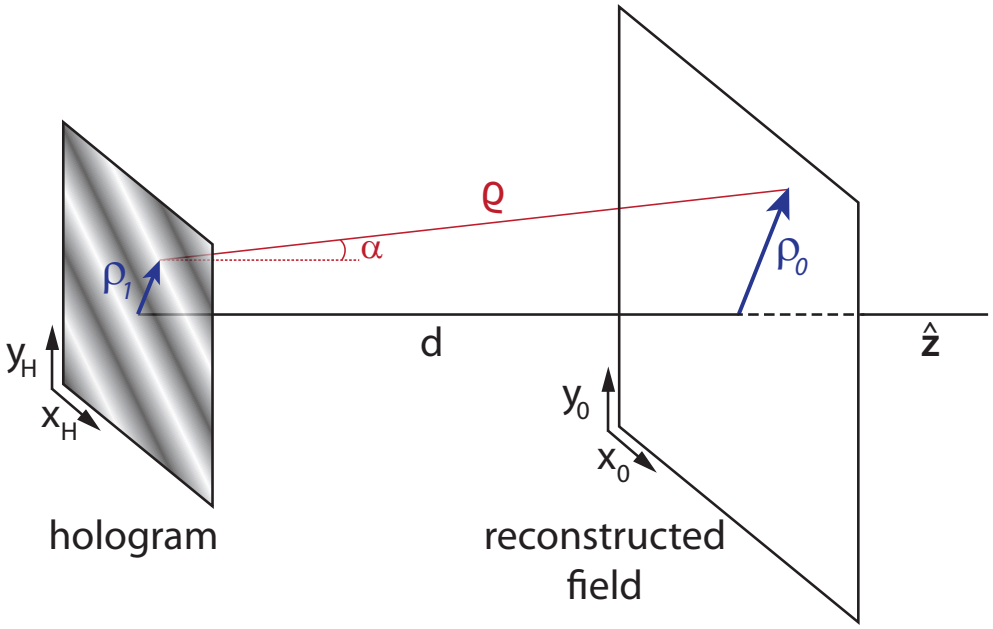

Figure 2.14: The geometry of the holographic reconstruction problem. The hologram on the left can be considered an 'aperture' through which a reference beam diffracts, retracing the path taken originally to record the hologram.

The Rayleigh-Sommerfeld integral of equation 2.14 can be rewritten with the explicit holographic reconstruction geometry:

$$\tilde{U}_0(\mathbf{r}_0, 0) = -\frac{i}{\lambda} \iint_{Hologram} \tilde{U}_H(\mathbf{r}_H, d) \left(1 - \frac{1}{ik\varrho}\right) \cos\alpha \frac{e^{ik\varrho}}{\varrho} \mathrm{d}^2\mathbf{r}_H \tag{2.49}$$

The subscript $_H$ represents the hologram plane and $_0$ indicates the original position of the wave we wish to find through reconstruction. $\mathbf{r}_H = (x_H, y_H)$, a 2D position vector in the hologram plane, and similarly for $\mathbf{r}_0$. The distance from a point in the hologram to the reconstructed object is now explicitly:

$$\varrho = \sqrt{(x_H - x_0)^2 + (y_H - y_0)^2 + d^2} \tag{2.50}$$

The integral expressed in equation 2.49 can be written as a 2D convolution using

the result shown in section 2.1.5:

$$\tilde{U}(\mathbf{r}, z) = \{\tilde{H}(\mathbf{r}, z) * \tilde{U}_H(\mathbf{r}, d)\}_{\mathbf{r}} \tag{2.51}$$

where the subscript on the reconstructed scalar field has been omitted for generality. $\mathbf{r}$ is the convolution variable, shown in the subscript on the right hand side, and $*$ indicates the convolution. The function $\tilde{H}(\mathbf{r}, z)$ is known as the 'Rayleigh-Sommerfeld free-space propagator' and can be thought of as propagating the scalar field from the hologram plane at $z = d$ ('backwards') through space to an arbitrary plane $z < d$. Explicitly, the propagator is:

$$\tilde{H}(\mathbf{r}, z) = -\frac{i}{\lambda}\left(1 - \frac{1}{ik\varrho}\right)\cos\alpha\frac{\mathrm{e}^{ik\varrho}}{\varrho} \tag{2.52}$$

The approximations used in section 2.1.2 are not required for finding numerical solutions. We can determine ϱ through knowledge of the hologram coordinates (x_H, y_H) and the distance z at which we wish to reconstruct. Applying the definition for $\cos\alpha$ in equation 2.16 and making a substitution for wavenumber, the propagator expression can be simplified to:

$$\tilde{H}(x_H - x, y_H - y) = \frac{z\mathrm{e}^{ik\varrho}}{\varrho^2}\left(\frac{1}{2\pi\varrho} - \frac{i}{\lambda}\right) \tag{2.53}$$

where the explicit Cartesian coordinate system has been reintroduced.

Thus, in order to find the three-dimensional complex field generated by an object we have imaged holographically $\tilde{O}(x, y, z)$, we simply need to convolve the recorded object field in the hologram $\tilde{O}_H(x_H, y_H, d)$ with the Rayleigh-Sommerfeld propagator expressed in equation 2.52:

$$\tilde{O}(x, y, z) = \tilde{O}_H(x_H, y_H, d) * \tilde{H}(x_H - x_0, y_H - y_0) \tag{2.54}$$

From the convolution theorem stated in equation 2.37, the reconstruction of the object field at any distance z along the optical axis can be arrived at by first taking the Fourier transform of the object hologram and the propagator, then finding the inverse Fourier transform of the product of these two terms:

$$\tilde{O}(x,y,z) = \mathscr{F}^{-1}\Big\{\mathscr{F}\{\tilde{O}_H\}\mathscr{F}\{\tilde{H}\}\Big\} \tag{2.55}$$

This operation can be achieved quickly with the fast Fourier transform algorithm on graphics processing units.

Now, all that remains is to isolate the object term from the other terms in the recorded hologram intensity.

2.6.2 Isolating the Object Term

Inline Holography

In order to isolate the object term for an inline recording, a background intensity corresponding to the reference beam needs to be generated first. This can either be a separate recording of the illumination (that is, reference) beam with the sample removed, or, if the sample is a moving specimen, a time-averaged mean or median of the recorded image stack. The hologram, $I_H(x,y)$ in equation 2.39, can thus be normalised by dividing through by the intensity of the reference beam $|R(x,y)|^2$:

$$\frac{I_H(x,y)}{|R(x,y)|^2} = 1 + \frac{|O(x,y)|^2}{|R(x,y)|^2} + \frac{\tilde{R}(x,y)\tilde{O}^*(x,y) + \tilde{R}^*(x,y)\tilde{O}(x,y)}{|R(x,y)|^2} \tag{2.56}$$

A number of assumptions are made to further simplify this expression (as seen in, for instance, [108]). Firstly, we assume that the reference beam intensity is much greater than that of the object beam, which is not unreasonable given the condition of high average transmittance of the sample. The second term of the right hand side

thus becomes insignificant. Secondly, it is assumed that there is no change in phase between $\tilde{O}(x,y)$ and $\tilde{R}(x,y)$. Finally, the reference beam is assumed to be a plane wave, meaning $\tilde{R}(x,y) = |R(x,y)|$. Equation 2.56 further reduces to:

$$\begin{aligned} \frac{I_H(x,y)}{|R(x,y)|^2} &\approx 1 + \frac{2\mathbb{R}\{\tilde{R}(x,y)\tilde{O}(x,y)\}}{|R(x,y)|^2} \\ &\approx 1 + \frac{2\mathbb{R}\{\tilde{O}(x,y)\}}{|R(x,y)|} \end{aligned} \tag{2.57}$$

where $\mathbb{R}$ represents the real part of a complex number. An expression for $\mathbb{R}\{\tilde{O}(x,y)\}$ can thus be arrived at from the recorded hologram and plane wave reference beam amplitude:

$$\mathbb{R}\{\tilde{O}(x,y)\} \approx \frac{|R(x,y)|}{2}\left[\frac{I_H(x,y)}{|R(x,y)|^2} - 1\right] \tag{2.58}$$

Note that this technique does not allow for the reconstruction of the phase of the object, one of the drawbacks of the inline technique.

Off-Axis Holography

For an off-axis geometry, we have the intensity of the recorded hologram given in equation 2.43. The effect of the linear phase shift applied along the x-axis is evident when we consider the spatial frequency domain of the hologram. Assuming the reference beam is a plane wave of the form given in equation 2.42, this can be observed by taking the Fourier transform of I_H:

$$\begin{aligned} \mathcal{I}_H(k_x,k_y) &= \mathscr{F}\{I_H(x,y)\} \\ &= |R|^2\delta(k_x)\delta(k_y) + \tilde{\mathcal{O}}(k_x,k_y)\tilde{\mathcal{O}}^*(k_x,k_y) \\ &\quad + |R|\tilde{\mathcal{O}}(k_x - k\sin\delta, k_y) + |R|\tilde{\mathcal{O}}(k_x + k\sin\delta, k_y) \end{aligned} \tag{2.59}$$

where $\mathscr{F}$ indicates the Fourier transform operator and $\mathcal{O}$ is the Fourier-transformed object function. k_x and k_y are the coordinates in Fourier space and $\delta(k_{x,y})$ is the delta

function. z is assumed to be constant in the hologram plane; that is, $z \equiv z_H$.

The spatial frequencies of the reference beam and the object halo are at the centre of the Fourier plane. The spatial frequencies of the real and virtual images have been shifted along the k_x axis and are now centred on $k_x \pm k \sin \delta$, as seen in figure 2.13. Of course, in practice we can orient the spatial frequency shift along a linear combination of both the k_x and k_y axes by adjusting the angle of the reference beam.

In order to isolate the real image from the reference beam, the object halo and the virtual image, we simply need to apply a one-sided high-pass filter to the hologram intensity. This process is demonstrated visually in figure 2.15. The high-pass filter removes the unwanted spatial frequencies from the hologram. Taking the inverse Fourier transform of the filtered data yields the isolated object beam, which can then be used for three-dimensional reconstructions. A crucial difference to the procedure for isolating the object data from an inline hologram is that the off-axis method results in complex data from which we can extract the phase of the hologram.

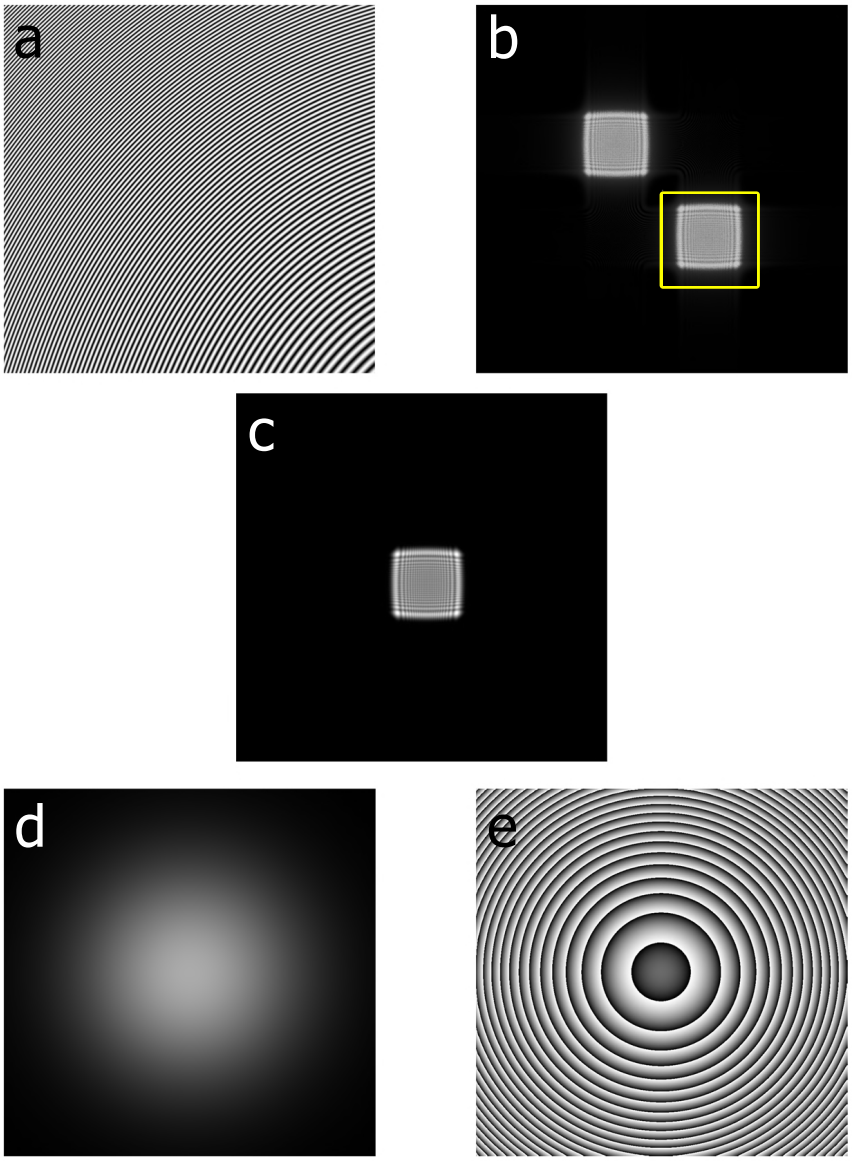

Figure 2.15: Isolating the object term from a simulation of an off-axis hologram. A phase shift is applied equally along the x and y axes in this case. a) shows a simulated off-axis hologram of a point source and a plane wave. b) is the Fourier transform of this hologram represented on a logarithmic scale. The real and virtual images are spatially separated and the square distribution of frequencies is what we would expect from the two-dimensional Fourier transform of a point source on a square recording medium. A one-sided high-pass filter is applied: the real image inside the yellow box is extracted and moved to the centre of the Fourier plane, shown in c). This is the basis of the Fourier filtering. The inverse Fourier transform of this filtered Fourier transform results in images d) and e). These are, respectively, the amplitude and phase of the original point source, which has now been recovered from the plane wave reference beam and from the twin virtual image. Phase images from real holograms of polystyrene microspheres demonstrate this phase pattern and can be seen in chapter 5.

Chapter 3

Design Considerations in Building a Digital Holographic Microscope

3.1 Introduction

The aim of this project was to develop a modular, transmission mode, digital holographic microscope (DHM), capable of performing both inline and off-axis holography with minimal change in the apparatus to the end user. The entire microscope was constructed from individual optical elements and optomechanical components rather than using a commercial microscope as a base. Attention was also given to incorporate an ability to record measurements at different magnifications, again, with minimal change to the optical system by the operator. Discussion is included in this section that details the design process and the ultimate success of these aims. This project concentrated on recording holograms such that they could be reconstructed on a graphics processing unit (GPU) in a bespoke numerical environment developed by Irwin Zaid and outlined in section 4.2.1. Unless stated, I was responsible for the design and development of the optical microscope outlined in this section under the supervision of Dr Richard Berry. An undergraduate project student, Vitaliy Babenko,

worked for eight weeks on a low-magnification microscope under the joint supervison of Richard, Irwin and myself. Vitaliy took my original microscope implementation as a starting point from which to develop improved acquisition protocols using the Andor sCMOS camera. Images obtained by him have been credited in this chapter.

A number of hardware considerations must be taken into account when designing a digital holographic microscope. Specifically, these are: the illumination source, the digital camera, the optomechanical components, the sample chamber and the stage upon which it is held. In addition, the computer hardware must be tailored to the application to ensure sufficient data transfer rates exist when recording high-speed and/or high-resolution video. Finally, the entire optical setup is subject to ergonomic and safety constraints given available space and the work environment.

3.2 Illumination Source

3.2.1 Coherence Length

As seen in section 2.1.3, all sources of light come with an associated coherence length L related to its spectral width Δf. For any two interfering components of a light source, the path difference between the two beams must be less than the coherence length for interference to be observed. The requirement for interference necessitates a coherent, monochromatic light source for a clear and relatively easily-achievable interference pattern.

For off-axis holographic applications, the lengths of the two beam paths (which may be several metres) must be brought to within this coherence length for interference to be observed. The coherence length of light from thermal sources − filament bulbs for instance − is in the range of several microns. This implies that the path difference between the reference and object beam must be adjusted to about 1 in 10^6, a feat that is possible, but technically challenging. A long coherence light source

would thus be preferable for an off-axis holography application, especially for a DHM with many optical components required to produce the desired magnification of the sample.

For an inline holographic application, the coherence length gives a direct measure of the effective depth of field of the DHM. A filament source would thus give an interference range that is not particularly useful for microscopic applications. By contrast, a light source with a coherence length of the order of metres − a helium-neon gas laser for instance − produces interference patterns from any scattering source along the entire optical train. This includes dust on, and imperfections in, the lenses, mirrors and other necessary optical components. These are considered to be 'parasitic' scatterers as the signal emanating from them is detrimental to image quality. Minimising the number of optical surfaces in the microscope design, protecting against dust, and cleanliness of optics are all good ways of reducing the effect from parasitic scatterers. However, the sample chamber, the sample itself, impurities in the objective oil and the objective itself can all be sources of unwanted scattering and in reality it is difficult to mitigate the effects of all of them.

Back-scattering off optical surfaces, and the camera sensor itself, can also contribute to undesirable interference patterns. Anti-reflection coatings on lenses alleviate some of these issues. However, it was found that the slide chamber itself was a primary source of such interference patterns, especially at high-intensity illumination. Little can be done about this without resorting to expensive anti-reflection coatings on glass slides and coverslips. As long as these unavoidable surface reflections are constant over time, their presence is not significant and can be compensated for in image post-processing.

The origin of certain features in the parasitic scattering pattern can be determined by carefully rotating or adjusting each individual optical element in turn and observing the effect on the image.

Providing the interference pattern from parasitic scatterers is constant, and the sample itself is moving, much of the scattering noise can be eliminated in post-processing by dividing each image by a mean image taken over a suitably long time period. This approach requires wavelength-scale stage stability over the required time period. Given appropriate stage stability, a parasitic background image could be obtained by moving the sample away from the illumination source. This not only requires fine control of a very stable stage, but the walls of the sample chamber should be parallel to each other and normal to the incident light. They should also be free from imperfections to give the best result. In practice, these conditions are difficult to satisfy.

For an inline DHM, perhaps the most effective method of minimising the effects of parasitic scatterers is to use an illumination source with a coherence length similar to the desired imaging depth of field. In the ideal case, the only interference pattern that will reach the camera is that generated by the scatterers inside the sample chamber. In practice, this would mean an illumination source with a coherence length of several hundred microns. In the desired application of a modular apparatus that can perform both inline and off-axis holographic microscopy, a compromise between long and short coherence length sources must be reached. The two optical arms must be accurate to within the coherence length or an alternative, switchable, light source used for off-axis holography.

Initially, a helium-neon (HeNe) gas laser (25LHP 991-230; 10mW, 632.8nm, linearly polarised; CVI Melles Griot) was used. A home-built Michelson interferometer was used to determine the coherence length of the laser, which was found to be at least several metres (greater than the available travel on the adjustable interferometer arm). For inline applications, this laser produced a poor signal that was obscured by parasitic scattering effects as detailed above. These effects could be mitigated somewhat through dividing by a mean of the image stack. Unfortunately, the sample

was found to move relative to the objective over the course of such an image stack acquisition, resulting in a residual pattern after normalisation. This pattern is due primarily to the scatterers in the objective, or back-reflections between the objective and the sample holder. This effect can be seen in the top set of images in figure 3.1.

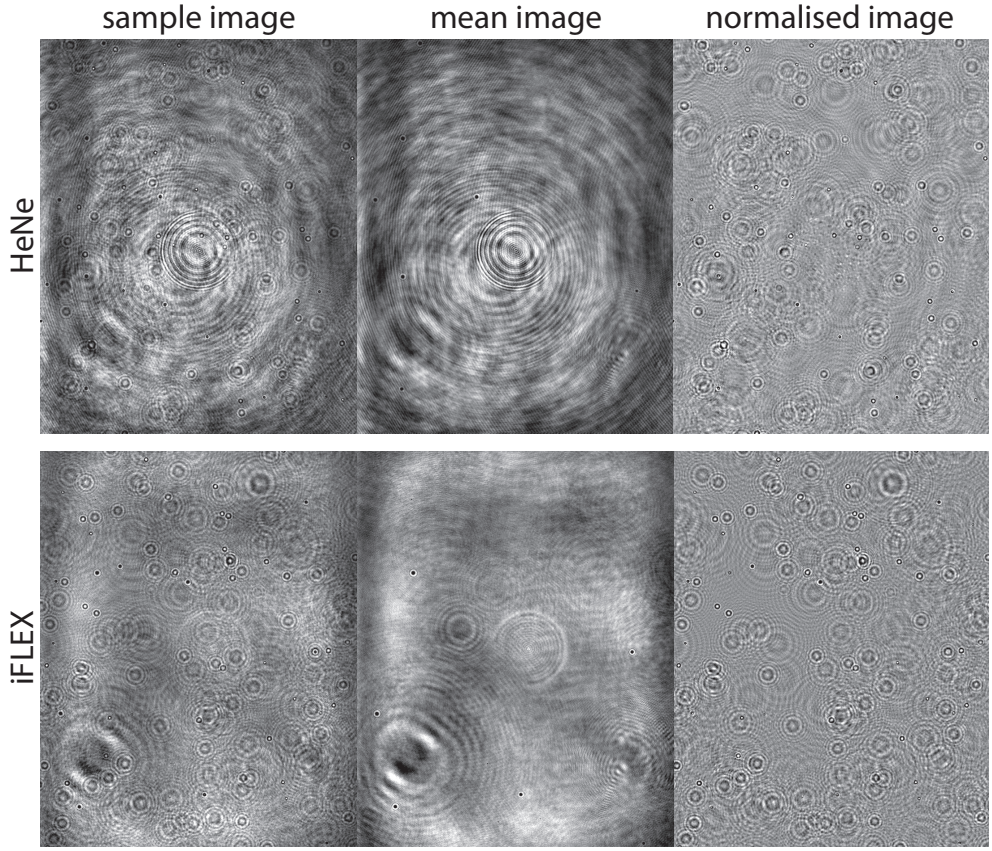

Figure 3.1: Comparison of long coherence length HeNe laser with short coherence length iFLEX fibre laser as an illumination source for inline holography. The left-hand images are sample holograms of 1μm polystyrene beads magnified by a 100$\times$ objective. Each image displays a field of view of 143μm $\times$ 179μm. The centre images are means taken of the image stacks of 2,000 images recorded over 50s. The right-hand images show the results of normalising the hologram through dividing by the mean. The difference in image quality between the two lasers is immediately apparent. Whereas the HeNe laser picks up parasitic scattering from throughout the image train, the fibre laser picks up scatterers due only to the objective surface (notably the dirt in the lower left). These are all effectively removed by normalisation, whereas the HeNe shows a residual pattern due to its sensitivity to changes in path difference over time caused by mechanical vibrations of the optical table.

A fibre laser (iFLEX 2000; 20mW, 635nm, linearly polarised; Qioptic Photonics

Ltd) was then installed on the apparatus. The coherence length of this laser was determined on the Michelson interferometer to be $800 \pm 50 \mu$m. As can be seen in figure 3.1, the effect of parasitic scatterers throughout the optical train has been greatly reduced for inline microscopy due to the shorter coherence length. It was decided to use the same laser for off-axis imaging to avoid the inherent instabilities of coupling in a second light source via a flip-mounted mirror. This required matching the two arms of the off-axis to within several hundred microns. The practical implementation of this is discussed in section 3.8.4.

3.2.2 Spatial Coherence

The spatial illumination profile should also be mentioned. The illuminating beam should be spatially coherent; that is to say, there should be no phase difference over a given cross-section of the beam at any point prior to illumination (for inline holography) nor along the reference beam (for off-axis holography). This requirement is met by having a beam of sufficient quality.

In an ideal case the amplitude of the beam would be constant across the desired illumination field. Given the Gaussian profile of laser beams, this is not easily achievable in practice. An uneven illumination is possible to work with, providing the beam amplitude is stable, and that the recorded hologram is within the bit depth of the digital camera. Numerical averaging and normalising, which is generally a requirement due to parasitic scatterers, was found to compensate for imperfections in the beam alignment.

Some effort was made to spatially filter the beam; however, given the eventual choice of the iFLEX 2000 laser, it was found that the fibre itself provided sufficient spatial filtering.

3.2.3 Illuminated Field of View

When a small field of view is required, it is advantageous to form a diffraction-limited beam waist at the objective focal plane of the appropriate diameter. This means objects in the sample chamber that are not in the imaging field of view are less likely to contribute to an off-image diffraction pattern that could obscure objects in the desired region of interest.

3.2.4 Polarisation

To achieve optimal interference, both the reference and object beams should be identically polarised. This is achieved in inline holography by ensuring the laser light source is linearly polarised. For the off-axis application, a polarising beam-splitter is used to separate the reference and object beams. Rotatable half-wave plates are placed before the beam-splitter and after it in the object beam arm to ensure the two beams have the same polarisation axis. The fringe interference pattern is observed prior to image acquisition and the rotatable polariser adjusted until maximum contrast exists in the fringe pattern. This is discussed further in sections 3.5 and 3.8.

3.2.5 Other Illumination Options

Other means of illumination were considered. Prior to acquisition of the iFLEX 2000 laser, a set of off-the-shelf laser pointers were tested for their perceived low coherence length properties. When tested on the Michelson interferometer, it was found that in some cases these diode lasers had surprisingly long coherence lengths – greater than the desired several hundred microns. Others were not spatially coherent, had non-ideal illumination profiles or were not temporally stable. Inline digital holographic microscopy has been shown to work, however, with a store-bought laser pointer [133], thus the technology exists for a cheap, simple microscope with myriad applications,

given the appropriate illumination source.

A 'super-bright' (130 lumens) light emitting diode (LED) with a comparatively narrow spectral width was considered as a low coherence length illumination source (LUXEON Rebel Amber; 590.6nm central wavelength, 80nm spectral half-width corresponding to $\sim$4.4μm coherence length; Philips Lumiled Lighting Co.). Ultimately, it was found that the LED was not adequately bright to illuminate a sample at high magnification for sufficiently high framerates. Brighter LEDs exist, with maximum luminous flux readings up to 235 lumens, however these LEDs are typically white light sources with spectral widths too wide for practical holography. LED technology is improving all the time and may find a use in a high magnification setup in the future. However, in the meantime LED illumination was found impractical for our purposes, although it may have a place in a low-cost, inline apparatus with minimal magnification, or where exposure times can be longer.

3.3 Camera

3.3.1 Resolution

There are a number of factors to take into account when selecting a digital camera for use in recording video holograms. Firstly, the camera sensor must be of sufficient resolution. As discussed in section 2.5, of the two proposed methods of implementing holography in this project, off-axis holography provides the most stringent constraint on resolution. Assuming plane wave interference between the reference and object beams, an interference pattern of fringes is recorded. Both the orientation and the spacing of these fringes depend on the angle at which the two beams meet. To achieve optimal separation between the spectra of the twin images and the undiffracted through-term in Fourier space, a fringe angle of about 45° is suggested. This is to maximise the spatial frequencies able to be captured by the camera by ensuring

the separation angle between the reference and object beams is as small as possible. Equation 2.44 becomes:

$$k \sin \delta_{\min} \geq \frac{3}{\sqrt{2} k_{x,y}^{\max}} \tag{3.1}$$

along k_x and k_y if the fringe angle is at 45°.

The minimal criterion for resolving the spatial frequency of the interference pattern is set by the Nyquist condition: that is, a fringe period of two pixels for vertically- or horizontally-oriented fringes. In Fourier space, this corresponds to twin images at the far edges of the Fourier plane as displayed in the upper set of images in figure 3.2. While this offers maximum separation between the images and the low-spatial frequency through-term, it is not suitable for extracting the desired image for reconstruction. In addition, the experimental practicalities of the object beam not being necessarily a perfect plane wave and the difficulties with which the absolute alignment of the two beams can be known, mean that a greater pixel displacement of interference fringes is deemed optimal, shown in the lower pair of images in figure 3.2.

The requirement on resolution for inline applications is less stringent, save to say pixels should be sufficiently small relative to the magnification of the objects to be able to resolve relevant features. With some cameras, higher framerates can be achieved by selecting a subregion of the chip before recording the image. If this option is to be used, care must be taken to ensure the resolution is still adequate for the application.

3.3.2 Chip Size

The overall chip size has a bearing on the expansion size of the off-axis reference beam and the field of view of the object beam as magnified by the objective and lenses further downstream. The field of view (FoV) able to be imaged on a chip of

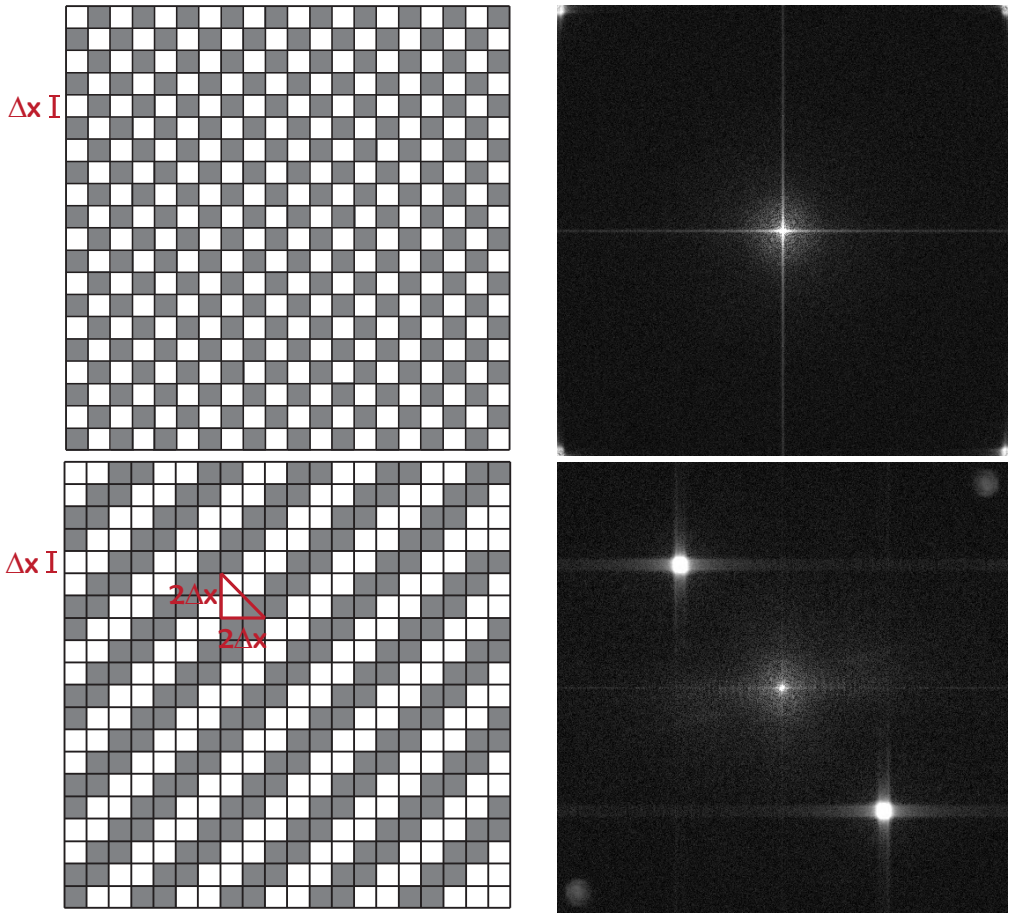

Figure 3.2: The upper set of images demonstrates the Nyquist sampling condition on a digital sensor. The left-hand image shows a cartoon example of a digital sensor. The right-hand image shows the Fourier transform of a real holographic image. In this case, the spectra of the twin images are observable at the far corners of frequency space. The lower set of images demonstrates the optimal condition for off-axis holographic imaging. Fringes are oriented at 45° to the pixel axis with a spacing of $2\sqrt{2}\Delta x$, where Δx is the side dimension of a pixel, shown in the left-hand cartoon image. The 2D Fourier transform of actual data on the right shows the location of the resulting twin image spectra. These are maximally separate from one another and from the low-spatial frequency term in the centre. Some aliasing is visible in the top-right and bottom-left quadrants.

dimension w is related to the total magnification M_{tot} of the optical system:

$$\text{FoV} = \frac{w}{M_{tot}} \tag{3.2}$$

A typical chip dimension is 14mm. If the entire chip area is to be used and given a typical laser beam waist diameter at source of 0.6mm, the reference beam would

need to pass through a telescope with at least 24× magnification.

3.3.3 Bit Depth

The bit depth of the camera is also of importance as it must be able to capture both the maximum and minimum intensities of the interference pattern. Saturated and zero-value pixels lead to errors in the numerical reconstruction and unsatisfactory results. On the other hand, increasing camera bit depth will generate larger volumes of data that must be accounted for in the recording speed, data transfer and GPU memory (see section 3.4).

3.3.4 Framerate

For video imaging, the recording framerate needs to be sufficiently high to suit the application. In the bacterial context, while tens of frames per second (fps) may be sufficient to track individual cells, framerates of several hundred per second are required to probe the flow field around flagellar filaments at high magnifications. Cameras that can record the necessary large fields of view at high framerates are both rare and expensive.

High framerates necessitate short exposure times, which means the illumination of the sample must be bright enough relative to the sensitivity of the chip. Even for applications that require lower framerates, a short exposure time is ideal to reduce motion blur of moving objects.

Assuming a camera can record images at a sufficiently high framerate, care must also be taken that the camera can record at this framerate long enough to be experimentally useful. Ideally, the data will also be downloadable to the computer in a reasonable time. Potential bottlenecks in data buffering and downloading should be identified before committing to one camera. These are discussed in more detail in section 3.4.

Not only does the camera need to record at a sufficiently fast framerate, but the time intervals between each frame need to be recorded accurately. Experience has shown that internal computer clock triggers when used with commercial software are not reliable for this, despite attempts to optimise computer RAM and to prioritise the software process. One option around this is to use an external electronic trigger, which many cameras allow for. We found that custom software and effective computer memory management were required to ensure an even acquisition of frames and to reduce the number of dropped frames.

3.3.5 Prosilica Firewire and Ethernet Cameras

Two Prosilica digital cameras (Allied Vision Technologies GmbH) were tested based on the advice of collaborators. The EC1280 is a 1280×1024 resolution (1.3 Megapixel) 8-bit monochromatic CMOS camera with 6.7μm × 6.7μm pixels. Computer connection is by IEEE-1394 Firewire and the maximum framerate for full-frame acquisition is 24fps. The framerate increases, however, if a smaller subregion is selected for output: up to 1,000fps for a 16px × 16px region of interest (RoI). The original application envisaged for this camera was to have it connected to a laptop as part of a mobile workstation for digital video acquisition on custom-built microscopes. The orginal target of interest was a polystyrene microsphere adhered to the filamental stub of a surface-bound bacterium, and rotating at rates of up to several hundred hertz. The camera was assessed in this context initially and then for possible use with digital video holography.

It was determined that the actual framerate of the camera differed varyingly from that specified, which is suboptimal for quantitative data analysis. In addition, the camera would routinely drop frames. This was examined by saving the timestamp output of when each frame was received by the computer for a range of framerates and RoI sizes, a sample of which is shown in figure 3.3. Additionally, the camera was used

to record the position of a polystyrene microsphere adhered to a microscope slide while the microscope stage underwent controlled motion. Motion was supplied by connecting a signal generator with a triangular wave output to a piezoelectric nanopositioning stage (P-611.3S NanoCube; Physik Instrumente GmbH) via an amplifier and servo controller (E-664 LVPZT; Physik Instrumente GmbH). Bespoke LabVIEW software (National Instruments Corporation), courtesy of the Padgett group at Glasgow University, used a simple threshold analysis to determine the centre of the microsphere in each frame. A sample output showing dropped frames is in figure 3.4.

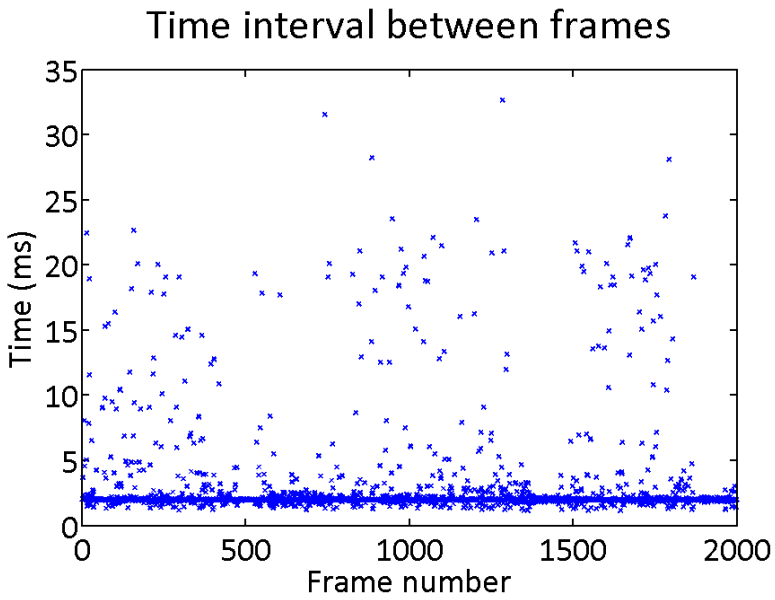

Figure 3.3: Typical output of recorded time interval between subsequent frames acquired by the Prosilica EC1280 Firewire camera for a prescribed framerate of 500fps at a reduced region of interest. While the majority of time intervals cluster around 2ms, a large number of frames are acquired at time intervals many times this.

The cause of this is inadequate optimisation of the IEEE-1394 Firewire data transfer protocol to the computer at framerates higher than conventional video (24fps). Custom software had been written with LabVIEW to optimise data transfer rates. Nevertheless, the supplied drivers did not permit any further improvement in frame time accuracy. The solution to this problem would be to write a bespoke driver, which was not deemed worth the effort.

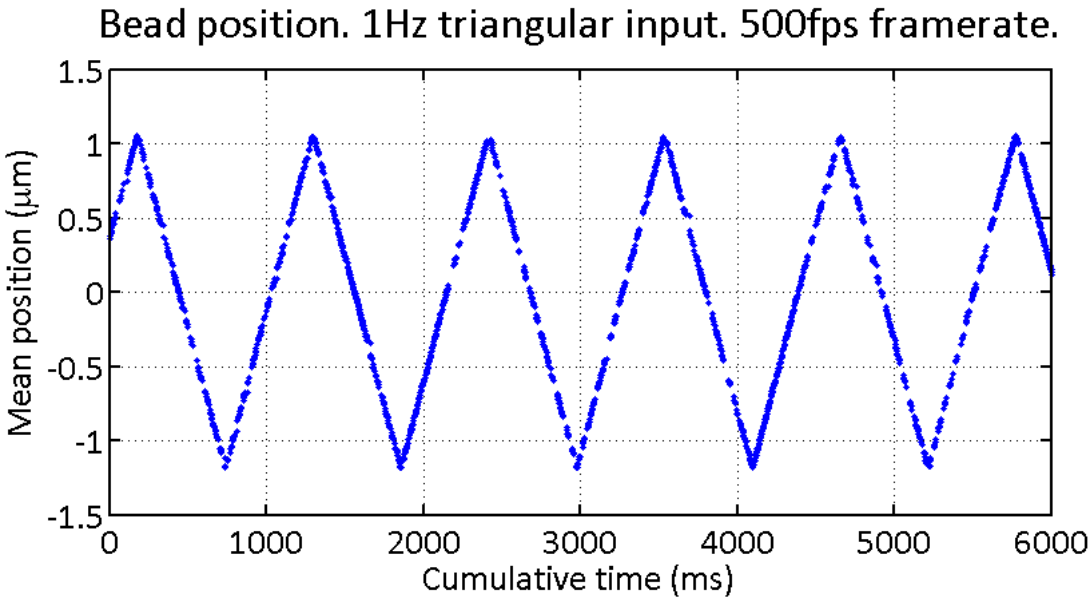

Figure 3.4: Sample output of the position of an immobilised microsphere undergoing periodic triangular wave motion from a signal generator and recorded with the Prosilica EC1280 Firewire camera. The camera is set to a framerate of 500fps. The breaks in the acquistion data indicate dropped frames.

A Gigabit Ethernet camera was then trialled, the GC1280. The specifications of this camera are similiar to those of the EC1280: 1280×1024 pixel resolution, 8-bit monochromatic CMOS chip, 6.7μm × 6.7μm pixels. The maximum framerate at full-frame acquisition is 27fps with increasing rates for decreasing region of interest size. The computer connection is through an IEEE 802.3 1000baseT Ethernet port. Bespoke software was written for this camera by Irwin Zaid in Python, to run on a Linux operating system. Dropped frames and varying time intervals between frames could be reduced to acceptable levels by running the camera software preferentially to all other processes on the CPU. This is relatively easy to do in the Linux environment compared to using a Microsoft Windows operating system.

When this camera was used for inline holographic imaging, it was found that the camera could not reliably capture the dynamic range of the hologram. Both 0- and 255-value pixels were recorded in the same image, shown in figure 3.5. Saturated bright pixels can be compensated for by decreasing the illumination or reducing the

exposure time, and zero value pixels can be eliminated by doing the opposite. However, the only way to compensate for both 0- and 255-value pixels is to alter the 'dark level'[1] – the current level below which a pixel assigns a 'zero' value. This feature is not supported by the camera firmware and the loss of information in such images was too great for the camera to be used for holographic imaging in our situation.

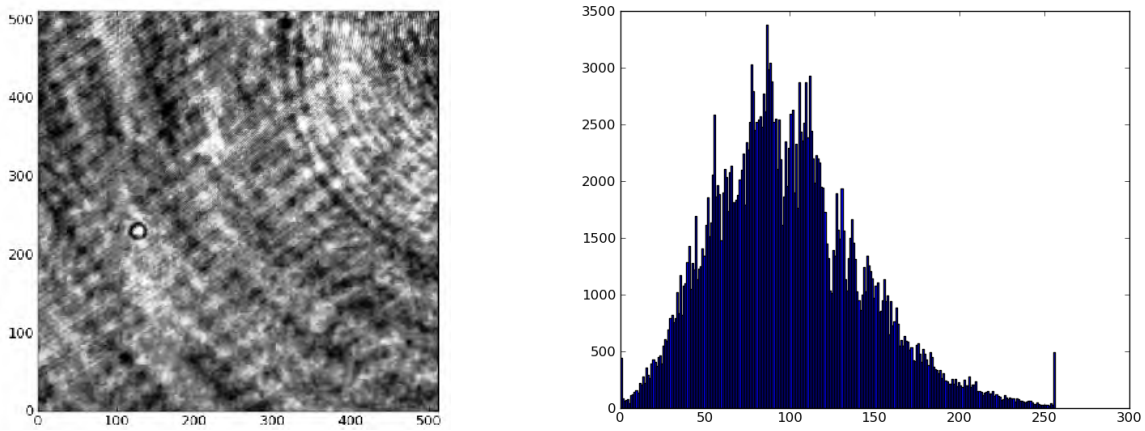

Figure 3.5: *Left*: Sample inline hologram of a solution of 1μm polystyrene microspheres acquired with the Prosilica Ethernet EC1280 camera. *Right*: Histogram of this image with pixel value on the abscissa showing the presence of both 0-value and saturated pixels.

3.3.6 Mikrotron EoSens Camera

The solutions to the problems found in the Prosilica cameras were met by the Mikrotron EoSens CL (Mikrotron GmbH). This camera contains a monochrome 8-bit CMOS chip with a pixel resolution of 1280×1024. Pixel size is notably larger than the Prosilica cameras: 14μm × 14μm. However, the framerate is significantly faster: 500fps at full frame and up to 120,000fps for a reduced region of interest. A 512px × 512px subregion can record frames at up to 2,000fps, which is ideal for the fastest envisaged application of this microscope. Connection to the computer was via a Full CameraLink protocol to a framegrabber; the dataflow specifics are discussed in section 3.4.

[1] Also called a 'black level'.

The supplied camera and framegrabber software allowed for much greater control over the camera acquisition than the two Prosilica cameras. In particular, the dark level is able to be adjusted; thus, an exposure setting can be found that ensures the intensity values of the recorded holograms lie within the 8-bit range of the camera. The usual settings of RoI location and size, exposure, framerate and duration of recording are able to be set by the user.

While perfectly adequate for viewing the live camera output and for adjusting settings, the supplied software interface was not deemed sufficient for video recording, especially when knowledge of the timestamp of each frame is desirable for quantitative analysis. Custom software was written in Python by Irwin Zaid to interface with the camera and to record image data along with the timestamp of each frame. The acquisition process can be run in both a Microsoft Windows and Linux environment. When run in Linux, the camera operation can be prioritised over other CPU processes to ensure accurate temporal recording of frames. Figure 3.6 shows the time interval between frames for a sample 6,000 frames recorded at 25fps. The mean time interval is 39.872 $\pm$ 0.009ms, with the standard deviation given as the uncertainty. This corresponds to a framerate of 25.08 $\pm$ 0.06fps, a vast improvement over the Prosilica EC1280 and acceptable for our application.

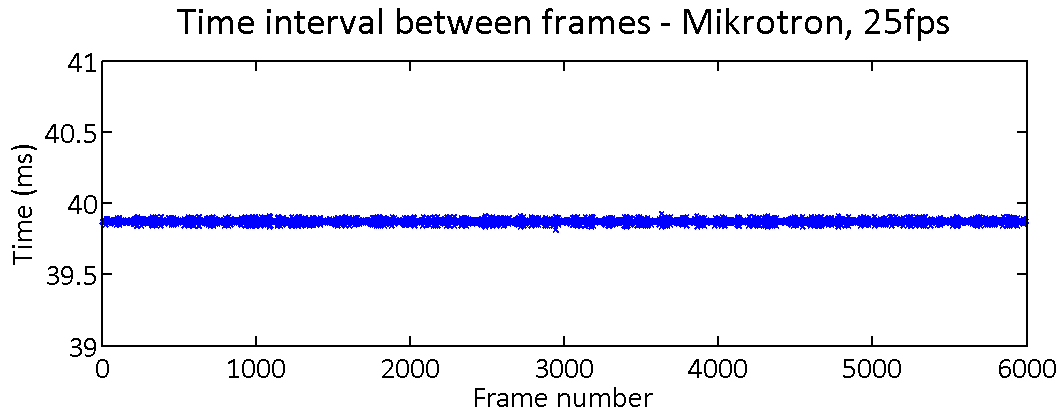

Figure 3.6: Typical output for timestamps recorded with the Mikrotron EoSens camera running at 25fps over 4 minutes using bespoke software. The mean interval between frames is 39.872ms with a standard deviation of 0.009ms.

Screenshots and practical information on using the Mikrotron CL EoSens may be found in appendix A.

3.3.7 Andor sCMOS Camera

The high-resolution and highly sensitive Andor Neo sCMOS camera (Andor Technology plc.) was also tested. This camera records 16-bit monochrome images and has a pixel resolution of 2560×2160 (5.5 Megapixel) with a pixel dimension of 6.5μm. While significantly higher resolution than the Mikrotron EoSens, the maximum framerate is a lot lower, with 100fps able to be recorded at full frame. 16-bit images also take a lot more memory, thus fewer frames are able to be stored in a given memory buffer.

The accompanying Andor software 'Solis' was only very recently released for Windows 64-bit operating systems (the current lab standard) and a Software Development Kit is still forthcoming for Linux development. Thus, software has not yet been written that can optimise the output of this camera as has been done for the Mikrotron.

As it currently stands, video recording is limited by the 4GB onboard memory buffer, which must be filled and the recording stopped before data may be transferred to the computer. As recorded images are 16-bit, rather than 8-bit, only 360 frames can be recorded at full frame before the recording stops. A smaller RoI, however, may allow for an adequate number of frames to be recorded in a single acquisition, before data must be downloaded to the computer.

The advantage of the Neo sCMOS over the Mikrotron EoSens is its smaller pixel size, allowing for an increase in resolvable angle in off-axis holography, as per equation 2.48. The slower framerate and larger image filesizes may restrict its application to slow moving objects. Future work will explore this further.

3.4 Data Transfer Considerations

As alluded to above, the flow of data throughout the acquisition and reconstruction process needs to be mapped out and hardware needs to be selected based on its ability to handle data generated by the desired application. Image data need to be transferred to a computer hard drive. This occurs either directly if the camera data transfer protocol allows it, or via a memory buffer located on the camera, a framegrabber, or the RAM of the computer. Transfer rates through interface cables and using the protocols supplied with the hardware, along with hard drive write speeds are limiting factors.

Firstly, the datarate during an acquisition for a given application needs to be determined. This is a function of the bit depth of the camera, the size of the captured image and the number of frames captured per second. In selecting appropriate hardware, a typical high-speed application using the Mikrotron camera was used as an example. The datarate for 8-bit acquisition of a reduced field of view (512px × 512px) at 1,000fps is thus:

$$\begin{aligned} \text{datarate} &= \frac{512\text{px} \times 512\text{px} \times 8\text{bits}}{8\text{bits/byte}} \times 1000\text{fps} \\ &= 260\text{MB/s} \end{aligned} \tag{3.3}$$

Out of several options the microEnable IV framegrabber (VD4-CL; Silicon Software GmbH) was determined to be the most appropriate for this application. This framegrabber makes use of the Full CameraLink protocol, with data transfer rates of up to 900MB/s. The framegrabber has a 512MB buffer, which it utilises while simultaneously downloading to the computer.

A solid-state hard drive (SSD) (OCZ IBIS 240G; OCZ Technology Group Inc.[2])

[2]Datasheet available at http://www.ocztechnology.com/res/manuals/OCZ_IBIS_Product_sheet_3.pdf

was purchased for its superior write-speed when compared to conventional magnetic hard drives. This drive has a maximum write-speed of 720MB/s and a capacity of 240GB. As a point of comparison, the conventional hard drive used in our computer (WD15EARS, 1.5TB capacity; Western Digital Corporation[3]) has a write-speed of 110MB/s.

The final stage of data transfer is to make the data available to the graphics processing unit for holographic reconstruction. Due to practical limitations of the amount of hardware able to be supported by a single motherboard, it was decided to perform the reconstruction on a separate, dedicated computer. Data transfer between the two systems occurs at leisure over a network.

In the two critical data transfer stages − camera to framegrabber and framegrabber to hard drive − the transfer rates exceed those of the given application. Thus the limiting factor in recording data is the capacity of the SSD. For a 512px × 512px field of view, 100,000 frames may be recorded continuously with this arrangement, or 100 seconds at 1,000fps.

By overspecifying data transfer capacity, applications at faster framerates and/or with larger fields of view may be undertaken should the need arise.

3.5 Optics and Optomechanics

As holography is an interferometric technique, the image quality is highly sensitive to mechanical and acoustic vibrations. The minimisation of environmental noise is even more crucial for off-axis holography due to the need for precise alignment of path lengths. The DHM was constructed on a 1.2m × 0.9m isolation air table (Thorlabs Inc.) using a compressor to provide the air support. An inverted microscope arrangement was employed with the microscope objective directly thread-mounted

[3]Datasheet available at http://www.wdc.com/wdproducts/library/SpecSheet/ENG/2879-701229.pdf

into a optical breadboard (visible in figure 3.9 in section 3.6). The illumination beam was coupled into the sample vertically; the imaging optics were all positioned at table level.

Conventional planoconvex lenses and plane mirrors, all with anti-reflection coatings in the visible range, were used throughout. Two-inch optics were used to avoid edge distortions for beam expansions greater than 15mm in diameter.

A 12.5mm polarising beam-splitter cube was used to separate the laser source into the two arms required for off-axis microscopy. A rotatable half-wave plate placed before the beam-splitter allowed the relative intensities of the two beams to be adjusted. For maximum interference, a second adjustable half-wave plate was placed after the beam-splitter in the object beam arm in order to ensure the polarisation of the two paths was colinear.

Two different beam-splitter options were tested for recombining the two paths immediately before the camera: a pellicle beam-splitter and a non-polarising cube. As the beam diameter necessitated large optical elements (>25mm) and with table space at a premium, the pellicle was initially preferred over the bulky cube. However, the membrane of the pellicle was found to be more susceptible to air currents in the room, affecting the stability of the interference pattern.

The pixel intensity values for a recorded interference pattern (figure 3.7) were analysed for both the pellicle and the cube. 400 frames were recorded at 200fps with the 8-bit Mikrotron camera. The standard deviation of each pixel was determined throughout the image stack to give an indication of how much each pixel was changing. The mean of these values for all pixels in the image was then determined, to arrive at a single value for the variation in pixel value over the entire image stack.

Over the entire image, the mean of the standard deviation for the pellicle beam-splitter was found to be 16.57, or 6.47% expressed as a percentage of 256. The mean of the standard deviation for the beam-splitter cube is 5.74, or 2.24% expressed as

a percentage of 256, indicating a significant improvement in stability over the short term.

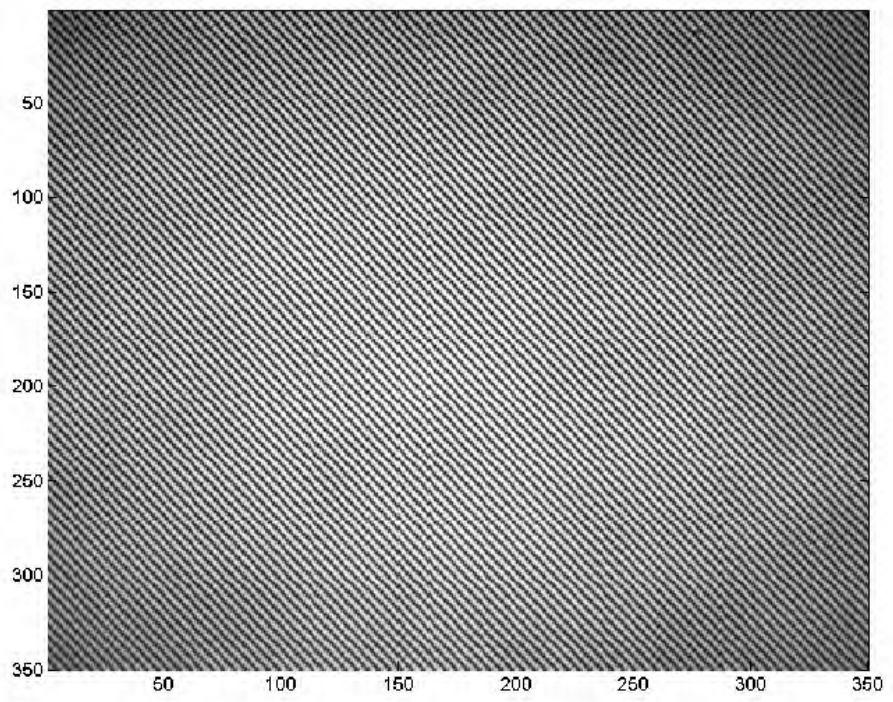

Figure 3.7: 350px × 350px interference pattern for which each pixel was analysed over 400 frames recorded at 200fps to compare the stability of a pellicle beam-splitter and a beamsplitting cube.

Microscope objectives of three different magnifications were used during the development of the DHM: 40× (CFI Plan Fluor), 60× (CFI Apo λS, oil) and 100× (CFI Plan Fluor, oil; all from Nikon Instruments Inc.). It was originally hoped to design a microscope that would allow for different magnification settings to be employed by simply replacing the objectives. However, it was determined that the back focal planes of each of these objectives were in different locations in the objective barrel, and thus relative to the tube lens. The idea of simply changing the magnification settings on the microscope proved to be unfeasible without significant realignment of downstream optics or mounting the objective on a height-adjustable stage. Neither

of these options was thought compatible with the principles of ease of use and sample stability. It was thus resolved to concentrate on this apparatus as a high-magnification microscope and to build a dedicated 40× microscope for wide-field, low-magnification applications.

The 60×λS objective has a novel 'Nano-Crystal' antireflection coating. It was tested to determine whether this coating would reduce parasitic scattering from the objective and improve the overall image quality. Figure 3.8 shows a comparison of the three different objectives. The illumination source is a HeNe laser and the sample is a dilute suspension of *E. coli* imaged in inline holography mode. Objective ring structures are clear in both the 40× and 100× images. The 60×λS objective improves the overall image quality greatly, when illuminated with a long coherence length laser. For all objectives, most of these effects are eliminated by using a short coherence length laser and normalising each image with a mean of the image stack (see section 3.2.1). It should also be pointed out that the 60×λS objective is Apo, rather than Plan, meaning the focus is not constant over the entire field of view. This situation is best avoided in holographic applications.

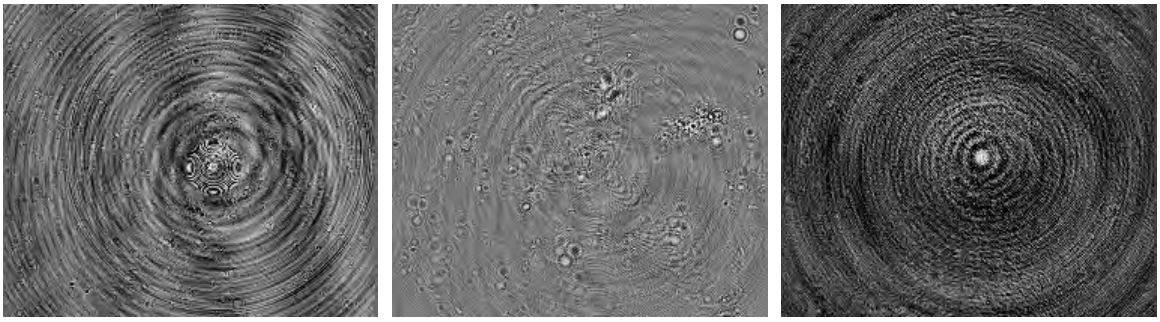

Figure 3.8: *Left to right:* Inline holograms of *E. coli* illuminated with with a HeNe laser and imaged with: 40× (CFI Plan Fluor); 60× (CFI Apo λS, oil); and 100× (CFI Plan Fluor, oil) Nikon objectives. The antireflection coating of the 60×λS objective results in a reduced diffraction pattern due to the objective, and a cleaner image when using a long coherence length laser. *Images courtesy of Vitaliy Babenko.*

3.6 Sample Holder and Stage Control

Standard microscope slides were attached to a metal plate mounted on a xyz piezoelectric nanopositioning stage (P-611.3S NanoCube with E-664 LVPZT amplifier and servo controller; Physik Instrumente GmbH). This provides fine control of the sample in three dimensions with 100μm travel and 50nm resolution in each direction when the amplifier was adjusted by hand[4]. The NanoCube was in turn mounted, via a custom-built aluminium bracket, to an xyz lockable dovetail stage (460PD-XYZ; Newport Corporation) for coarse adjustment over 12.7mm in each direction.

Originally, the slide was simply clamped onto the NanoCube and held in place over the objective. It was noted that this arrangement was particularly susceptible to environmental mechanical and air vibrations. The stability worsened when a low-magnification objective − one that did not require immersion oil − was used. It is likely that back-reflections between the objective top surface and the lower surface of the slide contribute to unwanted interference patterns that shift over time unless the sample is kept absolutely still. The interferometric nature of holographic imaging means this technique is particularly susceptible to such noise artifacts. This problem was mitigated somewhat through using viscous immersion oil to damp any vibrations experienced by the slide. In addition, a 3mm thick aluminium plate with an aperture cut for the coverslip was used to provide a more rigid attachment to the NanoCube. Figure 3.9 shows the aluminium slide holder.

The stability of various configurations of holding the slide was tested in a manner similar to that outlined in section 3.5 for comparing the pellicle and cube beam-splitters. 200 frames of an interference pattern were recorded with the 8-bit Mikrotron camera at 50fps for the following configurations: aluminium holder and viscous oil; aluminium holder and regular oil; clamped slide and viscous oil; clamped slide and regular oil. The standard deviation σ of each pixel in a 350px × 350px region was

[4]Computer control over voltage input can increase resolution to 1nm.

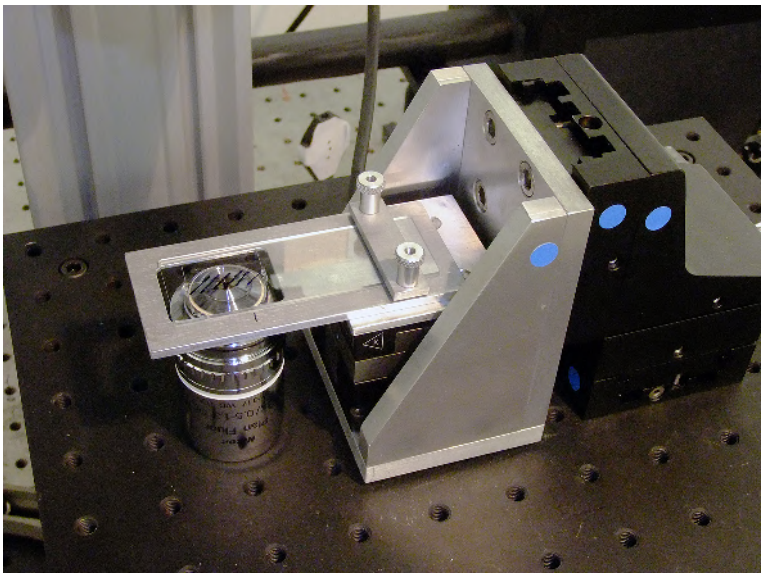

Figure 3.9: Slide holder fashioned out of aluminium to provide additional support to the sample. The coarse-adjustment, lockable dovetail stage, the piezoelectric NanoCube and the aluminium coupling between them are also visible. The 100× objective directly mounted into the breadboard is shown below the sample.

determined throughout the image stack to give an indication of how much each pixel was changing. The mean of these values for all pixels in the image was then calculated, to arrive at a single value for the variation in pixel value over the entire image stack. Table 3.1 summarises these results.

Slide: Oil:	Holder Viscous	Holder Regular	Clamped Viscous	Clamped Regular
Mean of σ over 200 frames	3.00	4.51	6.73	7.65
Expressed as percentage of 256	1.17	1.76	2.63	2.99

Table 3.1: Comparison between simply clamping or using an aluminium plate to support the slide over the objective, and using viscous or regular immersion oil. Values are the mean over the whole image of the standard deviation σ through the image stack of each pixel expressed in absolute pixel values (upper) and as a percentage of 256, which is the bit range of the camera (lower).

It is clear that the combination of aluminium slide holder and viscous immersion oil leads to the greatest stability of the sample. The effect of the holder is also greater

than that of the oil in terms of providing stability.

3.7 Novel Strategies for Off-Axis Holographic Microscopy

In order to neglect the object halo $|O|^2$ term in holographic reconstruction (see section 2.3), the amplitude of the object beam must be significantly smaller than that of the reference beam. This is easily achievable with inline holography, where the illumination and reference beams are one and the same, given a suitably transparent and weakly-scattering sample. A bright illumination source can be used to produce sufficient scattering off a sample and in itself be an appropriate reference beam.

However, given the same sample in an off-axis geometry, the necessarily bright illumination beam would obscure the interference signal from the object and reference beams if incident on the recording medium. Thus, the illumination beam must be either diverted from the camera after illuminating the sample, or it must be blocked in some other way.

Steering the illumination beam is a relatively simple exercise in low- or no magnification setups. It is also not required for reflection mode holography used in metrology applications [98], where the reflected beam is itself the object beam. The extremely short focal lengths of high-powered (100×) objectives mean that, in this case, beam diversion must occur over a very short range, before the signal is irretrievably merged with that of the scattered light from the sample.

Two novel approaches to high-magnification off-axis digital holographic microscopy were attempted. The first utilises a 100× objective with an iris to image the sample and a condenser to provide a narrow beam of laser illumination that can be steered into the iris, leaving the object beam to pass through the aperture. The second provides direct illumination to the sample, while a conjugate Fourier plane of

the image is formed after the objective, into which a mask is inserted that blocks the low spatial frequency illumination beam.

3.7.1 Illumination Beam Control through Condenser

Figure 3.10 is a schematic illustrating the arrangement of optical elements used to facilitate the steering of an illumination beam via a condenser lens.

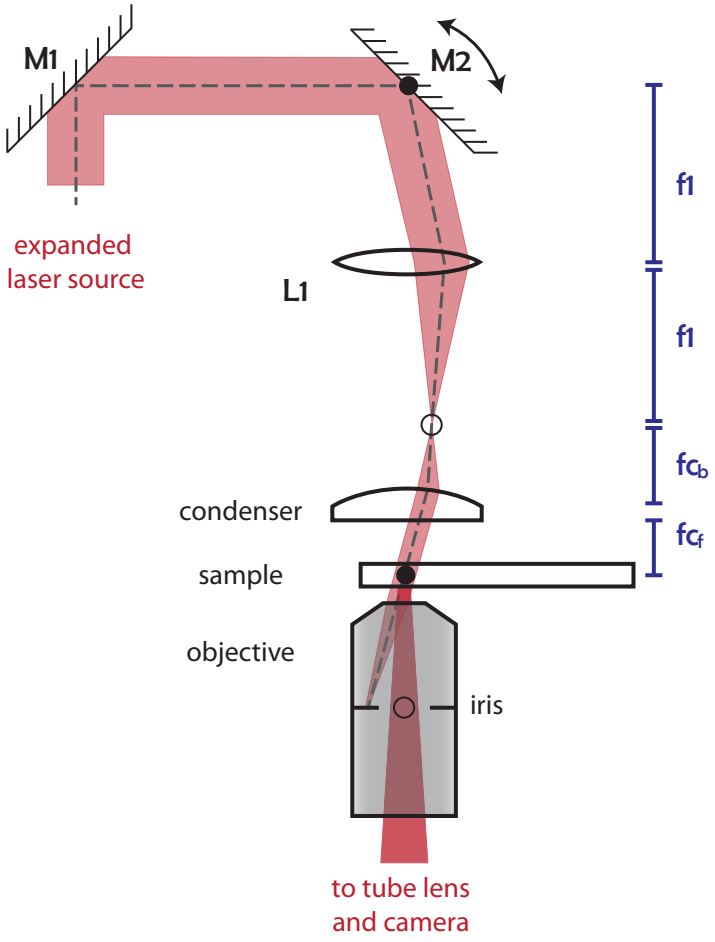

Figure 3.10: By focusing an expanded laser source onto the back focal plane of a condenser, the illumination beam can be steered such that it is incident on the sample at an oblique angle. In this schematic, the grey dashed line indicates the optical axis; the black circles indicate planes conjugate to the sample; the open circles are conjugate to the back focal, or Fourier, plane. L1 is a plano-convex lens with focal length f1. The front and back focal lengths of the condenser are indicated, respectively, by fc_f and fc_b. The principle of beam-steering to provide oblique illumination is described in the text.

The beam from the laser source is expanded through a Keplerian telescope[5]. A minimum of two steering mirrors is then required to adjust the beam. The second of these is at focal length away from a focusing lens, which is itself at focal length away from the back focal plane of the condenser (TC-HNA OIL, 1.4 NA DIC oil lens; Nikon Instruments Inc.). The light focused onto the back focal plane of the condenser results in parallel illumination out of the condenser and incident on the sample, which must be positioned at the front focal plane of the condenser.

Adjusting the mirror M2 has the effect of moving the position of the focused beam at the back focal plane of the condenser. This in turn steers the beam out of the condenser while still ensuring parallel illumination.

A 100× objective with an iris (CFI Plan Fluor 100×S Oil; Nikon Instruments Inc.) is used to magnify the sample. The illumination beam is directed through the sample such that the beam is blocked by the iris, while still allowing the light scattered by the sample to proceed through the aperture to the tube lens and the camera.

While this approach worked in principle, it was found that the scattering signal off typical dielectric objects of interest (polystyrene microspheres and bacterial cells) was too poor to be observed when illuminated at an oblique angle. Sowa *et al.* have shown that the scattering intensity of polystyrene beads is strong along the direction of illumination, yet weak in other directions [143], a result which can be explained by Mie scattering [144]. Some success was observed with gold nanoparticles [145, 146], which have an isotropic scattering profile. However, the method discussed below was seen as an improvement over the condenser illumination due to its versatility.

3.7.2 Fourier Plane Mask

A second approach to eliminating the illumination beam in a high-magnification off-axis DHM was trialled. It was proposed to retain the direct illumination of the

[5]That is, a telescope made from two convex lenses.

sample in order to produce a sufficiently strong object scattering signal, and then to remove this low spatial frequency illumination through a mask in a Fourier plane. This effectively provides forward-scattering dark field microscopy of the object. It was originally hoped to achieve this directly in the back focal plane of the objective; however, this proved to be inaccessible. Instead, a conjugate back focal plane was set up through the addition of a Keplerian telescope after the tube lens. This approach has the additional advantage of providing an opportunity to adjust the magnification of the image. However, it increases the path length of the imaging optics, which has a bearing on the ergonomic design of the microscope in relation to available space on the optical table, and requires an equivalent increase in path length for the reference beam. Additional lenses are also a potential source of parasitic scatterers, impacting negatively on the quality of the image. To mitigate this effect somewhat, the condenser was removed and illumination of the sample was achieved by creating a diffraction-limited spot of the required diameter at the sample plane, via a single lens. The low coherence length laser goes a long away toward minimising these effects, however. Figure 3.11 demonstrates the arrangement of optical elements in this apparatus.

A mask was mounted onto a blank optics adapter and thence in an x-y adjustable lens mount. This was attached to a micrometer-adjustable linear travel stage, thus allowing for fine adjustment of the mask in x, y and z. The assembly was installed in approximately the correct position. Fine adjustment of the mask position was achieved by looking at a live feed of the 2D Fourier transform of the video image. The mask was adjusted in z until it appeared in focus in the Fourier transform, and then adjusted in x and y until the zero-order illumination beam was effectively blocked.

A number of different objects for masks were trialled. Firstly, the size of the back focal plane between lenses L5 and L6 was estimated. The back focal plane of the

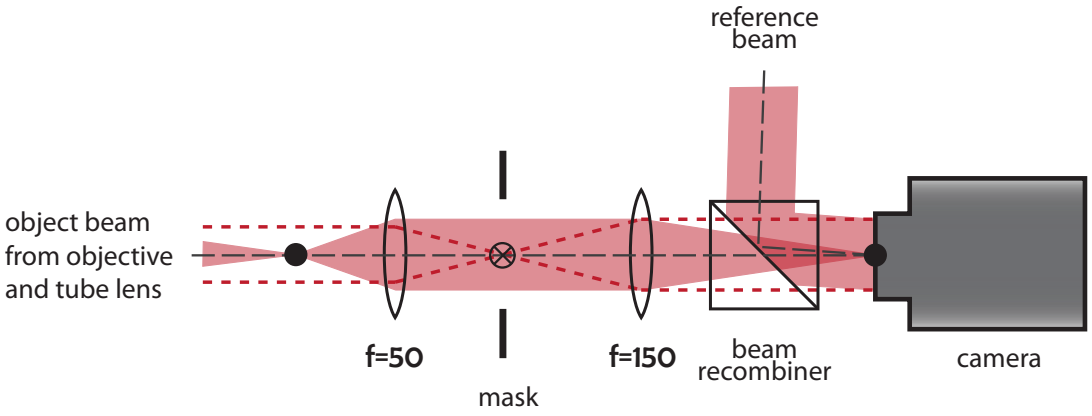

Figure 3.11: An optical schematic of the Fourier plane mask approach to eliminating the illumination beam as described in the text. The dashed grey line indicates the optical axis. The angle between the object and reference beams is shown, although exaggerated. The black circles indicate planes conjugate to the sample and the open circle indicates a plane conjugate to the back focal plane, into which the mask is positioned. The solid red indicates the image formation and the dashed red lines indicate the back focal plane. Focal lengths of the two lenses shown are given in millimetres.

100× objective is approximately 6mm in diameter. The focal lengths of L5 and L6 were set at, respectively, 50mm and 150mm (see section 3.8). Thus the diameter of the back focal plane at the location of the mask is approximately: $\frac{50}{150} \times 6 = 2$mm. The aim of the mask is to block out the centre of this region to sufficiently remove the low spatial frequency illumination beam, while still allowing enough of the higher spatial frequency scattered light to pass, in order to reconstruct the object.

Figure 3.12 shows 2D Fourier transforms of images obtained with this dark field off-axis holography approach using four different materials for the Fourier plane mask.

A black human hair (thickness $\approx 100\mu$m) was first used as a mask. The hair blocked the correct region of the back focal plane; however, it was not entirely opaque to the laser and had the disadvantage of burning at high laser power. Metal wires of Standard Wire Gauge 40-46 (120 to 60μm) were trialled. The round profile of the wire tended to produce unwanted scattering effects at the edges and it proved difficult to flatten such thin wires to reduce this effect. The thinnest flat wire able to be sourced was too wide (0.6mm) and blocked a significant part of the desired object

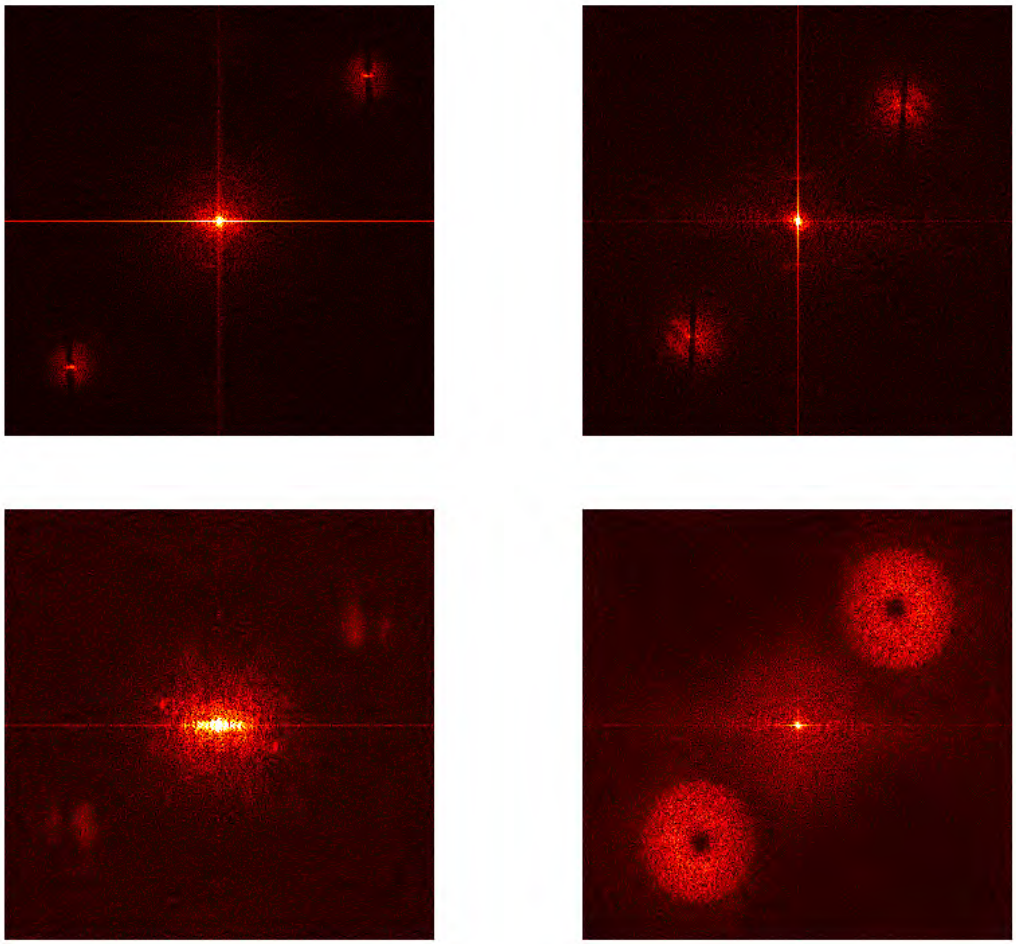

Figure 3.12: The Fourier plane of dark field off-axis holograms obtained using four different materials for masks. The images are displayed on a logarithmic scale and in false colour. At the centre of the plane is the direct illumination term, which is blocked to a greater or lesser degree depending on the material of the mask. The upper-right and lower-left quadrants of each image show the spatial frequency information of the real and virtual twin images. The masks used to obtain each image are: *Top left*: human hair, which is only moderately effective at blocking the illumination beam; *Top right*: 60μm diameter copper wire, which is again not wide enough for sufficient blocking of the illumination beam; *Bottom left*: flat 0.6mm steel wire, which blocks too much of the object beam; *Bottom right*: 0.5mm steel ball bearing mounted on two human hairs. This mask effectively blocks the illumination beam while still leaving a sufficient proportion of the object beam to enable reconstruction. The spatial frequency range of the object appears larger in this image due to the logarithmic intensity scale and a more successful blocking of the high-intensity illumination beam.

beam.

In order to effectively block the illumination beam, while mitigating unwanted scattering effects from the mask and reducing the impact of the mask on the desired

object beam, it was decided to trial a circular mask in the centre of the conjugate back focal plane. A 0.5mm diameter ball bearing (Grade 10 Hardened AISI 52100 Chrome Steel; Simply Bearings Ltd) was attached to a crosshair support provided by two human hairs and a tiny amount of epoxy resin. The hairs were first attached by epoxy to the blank optical mount under tension and allowed to set overnight. A 10× to 63× stereomicroscope (SMZ800; Nikon Instruments Inc.) was used to view the arrangement while a small amount of epoxy was first attached to the bisection of the hairs and then a ball bearing was lowered in place. The mask was examined after a further settling period to ensure no epoxy was visible from underneath the ball bearing. This approach produced satisfactory results. Figure 3.13 shows the ball bearing mask as used in the microscope.

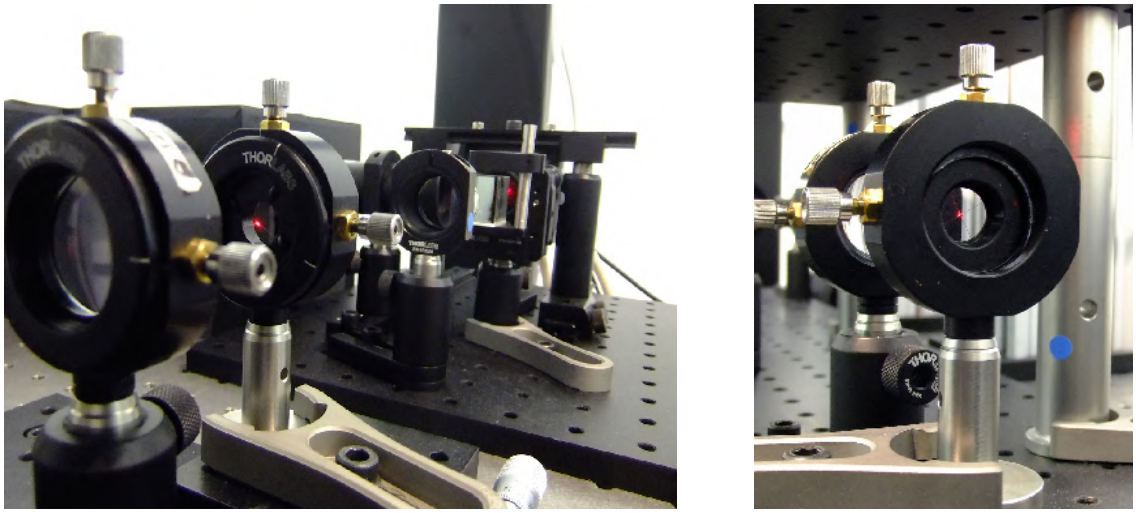

Figure 3.13: A 0.5mm diameter ball bearing was used as a mask in the Fourier plane to obtain dark field imaging. The bearing was attached to a crosshair made from two human hairs and mounted in an adjustable lens mount. The left-hand image shows the mask (second optical component from the left) looking toward the 150mm focal length lens (L6), the beam recombiner and the camera. The right-hand image shows the other view looking towards the illumination source. The 50mm focal length lens (L5) can be seen behind the mask. In each image, the ball bearing can be seen blocking some of the incident laser light. Please refer to the schematic shown in figure 3.14 to see the mask in context.

3.8 Final Design of High-Magnification DHM

In the research and development process, it is difficult to determine whether there is ever a clear-cut 'final design'. As is clear from the preceding sections, a large number of variables must be considered before the final microscope design. Crucially, the application of the instrument must be made very clear. Originally, it was hoped that a modular instrument could be developed, capable of both inline and off-axis holography, and at a range of magnification settings. The approach to off-axis holography eventually settled upon − that of the Fourier plane mask detailed in section 3.7.2 − and the variation in back focal plane position across different objectives meant that this was not feasible. Certainly not without height-adjustable objective mounts and matching adjustable linear stages for the downstream optics and camera. It was ultimately felt that this microscope should be solely for high-magnification studies of one or a few individual cells, and that a second microscope with a lower magnification could be constructed. This is detailed in section 3.9.

3.8.1 Optical Configuration

With this in mind, it was decided that a 30μm to 60μm (side length) field of view would be appropriate for individual bacterial cell studies, corresponding to using either a 512px × 512px subregion or the full frame (1024px × 1280px) of the Mikrotron camera. It was decided to use the Mikrotron camera for its high-speed recording ability, and to use the iFLEX laser for its low coherence length properties, which are ideal for inline applications.

The decision on the size of the field of view has bearing on all of the illumination and imaging optics, as does the general principle of keeping the number of optical surfaces to a minimum in order to reduce the occurence of parasitic scattering. The physical size of the optical table also has an impact on the choice of imaging optics,

especially with the desire to avoid wrapping beams to keep optical surfaces to a minimum.

A schematic of the final design is shown in figure 3.14. All optical element labels refer to this diagram. Figure 3.15 shows a photograph of the final microscope design.

Firstly, a total magnification of 225× was settled upon by using a 100× objective, a 150mm focal length tube lens, and a Keplerian telescope formed by lenses with focal lengths of 50mm and 150mm. The Mikrotron CMOS chip contains 14μm square pixels. Thus, this arrangement gives a characteristic magnification of 62.5nm/px, meaning a 512px × 512px subregion shows a field of view of 32μm × 32μm and the full frame shows a field of view of 64μm × 80μm. The Fourier plane mask described in section 3.7.2 was positioned between the 50mm and 150mm telescope lenses.

Secondly, a single lens (L3) was chosen to produce a diffraction-limited beam waist of sufficient diameter to illuminate the maximum field of view. The fibre of the iFLEX laser provides effective spatially filtering, meaning a separate spatial filtering arrangement is not required. The diameter of the desired waist, a, was calculated to be: $a = \sqrt{80^2 + 64^2} = 102\mu$m at the sample plane. The equation for a focused beam waist is given by:

$$a = \frac{1.220\lambda f}{d} \tag{3.4}$$

where 1.22 comes from the Rayleigh criterion (see section 2.1.4), λ is the wavelength of the laser (635.0nm in the case of the iFLEX), f is the focal length of the lens, and d is the initial waist diameter of the laser (0.63mm for the iFLEX). A 100mm focal length lens was found best to satisfy this requirement ($a = 122\mu$m).

Finally, the reference beam needed to be expanded to fill the area of the CMOS chip via a single telescope. Given the available table space, the only combination of lenses that was feasible were 50mm (L1) and 1000mm (L2) focal length lenses arranged in a Keplerian telescope. A shorter focal length lens was not used in the place of L1 due to concerns over lens quality with the available options. Notably,

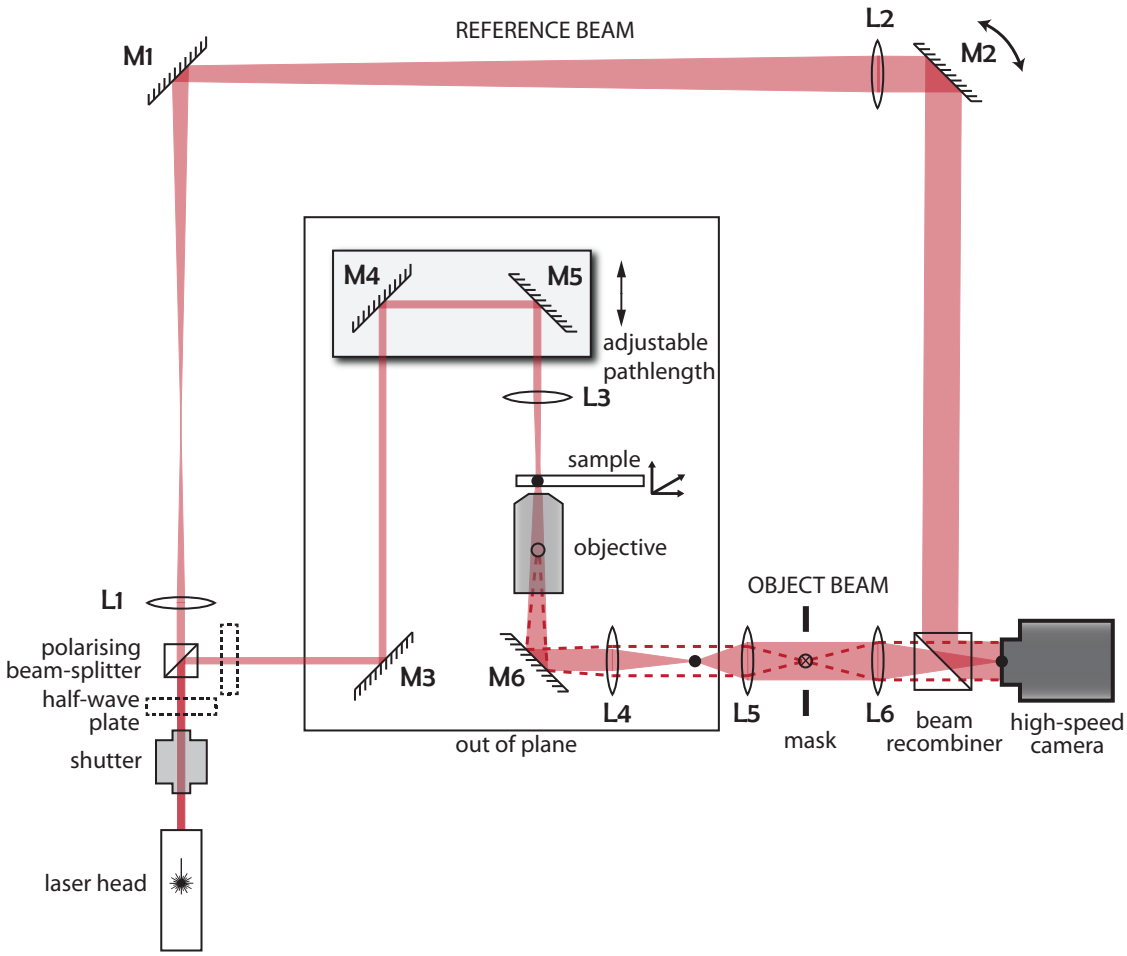

Figure 3.14: Final design of a high-magnification digital holographic microscope capable of recording inline and dark field off-axis holograms. Closed circles correspond to planes conjugate to the sample; open circles are conjugate to the back focal plane. Lenses are all plano-convex. The specific function of each optical element is referred to in the text.

this combination results in only a 20× magnification of the 0.63mm diameter source beam, thus not filling the entirety of the Mikrotron CMOS chip. There is a limited number of solutions around this issue, given the constraints of the table and the design parameters. A Galilean telescope[6] could be used; a low-powered objective could provide the magnification of the beam; or a best-form lens with a shorter focal length could be used in place of L1. In the meantime, it was deemed sufficient to use a subregion of the chip for imaging purposes.

[6]A telescope with one convex and one concave lens.

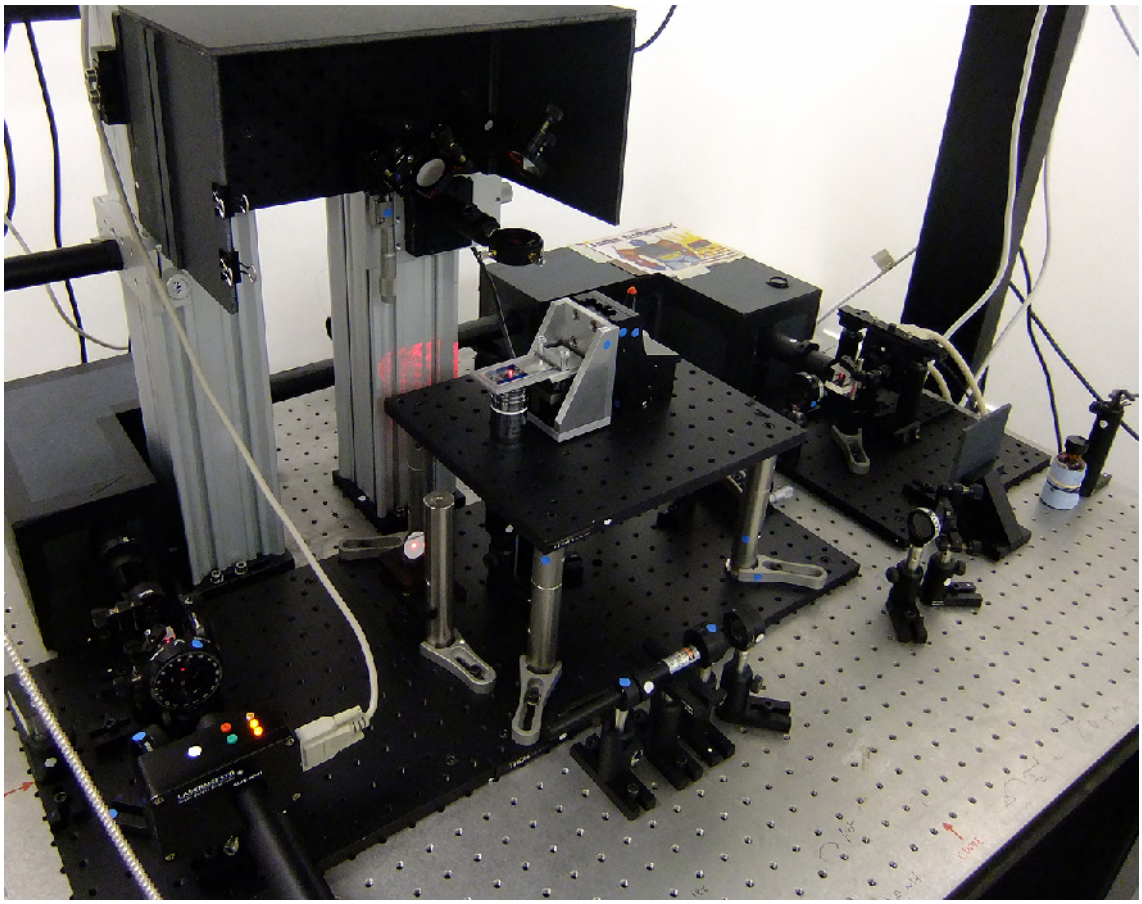

Figure 3.15: The final design of the high-magnification digital holographic microscope. The laser head is at the bottom left of the image, entering the safety shutter. After a half-wave plate the beam diverges via a polarising beam-splitter. The reference beam proceeds around the back of the table under the cardboard dust covers. The illumination beam proceeds through a second half-wave plate then is coupled into the objective via the periscope. The recombining beamcube can be see at the far right of the image just before the Mikrotron camera. The laser pointer in the front centre of the image was used for initial alignment of the microscope.

3.8.2 Beam Splitting

Creating two mutually coherent beams for off-axis holography is achieved by splitting the laser source with a polarising beam-splitter after the required interlock-connected shutter. A half-wave plate in front of the polarising beam-splitter allows the relative amplitude of the two beam paths to be adjusted. Adjusting a second half-wave plate in the illumination path ensures the two beams can be made mutually polarised. Additional control over the laser intensity can be achieved with a combination of

neutral density (ND) filters placed either directly at the laser head or in one of the two paths. It should be noted that a neutral density filter in one path will necessitate an adjustment in the path length to generate an interference pattern for off-axis holography.

The use of a beam-splitter cube to recombine the beams has been discussed in section 3.5. This cube is mounted on a kinematic platform mount. By using this control in conjunction with the adjustable mirror M2, the reference beam can be aligned to be incident on the camera at an angle suitable for off-axis holography, as discussed in section 3.3.1. This alignment is achieved after the imaging optics have been placed and is an iterative process. First, a live 2D Fourier transform of the image is used to position the twin image spectra optimally, then a live camera image is used to ensure the centre of the beam is incident on the centre of the camera. These steps are repeated until both conditions are satisfactorily met.

The reference beam path is enclosed in a home-built box and tubing made from laser-proof card from L1 through to the beam recombiner to give protection from dust.

3.8.3 Objective and Stage

The objective is mounted directly into a 12.7mm thick breadboard (250mm × 300mm, Thorlabs Inc.) via a custom-threaded hole. This breadboard is mounted to the isolation air table through four 25mm-diameter posts to provide a platform upon which the manual and piezo adjustment stage (section 3.6) is secured.

3.8.4 Ensuring Identical Path Lengths

Mirror M3 is the lower arm of a periscope that couples the illumination beam vertically in order to illuminate the sample from above. M4, M5 and L3 are supported by two 0.5m high vertical rail posts with a base of 95mm × 95mm. M4 and M5 are mounted

on an additional plate, the height of which can be adjusted by a micrometer screw with a travel range of 25mm. This allows the path length of the object beam to be adjusted relative to the reference beam for off-axis holography. This is particularly useful for fine alignment of the interference pattern and for correcting the path difference should a neutral density filter be introduced into one beam.

There are disadvantages to having the vertical coupling mirrors adjustable in this way. For instance, the micrometer is subject to long-term drift and the interference pattern should be checked at the start of each day prior to acquiring data. Additionally it is imperative that the verticality of the beam from M3 to M4 and from M4 to L3 is ensured. However, these two mirrors were selected for adjustment as they form a natural dogleg in the optical system. Thus, additional optics are not required by inserting a dogleg elsewhere in the setup, which would go against the design principle of minimising the number of optical surfaces.

The building of the two arms of the microscope was an iterative process. The approximate length of each path, allowing for the thickness and refractive indices of lenses and other optical components, was calculated and positions of optical components were adjusted accordingly until the two were similar. After placement of optical components, the paths were measured with a tape measure and the plate upon which M4 and M5 are mounted was adjusted coarsely by hand up or down the vertical rail post until interference was observed. The imaging path was realigned and fine adjustment of the path length was undertaken with the micrometer screw. The final path length for each arm in between the two beam-splitters is $\sim$1.35m.

3.9 Low-Magnification Inline DHM

As mentioned in section 3.8 it proved unfeasible to create a holographic microscope capable of both high- and low-magnification imaging. Thus, a separate prototype

low-magnification inline microscope was developed.

For a number of reasons − simplicity of design, space constraints on the isolation air table (I-2000 Stabilizer; Newport Corporation) and to make the instrument safe for an undergraduate project student − the microscope was built in a horizontal, single-plane configuration. This also removed any stability concerns in introducing a periscope to the optical path.

Figure 3.16 shows an optical schematic of this microscope in its original configuration. This microscope was used as a test-bed for the Andor Neo sCMOS camera described in section 3.3.7. The illumination source is a 1mW helium-neon gas laser (05-LLR-811, 632.8nm, linearly polarised; CVI Melles Griot). Mirrors M1 and M2 allow for alignment of the illumination beam onto the optical axis. Lens L1 has a focal length of 400mm and is positioned so that it provides a beam waist of $\sim$400μm at the sample. The objective is a 40$\times$ CFI Plan Fluor from Nikon Instruments Inc. Coupled with the 200mm focal length tube lens (L2) it provides a total of 40$\times$ magnification at the CMOS plane, with a maximum field of view of 410μm $\times$ 350μm.

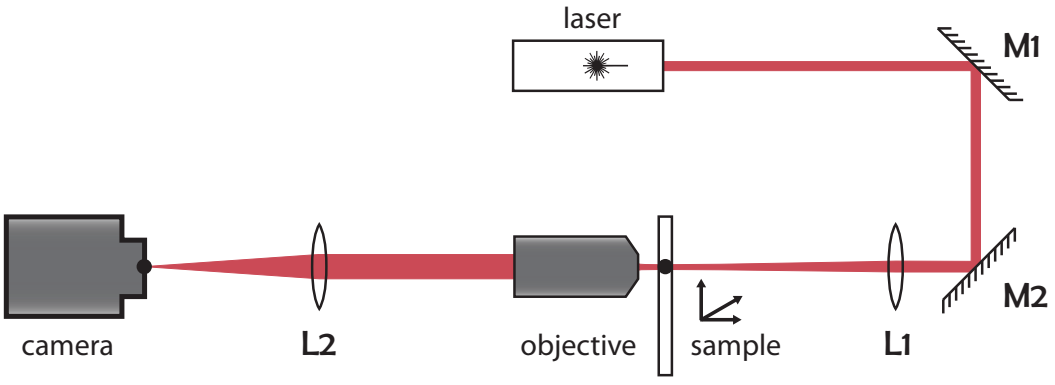

Figure 3.16: Optical schematic of the low-magnification (40$\times$) inline digital holographic microscope. The black circles correspond to planes conjugate to the sample. The optical components are described in the text.

A custom, threaded mount was manufactured out of 20mm aluminium plate to hold the objective in place (figure 3.17). To make this arrangement as stable as

possible, no vertical adjustment was built in, thus all other optical components were adjusted to this height.

Samples are configurations of conventional glass slides and are clamped to a lockable dovetail stage (460PD-X; Newport Corporation) to provide up to 12.7mm travel vertically. This in turn is bolted to a spring-loaded micrometer screw-adjustable stage (460A-XY; Newport Corporation) for 12.7mm travel in both directions in the plane of the table. The slide was supported underneath by an aluminium ledge bolted to the stage. The sample holder is shown in figure 3.17.

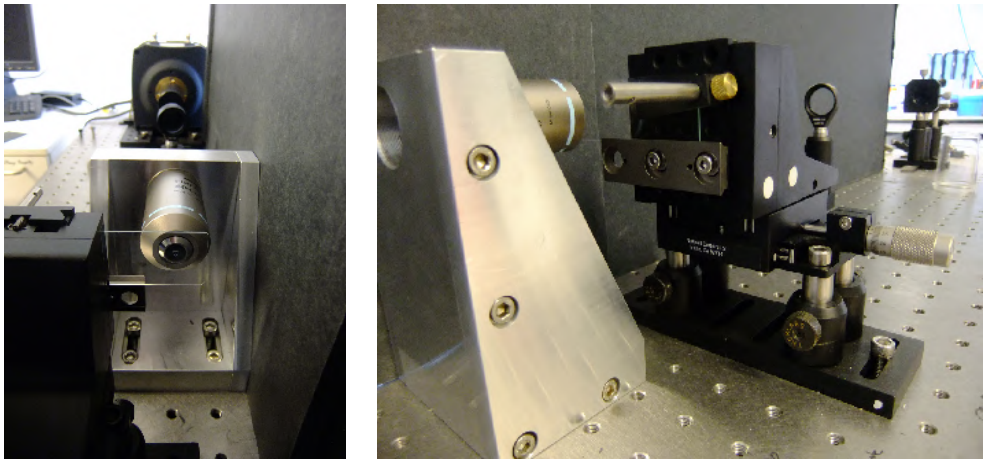

Figure 3.17: Detail of the sample holder and custom-built objective mount used on the 40× DHM. The solid construction of the aluminium objective mount is apparent. The Andor camera and tube lens can be seen in the background of the left-hand image. The sample clamp and aluminium ledge to support the slide are visible in the right-hand image.

Chapter 4

Characterisation of Inline Holography

4.1 Introduction

This chapter details the experiments used to specify the performance of the digital holographic microscope described in section 3.8, operating in its inline mode. Key parameters for characterisation are: the in-plane (x-y) resolution of the system; the through-plane (z), or depth, resolution; and the maximum concentration of particles able to be imaged effectively in a typical sample. Held in consideration with these calibration experiments is the proposed end-user applications for these microscopes. Chiefly, these are the ability to localise and track a number of swimming bacteria in three dimensions in a given volume and to do similarly for small tracer particles that could be used as a proxy for the fluid flow.

Using the mean squared displacement of a diffusing microbead to determine the diffusion coefficient in three dimensions is seen as a classic and simple calibration experiment illustrating the basic capabilities of the microscope and thus these results are included here.

The performance of the cameras used on this microscope, covering aspects such as framerate and data transfer rates, has been discussed already in sections 3.3 and 3.4.

The high-magnification digital holographic microscope is able to record a 512px × 512px region of interest, corresponding to a 32μm × 32μm field of view (FoV), with a total magnification of 225× at up to 2,000 frames per second. Specific framerates and fields of view will be stated where they differ from these figures.

4.2 Methods for 3D Holographic Imaging

4.2.1 Numerical Reconstruction in Practice

The theory of reconstructing digital holograms to obtain the three-dimensional electromagnetic field of the sample is described in section 2.6. The code to implement the practical reconstruction of recorded holograms was written by Irwin Zaid, a fellow doctoral student in the Department of Physics, University of Oxford, and jointly supervised by Prof. Julia Yeomans and Dr Richard Berry. A complete description of this code will be published at a later date. In the meantime, I outline some relevant features here, especially for an end-user of the microscope described in chapter 3.

Recorded holograms are transferred to a dedicated computer system for reconstruction. Hologram data may be in tagged image file format (tif), in which case a number of files are stored corresponding to the number of frames captured, or in hierarchical data format (HDF5), which saves a single file. Hierarchical data format has the advantage of encoding additional parameters of interest, such as the exposure setting and timestamp, alongside each frame.

Reconstruction proceeds on an NVIDIA Tesla graphics processing unit (GPU) (Tesla C2070, 448 CUDA cores, 5376MB memory; NVIDIA Corporation). The bespoke software is written in Python to interface, via PyCUDA [147], with CUDA

(Compute Unified Device Architecture) – NVIDIA's proprietary language to perform parallel computing operations on its graphics processors.

A GPU is used for our holographic reconstructions because of the high level of parallel processing available – shown in its ability to perform up to 515×10^9 double precision floating point operations per second (515 Gflops). This is over a factor of two more than Intel's recent Sandy Bridge series CPU chips [148]. The difference in performance speeds is even more marked for single precision floating point operations. The downside is that many mathematical and array operations taken for granted on more established computing systems are not yet standard on CUDA and thus require workarounds through conventional CPU-based software. Additionally, the way in which GPUs operate – through dynamic restructuring of processing operations to fit the available memory architecture – provides an additional level of complexity, requiring metaprogramming to update these parameters as required.

In a nutshell, Irwin has written a number of packages on the GPU to: preprocess the raw hologram to isolate the object term as described in section 2.6.2; reconstruct the 3D electromagnetic field as described in section 2.6.1; apply a global or local threshold to identify particles of interest in the 3D reconstruction; and determine a centroid or amplitude-weighted centroid (also known as 'centre of mass') to the regions above the threshold to output the three-dimensional coordinates of particles.

Each of these packages can be called in turn by the user, either through a graphical user interface (GUI) or by a custom-written Python script, to output the detected positions of particles in a 3D volume. In practice, I found it most efficient to write my own script to output particle position data for large numbers of frames (reproduced in appendix B.1), although the GUI was used to visualise reconstructions and to identify appropriate threshold values. A script could be written to automate the reconstruction process, allowing the GPU to run continuously and to process many datasets without user input, providing the threshold values and filenames are set

initially.

Through the graphical user interface, the operator can load, examine and reconstruct holograms from either tif or HDF5 format files. Both inline and off-axis holograms are able to be treated. Firstly, a hologram dataset is loaded and preprocessing performed. For inline holograms, the mean of a dataset can be generated for use as a reference beam that can normalise the hologram as per equation 2.58. The following values must be input by the user: wavelength of light, refractive index of medium and effective pixel size (pixel size / magnification). Raw and normalised holograms are able to be viewed onscreen. A screenshot illustrating the GUI in use at this stage is shown in figure 4.1.

Slicewise reconstruction of the hologram can also be displayed. This is far less computationally-intensive than a full volume reconstruction and is thus useful for determining the approximate location of a particle of interest at a particular depth in the sample. The slicewise reconstruction is obtained by setting a particular d value for the propagator in equation 2.52 (by way of equation 2.50). Both amplitude and phase of the reconstructed hologram are able to be displayed. The typical aim of analysing a recorded dataset in the context of this thesis is to localise in three dimensions the positions of an ensemble of micro-objects: polystyrene beads or bacterial cells, for instance. In this case, a global threshold is set, above which objects are identified and their positions logged. The slice reconstruction viewer is useful for finding and adjusting an appropriate threshold. This process is demonstrated in figure 4.2.

The full volume reconstruction of a hologram is able to be performed and visualised onscreen. The floor and ceiling of the desired volume for reconstruction can be set, along with the desired resolution in z, expressed as the number of slices in the prescribed volume. The volume reconstruction proceeds through calculating the object field via equation 2.52 at every plane set by the z-resolution. For display purposes, the values of the reconstructed object field are interpolated between voxels.

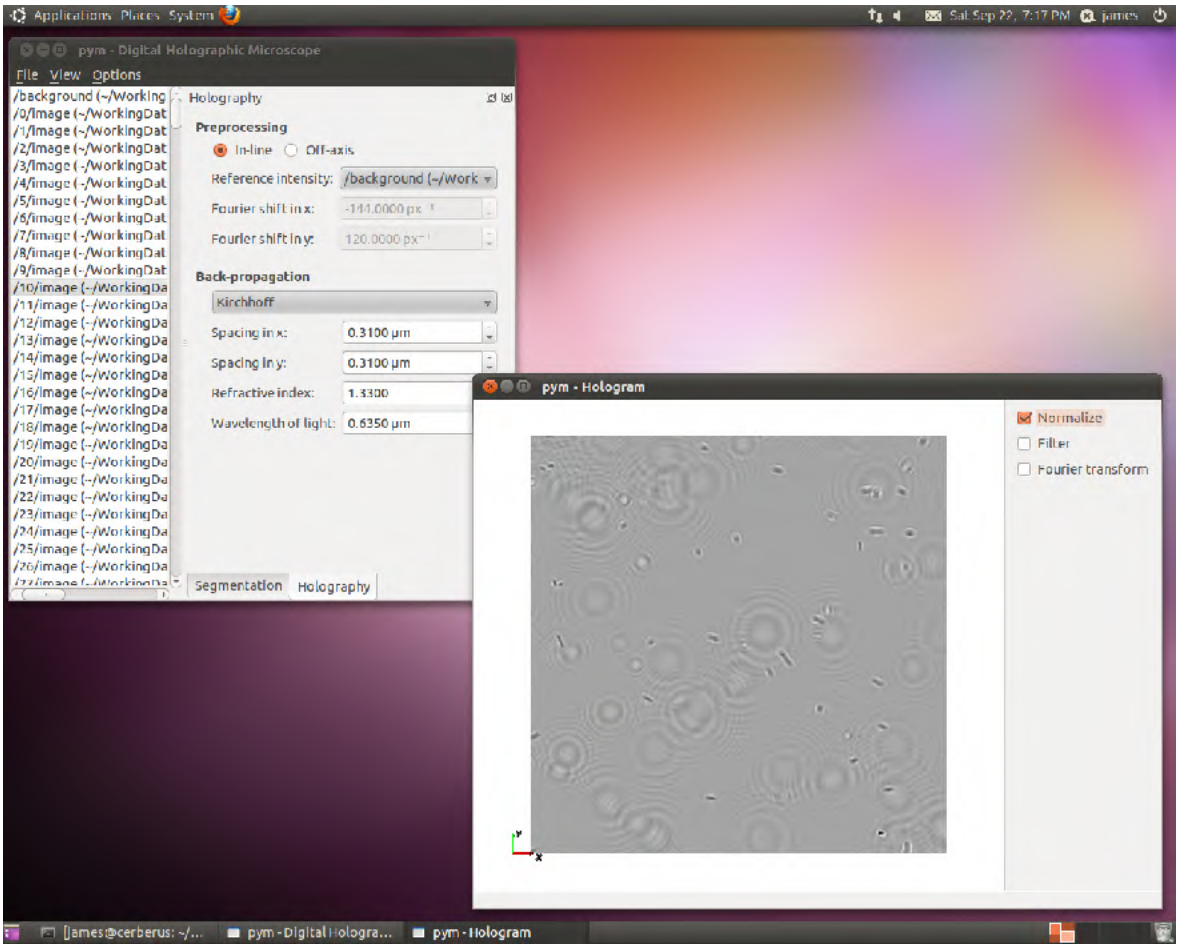

Figure 4.1: A screenshot of Irwin's GUI for examining holograms is displayed. The window in the top left allows the user to load and select holographic data. An image to be used as the reference intensity can be selected. Parameters such as the effective pixel spacing in x and y, the refractive index of the medium and the wavelength of light used must be input. The window in the bottom right shows a normalised inline hologram of motile *E. coli* acquired at a total magnification of 45×.

The reconstructed object field above the set threshold is displayed on a ROYGBIV colour scale, with red indicating the highest intensity. Figure 4.3 shows a 3D render of the reconstructed light field for the data displayed in figures 4.1 and 4.2.

Finally, data from the reconstruction can be output. Videos of multiple frames of either 2D or 3D data may be saved. In addition, the positions of objects of interest in each frame may be output. Positions are determined by locating a centroid, which can also be amplitude-weighted, on the reconstructed light field above the prescribed

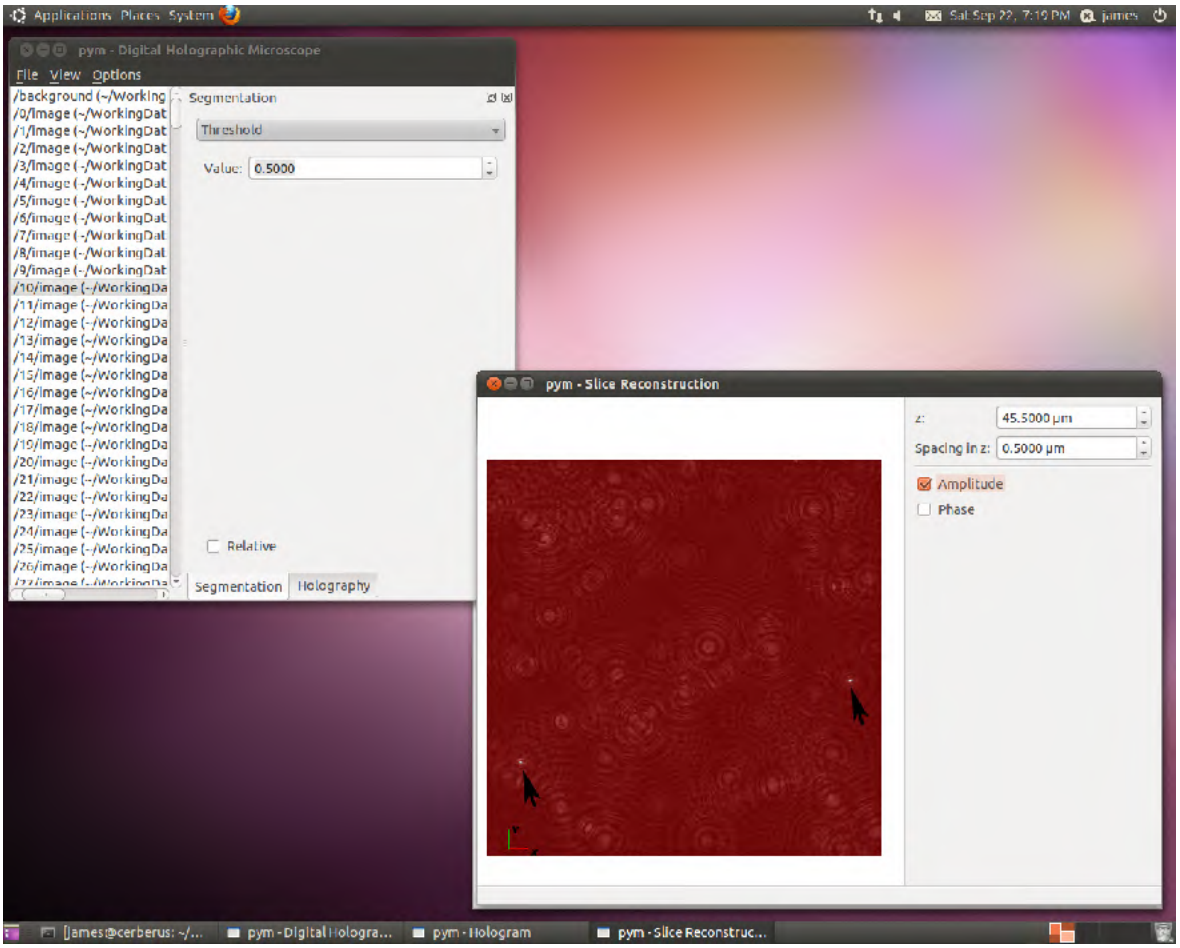

Figure 4.2: A screenshot of the GUI showing slicewise reconstruction of a hologram. The same holographic data presented in figure 4.1 are used. In the window in the top left the global threshold value discussed in the text can be adjusted. The bottom-right window shows the reconstructed hologram in a plane 45.5μm above the specimen plane. In this plane, the intensity of two cells rises above the set threshold level. This is shown by the two white dots located by the arrows and surrounded by the red background.

threshold. The equation describing the centroid $\bar{\mathbf{r}}(x, y, z)$ in three dimensions is:

$$\bar{\mathbf{r}}(x, y, z) = \frac{\sum_{x,y,z} w(x, y, z)\mathbf{r}(x, y, z)}{\sum_{x,y,z} w(x, y, z)} \tag{4.1}$$

where $\mathbf{r}(x, y, z)$ are position coordinates of the light field above the applied threshold. $w(x, y, z)$ describes the amplitude of the light field at each coordinate for finding the centre of mass, although the function could be set to any relevant weight parameter.

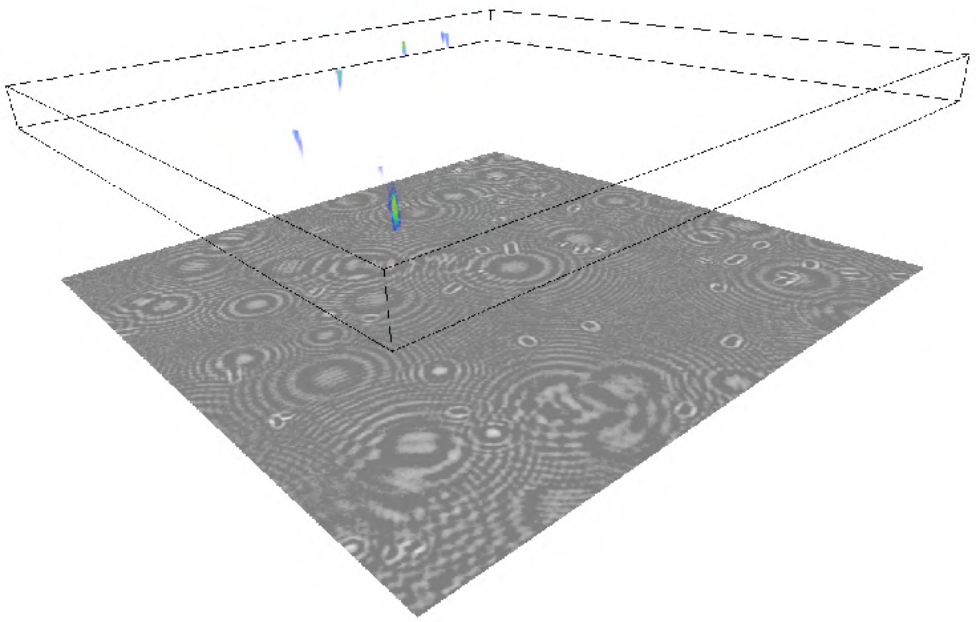

Figure 4.3: A screenshot from the GUI interface showing volume reconstruction of a hologram. The same holographic data presented in figures 4.1 and 4.2 are used. The original normalised hologram is displayed in the specimen plane. A subset of the volume has been reconstructed: its limits are shown by the bounding box, which indicates a floor value of 40μm and a ceiling of 50μm. These values can be changed to examine the entire reconstructed volume or any subset range in z. The same threshold value used for the slicewise reconstruction in figure 4.2 has been applied. The presence of *E. coli* cells within the specified z-range can be seen by the ROYGBIV-coded light field intensities, the values of which are higher than the prescribed threshold value.

For a simple centroid, $w(x, y, z) = 1$.

These position data are saved in HDF5 format in the form of x, y, z coordinates for the centre of each particle in each frame. Additional parameters, such as the volume of the light field corresponding to each object, the timestamp of the frame, and the pre-processed hologram can also be stored. These position data can then be analysed further and the large filesize image data archived or deleted if desired.

A typical timescale for the reconstruction, thresholding, position identification and output is 15ms per slice, assuming a 512px $\times$ 512px hologram. Thus, obtaining the output of object positions for a 100μm deep chamber at 50nm resolution in z takes around 30 seconds.

4.2.2 Samples

Sample Chambers

Samples are introduced into the microscope chiefly through 'tunnel slides' of approximately known heights. A tunnel slide is made by sandwiching a spacer medium with a conventional glass slide (Fisherbrand, 25mm × 75mm, 0.8 to 1.0mm thick; Thermo Fisher Scientific Inc.) and coverslip (Menzel-Gläser, usually 22mm × 22mm, 0.17mm thick; Thermo Fisher Scientific Inc.). The original spacer material was two pieces of double-sided tape (Scotch, 12mm wide, ∼100μm thick; 3M plc) placed ∼3mm apart. For shallower chambers, two thin lines of vacuum grease (Dow Corning GmbH) were laid on the slide using a narrow gauge syringe. Small pieces of plastic or metal shim (20 to 75μm; Auto Aero Manufacturing (Hughes Wynne Ltd)) were placed on the outside of the grease lines to provide a height gauge. The coverslip was then pressed carefully onto the grease to form a tunnel.

Glassware was cleaned with ethanol before use. An aqueous sample could be introduced into the tunnel with a pipette, using capillary action. The sample would be sealed at each end of the tunnel with nail varnish or a line of vacuum grease. Prior to tunnel assembly, a fine marker pen is used to mark the inner surface of the coverslip, that is, what becomes the floor of the tunnel. To ensure the holographic reconstruction proceeds through a single medium of known refractive index, the sample is usually moved so that the objective focuses on the pen mark. Prior to image acquisition, the manual stage would be bolted down and the pen mark moved out of the field of view by the fine-adjustment piezo stage.

Some experiments required a chamber of an independently measured spacer height. As the compression of the double-sided tape and grease that occurs in manufacturing the tunnel slide is unquantifiable, they were rejected for this purpose. Aluminium tape (Advance Tapes Int. Ltd) was seen as a better candidate as a spacer as it is relat-

ively incompressible yet still easy to work with and less expensive than custom-made PDMS[1] or plastic structures. To determine the thickness of the tape, ten slices were laid on top of each other and the thickness of these ten measured with a micrometer ten times. The micrometer has an error of ±0.01mm. This procedure was repeated for three samples and the final thickness for a single piece of tape determined to be $100.3 \pm 0.2\mu$m.

As the aluminium tape had adhesive on only one side, it was necessary to secure the coverglass to the non-sticky side of the tape. A mass (∼700g) was placed on the assembled tunnel slide to keep the coverslip in place and nail varnish was used to seal around the coverslip, leaving two gaps to allow entry to the tunnel.

Shim spacers were used in an attempt to create tunnel chambers of known heights other than 100μm. Two pieces of shim were sandwiched between an ethanol-cleaned slide and coverslip. A mass was placed on the coverslip while epoxy resin was used to seal around the coverslip. Two gaps were left in the resin to allow for an aqueous sample to be flowed into the chamber. The resin was left to cure overnight. Epoxy was used for these chambers rather than nail varnish as it was found the varnish would permeate the plastic shim and dissolve the pen markings on the coverslip.

Figure 4.4 shows a grease tunnel slide with a shim spacer and an aluminium tape slide sealed with nail varnish.

Microspheres and Nanoparticles

Samples used in these calibration experiments were different concentrations of 1μm or 0.5μm diameter polystyrene microspheres or 100nm diameter gold nanoparticles diluted from the stock solutions into ultrapure water. Four different products were used: 1μm plain polystyrene beads (Polybead 07310, 1.025μm diameter with 0.01μm standard deviation; Polysciences Inc.); 1μm amino-coated polystyrene beads (Poly-

[1] polydimethylsiloxane

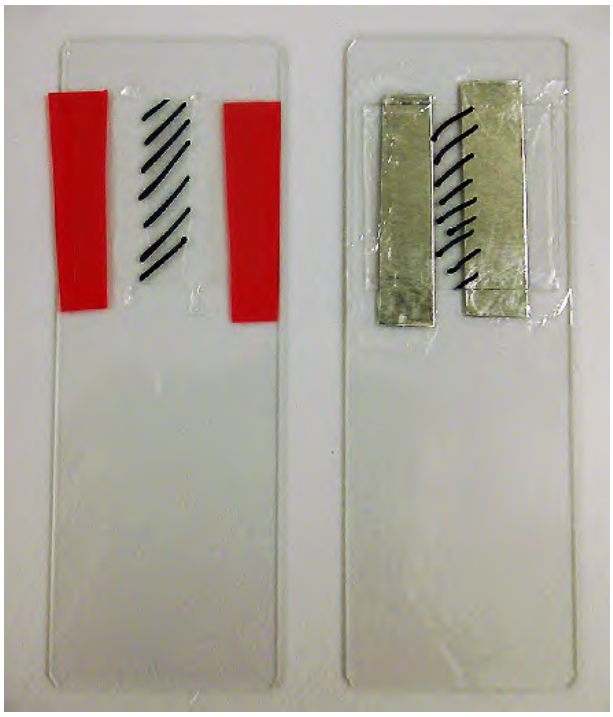

Figure 4.4: Tunnel slides made with grease and shim spacer (left) and aluminium tape (right). The aluminium tape is adhered to the coverslip with clear nail varnish. Pen markings to aid focusing on the floor of the chamber are made across the tunnel on the inside surface of the coverslip prior to assembly.

bead 17010, 0.913μm diameter with 0.024μm standard deviation; Polysciences Inc.); 0.5μm plain polystyrene beads (Polybead 21402, 0.502μm diameter with 0.009μm standard deviation; Polysciences Inc.); and 100nm gold colloids (GC100, 100nm diameter with $\leq$8% coefficient of variation; BB International). The number density of the gold beads was indicated on the product: $N = 5.60 \times 10^9 \text{ml}^{-1}$. The polystyrene beads were supplied with a percentage solids value: 2.65%, 2.63% and 2.02% respectively. To determine the number density of the polystyrene bead stock solutions, and thence the dilution factor for desired concentrations of beads in experiments, the following formula is used:

$$N = \frac{W}{\rho V} \tag{4.2}$$

N is the number density of particles in ml^{-1}; W is the mass, in grams, of beads per ml, derived from the percentage solids value; ρ is the density of polystyrene (1.05g.ml^{-1});

and V is the volume of one microsphere calculated from the given particle diameter value.

Three types of sample are used for characterisation experiments in this chapter. One sample consists of freely diffusing micro- or nanoparticles in aqueous solution. In such cases the desired concentration of particles is determined and the required dilution factor calculated from the number density specified by the manufacturer. To reduce the effects of aggregation due to electrostatic interactions, samples are sonicated in a water bath for 10 minutes before being introduced to the tunnel slide.

The second sample type involves adhering beads to the surface of either the coverslip (floor of the chamber) or slide (ceiling) or both. 10μl of poly-L-lysine (0.1%; Sigma-Aldrich Co. LLC) is introduced to the tunnel chamber and allowed to remain for 30 seconds before a 50μl wash with ultrapure water. The diluted bead sample is then introduced and beads are allowed to settle on the surface for a certain period. The sample must be inverted if the coverslip is the desired surface for adhesion. The settling time is determined by the sedimentation velocity of the particles due to gravity. Neglecting the effects of diffusion, this can be calculated for a sphere by first detemining the force due to gravity on a single sphere of radius r and mass m:

$$\begin{aligned} F_g &= mg \\ &= \rho V g \end{aligned} \tag{4.3}$$

where ρ is the excess density of the sphere over the medium (water in this case) to account for buoyancy and $V = \frac{4}{3}\pi r^3$, the volume of a sphere. Thus equation 4.3 becomes:

$$F_g = (\rho_{bead} - \rho_{medium})\frac{4}{3}\pi r^3 g \tag{4.4}$$

The drag force on a moving sphere at low Reynolds number can be assumed to follow

Stokes' law [26]. The Stokes drag on a sphere is given as:

$$F_d = 6\pi\mu r v_s \tag{4.5}$$

where v_s is the sedimentation velocity, and μ is the dynamic viscosity of the medium. For water at 20°C, μ is 1.002×10^{-3} Pa.s.

F_d and F_g can be equated to solve for the sedimentation velocity, which gives indicative settling times for a chamber of a given height. Sedimentation velocities were calculated to be: 100nm.s^{-1} for both a 1μm polystyrene bead and a 100nm gold colloid, and 6.8nm.s^{-1} for a 0.5μm polystyrene bead. After a period of settling, any remaining freely diffusing microbeads are washed out with water before the ends of the tunnel are sealed.

The third sample type requires both freely diffusing beads and beads adhered to one or more surfaces. For these cases, beads were attached to the surfaces with poly-L-lysine as described above. A desired dilution of amino microspheres was then introduced into the sample chamber. Amino beads have positively-charged amine groups attached to their surfaces. This positive charge repels the particles from the similarly positively-charged poly-L-lysine surfaces, leaving them diffusing freely in solution.

4.2.3 Experimental Conventions

The convention adopted when describing the coordinate system of the sample is that x and y signify the in-plane axes. The z-axis corresponds to the optical, or through-plane, axis. The plane of the recorded hologram (that is, objective focal plane, or specimen plane) is designated $z = 0$, with positive z (or 'upwards', or 'deeper' into the sample) in the direction away from the focus, towards the illumination source. For instance, a tunnel slide with the inner surface of the coverslip brought to the

objective specimen plane has the 'floor' of the chamber at $z = 0$ and the 'ceiling' of the chamber (the inner surface of the slide) at a positive z-value.

The 3D reconstructions of the hologram follow this convention precisely. The recorded hologram is at the focus of the objective ($z = 0$) with reconstruction proceding upstream (positive z values) of this plane, towards the illumination source and the scattering objects. Figure 4.5 demonstrates the experimental coordinate system and how it relates to a 3D holographic reconstruction.

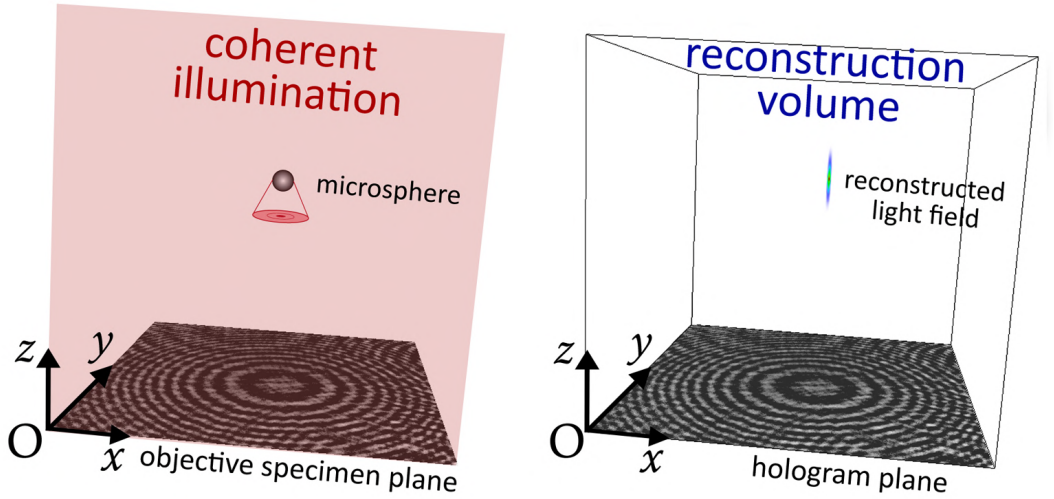

Figure 4.5: Coordinate system conventions in recording and reconstructing holograms.The left-hand image shows the recording geometry of a magnified inline hologram. The objective specimen plane is defined as $z = 0$. A magnified image of the hologram created in this plane is formed on the camera sensor. A real inline hologram is displayed with a cartoon representation of a coherently-illuminated microsphere. The right-hand image shows the numerical reconstruction geometry. The recording coordinate system convention is maintained. Holographic reconstruction proceeds from the hologram plane at $z = 0$ in the positive z-direction. The reconstructed light field for the microsphere is shown. x and y describe the in-plane axes, with the origin at the corner of the field of view.

The origin of the x and y axes is not as important, as relative displacements between objects or between frames are of greater concern. However, the convention adopted is that the origin is at the corner rather than in the middle of the hologram.

While most experiments were conducted with the objective focus set at the chamber floor, in some cases the focus was deliberately adjusted. In these cases, the point of view taken here is that the objective, and thus the objective focal plane, remains

fixed, and the sample moves relative to the rest of the microscope. Thus, 'setting the focus of the system *below* an object' is really 'moving the sample such that the object is *above* the objective focal plane'.

4.2.4 Numerical Analysis

The reconstruction and particle identification routines on the GPU, detailed in section 4.2.1, result in a series of x, y, z coordinates for all of the objects identified in each frame. Depending on the reconstruction parameters, positions may be a result of finding a centroid or centre of mass of each object, or both. The volume of the light field for each object may also be stored. These data then need to be analysed to understand the results of a particular experiment.

For this analysis, I wrote custom routines in MATLAB (The MathWorks, Inc.). Some of the general practices will be outlined in this section, while more specific details appear alongside respective experimental sections. Selected MATLAB scripts used in this analysis are included in appendix B.2.

A brief word on terminology: I use the term 'object' to represent a position localised via the centroiding process on the GPU. Each localised 'object' is not necessarily an object of interest as the thresholding and centroiding process does not actively discriminate between spurious noise and 'real' objects. For objects of interest that are identified at a later stage in the numerical analysis, from this initial set of position coordinates, I use the terms 'particle', 'bead', 'cell', or another appropriate term.

The first step in any analysis is to convert the HDF5 file format into one readily accessible in the MATLAB environment. The volume data can then be used as an initial noise filter to differentiate legitimate objects of interest from spurious artifacts. A threshold was set, below which identified objects are discarded; this threshold value differed between datasets. In practice, however, it was not difficult to eliminate most artifacts in this way, as the volume of legitimate particles would be several orders of

magnitude greater than that of noise.

Moving Particles

Many experiments required the tracking of moving particles through time. Unfortunately, the numbering of identified particles as a result of the GPU routines was not necessarily consistent between frames. I wrote a program that took an initial particle position, then searched through the space of all particle positions in the next frame to determine the most likely candidate. Positive selection was based on being within a radial distance threshold that could be set by the user. In this manner track files could be constructed that traced the path of a single bead through time, and the algorithm could be iterated over each identified particle.

For datasets that traced the path of a diffusing bead, the selected threshold was determined by the mean bead displacement due to diffusion. Particles that failed the threshold criterion were excluded. In some cases tracks were found to be shorter than the length of the recording. This abbreviation could be due to the particle moving out of the field of view, two particles coming sufficiently close to give an ambiguous reading or a spurious artifact occuring. In this case the track was still preserved, although in its aborted state.

Static Particles

Some experiments looked at evaluating the position of surface-immobilised beads in the presence of optical artifacts due to other, freely diffusing, particles in the bulk fluid. The program described above for moving particles was modified slightly: with the assumption that an identified bead should remain static, the displacement threshold was set very small to avoid misidentification of another particle.

In datasets with many freely diffusing particles in the bulk fluid, some initially-identified static particles 'drop out' from view for one or more frames and then re-

appear. This is explained by other, moving, particles in the bulk fluid occluding the particle of interest for a few frames. The program accounts for this by preserving the last identified position of the particle, then searching the space of identified particles in subsequent frames for a corresponding position. If such a position is found and the particle remains localised within the threshold, the program returns the trace, yet counts the number of dropped frames as an indication of the particle identification success rate. Suitability of traces is ultimately assessed by the user.

To aid with identification of the positions of static particles on the floor of the sample chamber, snapshot images may be taken at the initial data acquisition phase. I wrote a program to plot the 2D positions of identified objects post-reconstruction and to compare them to these snapshot images. The program generates a 2D histogram of particle positions accumulated over all reconstructed frames. Particles above a certain threshold, indicating they remain static for a given time, are identified as being adhered to the coverslip. Identified objects below this threshold are considered to be noise or moving objects. The 2D positions of these identified particles are stored and the output is displayed. (A sample output can be seen in figure 4.10 in section 4.4.) These images can serve as a guide to locating surface-immobilised particles.

By moving the ceiling of the chamber closer to the focal plane, images may also be taken deeper into the sample. However, due to the fact that the objective is focusing in water and outside its optimal working distance, these images are rarely satisfactory. There is also an unquantifable chance of cross-talk when moving the piezo stage that makes such a technique impracticable beyond a few tens of microns.

4.3 Initial Assessment of Localisation Precision

4.3.1 In-plane Resolution

The precision with which a particle can be localised in-plane was assessed as follows. The aim was to obtain a single object in the field of view of the microscope, to move this particle relative to the objective by a known distance in x and y and to compare these distances to those found by holographic reconstruction.

A dilute solution ($N = 2.8 \times 10^7 \mathrm{ml}^{-1}$) of 0.5$\mu$m diameter polystyrene microbeads was made and sonicated. Beads were adhered to the ceiling of the sample chamber as described in 4.2.2. A single stuck bead was found in a field of view and, using the piezoelectric NanoCube and servo controller, the bead was set about 3μm above the objective specimen plane. Unlike experiments described in later sections of this chapter, the objective specimen plane was in water, rather than at the floor of the chamber. The NanoCube was then used to move the sample in increments of 1.00μm in-plane − first along the x-axis, then along the y-axis. The error in positioning the sample by hand with the NanoCube and servo controller is $\pm$0.05μm. At each location 50 holograms were recorded at 50fps, although only one frame per position was used in the hologram reconstruction.

To generate a mean image to use in the required normalisation process, holograms were recorded at 25fps for 20 seconds while the piezo servo controls were adjusted randomly to create a stack of images with the bead in arbitrary positions. The mean of this image stack was then calculated, and the 3D positions of particles were determined using the reconstruction, thresholding and centroid analysis detailed in section 4.2.1.

As a comparison, both centroid and amplitude-weighted centre of mass algorithms were used to determine the positions. The reconstructed positions along the axis of travel were plotted against the measurement shown on the servo controller and a

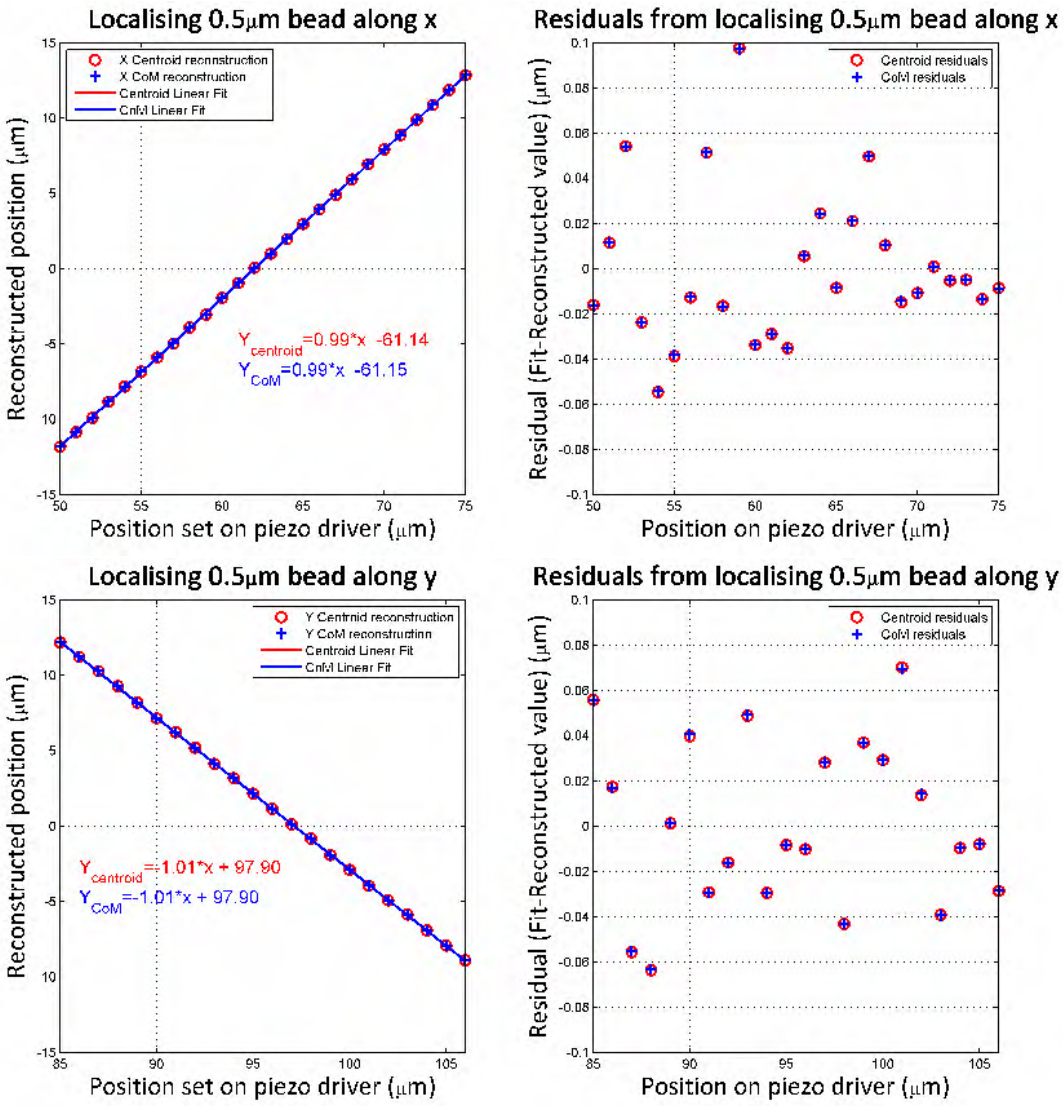

Figure 4.6: Results of comparison between moving an adhered bead along x (top) and y (bottom) and the holographic reconstruction of the position. The reconstructed data for both centroid and centre of mass (CoM) localisations are indicated by the data points in the left-hand plots. The lines show linear fits to the data, with the equation for each line displayed on the plots. The right-hand figures display a plot of the residuals of the fit; the random distribution indicates a good fit.

linear fit applied to the data using the inbuilt MATLAB function `polyfit`. A line gradient of 1 indicates a 1:1 correspondence between the displacement set by the piezo controller and the measured displacement from the holographic reconstruction. The residuals (fit value − data) were plotted to assess the quality of the linear fit. A random distribution of residuals indicates a good fit with no systematic errors. These

results are summarised in figure 4.6.

The first point to note is that the difference in position localisation between the centroid and centre of mass algorithms is virtually indistinguishable. Secondly, the residual plots show a random distribution indicating a good linear fit to the data. The gradients of the fit for displacement along both the x and y directions are within 1% of 1. This experiment does not provide sufficient data to produce likelihood estimates for the error on a single reconstructed position value. It also assumes no cross-movement in the other orthogonal directions and does not take into account any optical aberration that may be introduced by having the objective operate at suboptimal conditions (focusing through several tens of microns of water). However, it does seem reasonable to assume that any aberration is constant for a Plan objective providing z does not vary. We can therefore lay a claim to localising a micro-object in x and y at least as accurately as we can position the sample, that is to say, to within 50nm.

4.3.2 Depth Resolution

First Attempt

A similar experiment to that described in section 4.3.1 was conducted to assess the through-plane localisation accuracy, although ultimately it was unsuccessful.

The same dilute sample of 0.5μm diameter polystyrene microspheres adhered to the ceiling of the tunnel slide was used. A single bead was moved to the centre of the field of view and brought into focus (as assessed by eye) using both the manual and piezo stages. The NanoCube was used to move the sample upwards, away from the focus of the objective, in discrete intervals to a final displacement of 45.0μm. At each z-setting 100 frames were recorded at 50fps, although only one frame per position was used in the holographic reconstruction.

A mean image for normalising the dataset was acquired in the same way as de-

scribed in section 4.3.1.

Holographic reconstruction and particle identification proceded in the usual manner, with a slicewise resolution set at 50nm, which is comparable to the in-plane pixel resolution. Figure 4.7 shows the reconstructed z-positions against the displacement value shown on the servo controller. A linear fit has been applied to the reconstructed data using the MATLAB `polyfit` function. Firstly, it should be noted that the two methods of localising the particles − centroid and centre of mass − are in close agreement. It is clear, however, that the reconstructed positions of the microbead are not where they are expected. The discrepancy between reconstructed position and actual position is greater the further the bead is from the focus.

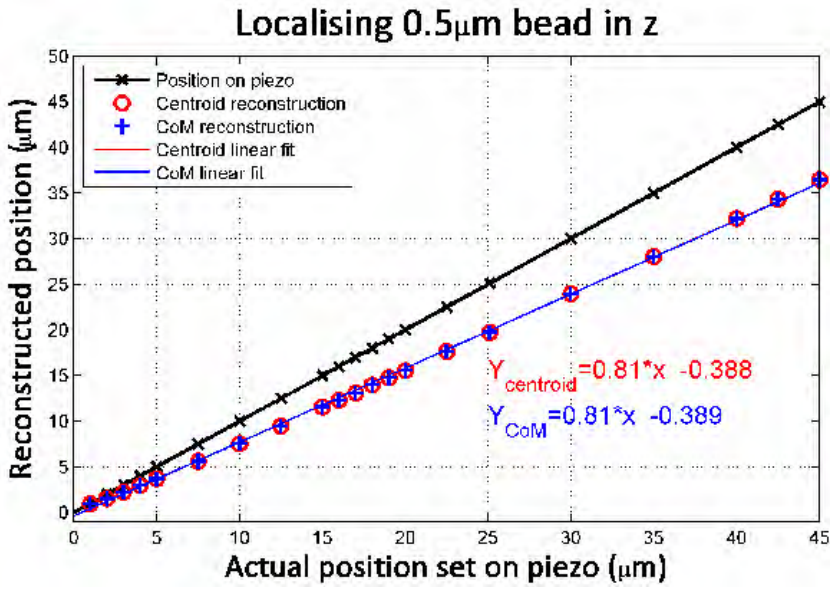

Figure 4.7: Results of reconstructing the z-positions of a 0.5μm diameter polystyrene bead adhered to the ceiling of a sample chamber as the sample is moved in z away from the focus of the objective. The plot shows the results for both centroid and centre of mass (CoM) identification strategies along with linear fits applied to data. The equations of the fitted lines are printed. The black line indicates the expected position of the reconstruction based on the setting of the piezoelectric nano-positioner.

It was recognised that in this experiment, the objective is far from its optimal operating condition and is subject to an axial spherical aberration. The objective is designed to have a focal plane just the other side of a 0.17mm coverslip. In this

experiment the position of the focal plane is altered by an additional depth of water. This results in an apparent focal plane closer to the bead and thus the apparent depth of the bead is reduced. This effect is more pronounced the deeper the layer of water.

It was hoped that if this effect were linear, a simple correction factor could be applied to the results. A plot of the residuals of the original linear fits (figure 4.8) reveals a non-linear relationship putting a simple correction factor out of the question. This result is not surprising, given the complex compound optics found in microscope objectives. The commercially-sensitive nature of the design of these lenses means that it is difficult to model their behaviour when operating outside optimal parameters.

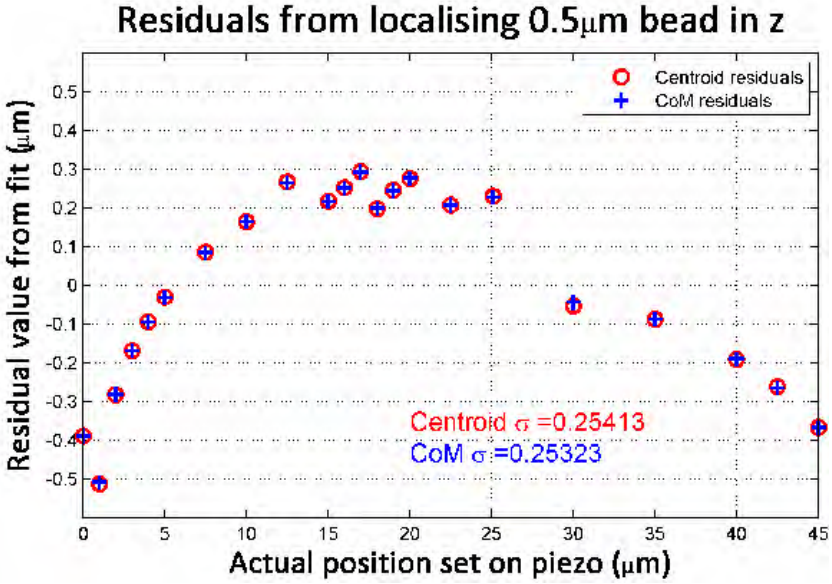

Figure 4.8: A plot of the residual values of the actual data to the linear fits showed in figure 4.7. The non-random nature of the distribution of these residuals indicates that the linear fit is not adequate to describe the behaviour of the observed discrepancy in figure 4.7.

Alternative Approach

A different approach was needed to determine the accuracy with which we can resolve a particle in z. It was decided to affix a microbead to the ceiling of a chamber of known height, to focus on the floor of this chamber and the reconstruct the resulting

hologram.

A sample chamber made with an aluminium tape spacer, as described in section 4.2.2, was used and a dilute sample of 0.5μm diameter polystyrene microbeads was adhered to the ceiling of the chamber.

The slide was scanned for a single bead on the ceiling of the chamber close enough to a pen mark on the floor such that the sample could be brought to focus on the pen mark and then moved laterally out of the way with the NanoCube to record the hologram of the bead. Ten beads were found in this manner and 250 holograms for each recorded at 50fps. A reference dataset was recorded as described above to normalise the holograms.

For each dataset ten frames were selected randomly for reconstruction. The z-positions were determined to a precision of 50nm with both the centroid and centre of mass algorithms. The mean and standard deviation of each dataset was calculated and then a global mean and standard deviation computed to compare to the measured spacer height.

The global mean for the centroid reconstruction was found to be 100.95μm with a standard deviation of 0.77μm, while the centre of mass reconstruction yielded the same result, with a difference seen only in the third decimal place.

This result is consistent with the measured spacing size. It should also be borne in mind that the centre of a 0.5μm diameter polystyrene bead will be found 0.25μm below the ceiling of the chamber. We can say that we can localise a polystyrene microbead in z at least as well as the error associated with the manufacture of the aluminium spacer chamber and its positioning on the microscope.

It would be desirable to repeat this experiment with a number of other independently measured chamber heights. Shim chambers sealed with epoxy resin described in section 4.2.2 were intended for this purpose. Unfortunately, it was not possible to create a chamber with a reliably known height with this method. The glass of the

coverslip was observed to flex upon release of the mass after the epoxy curing period and initial experiments using these chambers showed that the actual chamber height was 5 to 10μm above the expected chamber height, regardless of the thickness of the shim used as a spacer.

4.3.3 Discussion

Numerical Methods

It may seem surprising that the centroid and centre of mass methods are in such close agreement. However, it is clear that the majority of particle localisation is achieved through the threshold applied to the reconstructed light field. Any object whose amplitude lies above the threshold value is highly likely to return the same position for both the centroid and amplitude-weighted centroid routines.

Where the two might differ significantly is for a low threshold value or if the reconstructed light field is truncated by the floor or ceiling values of the reconstruction volume. For these reasons the amplitude-weighted centroid data are used for later experiments.

Localisation Precision

It proved to be very difficult to produce a sample with objects at known 3D positions that could be used as an effective ruler for these experiments. Microfabrication techniques such as etching and lithography on PDMS or plastic substrates could produce such a sample. We also considered some more fanciful methods such as embedding nanoparticles into agarose and recording the diffusion of agglomerates of this material in a refractive index-matched fluid medium. Such techniques require further consideration and time investment.

The first set of experiments involved having the objective focus through a depth of water in addition to the glass coverslip. The objective is manufactured specifically

for focusing through the coverslip only and operating outside of these conditions produced aberrations in the image. These were first noticeable when the position of an affixed bead was changed relative to the focus, although the lateral resolution experiment operated in suboptimal conditions. Given the objective is Plan, however, we can assume that the aberration remains constant in an x-y plane for a constant z-value.

The conclusion is that the floor of the sample should always be brought to the focus of the objective to avoid introducing unknown errors into the data. Focusing below the floor (into the glass of the coverslip) should not be a problem, however, as long as the sample is still within the working distance of the objective. One further alternative would be to use a fluid medium with the same index of refraction as the coverglass. Matching the indices of refraction would remove the axial spherical aberration; however, this is not practical for studies of biological samples in a natural environment.

In the meantime, the experiments demonstrated here show that we can localise a single microparticle over a 100μm depth to within the positioning tolerance of the piezoelectric NanoCube and the manufacturing procedure of the aluminium tunnel slide. That is to say, to within 0.05μm in x and y and 0.77μm in z. Given that an effective pixel size of the Mikrotron camera at this magnification is only 0.062μm, this localisation precision seems sufficient.

One point of consideration is that objects near the edge of the field of view may not have their entire Airy diffraction pattern (see figure 2.5) captured by the hologram field of view. An example of a hologram demonstrating this is shown in figure 4.9. This could lead to an error in detection of that object at the reconstruction stage. It is expected that this effect would be worse for particles further away from the focus as the radius of the Airy pattern increases with further distance from the specimen plane as per equation 2.21.

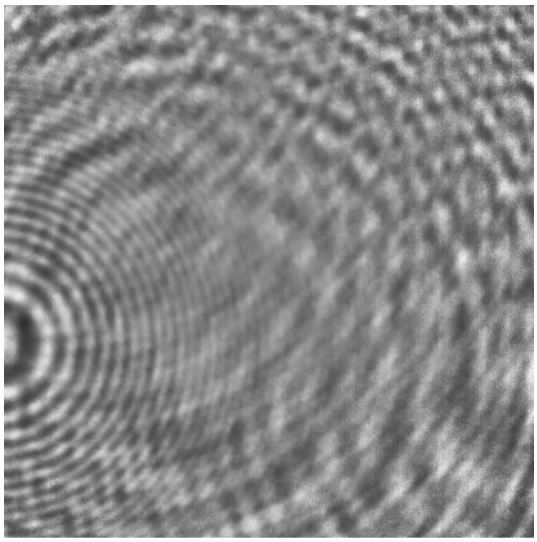

Figure 4.9: This inline hologram of a 0.5μm polystyrene microsphere at 225$\times$ magnification shows the diffraction pattern of one particle that is not completely captured by the field of view of the hologram. This could potentially lead to errors in localising the particle in z.

Thus, it would be ideal to obtain more data points for different values of z-displacements from the specimen plane and to assess any change in localisation precision for particles close to the edge of the field of view. As mentioned, there are difficulties in manufacturing sample chambers of reliable heights and also imaging aberrations introduced when having the objective focus through a depth of water. Such experiments will have to wait until these issues are addressed.

4.4 Drift of Microscope Stage

An experiment was conducted to assess the sensitivity of the microscope to small movements over the course of a typical experimental timeframe.

A dilute concentration of 1μm polystyrene beads ($N = 2.9 \times 10^8 \mathrm{ml}^{-1}$) was adhered to the floor of a grease tunnel slide with 50μm spacers. A field of view with five clearly visible beads on the floor was found; the manual positioning stage was bolted down and the piezo servo controller was set to closed loop to reduce hysteresis. Inline holograms were recorded at 5fps for 200 seconds.

Figure 4.10 shows a snapshot image recorded prior to acquisition and the subsequent identification of particles in the post-reconstruction analysis described in section 4.2.4.

A time trace for each particle was obtained and plotted. Some effort was made to fit various models to the data. Linear, cubic and four-parameter exponential models were obtained using the inbuilt MATLAB `fit` function. A three-parameter exponential model was obtained by a custom fitting routine based on the MATLAB `lsqcurvefit` function. Sample output for one bead is displayed in figure 4.11

4.4.1 Discussion

There are two reasons for applying a fit to the data. The first is to model the physical phenomena operating on the sample and causing the stage drift. The second is to smooth the data for subsequent analysis.

Movement of the stage is subject to many factors including thermal fluctuations, electrical and mechanical noise. As the characterisation of stage drift is not the chief concern here, it was decided that a simple polynomial fit would be the most appropriate for smoothing the data, rather than searching for a physical model.

For these particular data, an analysis of the sum of squares error for each fit showed that the cubic model provided the best fit. Later experiments (see section 4.5) used a 6th-order polynomial to counter stage drift.

The most important point of interest to come out of this experiment is that the overall drift of the microscope is very small. Moreover, the holographic imaging technique is sensitive to this tiny movement in x, y and z. Even taking the maximum displacement between points on each of the three axes, displacements of 33nm, 58nm, and 29nm in x, y and z respectively were observed over 200 seconds. This corresponds to an average drift velocity of the order of angstroms per second, which is sufficiently small to be neglected in all of our applications.

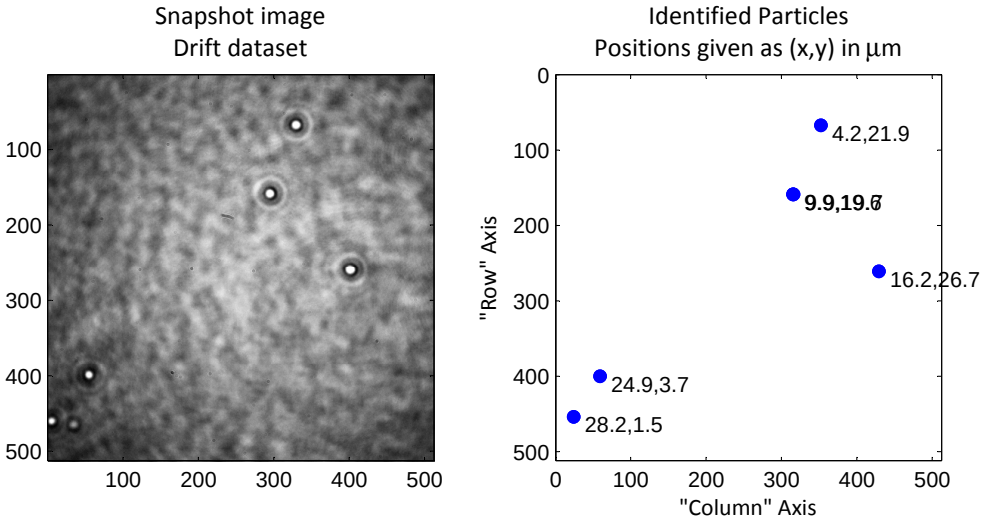

Figure 4.10: The left-hand image shows a snapshot of the drift data taken at the data recording stage. The right-hand image shows identified particles from the reconstruction data. Spurious artifacts have been succesfully excluded and there is good agreement between the snapshot and the reconstructed positions. The numbers beside each object are the identified x-y coordinates of each bead (converted from pixels, which are seen on the axis labels). These values give a good starting point for outputting particle position tracks over time.

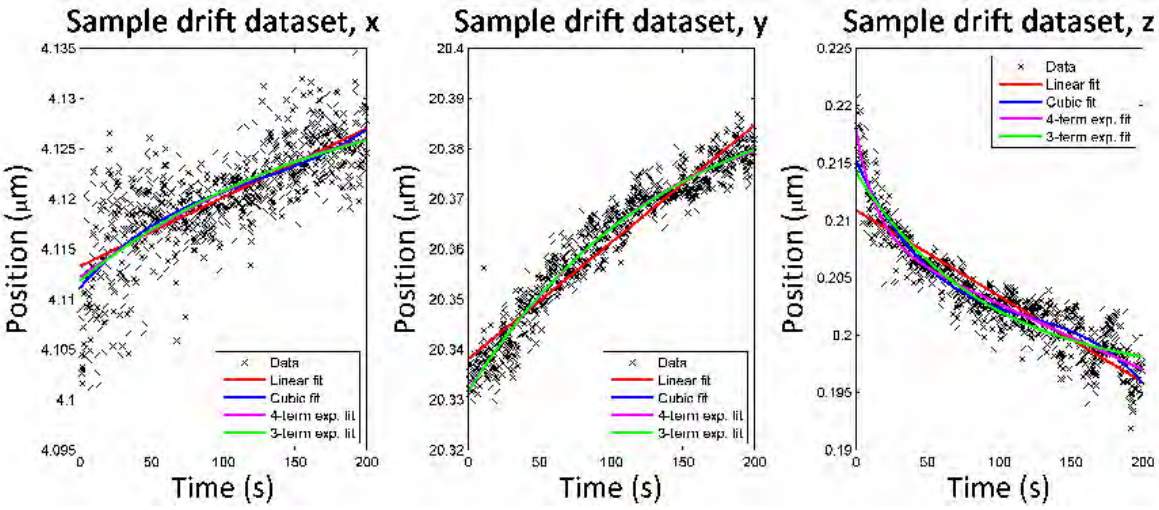

Figure 4.11: Sample x, y and z position data showing the drift of the microscope system over 200 seconds (1,000 frames recorded at 5fps). The different models used to fit to the data are displayed by coloured lines.

4.5 Crowding Experiment

The preceding experiments demonstrate the precision with which the high-magnification DHM can localise a small number of particles in empty chambers. Our ideal applications would see us imaging many particles at once, thus it is useful to know the degree of precision with which we can localise particles in a crowded chamber. A number of factors could contribute to the uncertainty in effectively localising a particle in three dimensions by inline holography. Objects near the edge of the field of view may not have their entire diffraction pattern captured by the camera, which could lead to an error in detection of that object at the reconstruction stage. The signal to noise ratio is also important for effective particle identification. Particles deep into the sample show attenuation of their scattering intensity through the medium (Intensity $\propto \frac{1}{r^2}$), and the signal may be occluded by other particles closer to the focus exhibiting a brighter scattering profile.

An experiment was designed to assess the ability to localise particles on the floor and ceiling of a sample chamber with varying degrees of noise introduced by different concentrations of freely diffusing beads. Samples were made using poly-L-lysine to adhere plain polystyrene microbeads to glass surfaces and with positively charged amino-coated beads as the diffusing particles, as described in section 4.2.2. The concentration of diffusing beads increased as a geometric series from $N = 2.8 \times 10^8 \text{ml}^{-1}$ and the microscope was focused on the chamber floor.

For each concentration of diffusing beads, several 2,000-frame datasets were recorded at 25fps. The positions of beads adhered to the floor and ceiling for each frame were reconstructed and analysed using methods described in section 4.2.4. The variation in position for each identified bead over time was used as an indication of localisation precision. In noisy datasets, some initially-identified beads would be 'lost' from the time trace. The proportion of dropped frames was also used as an indicator for the success of the localisation technique.

4.5.1 100μm Chamber

A 100μm deep aluminium tape chamber was initially used for this experiment, with 0.5μm diameter microbeads. Beads on the ceiling of the chamber could be identified quite readily. However, even the lowest tested concentration of diffusing beads, which corresponds to only 26 particles on average in a 30μm $\times$ 30μm $\times$ 100μm chamber, disrupted the diffraction pattern so much that the ceiling beads could not be detected reliably at the reconstruction stage.

The experiment was repeated with 1μm diameter microspheres as both static and diffusing particles. 1μm beads scatter more brightly in the forward direction, and because of their size they represent, perhaps, a better proxy for a bacterium. While microspheres on the floor and ceiling of the chamber could be localised accurately in a control sample, again the presence of, on average, 26 diffusing particles per field of view disrupted the signal sufficiently to prevent identification of ceiling beads.

4.5.2 50μm Chamber

This experiment was repeated using a 50μm deep chamber made with a grease tunnel and shim spacers, as described in section 4.2.2. While these chambers could be made swiftly and efficiently, the downside is that the height of the chamber cannot be independently measured. Thus, there is no *a priori* knowledge to guide the range of ceiling reconstruction heights.

In practice, chamber ceilings were found to vary between 49μm and 58μm from the hologram plane. This variation reflects the different pressures employed in making the tunnel slide.

Data Collection and Analysis

Four different concentrations of freely diffusing microspheres were used: $N = 2.86 \times 10^8\text{ml}^{-1}$; $N = 5.72 \times 10^8\text{ml}^{-1}$; $N = 1.14 \times 10^9\text{ml}^{-1}$; and $N = 2.33 \times 10^9\text{ml}^{-1}$. These

correspond to an average number of beads per 30μm $\times$ 30μm $\times$ 50μm volume of: 13, 26, 51 and 105, respectively. In addition to these four samples, a control sample was made with no diffusing beads. Figure 4.12 shows three-dimensional reconstructions of the control dataset and the most concentrated diffusing bead dataset tested to illustrate the raw data from which 3D positions must be extracted.

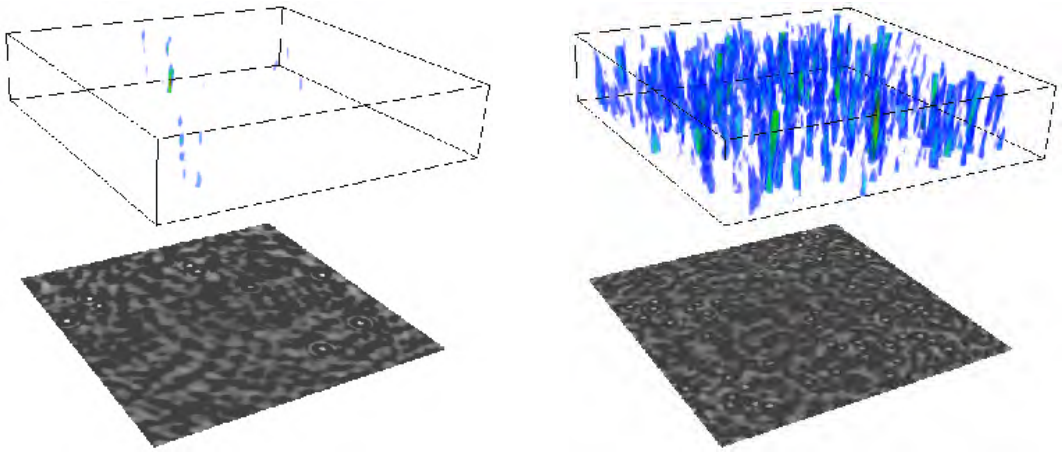

Figure 4.12: *Left:* 3D reconstruction of a frame from a recording of the control sample with no diffusing beads. *Right:* 3D reconstruction of a frame from a recording of the dataset with $N = 2.33 \times 10^9 \text{ml}^{-1}$ concentration of diffusing microbeads. In both images, the normalised hologram is visible at the floor of the reconstruction and the same threshold value has been used. The bounding box represents z-values from 45 to 60μm, thus encompassing the ceiling of the chamber. The reconstructed intensity of a few microparticles adhered to the ceiling in this field of view is clearly visible in the control dataset. It is a lot more difficult to differentiate between ceiling-adhered beads and freely diffusing particles in the right-hand reconstruction.

For each of the five samples, five 2,000-frame datasets at 25fps were recorded. x, y and z position traces for each identified bead were output for both floor and ceiling beads. A 6th-degree polynomial was fitted to compensate for any drift in the system and the fit was subtracted from the data to arrive at a residual position trace, demonstrated in figures 4.13 and 4.14. This procedure not only compensated for the effect of drift, but also for any differences in chamber height.

For each axis, the standard deviation of the residual position trace was determined to give an indication of spread of positions. A histogram of these standard deviation values for all identified beads was output, along with the total number of dropped

frames for a given concentration of diffusing beads. Figure 4.15 shows sample output of the histogram analysis for beads adhered to the floor of the control dataset and to the ceiling of the $N = 2.33 \times 10^9 \mathrm{ml}^{-1}$ dataset. These two datasets were selected for sample output as they represent the extremes of particle localisation in this experiment.

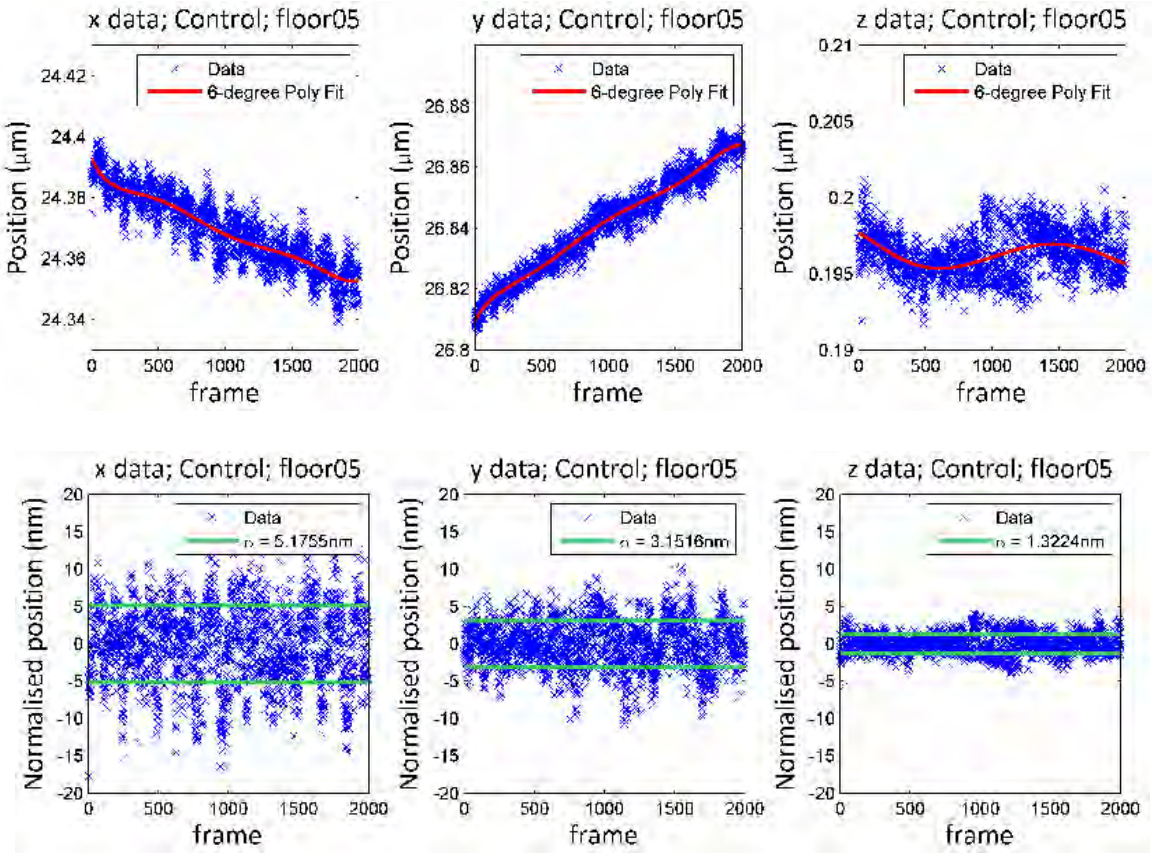

Figure 4.13: Output from the polynomial fitting and data normalisation process is shown for one microsphere located on the floor of a control dataset. The top set of plots shows the 2,000-frame position traces in x, y, and z for an identified bead ('number 5'). The drift of the sample over time can be seen, along with the 6th-degree polynomial fit to the data. Note that while the x and y data are displayed with the same range on the y-axis, the z data are shown with a much smaller range. The bottom set of plots shows the residual position traces found by subtracting the polynomial fit. The two green lines on each plot show $\pm$ one standard deviation (σ), the value of which is indicated in the legend. Standard deviation values were obtained for all microbeads located for each sample condition. A histogram of the σ values for this sample chamber can be seen in figure 4.15. The mean of all these values was determined and a summary for all experiments is presented in table 4.1.

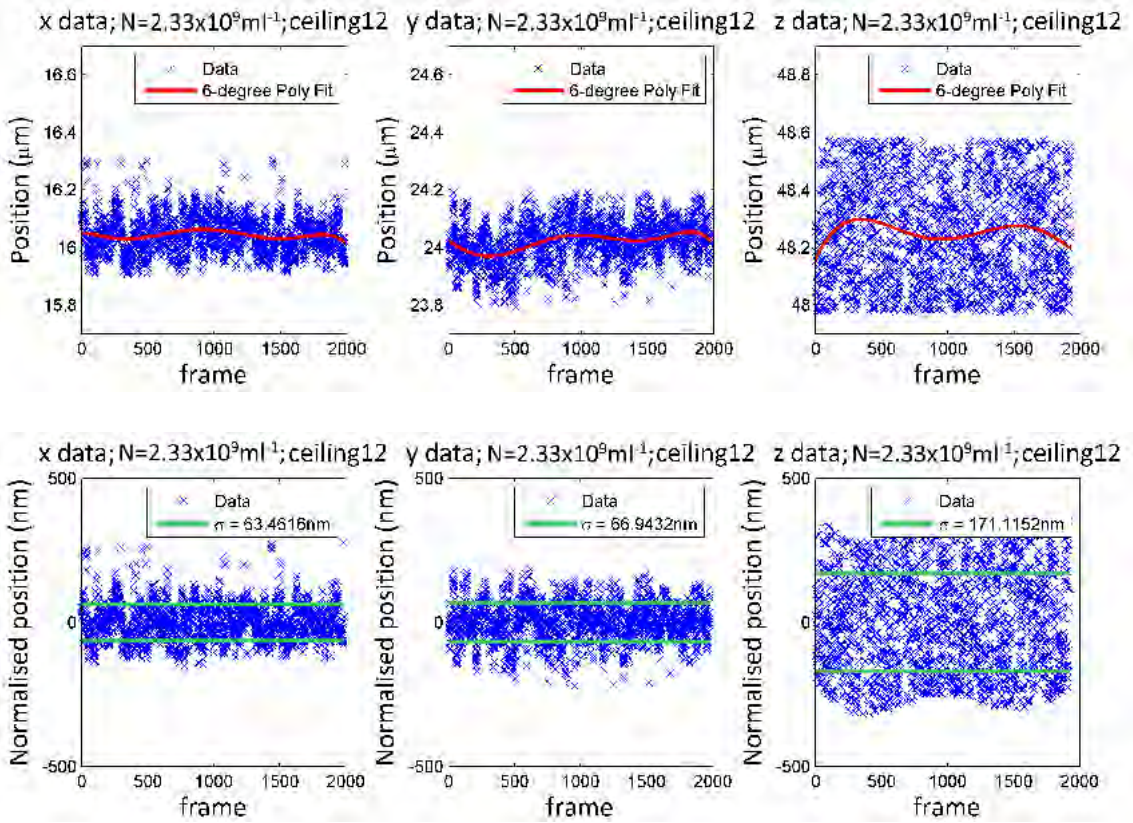

Figure 4.14: Output from the polynomial fitting and data normalisation process is shown for one microsphere located on the ceiling of the $N = 2.33 \times 10^9 \mathrm{ml}^{-1}$ dataset. The top set of plots shows the position traces in x, y, and z for an identified bead ('number 12'). Unlike the control dataset presented in figure 4.13, dropped frames through the particle localisation process mean that the data traces are not 2,000 frames long. The 6th-degree polynomial fit to the data can be seen and the bottom set of plots shows the residual position traces found by subtracting the polynomial fit. The two green lines on each plot show $\pm$ one standard deviation (σ), the value of which is indicated in the legend. A histogram of all σ values obtained for beads in this sample chamber can be seen in figure 4.15.

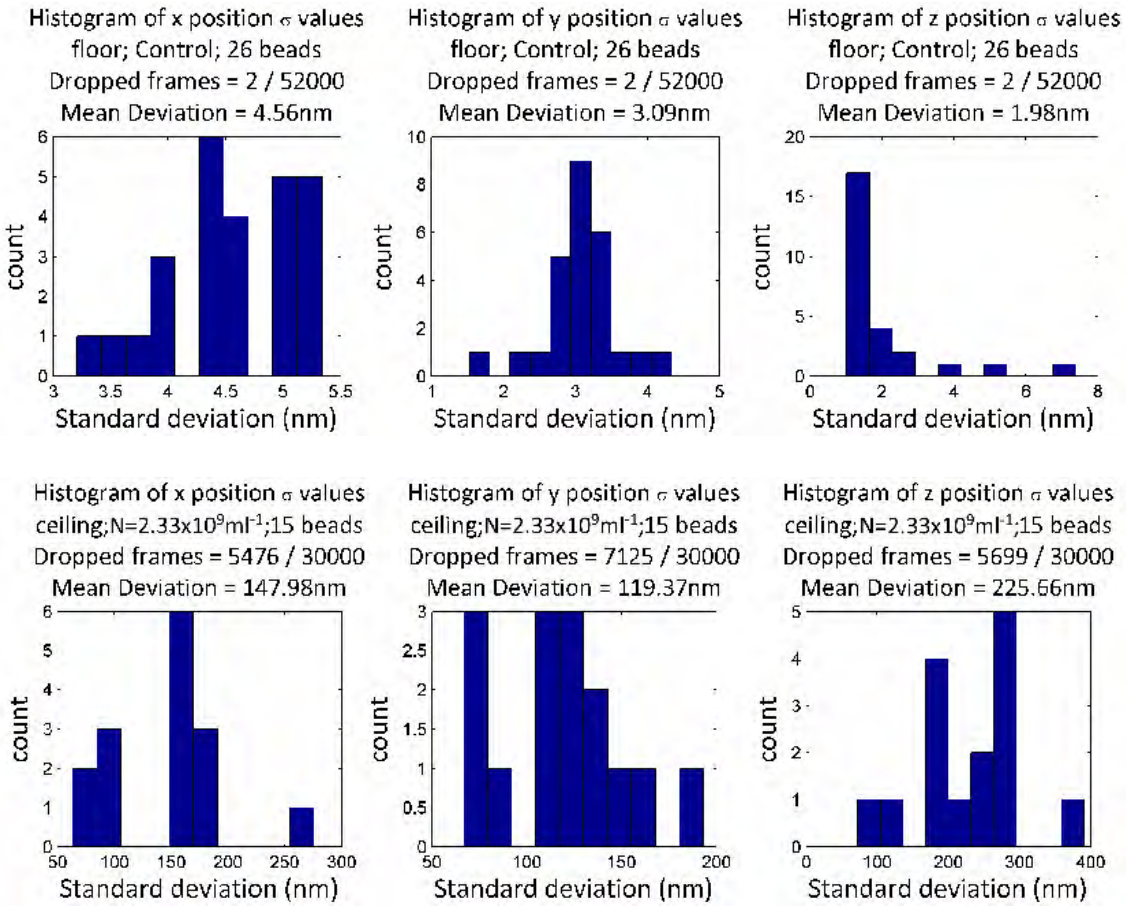

Figure 4.15: Histograms of the standard deviation (σ) values in x, y and z determined for all beads located on the floor of the control dataset (top) and the ceiling of the $N = 2.33 \times 10^9 \mathrm{ml}^{-1}$ dataset (bottom). The total number of beads detected in each dataset is shown along with the total number of dropped frames. The mean deviation figures are also stated, which are used as an indication of particle localisation precision for each experimental condition. A summary of these results for all datasets is presented in table 4.1 and figure 4.16.

Summary of Results

For each concentration of diffusing beads, the mean of all the standard deviations of the immobilised bead positions was calculated. The total number of dropped frames was expressed as a percentage of all bead-frames for a given concentration of diffusing beads. These results are summarised in table 4.1 and figure 4.16.

N (ml^{-1}):		Control	2.86×10^8	5.72×10^8	1.14×10^9	2.33×10^9
Floor	$\langle\sigma_x\rangle$	4.56nm	7.77nm	7.79nm	15.65nm	14.86nm
	$\langle\sigma_y\rangle$	3.09nm	7.08nm	6.61nm	14.63nm	13.49nm
	$\langle\sigma_z\rangle$	1.98nm	11.56nm	9.36nm	12.40nm	11.30nm
total beads		26	28	39	36	28
% dropped		0.0%	0.5%	2.4%	9.3%	3.9%
Ceiling	$\langle\sigma_x\rangle$	5.69nm	22.81nm	26.41nm	82.02nm	147.98nm
	$\langle\sigma_y\rangle$	6.42nm	23.87nm	25.54nm	81.02nm	119.37nm
	$\langle\sigma_z\rangle$	44.07nm	130.85nm	92.76nm	112.65nm	225.66nm
total beads		22	14	31	31	15
% dropped		0.1%	7.8%	6.6%	14.3%	20.4%

Table 4.1: Summary of the crowding experiment for 1μm diameter polystyrene beads in a $\sim$50μm deep chamber. Mean of the standard deviation data for floor and ceiling measurements are presented for different number densities of diffusing beads (N). 'Control' refers to a sample with no diffusing beads. 'Total beads' refers to the total number of beads localised over the five datasets recorded for each concentration value. '% dropped' indicates the number of frames dropped for the aggregate data at each concentration value.

4.5.3 Discussion

Tracking Algorithm

The tracking algorithm described in section 4.2.4 lacks the sophistication to be used effectively to track the positions of many particles in a crowded sample. One point is that it still requires significant human intervention to ensure the data output make sense. In some cases, a small adjustment to the radius displacement threshold can make a large difference to the length of tracks obtained. The danger of increasing the

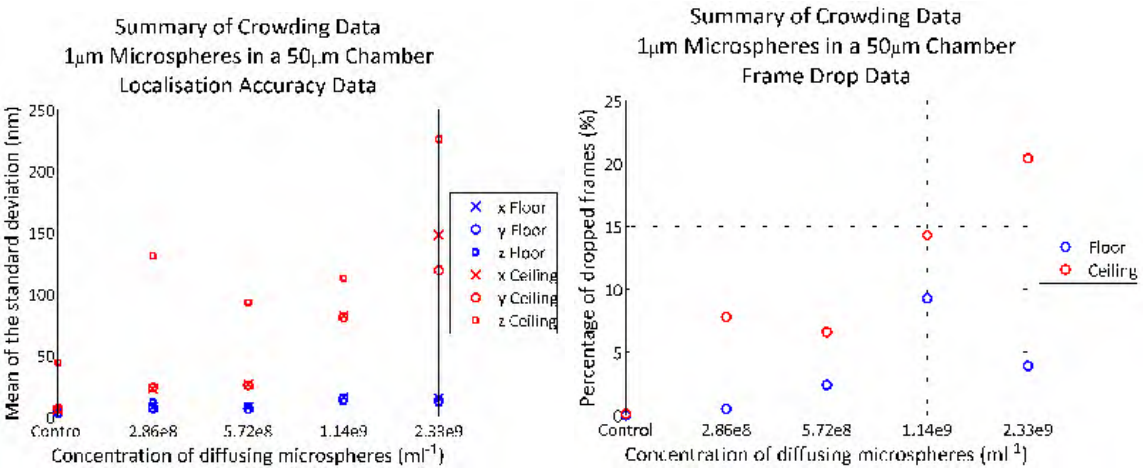

Figure 4.16: *Left:* The means of the standard deviation values determined for all experimental conditions are plotted. It is clear that positions on the floor, regardless of diffusing microsphere concentration, are a lot more precisely localised than the ceiling position. There is a general increase in localisation uncertainty with increasing concentration of diffusing particles. For the ceiling data, z localisation is generally worse than for x and y, although in all cases localisation precision is well below the diameter of the particle being detected. *Right:* The number of dropped frames is shown as a percentage of all recorded frames for the crowding experiment. In general we see more dropped frames with increased concentration of diffusing particles and ceiling data are worse than floor data.

threshold radius, especially in crowded samples, is of a diffusing particle close to the surface being located, causing erroneous results.

Every effort was made to ensure that the output tracks were indeed from surface-adhered beads by human examination of the each returned trace. Information from the trace, such as the standard deviation of displacement or the start and end positions, can aid in making an acceptance or rejection decision. Nevertheless, for the most crowded samples presented here, it is impossible to guarantee that no traces include even some position data from a diffusing microsphere.

Future versions of the software could perhaps include further automation to reduce the human dependency. An *a priori* map of the particle positions on the ceiling would also aid a future software version.

Localisation in Crowded Samples

Excluding the control dataset, it is clear that, in general, we detect fewer microbeads on the ceiling of a 50μm chamber than on the floor, regardless of the number of diffusing beads in the chamber. This effect is most pronounced in the highest density dataset recorded and in the $N = 2.86 \times 10^8 \text{ml}^{-1}$ dataset, which seems to be an outlier. It is possible that there are genuinely fewer microspheres on the ceiling, as sedimentation times were not strictly controlled for. Also, despite the use of amino beads for the freely diffusing sample, it is possible that some beads do end up settling on the floor surface over time.

It is entirely likely, however, that the presence of diffusing beads in the sample interferes with the diffraction signal of the beads on the ceiling, preventing a successful identification. This is supported by the fact that the presence of even a few diffusing amino beads in a 100μm chamber successfully prevented the localisation of microspheres on the ceiling that were easily resolvable in a control sample.

It would be good to know unambiguously the number of beads on both the ceiling and floor of a chamber prior to holographic reconstruction and numerical particle localisation. While it was possible to obtain snapshot images of the microparticles on the floor of the chamber prior to acquisition, this was less easy to achieve for the ceiling beads. The image of the polystyrene beads on the ceiling exhibits an aberration due to the objective having to focus through a depth of water: an issue that was discussed in section 4.3.2. Also, moving the sample chamber toward the objective nose by $\sim$50μm in order to focus on the ceiling risks squeezing the coverslip closer to the slide as the grease tunnel is easily compressible.

It would be ideal to repeat this experiment with a more rigid chamber to allow effective snapshots of the ceiling to be taken, and controlling precisely for sedimentation times in each sample. This would have the additional benefit of providing coordinates at which to look for adhered beads and lower the likelihood of picking up the positions

of diffusing beads with the tracking algorithm.

Nevertheless, these data demonstrate that we can localise and track particles close to the floor very accurately. Localisation for all datasets and in all directions is sub-effective pixel: that is, below 62nm. With increasing concentration of diffusing microspheres in solution, the proportion of dropped particles increases. Although, with the exception of the $N = 1.14 \times 10^9 \mathrm{ml}^{-1}$ dataset, which appears to be an outlier, this increase is not marked.

The ceiling data show that the presence of even a few freely diffusing particles reduces the localisation precision of the reconstruction. However, it remains sub-effective pixel until $N = 1.14 \times 10^9 \mathrm{ml}^{-1}$ in x and y and the worst localisation precision of the data shown in all three directions is less than a quarter of the diameter of the polystyrene bead on the ceiling surface. Of greater concern is the proportion of dropped frames for the ceiling data, which increases as N increases and is higher than that of the floor data across the board.

Explanations and Suggested Improvements

The most likely explanation for the observed results is that diffusing particles occlude the signal from microspheres adhered to the ceiling. The greater the concentration of diffusing beads, the more difficult it is to firstly localise, and then to retain that localisation for the full duration of the dataset. This effect is also seen, albeit to a far lesser degree, in the floor datasets.

Adequately capturing the signal from particles far from the specimen plane of the objective is a function of how well the camera can capture the dynamic range of the interference pattern. The present protocol is to avoid saturated pixels, sometimes at the expense of contrast that could aid in recording the signal from particles further from the objective focus. A camera with a higher bit depth would certainly aid in maximising the dynamic range, as would ensuring the full bit range is used. It is still

important, however, to avoid saturation effects and zero-value pixels as they lead to errors in the reconstruction.

It is also interesting to consider the role of the out-of-focus virtual image in the reconstruction of these data. As discussed in section 2.3, inline holography suffers from the so-called twin image problem, whereby the real and virtual images from the reconstruction are not spatially separable, leading to an unwanted term from the virtual image affecting the 3D position reconstruction of the real image. This is not so much an issue when we are attempting to localise only a few particles in a volume. However, with more densely-populated samples we see the scattering signal of particles disrupted by the higher-intensity signal from particles close to the specimen plane. This was immediately apparent in the crowding experiments initially attempted with the 100μm deep chambers. Thus, if we could reduce or remove this effect at the recording stage, we may have greater success in recovering position data in more densely-populated samples.

Consider the situation shown in figure 4.17. A hologram is shown with the positions of real particles to the left. The signal from the virtual image, which is represented as a mirror image of the particles on the right of the figure, is an unwanted term interfering with the real image. The scattering intensity of light is proportional to $\frac{1}{r^2}$, where r is the distance from the source. Thus, the signal from the virtual image of particles close to the hologram plane, in particular, is in danger of affecting the relatively weak signal of real particles far from the hologram plane. When it comes to reconstruction, these close-in particles mean it is difficult to reconstruct those further away.

One consideration for future inline hologram acquisition is to include some form of spacer between the hologram plane and the floor of the sample chamber. This situation is demonstrated in figure 4.18. Such a scenario would ensure that no virtual particles would be too close to the hologram plane to provide a crippling parasitic

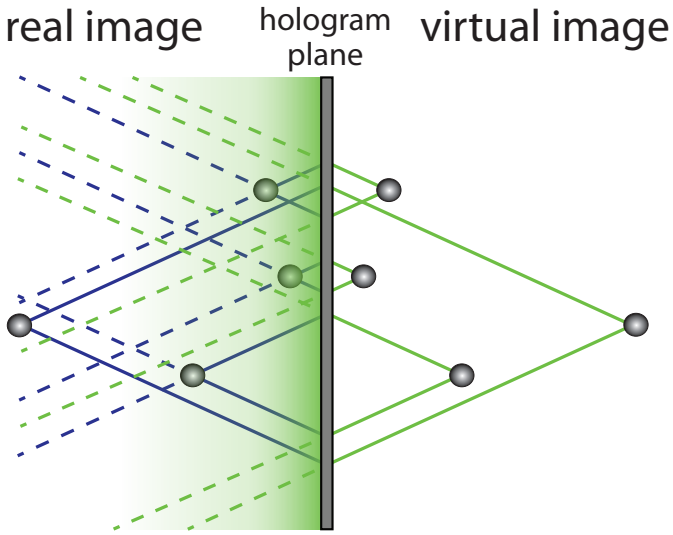

Figure 4.17: Schematic of an inline hologram. Reconstruction proceeds from the hologram plane to the left of the figure, identifying the particles in the real image. The virtual image can be represented by the mirror of the particles on the right of the figure. The unwanted recorded signal (represented by the green gradient) from the virtual image of particles close to the hologram plane, in particular, interferes with the successful reconstruction of the real image of particles far from the hologram plane.

signal. Of course, the signal from real particles would also be weaker, but less than that of the virtual image. All real particles would be closer to the illumination source, and the camera contrast and exposure settings could be adjusted to maximally capture the entire signal.

Finding a spacer in practice is not an easy job. One option would be to attempt to match the refractive indices of an agarose, or other hydrogel, medium with the fluid in which the objects of interest are free to move. Of course, any such medium would need to be compatible with any biological organisms we might wish to study. Another possibility is to deliberately translate the sample such that the focal plane is in the glass of the cover slip. Provided the distance from this plane to the floor of the chamber is accurately known, the change in refractive index from the glass to the aqueous medium could be compensated for in the numerical reconstruction.

Of course, the ultimate in virtual image removal is to use off-axis holography, which is discussed in chapter 5.

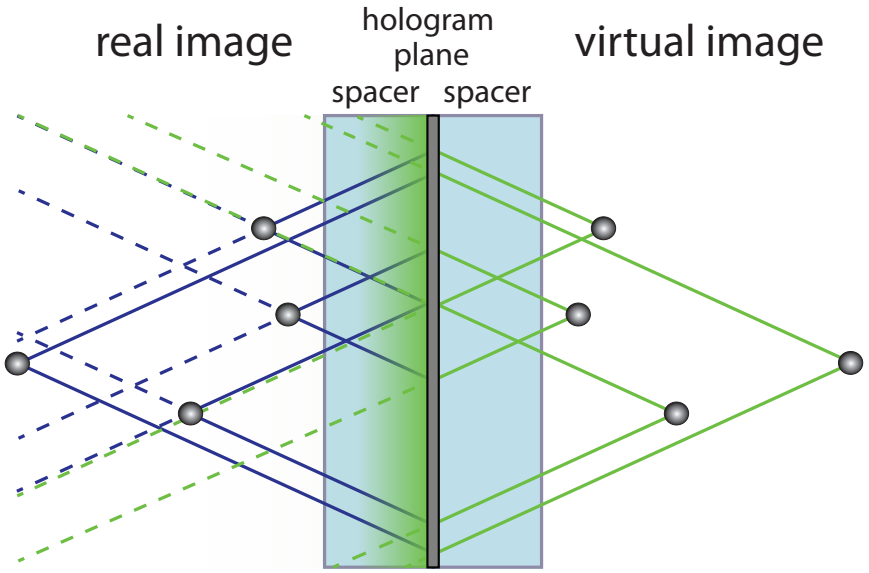

Figure 4.18: In this scenario a spacer is introduced between the hologram plane and the floor of the sample chamber. This reduces the parasitic effect of the signal from the virtual image. The signal from particles in the real image is also weaker requiring an increase in camera contrast or bit depth to compensate; however, all particles are closer to the illumination source, meaning the camera settings can be better adjusted to capture the entire signal.

Some further points for consideration from these experiments include the fact that the identification of beads is still fairly primitive. Improvements on the thresholding technique that could better differentiate between particles in dense solutions would help this accuracy. Additionally, my tracking algorithm is relatively basic. It relies on selecting the optimal radial distance threshold, which is difficult to do in practice for the more crowded datasets. Increasing the field of view may also help significantly as more particles would be captured completely due to the larger area to edge ratio.

In short, these results demonstrate the microscope is useful for bacterial tracking applications in that particle localisation in all three dimensions can be achieved to at least 0.25μm in a 50μm deep chamber. The basic analysis presented here is effective for relatively sparsely-populated samples. More sophisticated particle identification and tracking routines will need to be developed to handle more densely-populated chambers.

It is also likely that the number of diffusing particles able to be compensated for will increase for lower magnifications. Indeed, some evidence of this can be seen in chapter 6, where 50 bacteria are able to be tracked with these simple methods in a 100μm deep chamber at 45$\times$ total magnification.

A likely explanation for this can be seen in the fact that a lower-magnification objective has a lower numerical aperture (NA), thus it captures a smaller range of angles of light scattered from a specimen. The size and spread of diffraction rings in the image plane due to a defocused object depends on the object-to-focal plane distance and the scattering profile of the sample. Particularly for a sample with many defocused objects, these diffraction rings superimpose at the image plane and individual particles can be hard to extract from the background noise, especially with the thresholding technique used so far. While a lower-NA objective will not be able to resolve two nearby particles as well as a higher-NA objective, the smaller angular spread of the diffraction patterns means there will be less overlap between the diffraction patterns of different objects at the image plane. This is likely to be of benefit for polystyrene microspheres, which are known to scatter strongly along the direction of the incident illumination [143], and other dielectric media, such as bacterial cells. A low numerical aperture system would not be of use if fine detail of the sample were required. However, in many three-dimensional tracking applications, the position of the centre of an object is sufficient to inform on the behaviour of the that object over time.

A high-NA objective would be advantageous for samples that scatter light at a greater range of angles: gold nanoparticles for instance. However, as this section has shown, with the Nikon Plan Fluor 100$\times$ objective, which has a numerical aperture of 1.3, it is difficult to adequately resolve the position of particles 50μm away from the specimen plane in the presence of a few tens of diffusing particles. It may be that we need to select a numerical aperture for different applications. A lower-NA

objective would be better for relatively deep chambers of polystyrene microspheres or bacteria, where we are less interested in resolving fine detail and more concerned with the location of the centre of the object. A high-NA objective could be used for relatively shallow chambers with samples of isotropically-scattering particles. Gold nanoparticles, for instance, could be used in this manner to probe the flow field around a swimming bacterium.

The diffraction pattern fringes in a high numerical aperture system can be explained through Mie scattering [149]. Using Mie models to fit to holograms obtained in even high numerical aperture systems could resolve the 3D positions of objects in a densely-seeded field of view. The computation time of such an approach is, however, not insignificant [118] and must be taken into account.

4.6 Measurement of the 3D Diffusion Coefficient

The three-dimensional diffusion coefficient of a 0.5μm polystyrene microsphere was determined experimentally using the high-magnification DHM.

Assuming a particle is sufficiently far from surfaces and from interactions with other particles, its diffusion coefficient should be isotropic in three dimensions. The diffusion coefficient D is given theoretically by:

$$D = \frac{1}{f}kT \tag{4.6}$$

where k is Boltzmann's constant, T is temperature and f is the frictional coefficient. For a sphere, $f = 6\pi\mu r$, with μ the viscosity of the medium and r the radius of the sphere [150].

The diffusion coefficient can be determined experimentally by measuring the mean squared displacement (MSD) of a diffusing object over a given time interval Δt and

using the following equation:

$$\langle d^2_{\Delta t} \rangle = 2nD\Delta t \tag{4.7}$$

where n is the number of dimensions in which movement is measured and d may be substituted for x, y, or z for $n = 1$, $r = \sqrt{x^2 + y^2}$ (for instance) for $n = 2$, or $\rho = \sqrt{x^2 + y^2 + z^2}$ for $n = 3$.

Unrestricted Brownian motion should give rise to a linear relationship between $\langle d^2_{\Delta t} \rangle$ and Δt from which the diffusion coefficient can be calculated. For a spherical particle of 0.5μm diameter in water at room temperature (295K), equation 4.6 yields $D = 0.872\ \mu\text{m}^2\text{s}^{-1}$ for one dimension.

4.6.1 Experimental Procedure

A dilute ($N = 2.9 \times 10^7 \text{ml}^{-1}$) suspension of 0.5$\mu$m diameter polystyrene microspheres was introduced into a tunnel slide made with double-sided tape (Scotch, ~100μm thick; 3M plc). 0.5μm microbeads were chosen for their low sedimentation velocity as calculated by equation 4.3. The ends of the tunnel were sealed to prevent evaporation. With the microscope focused on the floor of the chamber, one to four beads were found in a field of view and recorded for 2,000 frames at various framerates.

A total of 24 datasets were recorded at 10, 50, 200 and 2,000fps. Each dataset was reconstructed at a z-resolution of 100nm and particle positions were output as described in section 4.2.1. A custom routine in MATLAB tracked particles through each dataset. Beads that came within 15μm of the floor were not included in the final analysis. Ultimately, a total of 55 individual bead tracks were analysed to calculate the diffusion coefficient.

4.6.2 Analysis

To determine the value of the diffusion coefficient, a series of non-overlapping time intervals were first chosen. For each time interval $\Delta t = t_1 - t_0$, $d^2_{\Delta t}$ was calculated thus: $|\mathbf{d}(t_1) - \mathbf{d}(t_0)|^2$, where $\mathbf{d}$ is replaced by the appropriate substitution specified above. That is to say, a 2,000-frame track recorded at 2,000fps would yield 1,999 $d^2_{\Delta t}$ values for $\Delta t = 0.5$ms, nine $d^2_{\Delta t}$ values for $\Delta t = 100$ms, and one $d^2_{\Delta t}$ value for $\Delta t = 1,000$ms. The $d^2_{\Delta t}$ values for each Δt were aggregated for all 55 tracks and divided by the sample size N to arrive at a single mean squared displacement value for each time interval.

The standard error, defined as the standard deviation σ of each sample divided by $\sqrt{N}$, was calculated for each time point and a weight parameter was defined as the inverse of the square of the standard error. This was calculated in order to use a weighted least squares model to provide a linear fit to the data.

The mean squared displacement data for diffusion along the x, y and z axes as well as in two (x and y) and three dimensions are displayed in figure 4.19. The MATLAB curve fitting toolbox was used to apply the fits and to determine the gradients, from which the diffusion coefficient can be calculated. The fitting toolbox generates 95% confidence intervals (1σ) for each parameter of the fit; these are cited below as uncertainties on the measured diffusion coefficients.

4.6.3 Results

Figure 4.19 shows the calculated mean squared displacement data for x, y, z, $r = \sqrt{x^2 + y^2}$ and $\rho = \sqrt{x^2 + y^2 + z^2}$. The error bars show the standard error at each time interval and the weighted linear fit is displayed. The gradient of each fit is shown on each plot.

These gradient values are adapted in table 4.2 to compare the experimentally determined diffusion coefficients of a 0.5μm diameter polystyrene bead to the theoretical

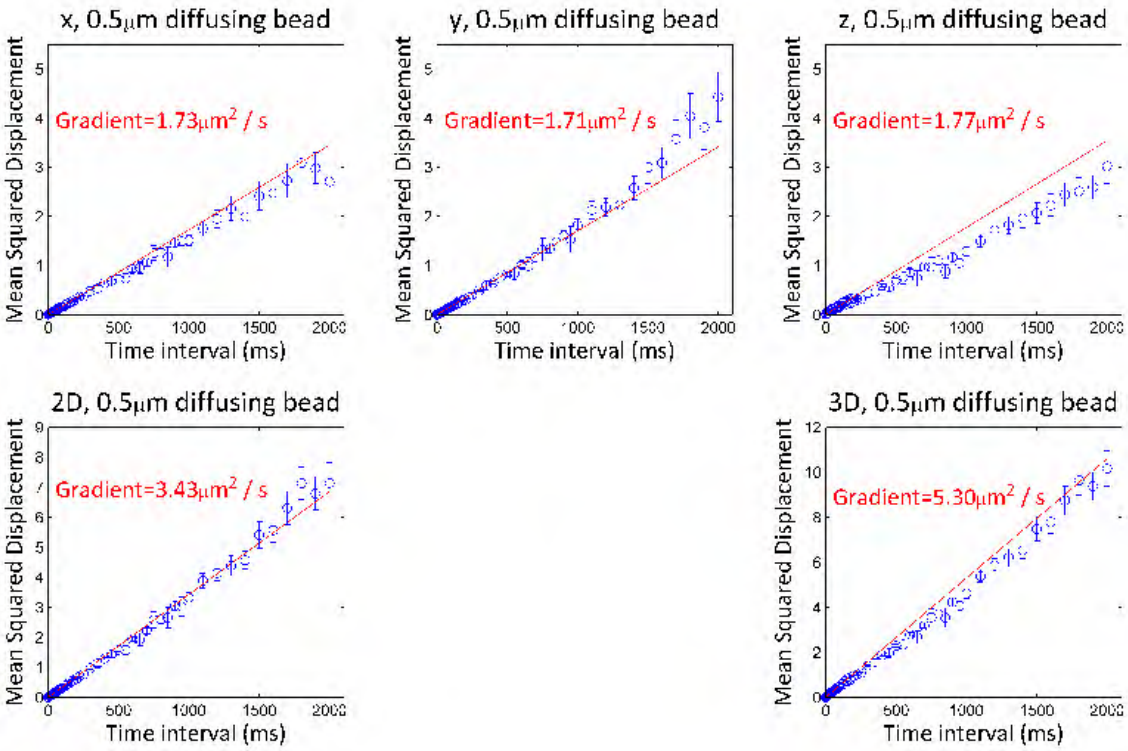

Figure 4.19: Mean squared displacement data (in μm^2) for a 0.5μm microbead are shown for x, y, z, 2D (x & y) and 3D for up to 2,000ms time intervals. The error bars display the standard error. The red lines and the displayed gradients result from weighted linear fits, with the fitting procedure described in the text. The diffusion coefficients can be calculated from the gradients of the fitted lines.

value. The uncertainties stated are from the 95% confidence values from the weighted linear fit.

$D_{theoretical}$	$0.872\mu\text{m}^2\text{s}^{-1}$
D_x	$0.863 \pm 0.024\mu\text{m}^2\text{s}^{-1}$
D_y	$0.854 \pm 0.018\mu\text{m}^2\text{s}^{-1}$
D_z	$0.885 \pm 0.076\mu\text{m}^2\text{s}^{-1}$

Table 4.2: Theoretical and experimentally-determined values for the one-dimensional diffusion coefficient for a 0.5μm polystyrene microsphere. Uncertainties shown are the 95% confidence value from a weighted linear fit to the experimental data described in the text. The experimental values show isotropic diffusion in x, y and z and give very good agreement to the theoretical value.

Figure 4.20 shows the mean squared displacement data for x, y and z with the theoretical gradient superimposed. The dashed lines indicate the 95% confidence values on the gradients.

The experimental data show very good agreement between the measured values for D in each direction and with the theoretical value, which lies within the 95% confidence values for all experimentally determined values. This indicates the expected 3D isotropic diffusion of the microspheres is being observed correctly by the microscope. One would expect that with even more bead traces, the accuracy of the experiment would be increased. The current primary limitation on achieving this is the ability to reconstruct and track many particles in a field of view in order to obtain 3D position data over time for a large population of beads. Improving our current reconstruction and identification techniques is the subject of ongoing future work. Additional three-dimensional diffusion experiments could also be envisaged, such as comparing the behaviour of particles close to and far from a surface.

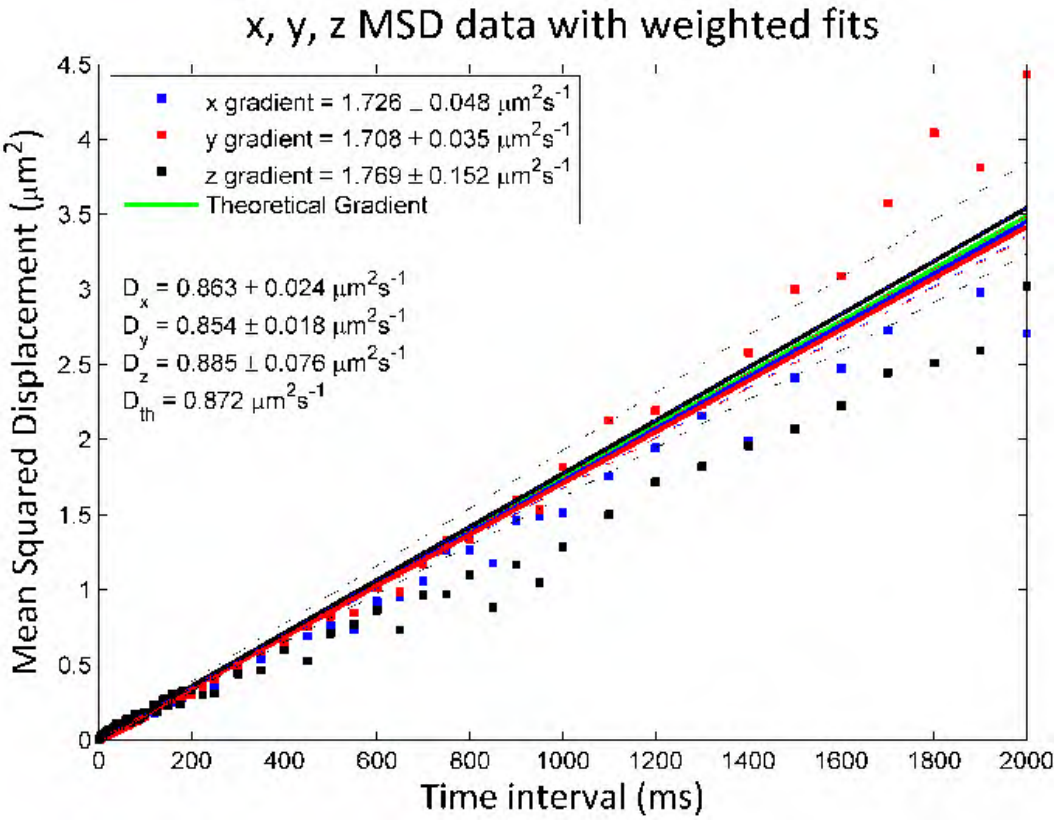

Figure 4.20: The x, y and z mean squared displacement data for a 0.5μm microsphere are superimposed onto a single plot. The error bars have been omitted for clarity. The solid lines show the gradients of the weighted linear fits and the dashed lines are the 95% confidence lines from the weighted fit. The gradient of the theoretical one-dimensional diffusion coefficient is shown on the plot in green for comparative purposes. The theoretical and experimentally-derived 1D diffusion coefficient values are displayed below the legend.

4.7 Using Inline Holography to Localise Gold Nanoparticles

On account of their size and their light-scattering properties, gold nanoparticles are an attractive probe for investigating the fluid flow around motile microorganisms such as bacteria. A preliminary investigation into the efficacy of high-magnification inline holographic microscopy for localising gold nanoparticles was conducted. These results are compared with the dark field off-axis configuration of the microscope in section 5.5.

A solution of freely diffusing 100nm diameter gold nanoparticles ($N = 2.8{\times}10^9\text{ml}^{-1}$) was introduced into a $\sim$50μm deep tunnel slide. Hologram image stacks were recorded at 2,000fps. Holograms were reconstructed and particles identified using the methods described in section 4.2.4. The diffusing nanoparticles were tracked through time using a threshold radius of 150nm between frames. The mean distance travelled due to diffusion for a 100nm gold particle in 0.5ms is 114nm.

For reasons discussed in section 5.4, holograms were reconstructed from the focal plane to a distance of 15μm above the sample chamber floor. Given the concentration of the gold sample, one would expect, on average, $\sim$126 particles in a $30{\times}30{\times}50\mu\text{m}^3$ field of view. Holograms were recorded within a minute of preparing the sample, thus the effect of particles settling due to gravity is expected to be negligible and we can reasonably assume particles to be randomly distributed throughout the volume. With this in mind, we might expect to see, on average, 38 particles in the volume prescribed by the recorded field of view and the lower 15μm.

Figure 4.21 shows the positions of gold nanoparticles from a typical frame acquired with inline holographic microscopy. Note that only six particles were identified out of the expected $\sim$38, indicating that inline holography is not very successful at localising 100nm gold nanoparticles in these experimental conditions. See section 5.5 for a

greater discussion on this result.

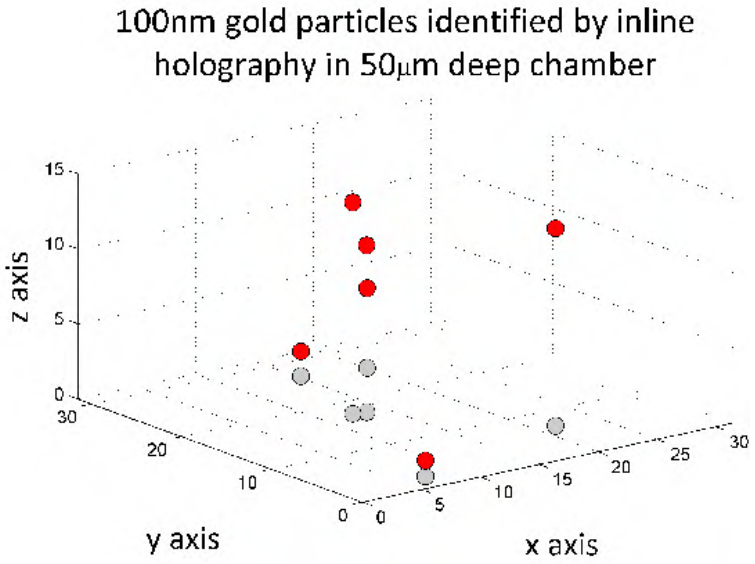

Figure 4.21: A typical result showing 3D positions of 100nm gold nanoparticles identified with high-magnification inline holographic microscopy. Red circles indicate the location of each nanoparticle in 3D and the grey circles are projections of each position onto the x-y plane. The scale is in μm. Only six nanoparticles are identified compared to an expected ~ 38 particles present in the volume.

Chapter 5

Assessment of Dark Field Off-Axis Holography

5.1 Introduction

Off-axis holographic microscopy is appealing for a number of reasons. Firstly, the technique allows for the recovery of both the amplitude and phase of the specimen. This may be of benefit when studying certain biological specimens [80, 89] as well as generally improving the axial resolution in digital holographic microscopy [98]. More pertinent for the applications discussed in this thesis, however, is the potential for off-axis holography to resolve the positions of a higher density of particles in a given sample [127]. This arises from eliminating the 'twin image problem' of inline holography, discussed in section 2.4, and by reconstructing only the real image of the hologram.

One of the issues with high-magnification transmission mode off-axis holography is diverting the illumination beam away from the camera, so as to optimise the signal from the sample. Section 3.7 outlines the approaches to this problem considered in this thesis, along with the final Fourier plane mask configuration.

This chapter details the first attempts at assessing the performance of the dark field off-axis holographic microscope. It was hoped to repeat all the experiments conducted for the inline digital holographic microscope (DHM), demonstrated in chapter 4, as a basis for direct comparison between the two modalities. Unfortunately, technical issues arose that were not easily overcome. Time constraints meant that this work will need to be completed at a later date.

The hardware performance of the microscope when operating in its off-axis mode is identical to that of the inline setting. That is, a 512px $\times$ 512px region of interest, corresponding to a 32μm $\times$ 32μm field of view (FoV) with a total magnification of 225$\times$ is able to be recorded at up to 2,000 frames per second.

5.2 Methods for Off-Axis Imaging

5.2.1 Operating the Microscope in Off-Axis Mode

A number of procedural changes must be made when using the DHM as an off-axis microscope.

Firstly, the relative intensities of the object and reference beams must be set appropriately. There is no firm guide for assessing this, save to say that the interference pattern caused by the object and reference beams must be visible, yet without any camera saturation effects from either beam.

Relative intensities may be controlled by adjusting the half-wave plate immediately after the laser head, and/or by inserting a neutral density (ND) filter into one of the beam paths. The user needs to ensure that, should a neutral density filter be used, the path length is readjusted to ensure maximal interference. Similarly, if the wave plate at the laser head is adjusted, the second wave plate in the illumination path must also be rotated to ensure the orientation of polarisation is preserved.

Complicating this is the desire for a bright illumination beam for dark field imaging

as most of the light is blocked by the Fourier plane mask. This intensity of illumination in the reference beam would cause the camera to saturate, requiring an ND filter in the reference beam path. The optimal intensities for both beams can be difficult to set in practice as it can be very hard to observe the maximal interference pattern with the Fourier plane mask in place, and the camera will saturate should the mask be removed.

In this matter, there is no substitute for experience; however, an outline of my methodology for setting up the microscope for an off-axis experiment is as follows:

1. Place a 1.0 ND filter in the reference beam path only. Remove the Fourier plane mask from the optical path using the adjustable screws on the lens mount.

2. With the wave plate set so that minimal light is incident on the sample and the camera exposure time set very short ($\sim 5\mu$s), observe the interference fringes and adjust the path length such that the pattern contrast is maximal.

3. Adjust the position and focus of the sample.

4. Reposition the Fourier plane mask to enable dark field imaging. Increase camera exposure time to avoid zero-value pixels.

5. Adjust the half-wave plate at the laser head to achieve desired ratio of reference and object beams. Adjust exposure if necessary.

6. Carefully observing the dark field interference pattern, adjust the second wave plate to align polarisations.

Fortunately, the final step is less critical than adjusting the path length in step two.

The reconstruction of off-axis holograms requires an image of the reference beam. Thus, the user must remember to obtain this for each dataset that sees a change in the exposure time or relative intensity of the two beams.

Other experimental methods such as sample preparation, coordinate system conventions and numerical analysis on reconstructed 3D position data are the same as those described in sections 4.2.2 to 4.2.4.

5.2.2 Off-Axis Numerical Reconstruction

The Python digital holography reconstruction graphical user interface (GUI), written by Irwin Zaid, is able to examine off-axis holograms. The wavelength of light, refractive index and effective pixel size (pixel size / magnification) must be set by the user. Additionally, the shift, in inverse pixels, of the centre of the desired twin image spectrum to the centre of the Fourier plane must be input. This allows the object term to be isolated as per the method shown in section 2.6.2. Figure 5.1 shows a practical example of filtering an off-axis hologram to extract the real image. The fast Fourier transform feature on the GUI greatly assists with finding the shift value by displaying the shifted Fourier transform along with the pixel coordinates of the mouse cursor.

The user must also select a dataset to be used as the reference image. Otherwise, the controls governing slicewise and volume reconstruction and particle identification are the same as described in section 4.2.1. One additional feature is, of course, the ability to display phase reconstructions.

5.3 Amplitude and Phase Holograms

As mentioned, one of the primary advantages of off-axis holographic imaging is the ability to reconstruct both amplitude and phase images from off-axis holograms. To demonstrate this, 1μm polystyrene microspheres were immobilised on the floor of a sample chamber. The specimen plane of the microscope was set below the floor, into the glass of the coverslip, by $\sim$21μm using the piezo servo controls. Figure 5.2 shows

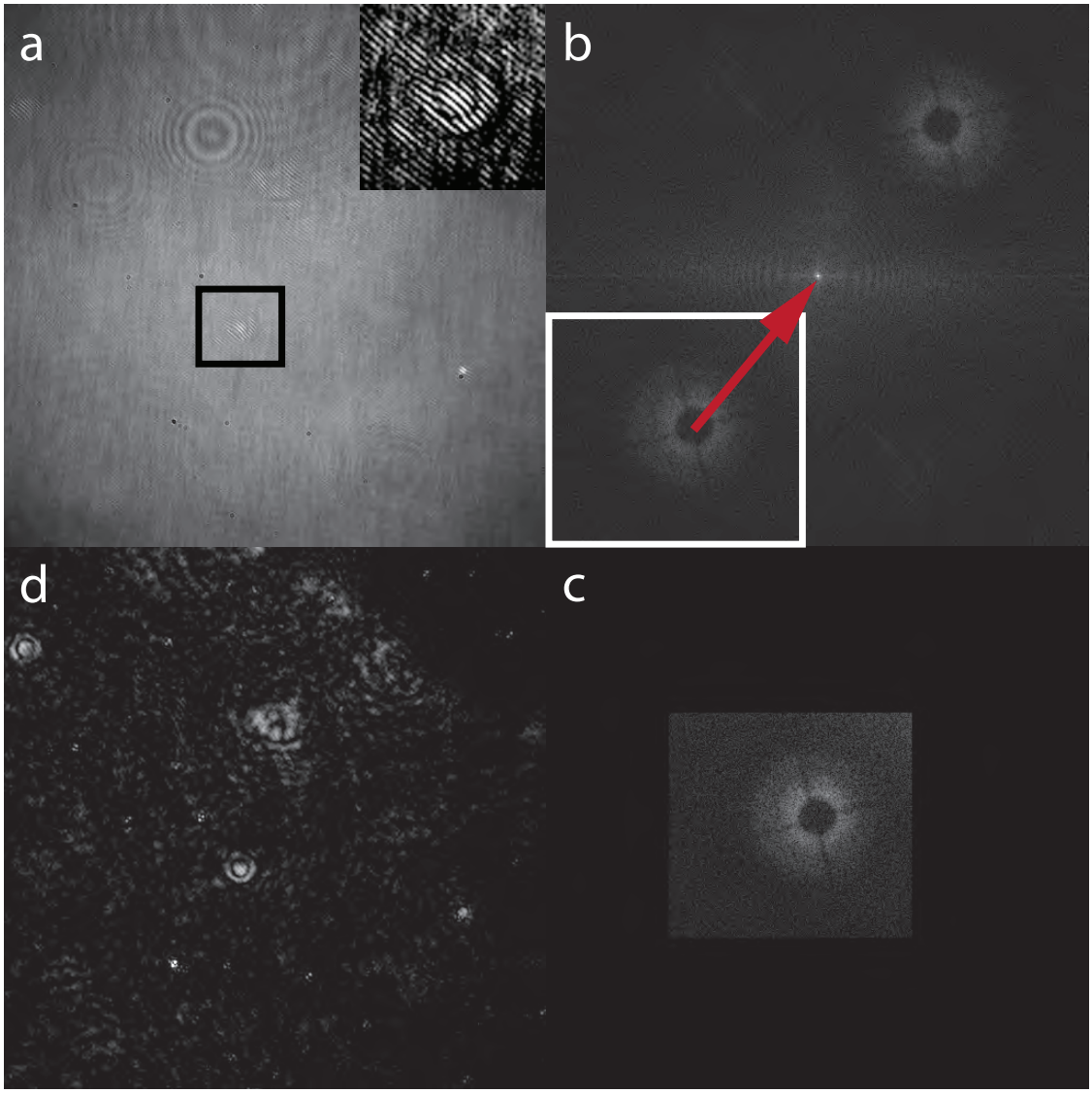

Figure 5.1: A practical example of isolating the object term from an off-axis hologram analogous to the method described in section 2.6.2. *a*) shows a recorded off-axis hologram of 100nm gold particles at 225× magnification. The inset in the top-right is a contrast-enhanced zoom of the region inside the black box. The striped interference pattern can be seen overlaying the dark field signal of a defocused gold nanoparticle. *b*) is the Fourier transform of the hologram represented on a logarithmic scale. The spatial frequencies of the real and virtual images are in the bottom-left and top-right quadrants. The centre of the Fourier transform contains the spatial frequencies of the reference beam that has not interfered with the object beam. The spatial frequency range of the real image is isolated (white box) and centred in the Fourier plane (red arrow) leading to *c*); an inverse Fourier transform is then performed, resulting in *d*). This image shows the amplitude of the object beam itself, from which the 3D positions of the nanoparticles can be determined through reconstruction.

a dark field snapshot image of the microspheres on the floor surface before refocusing.

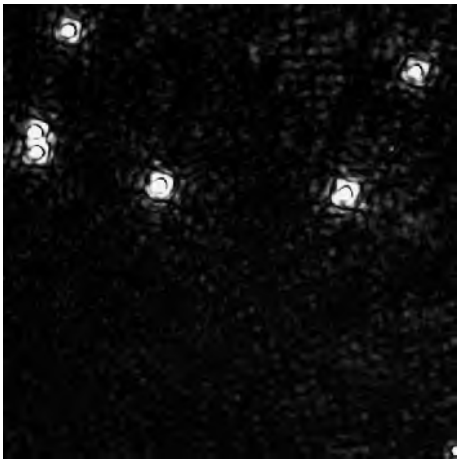

Figure 5.2: Dark field snapshot image of six 1μm polystyrene microspheres immobilised on the floor of a sample chamber.

Figure 5.3 shows the reconstructed amplitude and phase of the hologram at a range of different heights. The phase images show a ring pattern around each spherical object, expected from the Mie solutions to scattering off nanoparticles [149, 151], the radii of which decrease as the reconstruction plane is moved closer to the objects themselves. These phase rings act like Fresnel lenses[1], creating a focus at the location of the microsphere in the reconstruction volume.

The six polystyrene beads visible in the snapshot image of figure 5.2 are distinguishable in an amplitude reconstruction 21.5μm above the hologram plane. Two microbeads that appear to be stuck together in the left of the snapshot image are also resolvable as two individual particles in this reconstruction. The beads in the top left and top right corners of the field of view are less bright than the other four. This is most likely due to the fact that only about a quarter of the diffraction pattern from these beads is collected in the original hologram. Examination of the phase image in the original hologram plane (figure 5.3, top right) supports this. Whereas the phase rings from the other four beads can be made out reasonably clearly (although less so

[1]Lenses made up of discontinuous but thin, concentric, annular sections traditionally found in lighthouse lamps.

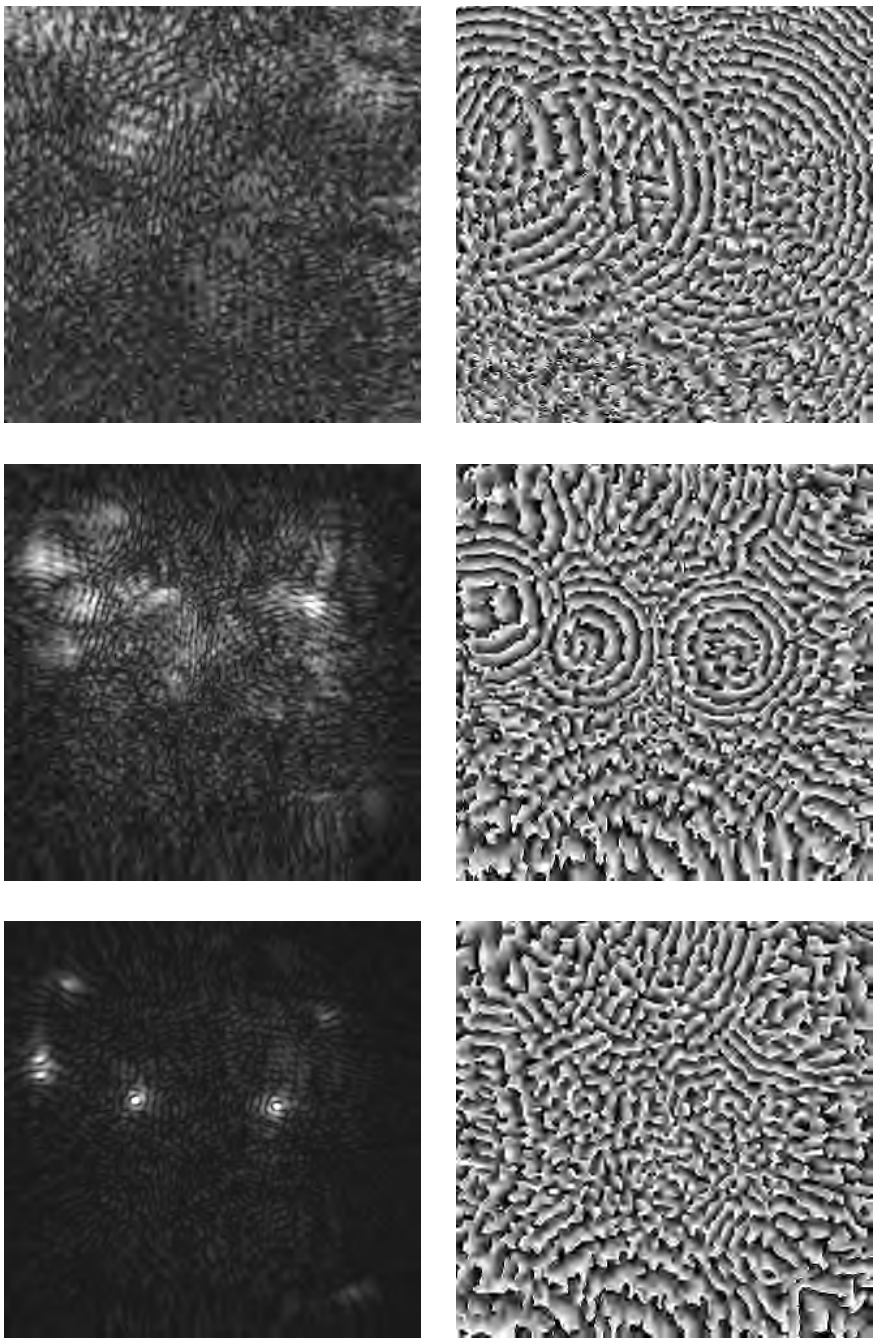

Figure 5.3: Reconstructed amplitude (left) and phase (right) images of a dark field off-axis hologram of six 1μm polystyrene beads. The hologram plane was set $\sim$21μm below the plane of the beads by the piezo controller. The top set of images shows a reconstruction in the specimen plane; the middle set is a plane 13μm above this plane; and the bottom set is 21.5μm above the specimen plane, where the beads were localised using the reconstruction software.

for the bead pair on the edge), it is difficult to see the phase pattern of these two beads in the corner.

The corner beads also appear to be closer to the centre of the reconstructed amplitude image (figure 5.3, bottom left) than they are in the snapshot image (figure 5.2). While the snapshot image is certainly not a one-to-one comparison with the reconstruction as the sample may have moved in-plane as it was refocused, there is the possibility of distortion occuring in the reconstruction should the phase pattern not be captured absolutely in the hologram. This feature merits further study in the future along with protocols to overcome any reconstruction distortions.

5.4 Depth Resolution

It was hoped to repeat the experiments performed in sections 4.3, 4.5 and 4.6 to compare directly the performance of the microscope operating in the inline and off-axis modes. Unfortunately, effective localisation of 1μm and 0.5μm polystyrene microspheres and 100nm gold nanoparticles adhered to the ceiling of a $\sim$50μm chamber was found to be impossible. Individual particles were unable to be identified from an artifact term that dominated the reconstruction, regardless of the threshold used.

Closer investigation showed that this dominant feature could be traced to a spurious scattering artifact off the ball bearing used as a Fourier plane mask. Figure 5.4 shows the recorded intensity of this artifact. This image was obtained by taking a mean through a stack of dark field images of diffusing gold nanoparticles so that the sample is averaged away and the static, parasitic scattering profile remains. The contrast in the image has been increased to make the pattern more visible.

This artifact obscures the weaker signal from particles sufficiently far from the specimen plane. In practice, this distance was found to be $\sim$15μm, with the ball bearing artifact manifesting itself as a large false object from $\sim$20μm in a 3D reconstruction.

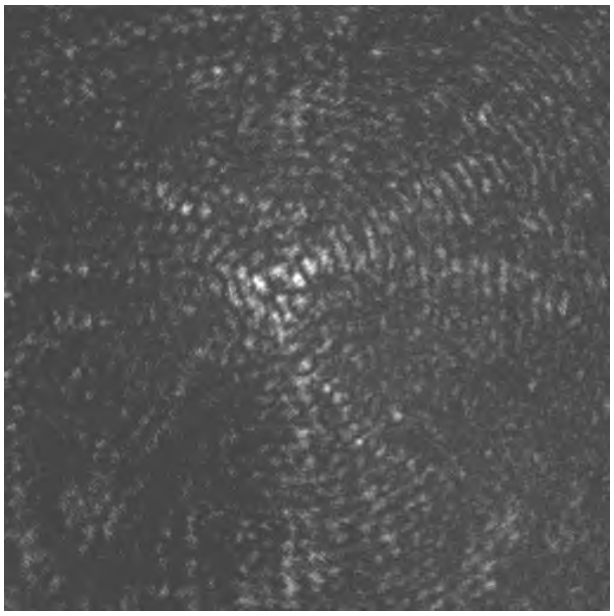

Figure 5.4: Dark field image of artifact due to scattering off the ball bearing Fourier plane mask.

Various attempts were made to remove this artifact in the post-processing stage of reconstruction by, for instance, subtracting the static artifact pattern from the recorded holograms. None, however, was successful and the solution seems to lie in improved dark field imaging. This could simply mean replacing the steel ball bearing with another object that scatters less brightly, or it could involve the redesign of the off-axis microscope along the lines of another form of dark field imaging − such as that described by Sowa *et al.* [143]. Time constraints have meant that improvements here must be attempted as future work.

5.5 Using Off-Axis Holography to Localise Gold Nanoparticles

Section 4.7 detailed using the high-magnification microscope operating in the inline configuration to localise 100nm gold nanoparticles. At the same time, off-axis data were taken and reconstructed for comparative purposes.

Gold nanoparticles are, in general, much more visible under dark field imaging conditions than bright field microscopy [143]. Thus, dark field off-axis holographic microscopy is a promising method for obtaining three-dimensional position data of gold nanoparticles.

As described in section 4.7, a solution of freely diffusing 100nm diameter gold nanoparticles ($N = 2.8\times10^9\text{ml}^{-1}$) was introduced into a $\sim$50μm deep tunnel slide. Dark field off-axis hologram image stacks were recorded at 2,000fps, then reconstructed and particles were identified using the methods described in section 5.2.2.

The scattering artifact from the ball bearing Fourier plane mask discussed in section 5.4 prevented the identification of any particles $\sim$15μm above the sample chamber floor, thus an accurate comparison between the two modalities was not possible. However, there are some encouraging signs for using dark field off-axis holographic microscopy to track gold nanoparticles. Taking the lower 15μm depth of the chamber, many more nanoparticles were detected, on average, in the off-axis reconstructions than for the inline reconstructions.

Figure 5.5 shows the positions of reconstructed gold nanoparticles from a typical off-axis hologram frame. The reconstruction was taken from the hologram plane up to $z = 15\mu$m. In this volume one would expect to see, on average, 38 nanoparticles randomly distributed. This off-axis snapshot shows 36 gold beads in this volume, while in contrast, only six nanoparticles were detected in a comparable, typical inline reconstruction (detailed in section 4.7).

While not conclusive, there is at least strong evidence that the dark field off-axis modality is detecting all the gold nanoparticles we expect to see in a sample volume up to 15μm above the specimen plane. Inline holography does substantially worse, with only about 16% of particles identified. More work needs to be done on this aspect of holographic imaging once the scattering artifact due to the Fourier plane mask has been resolved. However, the early signs are there that dark field off-

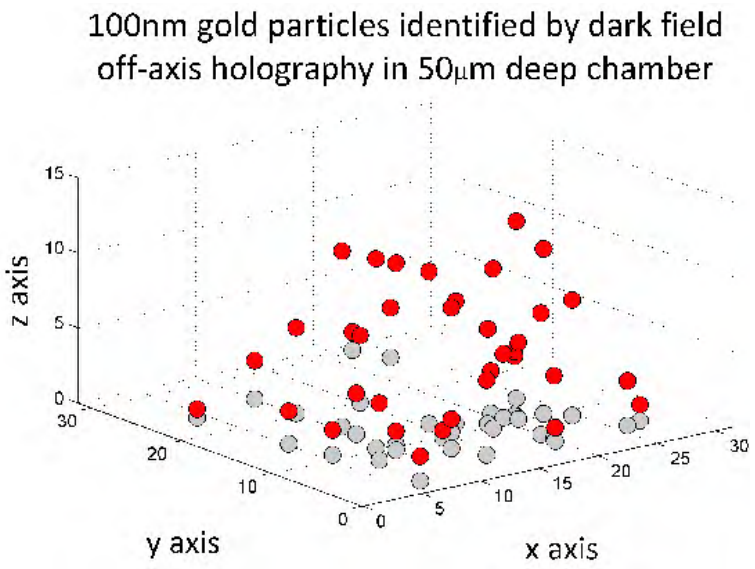

Figure 5.5: 3D positions of 100nm gold nanoparticles identified with high-magnification dark field off-axis holographic microscopy. Red circles indicate the location of each nanoparticle in 3D and the grey circles are projections of each position onto the x-y plane. The scale is in μm. 36 gold nanoparticles have been successfully identified in this frame.

axis holography will be of use in studying gold nanoparticles, and that it is superior to inline holography in this regard. A useful application of this technique would be to probe the three-dimensional flow field around swimming bacteria, using gold nanoparticles to mark the fluid.

Chapter 6

Microbiological Application

6.1 Comparison Betwen Inline and Off-Axis Techniques

Chapters 4 and 5 describe the high-magnification digital holographic microscope (DHM) operating in its inline and dark field off-axis modalities respectively.

The inline configuration is seen to be very good at localising very dilute suspensions of dielectric particles up to 100μm away from the surface (section 4.3.2). This represents an enormous increase in axial resolution over conventional imaging techniques; however, the ability to localise individual objects decreases as the sample becomes more crowded (section 4.5). There is a suggestion that using an objective with a lower numerical aperture (NA), while it would decrease the resolution of the system, would reduce the noise effect from overlapping object diffraction patterns and allow for more individual particles to be tracked successfully in a given volume (section 4.5.3).

Dark field off-axis holographic microscopy with the Fourier plane mask is shown to be superior to inline holography in detecting and localising 100nm gold nanoparticles (sections 4.7 and 5.5). However, due to a scattering artifact from the mask, it is

difficult to reconstruct individual objects that are more than $\sim 15\mu$m from the specimen plane (section 5.4). It is hoped that this restriction will be eased with further research; however, in the meantime, the off-axis configuration presented in this thesis is best suited to obtaining phase holograms of objects or to tracking the motion of gold nanoparticles in a region close[1] to the sample chamber floor.

The ultimate purpose of the digital holographic microscope described in this thesis is for three-dimensional studies of bacteria. Dark field off-axis holography lends itself to probing fluid flows around individual cells using gold nanoparticles as tracers. For the application of tracking individual bacteria in a three-dimensional volume, we wish to localise many cells in a region far from the effects of surfaces. In this context, the dark field off-axis configuration is not suitable and we are best using an inline modality. Additionally, as the fine detail of the cell shape is not required, a configuration with a low-NA objective would be more suitable in order to maximise the number of cells able to be localised in a given volume. Furthermore, an objective with a low numerical aperture is inherently lower magnification, leading to a wider field of view and a greater volume in which to track cells over time.

6.2 Studying Bacterial Motility

The scope of this thesis does not include an in-depth study of an aspect of 3D bacterial motility but I present here an outline of some of the capabilities of the DHM for such an application. It is hoped that the potential for holographic microscopy will be revealed, along with some of the challenges remaining for future work.

Three-dimensional information on the swimming behaviour of bacteria is extremely limited, with the canonical experiments conducted on a microscope capable of tracking only a single cell for a given time [35, 152]. The ability to observe the motile behaviour of many cells in a given sample volume, far from surfaces and in

[1] $\sim 15\mu$m

number densities sufficiently high to generate meaningful statistical data is one that is highly prized.

This chapter demonstrates the potential for the digital holographic microscope described in this thesis to do exactly that. Wild type *Escherichia coli*, which exhibit the natural chemotactic 'run and tumble' swimming behaviour discussed in section 1.3, were used for these experiments. In order to maximise the sample volume able to be interrogated adjustments were made to the high-magnification microscope described in section 3.8 to allow it to take inline holograms at a lower magnification.

Various experiments were conducted to optimise the number density of cells in a volume and the data analysis procedures to extract three-dimensional tracks of swimming bacteria over time. A representative sample of these data is presented in this chapter as a precursor to more rigourous statistical studies to follow in the future. The run and tumble behaviour of the chemotactic bacteria is clearly visible in some datasets as well as the widely reported circular swimming behaviour of *E. coli* near a surface [76–78].

6.3 Adjustments to Microscope

For the reasons discussed above, the high-magnification microscope described in section 3.8 was modified to acquire the following bacterial motility data. Modifications were made as minimally as possible to allow the microscope to be reconfigured easily to its previous arrangement.

The 100× objective was replaced by a 20× objective (CFI Plan Fluor, Nikon Instruments Inc.). The tube lens and downstream telescope (lenses L4, L5 and L6 in figure 3.14) were left in place, giving a new total magnification of 45×. This corresponds to an effective pixel size of: $\frac{14\mu\text{m}}{45\times} = 0.311\mu\text{m}$. Thus, the full frame of the Mikrotron camera equates to a field of view (FoV) of $398\mu\text{m} \times 319\mu\text{m}$ and a 512px

× 512px subregion to a field of view of 159μm × 159μm.

In the illumination arm, lens L3 was removed so that the beam incident on the sample was ∼0.63mm in diameter.

Finally, the Fourier plane mask was removed from the optical path as these experiments used inline holography only.

6.4 Bacterial Cultivation

Wild type *Escherichia coli* (strain RP437) was used for these experiments. In its motile phase, this strain exhibits the natural chemotactic 'run and tumble' swimming behaviour discussed in section 1.3.

Cells had previously been grown to saturation in lysogeny broth (LB) containing 1% bacto-tryptone (Difco; Becton Dickinson and Co.), 0.5% NaCl and 0.5% yeast extract. 100μl aliquots were flash-frozen in liquid nitrogen and then stored in a −80°C freezer. Before motility experiments, bacteria were grown to motile phase by inoculating 5ml tryptone broth (TB), containing 1% bacto-tryptone and 0.5% NaCl, with a 100μl aliquot of the frozen cell stock in a culture flask. The flask was incubated at 30°C on an orbital agitator platform at 140rpm for ∼6 hours, or until the solution reached an optical density of ∼0.6 at a wavelength of 600nm.

To prepare motility samples, 1ml of the incubated cell solution was placed into a sterile eppendorf. This aliquot was spun in a microcentrifuge at 8,000rpm for two minutes. The supernatant was removed and replaced by 1ml of motility buffer (MB). Motility buffer is a 10mM phosphate buffer containing 0.1mM EDTA[2], adjusted to pH 7.0 with hydrochloric acid [153]. The bacterial pellet was resuspended in the buffer by gently tapping the side of the eppendorf.

This procedure was repeated twice more to result in a total of two washes in motility buffer. After the third spin, the pellet was resuspended in a variable volume

[2]ethylenediaminetetraacetic acid

of MB depending on the desired number density of bacteria in a microscope sample.

6.5 Acquisition of Holograms

The first variable we encounter in acquiring experimentally-useful holographic data is the density of the motile cell solution. Unlike the polystyrene microbeads or gold nanoparticles used in chapters 4 and 5, which have known stock solution number densities, it is very difficult to estimate the number of bacteria in a given volume. Numbers depend on the optical density reached during incubation, whether any cells were lost during the wash cycles, and whether all of the supernatant was removed at each stage. In addition, not every cell in a given sample will be motile and healthy. Thus, there is a balance to be struck between having enough swimming cells in a given field of view to justify the computational expense of holographic reconstruction, and having too many cells that may result in unacceptable errors in localisation at some stage of the numerical analysis.

The ideal solution would seem to have as many cells in a field of view that can be successfully identified in three dimensions. This may be fine for a single-image application; however, for 3D video microscopy, the relative displacement between objects through time is also important. Too many particles, while perhaps successfully identified in an individual frame, may confuse a tracking algorithm. Optimisation of particle tracking is not the focus here; it is, however, flagged as an area of future concern.

In practice, I experimented with three dilutions of bacteria. Following the final wash in motility buffer, the bacterial pellet was resuspended in 1ml of MB. This was termed the 'concentrated' solution. A 1:5 dilution of this solution became the 'middle' solution and a 1:20 dilution became the 'dilute' solution. Figure 6.3 in section 6.7 shows the effect of different cell dilutions with respect to extracting bacterial tracks

and visualising 3D data.

It is very difficult to estimate the number of fast-moving bacteria in a given field of view when looking at a hologram. However, I estimate a 'dilute' sample would contain 10 to 20 swimming cells in a 159μm $\times$ 159μm $\times$ 100μm volume and the other dilutions scale from there.

Samples were introduced to the microscope via the tape tunnel slides described in section 4.2.2. As per most other experiments described in this work, the specimen plane of the objective was set on the floor of the chamber by focusing on a pen mark.

2,000-frame datasets were recorded at 50fps. 512px $\times$ 512px subregions were recorded to allow the holographic reconstructions to complete in a reasonable time-frame. As the sample was moving, it was not necessary to record a separate set of images to provide a background against which to normalise the holograms. Rather, the mean of the image stack was taken.

6.6 Holographic Reconstruction

Datasets were reconstructed through almost the entire volume at a z-resolution of 0.25μm. Given the likelihood of noise at the floor of the chamber due to accidentally-immobilised cells, reconstruction began from 2μm above the hologram plane. Most objects of interest are to be found well above this level in this study. Given this z-resolution, a 2,000-frame image stack of 512px $\times$ 512px holograms takes around $3\frac{1}{4}$ hours to process on our current GPU hardware. Figure 6.1 shows two views of a 3D volume reconstruction of a frame from a 'middle' dilution dataset.

At the reconstruction stage we have another variable affecting the potential quality of the final data: the threshold over which objects are identified. For experiments with spherical objects, the main complicating factor in using a simple threshold to identify high-intensity values of the reconstructed light field is that the scattering intensity

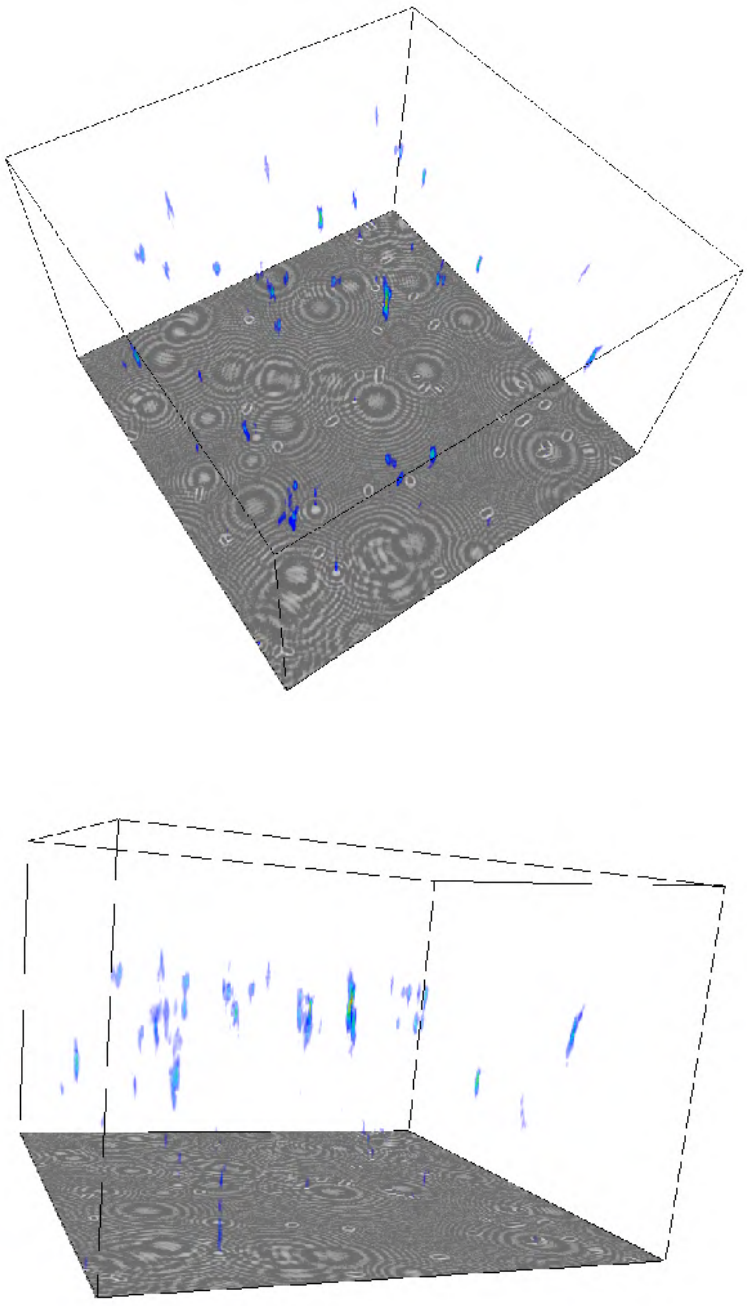

Figure 6.1: Two views of a 3D volume reconstruction of a frame from a 'middle' dilution dataset of swimming *E. coli*. The normalised hologram is visible at the floor of the reconstruction. The bounding box extends to a height of $z = 100\mu$m. The lobes of the reconstructed light field above the set threshold value are due to the presence of bacteria. The three-dimensional positions of these cells are determined by locating an intensity-weighted centroid on each lobe.

off the particle decreases in relation to the distance (r) from the hologram plane (Intensity $\propto \frac{1}{r^2}$). This is also true for bacteria; however, an additional complication was noticed. Bacteria that are oriented perpendicularly to the optical axis did not necessarily scatter light evenly across the rod-shaped profile of the cell. For some threshold settings, this results in multiple positive identifications for a single cell. Figure 6.2 shows the effect of different threshold values in a holographic reconstruction plane. The left-hand image shows how, at a certain threshold, one cell can generate more than one recorded position in a frame.

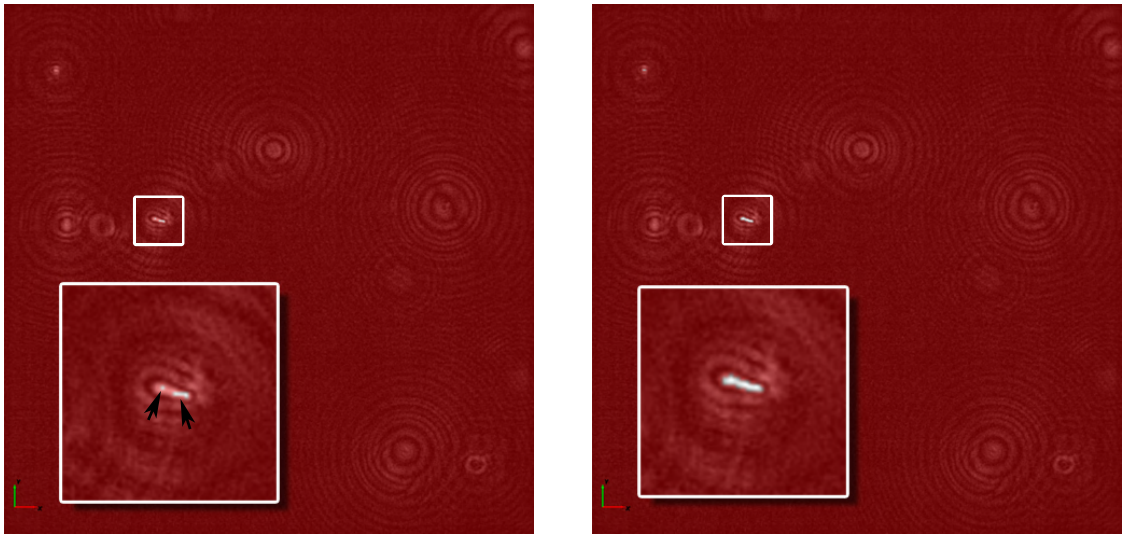

Figure 6.2: The effect of adjusting the threshold value when identifying bacteria position in a reconstructed plane is shown. In each image the inserted box shows a magnified view of the selected bacterium. Multiple regions of the cell (shown by the arrows) sit above the threshold value in the left-hand image resulting in multiple identified positions in the reconstruction. By lowering the threshold the entirety of the cell body is captured, shown in the right-hand image, leading to a single position for this cell. However, a lower threshold value could lead to more false positions due to noise elsewhere in the reconstructed volume.

Increasing the threshold value would typically mean all of the multiply-identified objects would disappear. Decreasing the threshold value opens the particle identification algorithm to more false positive identifications from spurious noise artifacts. Obviously, this is a dissatisfactory outcome, although not easily overcome given the available software.

The additional complexity of scattering intensity varying with the distance from the hologram means it is difficult to find an optimal single threhold value. To compromise, I set a threshold value that looked to cover the full depth of the sample volume, bearing in mind some cells may be multiply-identified.

Perhaps a better approach, for consideration in the future, is to use the GPU to identify smaller sub-volumes where a bacterium is likely to be. This could be achieved using a coarse threshold technique, perhaps with a $\frac{1}{r^2}$ factor to compensate for the drop off in intensity further away from the hologram plane. These sub-volumes could then be exported to a CPU for analysis of the volume, shape and orientation of a thresholded object, routines for which already exist. Due to the memory architecture of current GPUs, exporting sub-volumes is not a trivial operation.

6.7 Numerical Analysis of 3D Data

6.7.1 Display of 3D Data

One of the practical problems with dealing with three-dimensional information is how best to display it in only two dimensions. This problem is compounded by having a densely-populated volume and by the need to show the evolution of a system over time.

Consider, for instance, the data displayed in figure 6.3. These plots show all objects identified in a 3D volume by the reconstruction process for the 'concentrated', 'middle' and 'dilute' solutions of bacteria. (I have retained the convention of terminology whereby an 'object' is indiscriminately identified through the reconstruction process and remains to be confirmed as a bacterium or as a noise artifact.) A 3D view of each dataset is shown alongside a top-down view of the x-y plane. Firstly, one can immediately see the effect of different dilutions of bacteria. Visually, it is all but impossible to extract meaningful data from the 'concentrated' dataset, whereas

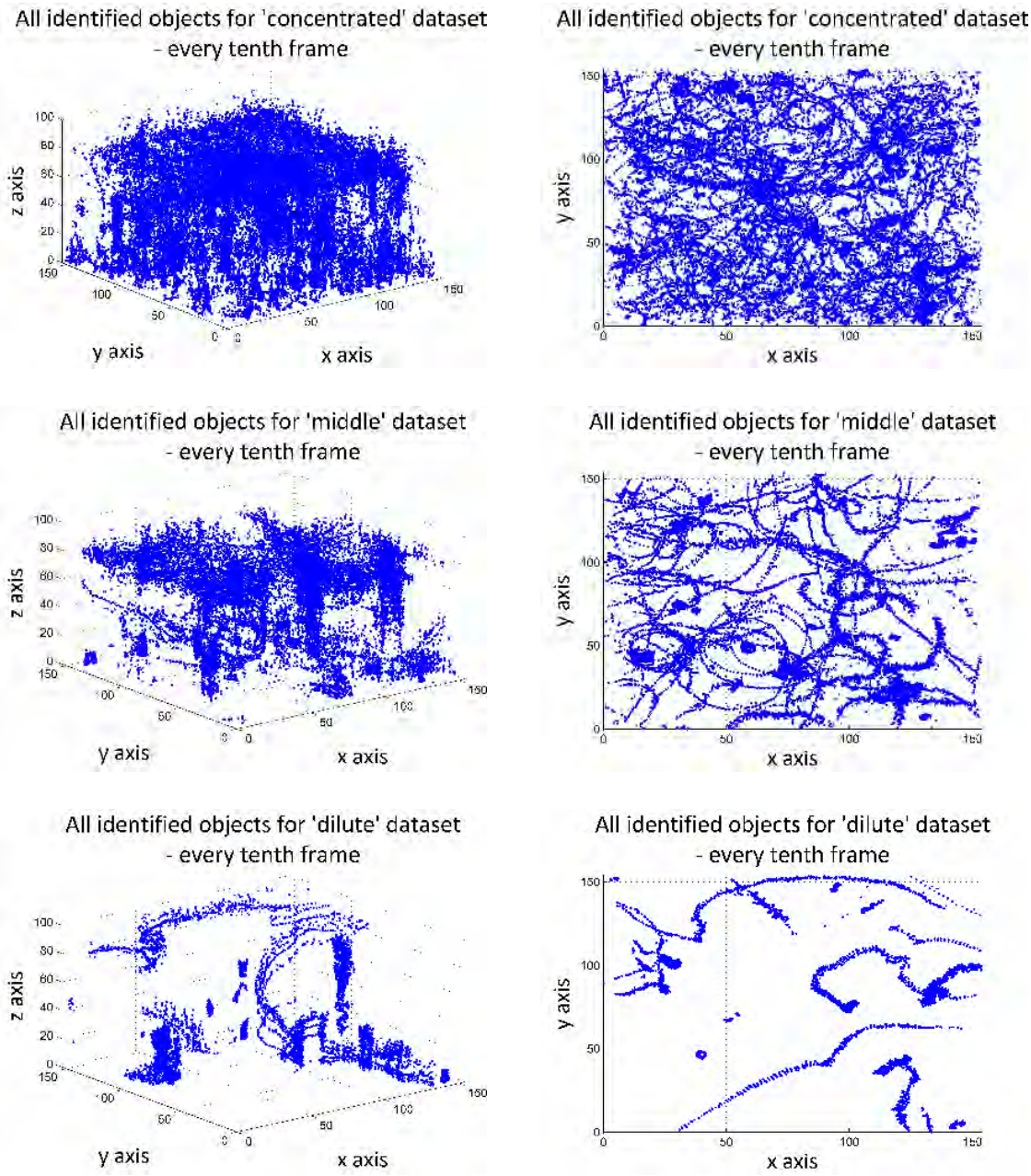

Figure 6.3: All objects identified by the reconstruction process for 'concentrated', 'middle' and 'dilute' suspensions of bacteria. Every tenth frame of an entire 2,000-frame dataset (corresponding to 40 seconds) is displayed. The methodology behind the reconstruction procedure and the cell dilutions is described in the text. The left-hand plots show a 3D view with the origin at the front centre. The right-hand plots show a top-down view of the same data; in this case the z-axis is coming out of the page. The scale is in μm. The effect of different concentrations of bacteria can be seen along with some of the difficulties of displaying and analysing 3D video data.

some clear tracks are visible in the 'middle' and 'dilute' datasets.

These plots represent identified cells; however, given the reconstruction and object identification protocols, there is the likelihood of multiply-identified cells appearing, along with possible spurious noise artifacts. Even in a 'dilute' sample, where we might expect 10 to 20 individual bacteria, 100 objects would typically be identified in a given frame.

6.7.2 Volume Filtering

It is thus necessary to provide a filter to eliminate at least some of the spurious artifacts. Following from the methodology applied to polystyrene microbead experiments, the simplest filter to apply at the individual frame level is to sort identified particles by volume. This assumes genuine bacteria will have a larger scattering profile than spurious noise artifacts and that for multiply-identified cells the largest scattering region remains in a constant position along the cell. This approach leaves a lot to be desired, with the assumptions not necessarily holding for the entire depth of a sample nor for all frames in a dataset. However, given the current identification method, it is seen as a useful first approach.

Volume filtering focused on the 'middle' and 'dilute' datasets with the rationale that, for the 'concentrated' data, it is too difficult to assess by eye the success of the filtering procedure when compared to the plots of all objects displayed in figure 6.3. Figures 6.4 and 6.5 shows the results of filtering the 3D position data in each frame by volume for the 'middle' and 'dilute' datasets respectively. The number of retained particles is identified in each plot.

Inspection of these figures, along with the plots of all particles in figure 6.3, shows that some volume filtering can be useful, in that noise and misidentified cells are removed while the tracks of genuine cells are still quite visible. Too much filtering clearly removes genuine cells as can be seen in the plots of the top 10 objects for both

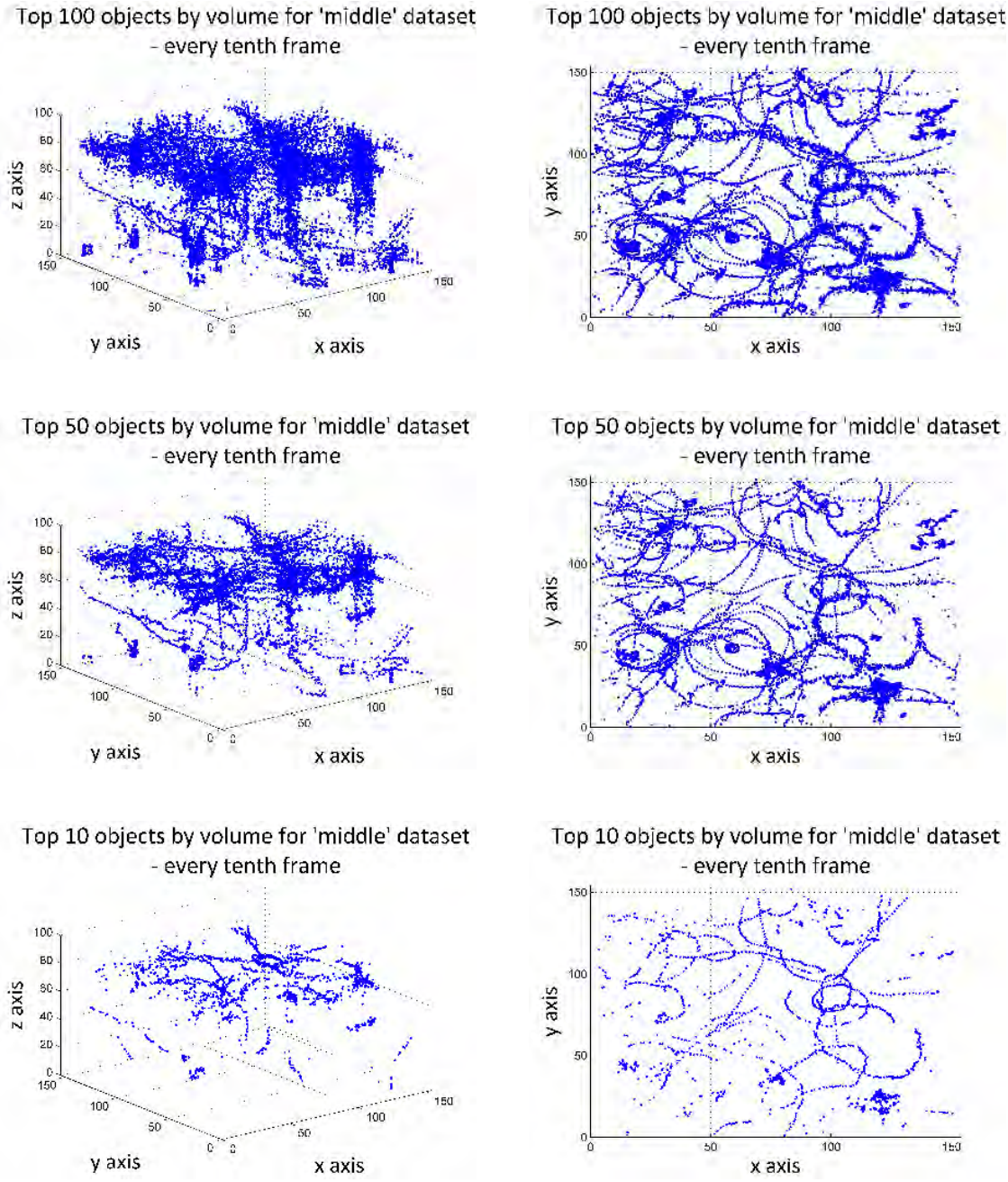

Figure 6.4: The top 100, 50 and 10 objects by volume are displayed for the 'middle' dataset for every tenth frame. The left-hand plots show a 3D view with the origin at the front centre. The right-hand plots show a top-down view of the same data; in this case the z-axis is coming out of the page. The scale is in μm. The 100-object filter still retains a lot of noise artifacts, whereas it is clear that with only 10 objects, we lose important data. 50 seems to be a happy medium.

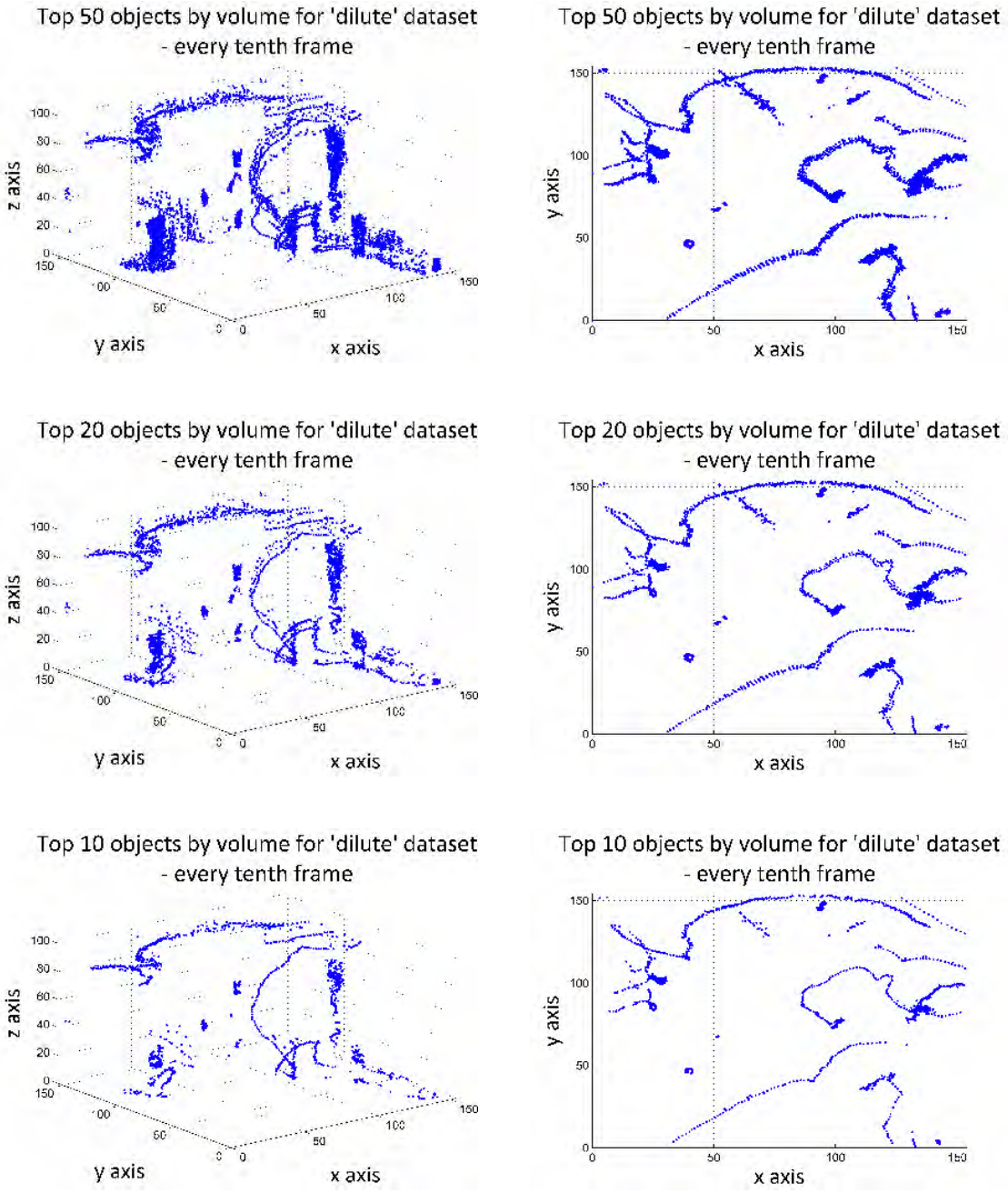

Figure 6.5: The top 50, 20 and 10 objects by volume are displayed for the 'dilute' dataset for every tenth frame. The left-hand plots show a 3D view with the origin at the front centre. The right-hand plots show a top-down view of the same data; in this case the z-axis is coming out of the page. The scale is in μm. We expect fewer objects in this dataset than in the 'middle' dilution. Even so, it is clear that noise artifacts are present in the top 50 filtered objects. It is difficult to pick, by eye, whether a 10-object filter removes critical data. Erring on the side of caution a 20-object filter was employed for these data.

the ‘middle’ and ‘dilute’ datasets.

Middle ground was found by using the top 20 objects for the ‘dilute’ dataset and the top 50 objects for the ‘middle’ dataset. Obviously, this is quite a simple initial approach. A more robust operation for the future would see cells differentiated from noise and from other particles based on their volume, shape and orientation. Adapting existing 2D artificial neural network routines [154, 155] to 3D data may also prove to be an efficient means of object identification and discrimination.

6.7.3 Extraction of Tracks

Having filtered some of the object artifacts through volume filtering, the next step is to extract tracks of individual cells. As mentioned previously, the particle identification program at the reconstruction stage does not necessarily preserve the numbering of identified objects between frames. My simple tracking program described in section 4.2.4 for tracking diffusing microbeads was employed to analyse the motion of the ‘dilute’ dataset presented above. The program takes an initial particle position in frame 1, then iterates through the available object positions in frame 2 seeking objects within a user-defined radius threshold. This then forms a new initial particle position and the process repeats through the entire dataset.

This is a crude tracking software that works satisfactorily for sparsely-seeded samples though runs into problems with higher concentrations of objects. One immediate issue is that this program relies on a particle being present in frame 1 for successful tracking. Bacteria that enter the field of view partway through the recording can be tracked by either running the tracking algorithm in reverse or by starting the algorithm at a midpoint.

It is at the threshold setting where another difficulty with extracting data becomes apparent. The choice of radius threshold on even relatively sparsely populated motility data can have a large effect on extracting tracks. For instance, wild type *E.*

coli swimming during a run will move significantly further between frames than when they undergo a tumble.

Figure 6.6 shows the effect of four different radius threshold values on the 'dilute' dataset. These data have been filtered to include only the top 20 objects by volume. Individual tracks are identified by different colours.

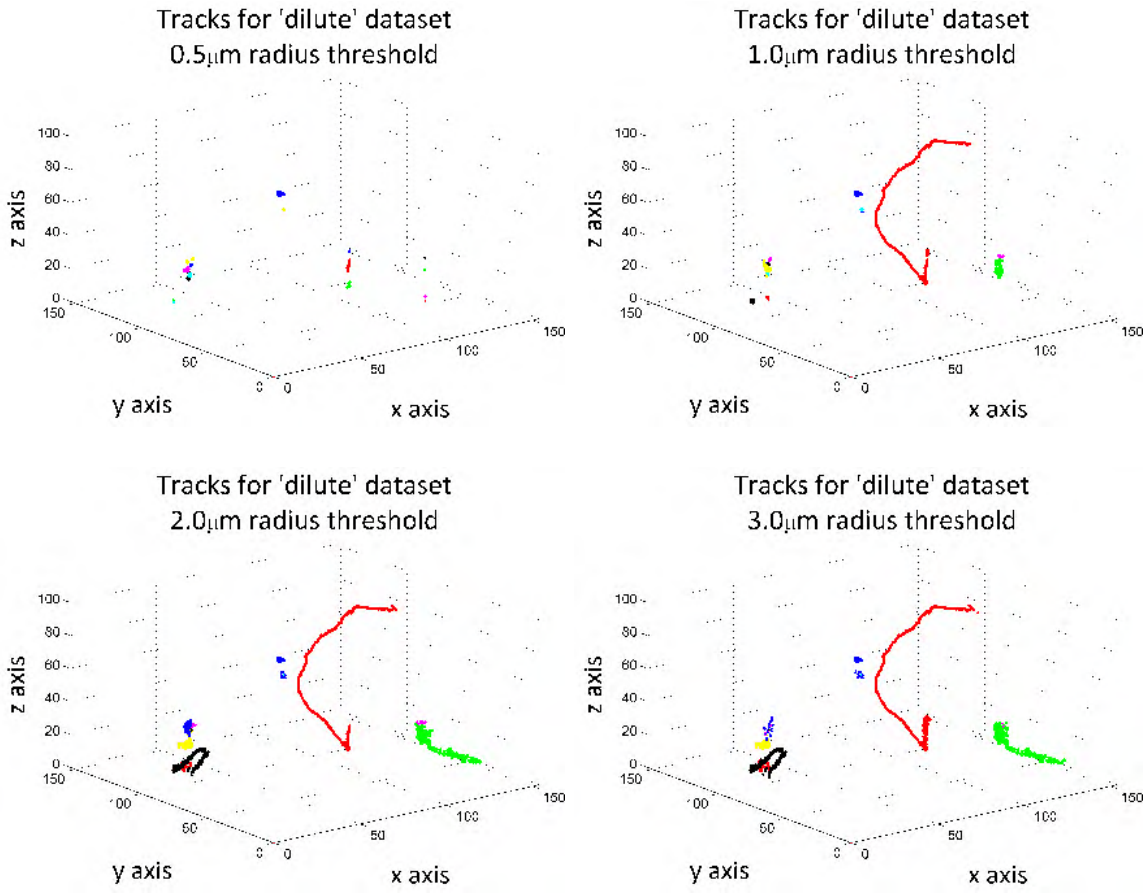

Figure 6.6: Four different radius threshold settings used to extract bacterial tracks from the 'dilute' dataset are displayed. All frames in the 2,000-frame dataset are plotted with different colours indicating the individual extracted tracks. The scale is in μm. While a small radius captures the diffusing motion of a tumbling cell, it fails to capture the larger intervals between frames of a swimming bacterium. This can be seen in comparing the 0.5μm and 1.0μm radius data, where the red track of a cell entering a run has not been picked up by the smaller threshold. The 1.0μm radius in turn fails to pick up the green track seen in the 2.0μm and 3.0μm data. Too large a radius, on the other hand, can lead to an increased chance of misidentifiying tracks in more concentrated samples.

While not all bacterial tracks are identified in these plots (this output only traces cells that were initially present in the recording) they do capture a clear run and

tumble event in the long red trace visible in three of the four plots. The cell is initially swimming toward the floor of the chamber and, early in the time series, undergoes a tumble to dramatically change its direction. The cell makes several other course corrections over the course of the 40-second recording, ending up close to the ceiling surface.

While a small threshold value (0.5μm) might adequately capture the diffusion-like motion of a cell undergoing a tumble, it fails to locate the cell when it swims at a greater linear velocity. This is shown most strikingly in the red trace, but is also true for the green and black traces. At the other end of the scale, too large a threshold value leaves the algorithm open to misidentifying tracks when two cells come close together. This is especially a problem in a more crowded sample, and one that is much worse in two-dimensional studies of swimming microorganisms as crossings are inevitable. Based on a qualitative analysis of these and other data (not shown), the 2.0μm threshold seemed to be the most appropriate to use. For bacteria with well-characterised swimming velocities, however, the threshold should be determined such that it is just greater than the maximum distance expected to be covered between frames.

6.8 Sample 3D Bacterial Track Data

By employing a radial threshold of 2.0μm and by compiling tracks that begin in different initial frames throughout the dataset, we can build up a complete picture of three-dimensional bacterial behaviour, subject to the assumptions made in the analysis described above. Figures 6.7 and 6.8 show different views of all tracks extracted from the 'dilute' dataset that has been discussed throughout this chapter. Tracks through the entire 40-second dataset are displayed, although not all tracks began in the initial frame. Thirteen individual tracks have been identified, which are numbered

at the start of each track and are all shown in different colours. Figure 6.9 shows cross-eye stereoscopic pairs from two different perspectives. The tracks are rendered in 3D by defocusing your eyes until the image pairs overlap. Steroscopic images are generated by the MATLAB function `stereoview v7.0`[3].

Examination of these figures provides a wealth of information. Firstly, cells through the entire volume are able to be identified successfully and their position through time tracked. Non-motile cells are easily differentiated from swimming cells by their classic diffusion profile (tracks 1, 4, 10, 11, 13). In some cases it is clear that the tracking algorithm has separately identified the same cell; for instance, a non-motile cell is identified as both particle 4 and 11. Cells that skirt too close to the edge of the recording field of view suffer from less clearly-defined tracks compared to those that remain near the centre of the FoV. This is due to their diffraction pattern not being adequately captured in the hologram, leading to greater uncertainty in localising their 3D position. This is demonstrated by the blue trace (number 9) in these images, which enters the field of view partway through the recording, undergoes a tumble to reorient itself and then swims close to the edge of the hologram, without completely leaving it. The trace for this cell is decidedly noisy at the edge of the field of view. This effect is amplified by the distance along z the cell is from the recording plane.

On the positive side, a number of traces demonstrating the run and tumble behaviour of wild type *E. coli* in three dimensions can be plainly seen (especially traces 2, 3, 7, 9 and 12). These demonstrate the success of the technique as an imaging modality for studying the three-dimensional swimming behaviour of bacteria. From these 3D position data information such as the run speed, run time, tumble orientation angle, tumble time and other biologically interesting parameters can, in theory, be calculated.

[3]Available at http://www.mathworks.com/matlabcentral/fileexchange/4715

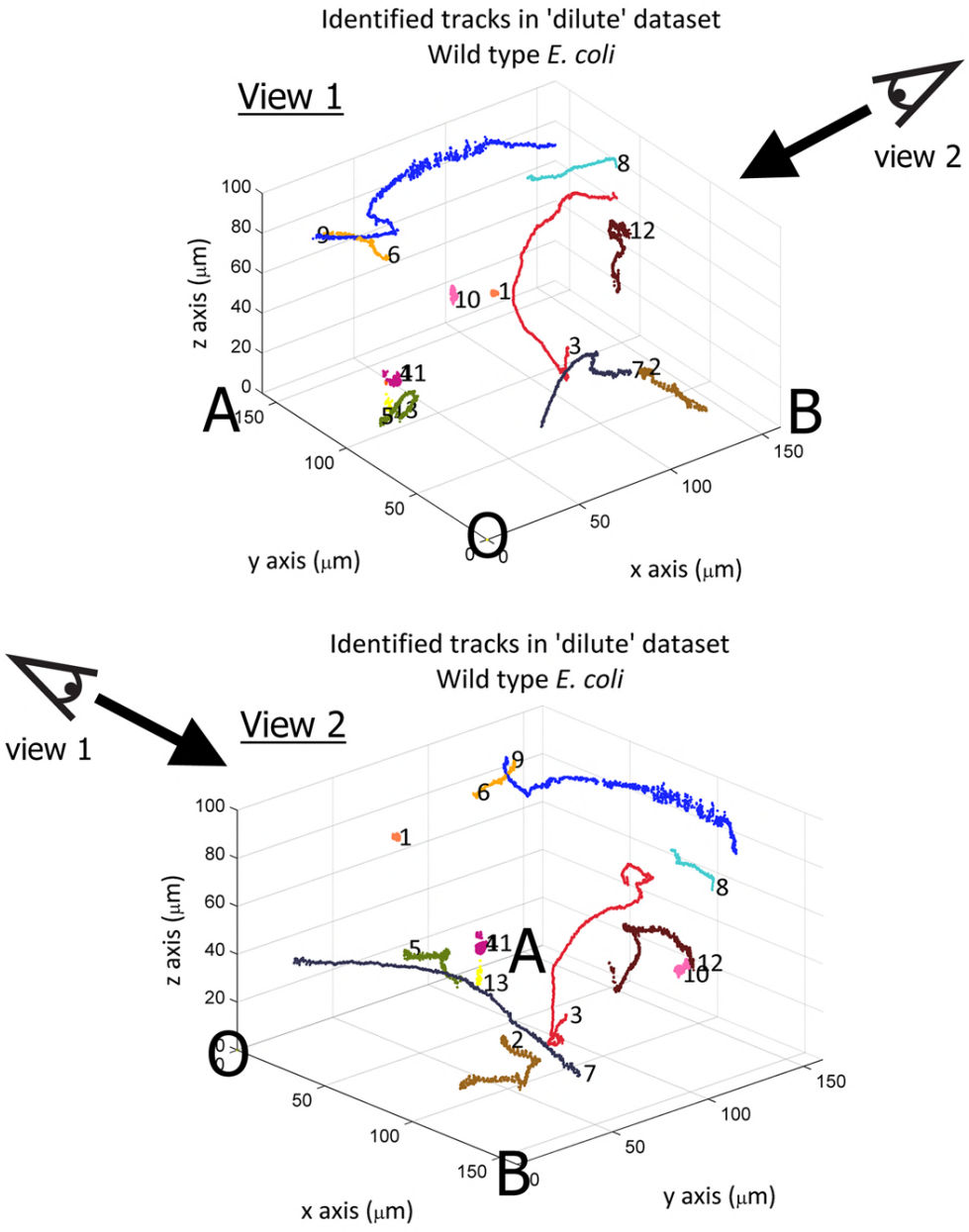

Figure 6.7: Two different 3D views of all tracks extracted for the 'dilute' dataset by the methods discussed in the text. Each of the 13 tracks is numbered and shown in a different colour; the numbers are shown at the start position of each track. In both figures, O denotes the origin, A is the coordinate (0, 160, 0), and B is at (160, 0, 0). The bottom image is a 90° rotation of the top plot about the z-axis. On each plot, the direction of the other view is shown by the arrow.

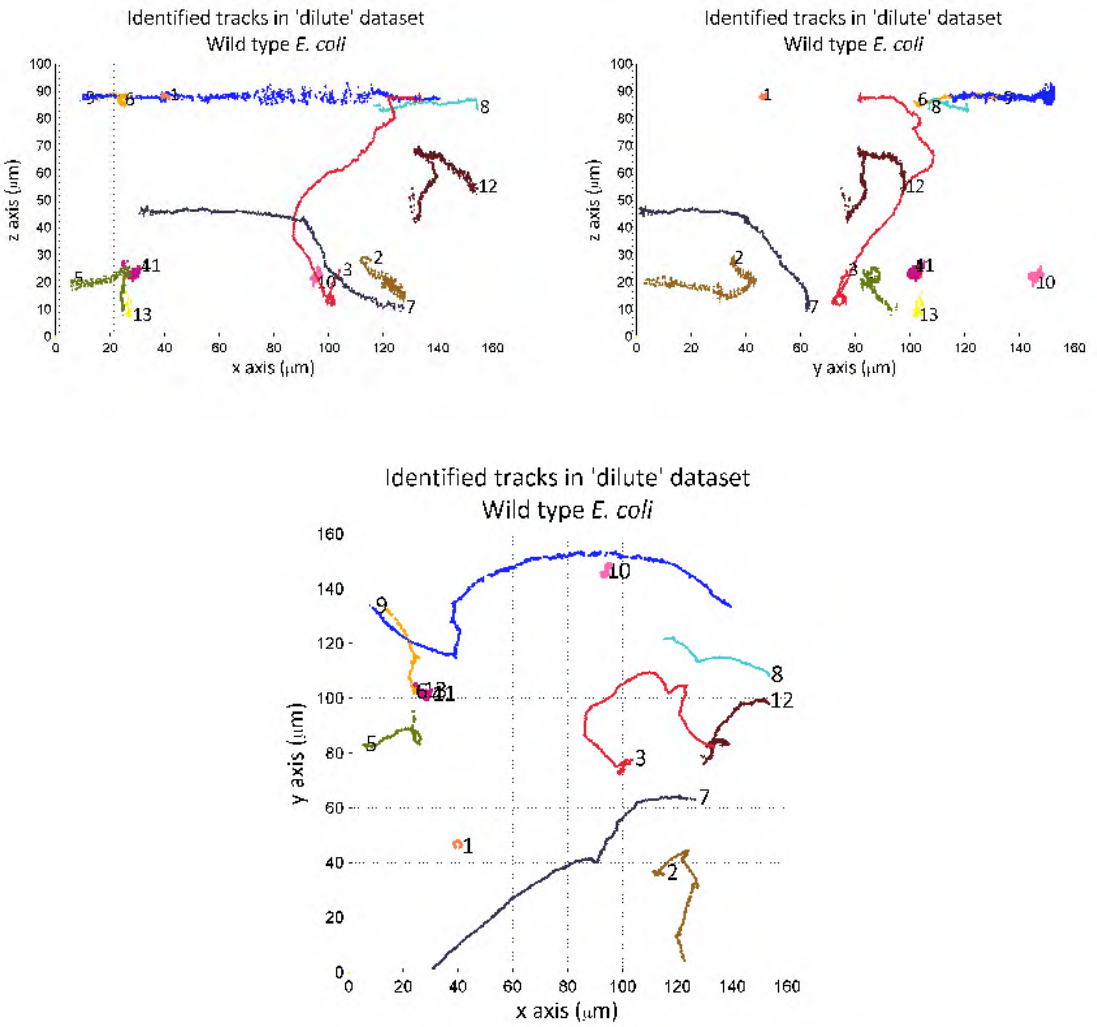

Figure 6.8: Projections onto the three orthogonal planes of the 'dilute' sample track data shown in figure 6.7. Each of the 13 tracks is numbered at the start of each track and is shown in a different colour.

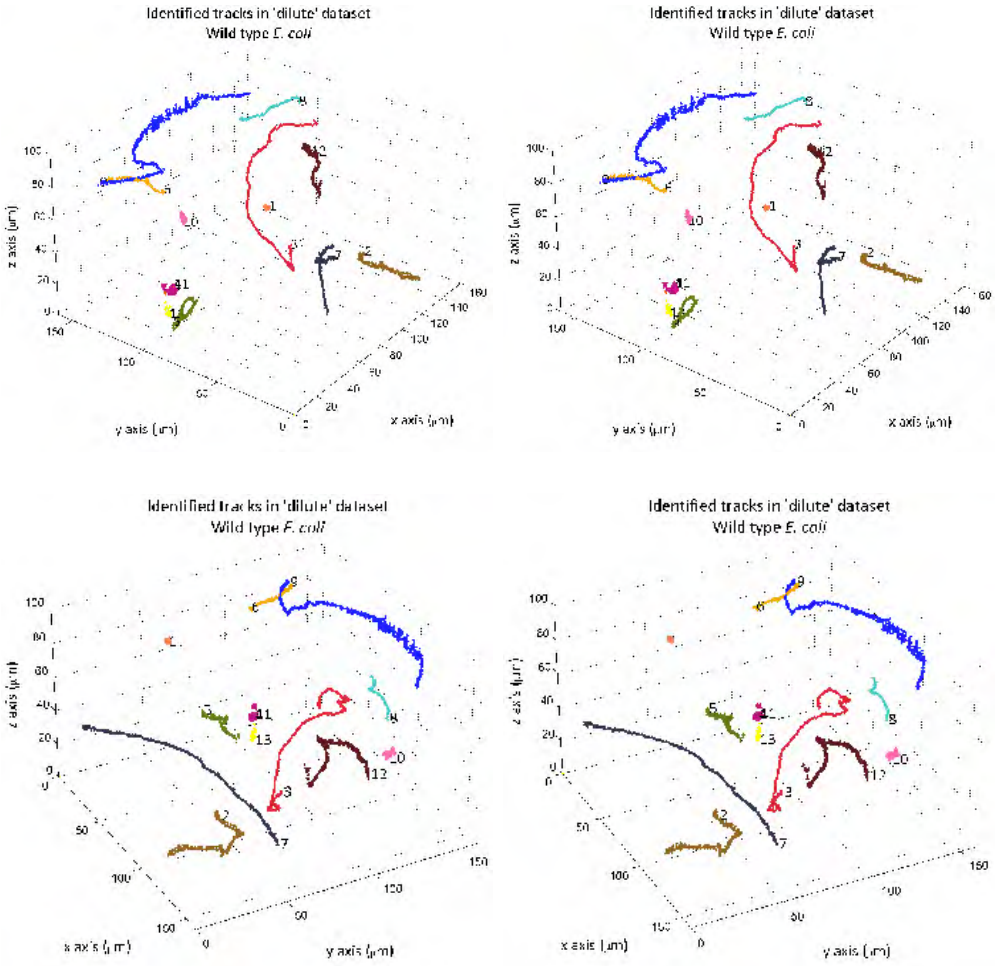

Figure 6.9: Two different stereoscopic views (analogous to those shown in figure 6.7) of the 'dilute' dataset. For best results, hold the page about 40cm away and defocus your eyes until the image pairs overlap.

Figure 6.10 shows these track data evolving over time. Eight snapshots of the tracks are presented at intervals of five seconds. The progression of a reorienting bacterium can be seen by following the progress of cell number 3, for instance. Cells entering the volume throughout the course of the recording can also be seen (cells 8 and 9, for instance).

To conclude this chapter I present the results of applying the same tracking procedure to the 'middle' dilution of bacteria. Different views of the top 50 tracks are displayed in figures 6.11 and 6.12; two different cross-eye stereoscopic pairs are shown in figure 6.13. A 2.0μm radius was also used to extract tracks from the 3D object position data.

Both diffusing non-motile cells and swimming bacteria are identifiable in these data. Despite the simplistic particle identification and tracking routines, the 50 different traces are still quite distinct. Interestingly, in this sample a number of bacteria are congregated at the ceiling of the chamber. The proximity of a motile *E. coli* cell to a surface results in the characteristic and widely reported circular swimming behaviour [76–78]; this is clearly visible in some of these traces.

The preliminary results presented in this chapter show that digital holographic microscopy is a useful tool for the bacteriologist. With improvements to the quantitative analysis of 3D tracks, digital holographic microscopy should allow for future studies of three-dimensional bacterial chemotaxis and other swimming behaviour on a population basis.

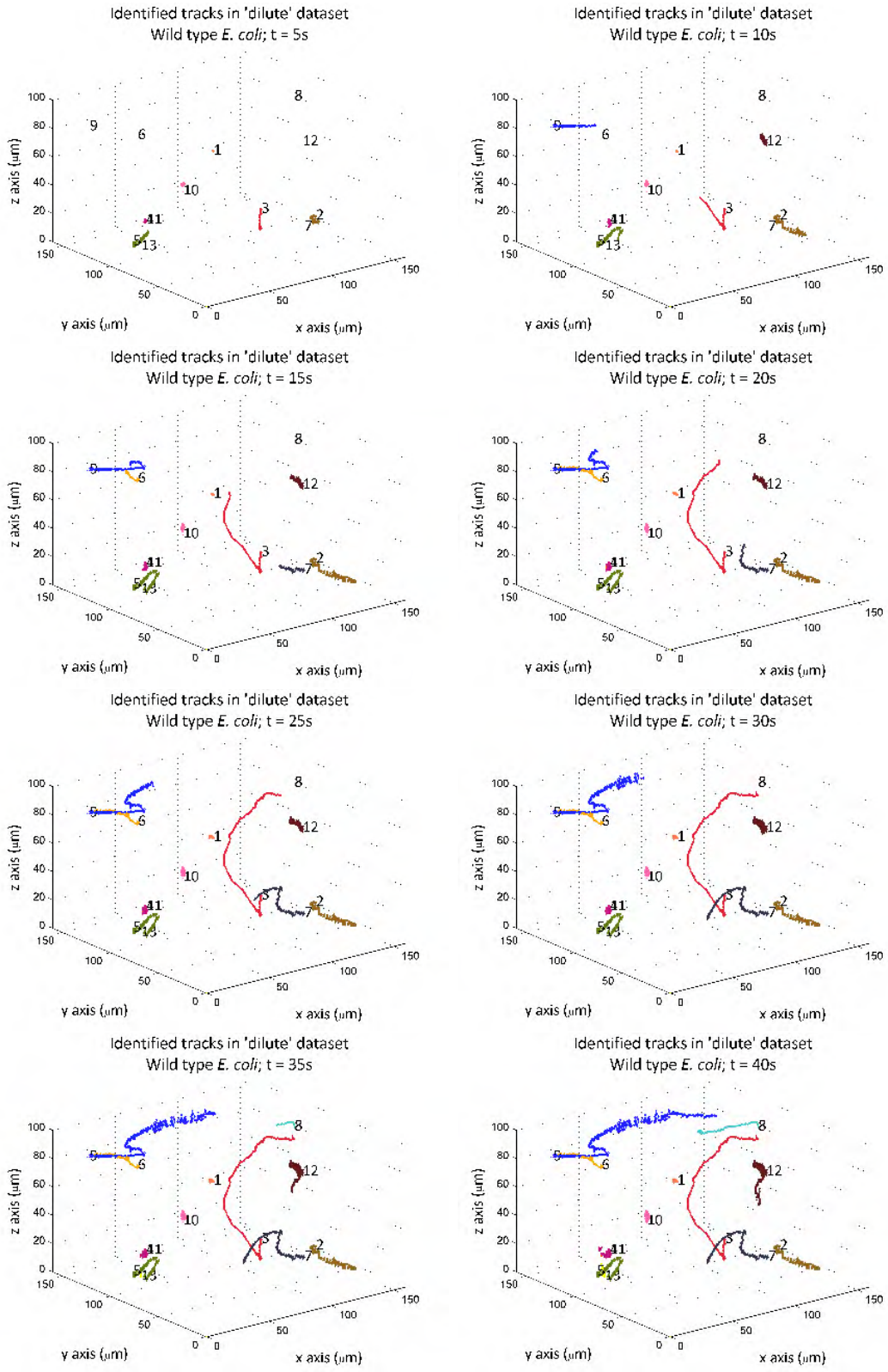

Figure 6.10: Snapshots of recorded 3D tracks of bacteria at different times throughout the 40-second recording. The numbers are placed at the start position of each trace, even if that trace is not visible at the start of the recording.

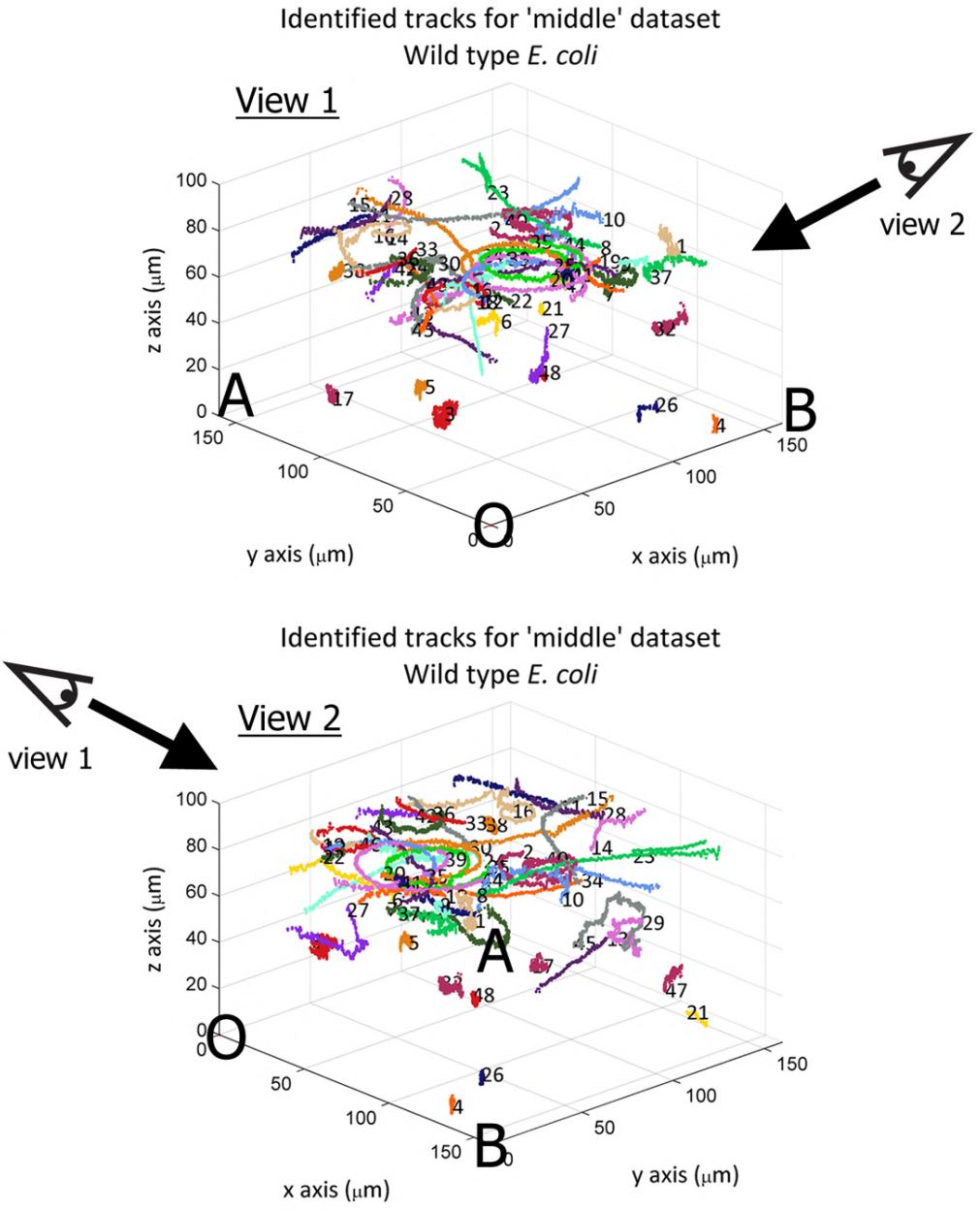

Figure 6.11: Two different 3D views of the 'middle' dilution sample. Different tracks are identified by different colours and by the numbering, which labels each track at the start of the trace. As per figure 6.7, O is the origin and A and B are at the coordinates (0, 160, 0) and (160, 0, 0) respectively. The bottom image is a 90° rotation of the top plot about the z-axis and the direction of the other view is shown by the arrow on each plot.

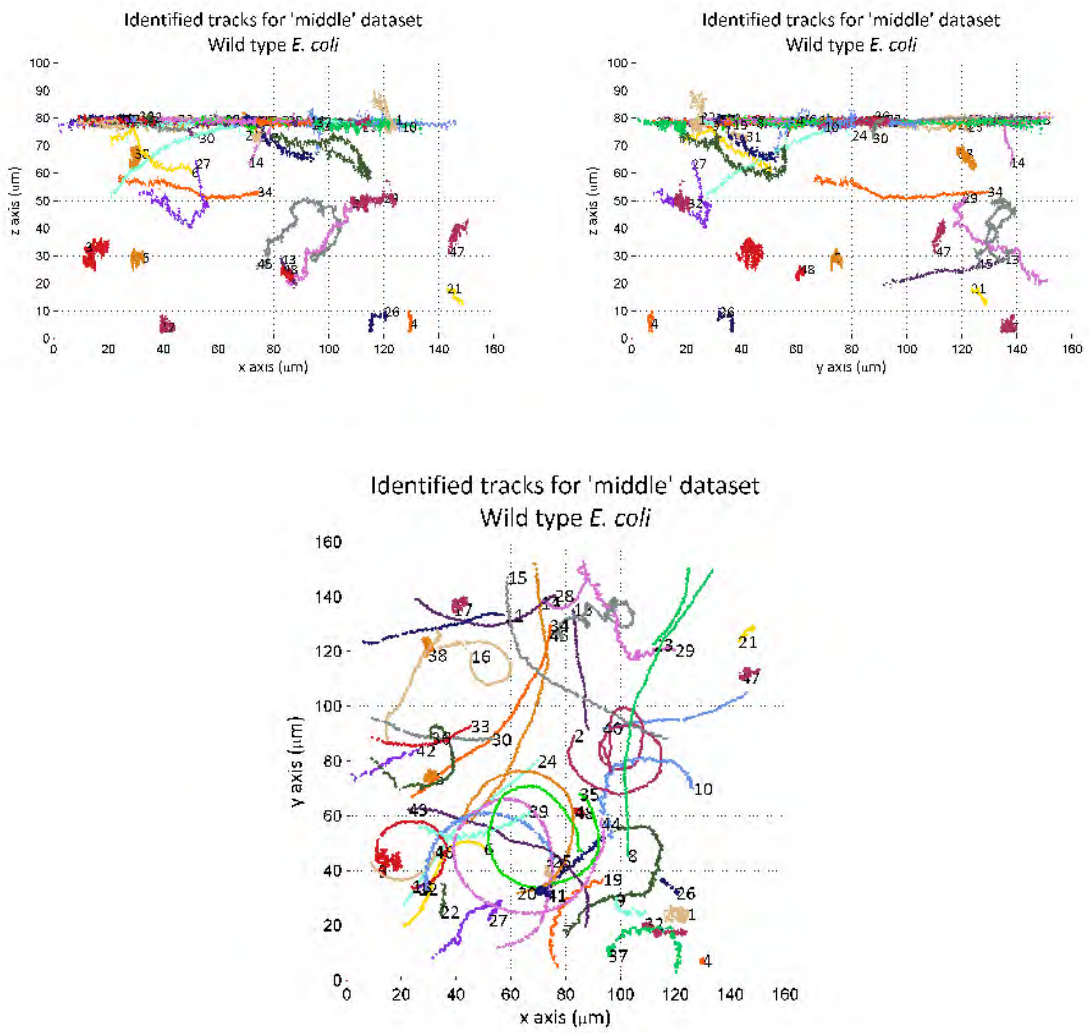

Figure 6.12: Projections onto the three orthogonal planes of the 'middle' sample track data shown in figure 6.11. The x-z and y-z projections show the proximity of many of the cells to the ceiling surface of the sample chamber. The circular motion of *E. coli* in the proximity of this surface is clearly visible in the x-y projection.

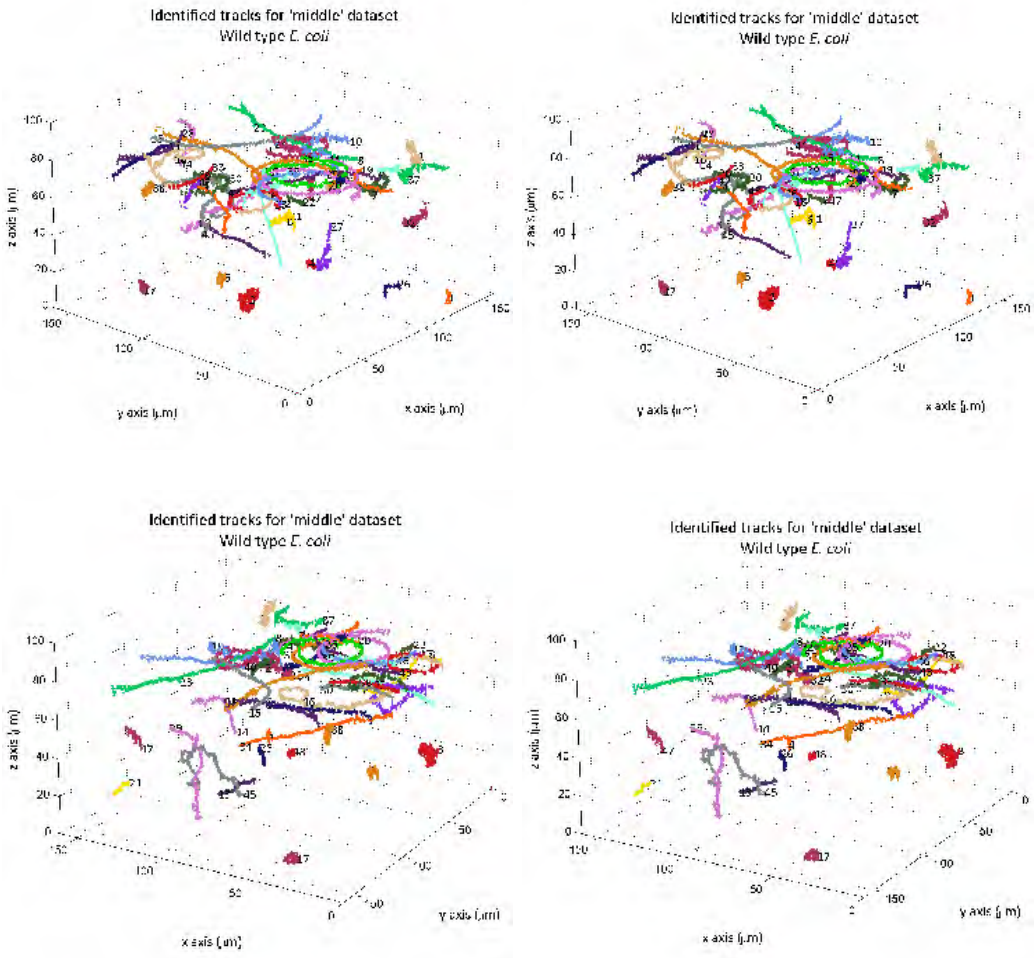

Figure 6.13: Two different stereoscopic views (analogous to those shown in figure 6.11) of the 'middle' dataset. For best results, hold the page about 40cm away and defocus your eyes until the image pairs overlap.

Chapter 7

Conclusions

Digital holographic microscopy is certainly a promising technique for three-dimensional (3D) imaging of microscopic objects. The technique has the ability to record quantitative 3D position data at speeds limited only by the framerate of the digital camera. This thesis has considered digital holographic microscopy with the potential applications of tracking motile bacteria and micro- or nanoparticles for the study of flow fields through particle image velocimetry analysis.

A high-magnification digital holographic microscope (DHM) was built with the original aim of investigating a small ($\sim$30μm $\times$ $\sim$30μm) region of interest around a swimming bacterium at a total magnification of 225$\times$. The microscope was designed to be easily switchable between inline and off-axis holography in order to compare the two imaging modalities directly.

Firstly, the illumination source for the microscope was considered. It became clear that a source with a long coherence length resulted in inline holograms of unacceptable quality. The long coherence length of a helium-neon gas laser meant that any dust along the optical path became a source of parasitic scatterers, generating a diffraction pattern visible in the recorded hologram. The iFLEX 2000 fibre laser − a source with a coherence length of about 800μm − was then used with much more satisfactory

results: only a small section of the optical path was mutually coherent with the specimen. Use of such a laser for off-axis holography, however, required matching the two beam paths to a factor of about 1 in 1700: not a trivial operation. Other illumination sources were considered and rejected: 'super-bright' light emitting diodes were too dim for high-speed recording and a range of laser pointers had issues ranging from insufficiently short coherence lengths to temporally unstable beams.

Several different digital cameras were tried with the apparatus. The Prosilica EC1280 Firewire camera did not record at a reliable framerate. The dark level could not be adjusted on the Prosilica GC1280 Ethernet camera, meaning the camera could not capture the full dynamic range of holograms. These issues were both addressed by the Mikrotron EoSens CL, which became the default camera for the microscope. Its inclusion on the apparatus meant we could record 512px $\times$ 512px regions of interest at up to 2,000 frames per second (fps). The use of the Andor Neo sCMOS camera was also investigated. This camera produces very high quality images with its 5.5Mpx 16-bit CMOS sensor. However, such high resolution produces a bottleneck in the transfer of image data from the onboard camera buffer to a computer hard drive. Overcoming this issue has not yet been addressed, although the higher resolution of the camera is appealing for off-axis microscopy and its increased bit depth could resolve less brightly-scattering particles than the Mikrotron can in inline applications.

The rate at which data could be written was carefully considered for each stage of the recording process. Framegrabber, data transfer protocol and hard drive were all investigated and selected to handle the writing of 512px $\times$ 512px holograms recorded at 1,000fps. A solid state hard drive has superior write speed over conventional hard drives at the expense of capacity. The capacity of the hard drive is currently the limiting factor in recording data with the Mikrotron camera, yet is still greatly overspecified for all our applications in the foreseeable future.

One issue with high-magnification off-axis holography is removing the illumina-

tion beam effectively from the recorded image to avoid the interference pattern of this beam with the reference beam dominating the hologram. Two novel strategies for providing high-magnification off-axis holography were trialled, both of which effectively produce dark field images of the sample to interfere with the reference beam.

The first method used a condenser to steer the illumination beam such that it provided oblique illumination to the sample. The illumination beam was then blocked by an iris in the objective. This method worked in principle but the scattering profile of objects of interest − namely dielectric microspheres − is not strong enough in the imaging direction to produce a signal suitable for high-speed imaging. It is possible that this technique would be better suited to particles whose scattering profile does not depend so strongly on illumination direction: gold nanoparticles for instance.

The second method retained direct illumination but a mask was inserted into a plane conjugate to the back focal plane to provide a high-pass spatial frequency filter. A number of materials were tested for this home-made mask; the one found to be best was a 0.5mm diameter ball bearing suspended across an optical mount on a crosshair of two human hairs. Again, this approach worked in principle; however, it was found that some illumination light scattered off the ball bearing and tended to dominate the signal coming from the sample. In practice, this meant that we could not reconstruct objects above 15μm from the sample chamber floor, whereas for inline holography, we can reconstruct objects at least 100μm from the specimen plane.

Implementing the Fourier mask method for off-axis holography duly restricted our imaging flexibility in that the microscope could not be easily modified to accommodate lower-powered objectives. Switching between inline and off-axis modes was still easily achievable by adjusting the position of the ball bearing mount so that the mask was no longer in the beam path.

It is hard to know when a design phase truly ends and you are left with an apparatus that is 'finished'. Perhaps it never does. There are still many improvements and

adjustments that could be made to this microscope in the future. For instance, the overall guiding principle when considering the optical design of the microscope was the minimisation of the number of optical surfaces to reduce the effect of parasitic scattering objects. This meant that, given the available table space, the reference beam could not be expanded to cover the full area of the CMOS sensor. A redesign on a larger table or use of alternative, more expensive, lenses would ensure that the full area of the camera sensor can be used for off-axis holography. A second, lower-magnification (40×) microscope was also constructed, but in a horizontal alignment with the sample slide mounted vertically. It could be that this arrangement is preferable for some future applications. Avoiding a periscope to couple the illumination beam vertically improves the stability of the setup, and such an arrangement could be used to study samples in cuvettes, which may be of interest in the future.

Nevertheless, the current incarnation of the DHM is shown to be successful in recording inline holograms in particular. Individual polystyrene microspheres can be localised in x, y and z in recordings at 50fps to a precision at least as good as our ability to position the sample. That is, to within 0.05μm in x and y over a range of 32μm and to within 0.77μm in z over a range of 100μm. Assessing the accuracy with which the microscope can locate particles is a more difficult matter. It proved difficult to manufacture calibrated samples that could be used as a three-dimensional ruler. We may have to look into microfabrication techniques to produce a sample that will allow us to better calibrate the microscope over the full range of imaging conditions.

An experiment to measure the 3D diffusion coefficient of a polystyrene microsphere returned the expected result of isotropic diffusion. This indicates that there are no systematic errors in our particle localisation routines along any of the three dimensions. The microscope is also very sensitive to drift, able to pick up motion of the stage on the order of angstroms per second.

The crowding experiment, using the microscope in its inline configuration, was designed to assess whether the localisation precision at the extreme z ranges of a sample decreased with the number of diffusing particles in the sample chamber. For particles located on the floor of the chamber, the localisation precision worsened with increasing numbers of particles in the chamber, but not significantly. The signal from microbeads attached to the ceiling of a chamber was much more greatly affected. The presence of a few tens of diffusing beads fatally affected the signal from microbeads 100μm from the specimen plane. Microspheres on the ceiling of a 50μm deep chamber had more success, although a hundred diffusing particles compromised the signal from the ceiling significantly. It seems likely that the out-of-focus virtual image interferes with the signal from objects far away from the specimen plane. Inserting a spacer medium between the chamber floor and the specimen plane could mitigate the effect of the virtual image. The camera would need to be adjusted to maximise the contrast of the signal; use of a higher bit-depth camera could also aid in recovering the signal from particles far from the focus.

Another effect to consider is that objectives with high numerical apertures capture a wider range of angles of light from the sample. This means that the observed diffraction pattern of a microbead occupies a greater proportion of the field of view, leading to more pattern overlaps in densely-seeded volumes. It may be that high-magnification holography is not suitable to such deep chambers and its use is best restricted to shallower samples with isotropically-scattering objects. Objectives with lower numerical apertures could have more success in imaging many particles in a single field of view. Although the lower resolution of a low numerical aperture objective would mean the loss of fine detail of a sample, this need not be a barrier to localising the centre of particles and successfully tracking them through time in three dimensions.

The ultimate form of twin image removal is to use off-axis holography. For the reas-

ons mentioned above, we struggled to reconstruct particles at a distance greater than 15μm from the specimen plane using the Fourier mask off-axis modality. Nevertheless, we can successfully reconstruct amplitude and phase images of a sample within this range. Dark field off-axis holographic microscopy also looks to be superior to inline holography in studying gold nanoparticles, which could be used to examine the micro-flows around swimming bacteria, especially in shallow chambers. Future work with off-axis holography will look to improve upon the optical quality of the object beam. A first approach would be to look into another, more optically-absorbent, material to replace the ball bearing as the Fourier mask. Ultimately, however, the answer in improved image quality could lie in a custom-built laser dark field microscope using a more established technique with an additional reference beam. Improved off-axis imaging could also aid in the reconstruction of more densely-populated samples.

A small modification to the microscope allowed inline holograms of wild type *Escherichia coli* to be taken at 45× magnification. Despite the relatively crude particle identification and tracking algorithms, this qualitative assessment demonstrated the suitability of holographic microscopy in studying the three-dimensional swimming behaviour of bacteria. Tracks of swimming cells were successfully extracted over 200 seconds at 50fps in a 100μm deep chamber. The run and tumble behaviour of wild type *E. coli* can be seen, as can the circular swimming behaviour of cells interacting hydrodynamically with a surface.

The reconstruction of holograms proceeded on a graphics processing unit (GPU) via bespoke software written in Python by Irwin Zaid. The great advantage of GPUs over conventional CPUs is their ability to perform many copies of the same calculation in parallel. Holographic reconstruction is ideally suited to such parallelisation and the effective use of GPUs is important for improving our reconstruction routines. Our current reconstruction time of ∼15ms per 512px × 512px slice could be improved upon by moving to the next generation GPU hardware or by further parallelising

the reconstruction process, especially for large datasets, through working on GPU clusters.

Looking ahead, one of the immediate challenges is to optimise the object identification procedure at the reconstruction stage. It is clear that a simple thresholding technique is not suitable for all applications: especially in studies of non-spherical biological microorganisms. There are a number of approaches to consider for how best to identify objects and it will come to a question of computation expense versus the benefits of identification. Fitting routines have been used by some groups to identify spherical particles, although these are comparatively slow. Artificial neural networks are appealing as they could efficiently differentiate between different shaped objects, thus leading to studies of interactions between different microorganisms or between microorganisms and inert marker particles.

The future for three-dimensional holographic microscopy certainly seems propitious. We are only beginning to explore the full capabilities of the available digital camera and parallel processing technologies, thus there are a host of potential improvements to be made to the digital holography reconstruction technique. There is also no shortage of applications in both the biophysical and physical fields, although the future may lie in specifically-built microscopes for different imaging applications. It is hoped that the microscope described in this thesis will provide a robust platform onto which a range of three-dimensional microscopy applications can be founded, revealing ever more discoveries in the microworld around us.

Appendix A

Using the Mikrotron Camera

The screenshots below illustrate the steps in using the Mikrotron EoSens CL high-speed camera for recording highly-magnified holograms as described in section 3.3.6. In this configuration of the microscope, a $\sim 30\mu$m $\times$ 30μm region is illuminated, thus only a central subregion of the camera corresponding to this area is used for recording.

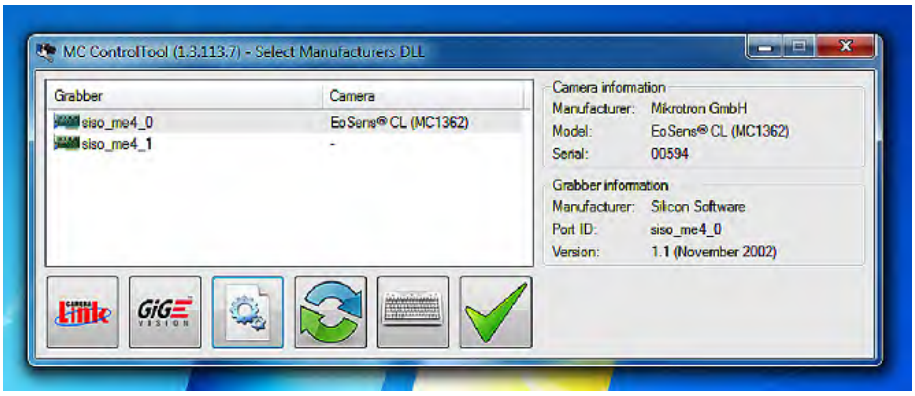

Figure A.1: Screenshot showing interface for selecting appropriate Mikrotron camera driver. The camera and framegrabber hard- and firmware version information is also available here.

The first step is to load the required drivers (figure A.1), followed by selecting the appropriate camera firmware settings (figure A.2) via the supplied 'MC ControlTool' program. The choice of region of interest (RoI) size is directly controllable at the firmware level and this directly governs the maximum available recording framerate.

While the full frame could be selected here and a smaller region of interest identified at the later framegrabber interface, this approach would still see the maximum recording framerate limited to that of the full frame regardless of the size of the framegrabber RoI. Correct firmware settings are thus crucial for optimal performance of the camera. This control tool also allows the user to adjust the digital gain and black level of the camera.

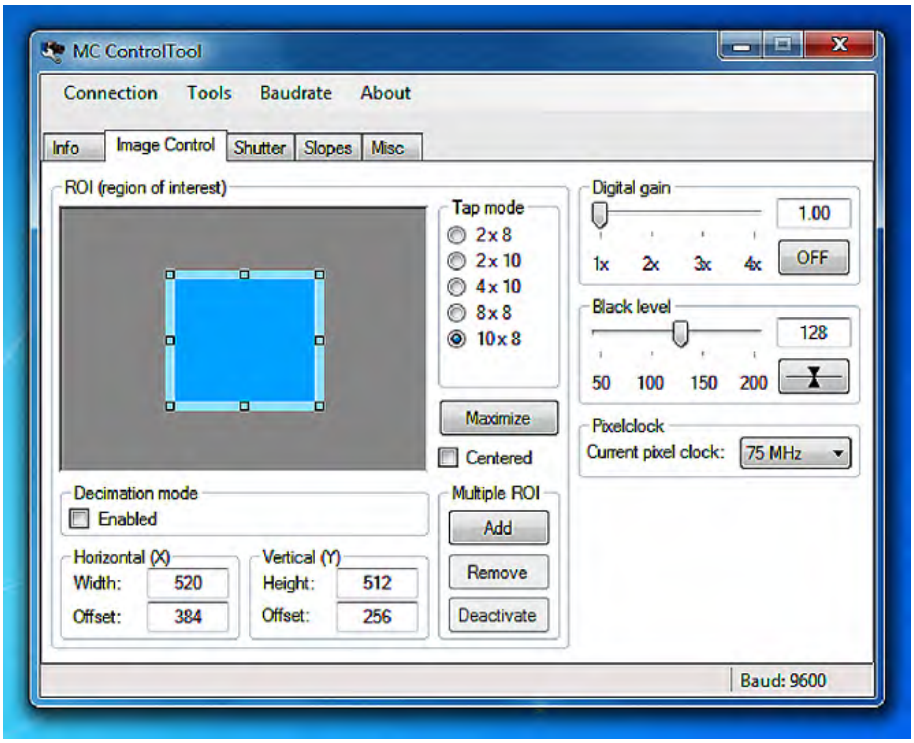

Figure A.2: Screenshot showing interface for adjusting Mikrotron camera firmware settings with the MC ControlTool program. The region of interest can be controlled by dragging the corners of the blue box or by adjusting the 'x', 'y', and 'offset' parameters in the text boxes below. Image black level and digital gain settings can also be changed here.

Following camera firmware settings, the Silicon Software 'microDisplay' framegrabber interface is used to visualise the sample (figure A.3). Live or static images of the sample can be seen and snapshot images may be recorded. The user may adjust parameters such as the exposure and framerate (shown in this image) to determine the optimal settings prior to recording. This software can also be used to see the effect, in real time, of adjusting the black level and digital gain via the MC ControlTool.

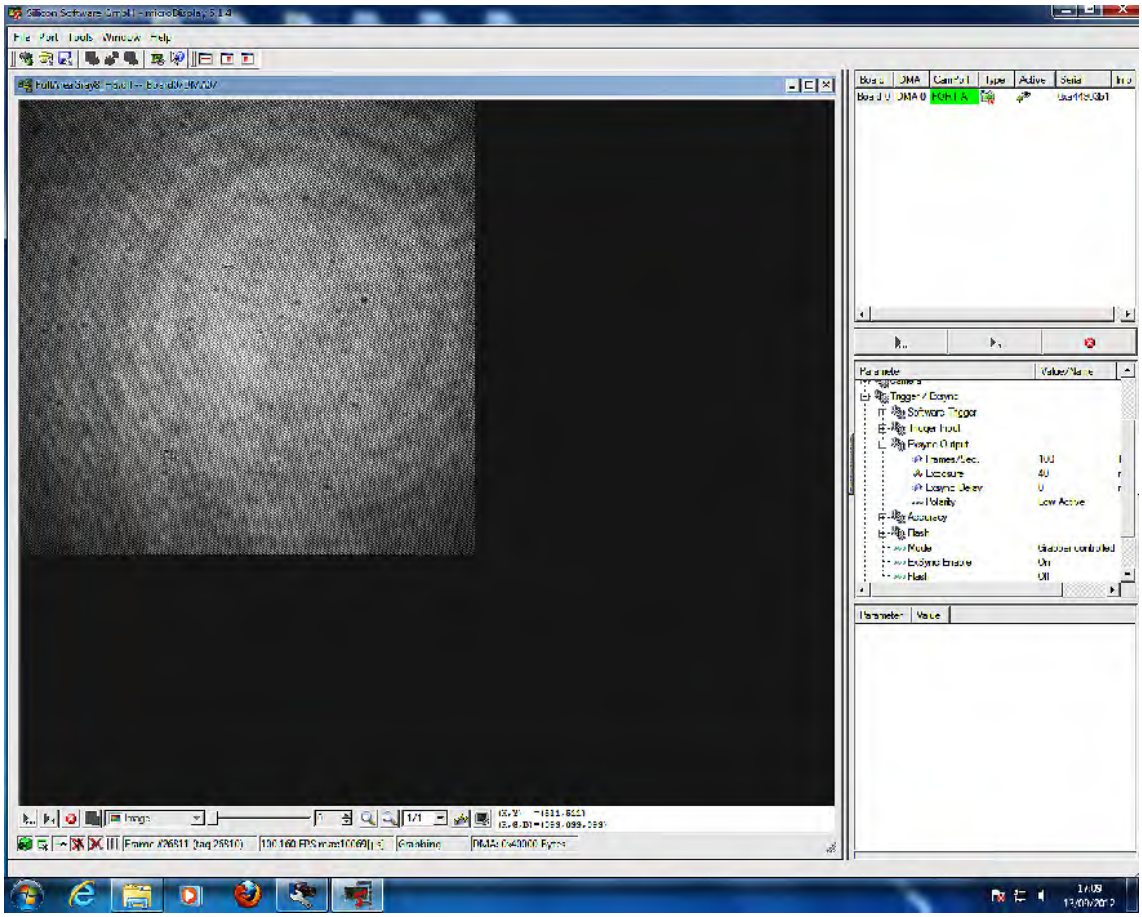

Figure A.3: Screenshot of the microDisplay framegrabber interface used to visualise the sample before recording. The full 512px × 512px region of interest can be seen in this image, along with the controls for adjusting the exposure and framerate. The sample is 100nm gold nanoparticles seen under bright field illumination but with an off-axis reference beam also present.

A typical recording session would begin with viewing the sample in order to focus on the floor of the chamber, as shown in figure A.4. This screenshot from the microDisplay framegrabber software shows an enlarged bright field off-axis view of a dilute suspension of 100nm gold nanoparticles. In the bottom right, a pen mark on the inner surface of the coverslip (the floor of the chamber) can be seen. The piezo servo controls are used to focus on the pen mark, which is then moved out of the field of view prior to acquisition.

The framegrabber interface has a useful live histogram tool, visible at the right of the image. The histogram can be examined to ensure there are no zero value nor

saturated pixels. It can also show the relative intensities of bright and dark fringes of an off-axis interference pattern, as can be seen in this figure. A typical off-axis recording would begin by ensuring the reference and object path lengths are identical through examination of the histogram. The Fourier mask discussed in section 3.7.2 would then be moved into place for dark field imaging.

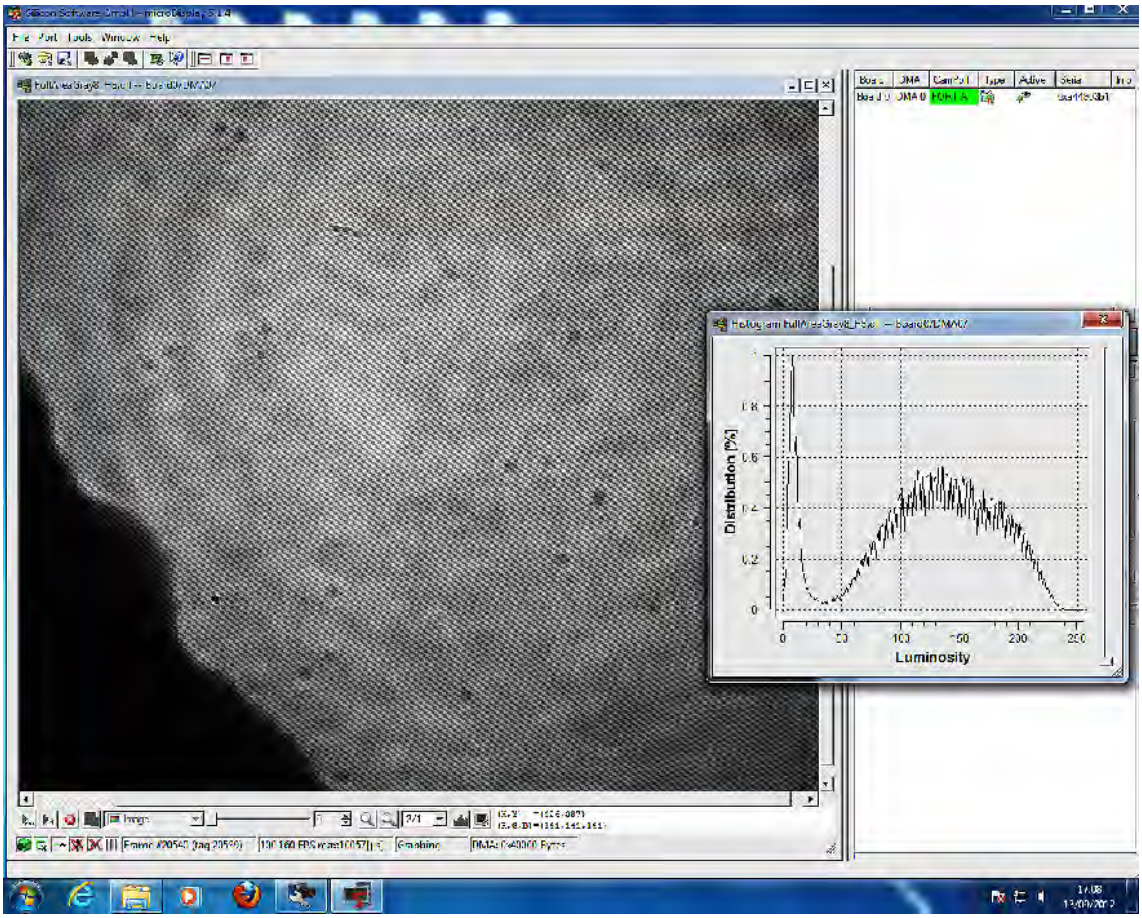

Figure A.4: Screenshot of the microDisplay framegrabber interface showing the floor of a chamber with 100nm gold nanoparticles in focus. The pen mark used for focusing is visible at the bottom left. A histogram of the image is shown at the right.

To achieve maximal recording rates, recording proceeds through a custom Python script that directly interfaces with the framegrabber. Unfortunately, this means the 'microDisplay' viewer must be closed so a live view of the recording is not currently possible.

Appendix B

Numerical Methods

B.1 Python Reconstruction Script

I wrote the following script in Python to call Irwin's GPU inline reconstruction and particle identification routines. The script iterates over multiple files and multiple frames within those files to export HDF5 files of three-dimensional position coordinates from recorded inline holograms. For each batch, the user is required to input: file locations and names; microscope parameters such as effective pixel spacing and illumination wavelength; and reconstruction parameters such as floor and ceiling values and z-resolution. I wrote a similar script for processing off-axis holograms.

```
#jf_recon.py

"""
James Flewellen, September 2012

Version 6.1 of reconstruction script. Calls functions from Irwin's GPU
reconstruction package (pym) to reconstruct inline holography data saved in
HDF5 (.h5) format. 3D position coordinates of identified objects above a
threshold are output. This version iterates over multiple frames and over
multiple data files.

Sample directories and datafiles are included in this version for thesis
output.

Required inputs are:

location:   directory location of h5 file
filename:   original filename, which has had a normalised file saved
spacing:    in um - the effective pixel size of the camera
wavelength: in um
z:          distance in um from hologram plane, can be an array of values
value:      threshold value, optimally determined from GUI

"""
#====================
#===== Imports ======
#====================

import h5py

import numpy

import pycuda
import pycuda.autoinit
import pycuda.cumath
import pycuda.gpuarray

import pym
import pym.gpu
import pym.gpu.holography
import pym.gpu.image
import pym.gpu.misc
import pym.gpu.stats

import PIL #Python Image Library
import PIL.Image
```

```
import matplotlib #Matlab-like package - for plotting etc
import matplotlib.cm
import matplotlib.pyplot

#====================
#==== Generators ====
#====================

#Generator to create amplitude mask of slice above threshold at each
z-value, using GPU functions
def masks_and_reconstructions(z, value):
    for i in range(len(z)):
        reconstruction = abs(propagator.propagate(z[i])).real #2D slices at
        array of z-values
        mask = pym.gpu.image.threshold(abs(reconstruction).real, value)

        yield mask, reconstruction

#Labels and counts masks
def labeled_masks_and_reconstructions(masks_and_reconstructions):
    for labeled_mask, count, reconstruction in pym.gpu.image.stack_label(
    masks_and_reconstructions):
        yield labeled_mask, count, reconstruction

#Storing object parameters (3 is number of dimensions acted upon):
fields = []
if True:
    fields.append(('centroid', numpy.float_, 3))
if True:
    fields.append(('center of mass', numpy.float_, 3))
if False:
    fields.append(('mass', numpy.float_))
if True:
    fields.append(('volume', numpy.float_))
if False:
    fields.append(('density', numpy.float_))
obj_dtype = numpy.dtype(fields)

#================================
#===== MultiFrame Function ======
#================================

# Function to iterate over individual frames in the normalised file

def multi_frame(location, filename, value, n, zFloor, zCeiling):

    #z values and z spacing:
```

```
    z, dz = numpy.linspace(zFloor, zCeiling, n, retstep = True)
    #read file:
    h5file = h5py.File(location + filename, 'r')
    #read background mean file:
    h5backgroundfile = h5py.File(location + 'mean_' + filename, 'r')
    mean_cpu = numpy.asarray(h5backgroundfile['/background'])
    h5backgroundfile.close()
    #convert to GPU array:
    mean_gpu = pycuda.gpuarray.to_gpu(mean_cpu)

    h5fileout = h5py.File(location + 'objects_' + filename, 'w')

    for i in range(0, len(h5file)):
        #read each frame:
        image_gpu = pycuda.gpuarray.to_gpu(numpy.asarray(h5file['/' + str(i)
        + '/image']))
        #inline normalisation:
        norm_im_gpu = pycuda.cumath.sqrt(pym.gpu.misc.clip(image_gpu / pym.
        gpu.misc.clip(mean_gpu, 1.0, numpy.inf) - 1, 0.0, numpy.inf))

        #Rayleigh-Sommerfeld propagation:
        propagator.observation = norm_im_gpu

        #output positions of objects:
        objs_gpu = pym.gpu.image.stack_find_objects(
        labeled_masks_and_reconstructions(masks_and_reconstructions(z, value
        )), spacing = (0.062, 0.062, dz), origin = (0,0,z[0]), dtype =
        obj_dtype)

        if (objs_gpu is None):
            objs_cpu = None
        else:
            objs_cpu = objs_gpu.get()

        if (objs_cpu is None):
            h5fileout.create_group('/' + str(i) + '/objects')
        else:
            h5fileout['/' + str(i) + '/objects'] = objs_cpu

    h5file.close()
    h5fileout.close()

    # display reconstruction parameters on screen:
    print location
    print filename
    print value
    print n
```

```
    print zFloor
    print zCeiling
    print dz
    print z

#================================
#====== MultiFile Function ======
#================================

#Iterates over multiple files:
def loop_over():
    for i in range(len(locationArray)):
        location = locationArray[i]
        filename = filenameArray[i]
        value = valueArray[i]
        n = nArray[i]
        zFloor = zFloorArray[i]
        zCeiling = zCeilingArray[i]

        multi_frame(location, filename, value, n, zFloor, zCeiling)

#====================
#======= Main =======
#====================

"""
Main part of file. Defines global constants and iterates through different
files
performing multi_frame() at each iteration.
"""
#Defines the propagator using the GPU reconstruction routine. Note,
'Kirchoff' is a misnomer; is actually Rayleigh-Sommerfeld.
#Effective pixel spacing, wavelength and refractive index input.
propagator = pym.gpu.holography.KirchoffDiffraction(spacing = (0.062, 0.062),
 wavelength = 0.635 / 1.333)

#======================
#Global constants - array of values:

#Locations of files:
locationArray = ['/home/james/WorkingData/DataToProcess/',
'/home/james/WorkingData/DataToProcess/',
'/home/james/WorkingData/DataToProcess/']

#Names of files:
filenameArray = ['samplefile001.h5',
'samplefile002.h5',
```

```
'samplefile003.h5']

#Threshold values for each file:
valueArray = [0.75, 0.5, 0.85]

#Number of slices for each file:
nArray = [100, 200, 400]

#z floor and ceiling values for each file:
zFloorArray = [0, 2, 2]
zCeilingArray = [50, 50, 100]

#=======================
#Execute the 'loopover' function to output positions for multiple frames and
multiple files:
loop_over()
```

B.2 Numerical Analysis with Matlab

The following excerpts of code are routines written in MATLAB for analysing three-dimensional position data returned by the GPU reconstruction routines.

The first file, `h5posnExtract.m`, takes HDF5 3D position data and converts them into a MATLAB-compatible storage array. This function also allows for filtering of particles by volume, as discussed in section 4.2.4.

The second file, `fitAndNormData.m`, is a function to remove drift from a dataset of position values. This technique is first shown in section 4.4. A polynomial is fitted to the data: degrees of 3, 4, 5 and 6 can be accommodated for in this file. The fitting is subtracted from the data and these residuals are returned. Additionally, the standard deviation of the normalised data and the number of frames that show 'zero' as a position are returned. This last piece of information can be used to identify the number of 'dropped' frames in a dataset, a technique used in section 4.5.

The third file, `findParticles.m`, compares position data from a holographic reconstruction with a snapshot image recorded of a scene. Output of this function is shown in figure 4.10.

The final file shown here, `posnTrackRlarge.m`, is a truncated form of the simple tracking algorithm employed throughout chapters 4, 5 and 6. This function can cope with up to 300 individual objects, to be iterated through to find an object in each subsequent frame within a user-defined radial threshold. I am the first to acknowledge the simplicity of this function and the need for greater elegance and sophistication in future versions.

```
% h5posnExtract.m
% James Flewellen, April 2012
%
% A file to read h5 files that contain (x,y,z) coordinates of multiple
% reconstructed particles, along with the reconstructed volume.
%
% The program receives input of the number of particles desired to extract
% and filters data based on largest volume.
%
% Output is an array [nFrames x nParticles x (x,y,z,vol)]
%
% Required inputs are: filename, nFrames, nParticles.
%
% Note, this version ignores centre of mass data and just extracts centroid
% positions.

%% INPUT VARIABLES
clear all; clc; close all

filenameIn = 'objects_data12_50fps.h5';
filenameOut = 'data12_50fps_objArray2.mat';
nFrames = 2000;
nParticles = 10;

%% INITIALISE ARRAY
dataOut = zeros(nFrames,nParticles,4); %4 is for (x,y,z,vol)

%% READ DATA & OUTPUT
for iFrame = 1:nFrames-1; %H5 data is from 0, MatLab from 1
    dataIn = hdf5read(filenameIn,['/',num2str(iFrame),'/objects']);

    theData = get(dataIn,'Data');
    %memberNames = get(dataIn,'MemberNames');

    %Array to temporarily store and arrange position and volume data
    dataTemp=zeros(numel(theData),4); % x ¦ y ¦ z ¦ vol

    nToIterate = size(theData);
    nToIterate = nToIterate(1); %Necessary as some frames have only 1 object
    if  nToIterate == 1
        iData = 1;
        centroids{iData} = theData{1}.Data;
        %com{iData} = theData{2}.Data; %Uncomment to extract centre of mass
        volume(iData) = theData{3};

        dataTemp(iData,1:3) = centroids{iData}(1:3);
        dataTemp(iData,4) = volume(iData);
    else
        for iData = 1:nToIterate
            centroids{iData} = theData{iData}{1}.Data;
            %com{iData} = theData{iData}{2}.Data;
```

```
            volume(iData) = theData{iData}{3};

            dataTemp(iData,1:3) = centroids{iData}(1:3);
            dataTemp(iData,4) = volume(iData);
        end
    end

    dataTemp;
    dataTemp = sortrows(dataTemp,4);
    dataTemp = flipdim(dataTemp,1);
    dataTemp(nParticles+1:numel(theData),:) = []; %Deletes superfluous entries

    A = size(dataTemp);     %In case fewer particles than expected detected
    if A(1) < nParticles
        newDataTemp = zeros(nParticles,4);
        newDataTemp(1:A(1),:) = dataTemp;
        dataTemp = newDataTemp
    end

    dataOut(iFrame+1,:,:)=dataTemp; %Stores temp array into dataOut array

    clear dataTemp
end

data = dataOut;

%% SAVING

save(filenameOut, 'data')
```

```
function [stdev normData droppedFrames newFrame fitting] = fitAndNormData(frame,↙
data,polyDegree)
% James Flewellen, April 2012
%
% Takes input static bead position and degree of polynomial to fit to
% remove noise. Returns data minus the polynomial fit, the standard
% deviation of the normalised data and the number of dropped frames
%
% Input: frame -> Array of frames
%        data -> data to fit, one column
%        polyDegree -> degree of polynomial to fit
%
% Output: std -> standard deviation of fitted data
%         normData -> the normalised data
%         droppedFrames -> number of missing frames
%         newFrame -> new frame array minus dropped frames


%% Remove Dropped Frames
data = data(any(data(:),2));
droppedFrames = length(frame)-length(data);

%% New frame array if any frames dropped
newFrame = [1:length(data)]';

%% Polynomial fitting

if polyDegree == 3
    [fitParams,fittingGoodness] = fit(newFrame,data,'poly3');
    fitting = fitParams.p1*newFrame.^3 + fitParams.p2*newFrame.^2 + ...
        fitParams.p3*newFrame + fitParams.p4;
    normData = data-fitting;
    stdev = std(normData);
elseif polyDegree == 4
    [fitParams,fittingGoodness] = fit(newFrame,data,'poly4');
    fitting = fitParams.p1*newFrame.^4 + fitParams.p2*newFrame.^3 + ...
        fitParams.p3*newFrame.^2 + fitParams.p4*newFrame + fitParams.p5;
    normData = data-fitting;
    stdev = std(normData);
elseif polyDegree == 5
    [fitParams,fittingGoodness] = fit(newFrame,data,'poly5');
    fitting = fitParams.p1*newFrame.^5 + fitParams.p2*newFrame.^4 + ...
        fitParams.p3*newFrame.^3 + fitParams.p4*newFrame.^2 + ...
        fitParams.p5*newFrame + fitParams.p6;
    normData = data-fitting;
    stdev = std(normData);
elseif polyDegree == 6
    [fitParams,fittingGoodness] = fit(newFrame,data,'poly6');
    fitting = fitParams.p1*newFrame.^6 + fitParams.p2*newFrame.^5 + ...
        fitParams.p3*newFrame.^4 + fitParams.p4*newFrame.^3 + ...
        fitParams.p5*newFrame.^2 + fitParams.p6*newFrame + fitParams.p7;
```

```
function [r,c,v] = findParticles(imFile,obDataFile,threshold)
% function reads data from reconstructed objects saved in .mat file
%
% JF 13-Aug-2012
% imFile is image data (.bmp, .tif or similar) of desired field to compare
% visually.
%
% obDataFile is .mat file with identified reconstructed objects.
%
% threshold is value for 2D histogram over which object positions are
% returned as successful particles. Below this is considered noise.
%
% [r,c,v] are row, col positions of particles over threshold. v is value.

%Load and rearrange data
load(obDataFile);
% data(:,26:100,:) = []; %Remove superfluous particle positions
allX = data(:,:,1); allY = data(:,:,2);

%2D histogram of identified objects
image = mk2dhistv([allX(:) allY(:)],512);

%Plot 2D histogram before thresholding
image = mk2dhistv([allX(:) allY(:)],512);
figA = figure; set(figA, 'Position', [800 500 600 300]);
subplot(1,2,1); surf(image); xlabel('X'); ylabel('Y'); zlabel('Count')
zlim([0 4000]); xlim([0 512]); ylim([0 512]);
title({'2D histogram before thresholding';obDataFile})

%Threshold
for i = 1:512
    for j = 1:512
        if image(i,j) <= threshold
            image(i,j) = 0;
        end
    end
end
image(1,1)=0; %Remove bias of zero-values
subplot(1,2,2); surf(image); xlabel('X'); ylabel('Y'); zlabel('Count')
title({'2D histogram after thresholding';['Threshold = ',num2str(threshold)]})
zlim([0 4000]); xlim([0 512]); ylim([0 512]);

%Output row, col coordinates of particles above threshold
[r,c,v] = find(image)

%Displaying data
im2show = imread(imFile);
figB = figure; set(figB, 'Position', [150 150 700 350]);
subplot(1,2,1); imagesc(im2show); axis square; colormap('gray')
title({'Snapshot image';'Drift dataset'},...
    'FontName','Calibri',...
```

```
    'FontSize',12)%imFile})
subplot(1,2,2); plot(c,r,'o',...
    'MarkerFaceColor','b');
xlim([0 512]); ylim([0 512]); axis ij; axis square
title({'Identified Particles';'Positions given as (x,y) in \mum'},...
    'FontName','Calibri',...
    'FontSize',12);
xlabel('"Column" Axis',...
    'FontName','Calibri',...
    'FontSize',11)
ylabel('"Row" Axis',...
    'FontName','Calibri',...
    'FontSize',11)

for iText = 1:length(r)
    %Convert to microns (14um pixel size, 225x magnification)
    xPos = r(iText)*14/225; yPos = c(iText)*14/225;

    text(c(iText)+15,r(iText)+10,[num2str(xPos,'%.1f'),',',num2str(yPos,'%.1f')])
end
```

```
function [posnArray] = posnTrackRlarge(filenameIn,distThreshold,startParticle)
% JF 1-Aug-2012
%
% Based on posnTrackStaticBeads.m - to track diffusing beads.
%
% This R version uses a radial threshold. 'Large' means it iterates over
% 300 particles.
%
% Note: does not pick out closest particle if more than one within
% threshold
%
% Input:
% filenameIn -> file to load.
%               Data format is: (Frame, object number,[x,y,z,vol] coord)
% distThreshold -> in um, distance between adjacent frames.
% startParticle -> which object to start with
%
% Output:
% posnArray -> array of x,y,z positions for one identified particle. Column
%              4 indicates which particle in original data was closest.
%
% Future version should iterate over particle options more intelligently.


%% INITIAL SETTINGS

load(filenameIn)
% data = volFilteredData;
dimensions = size(data);
data(:,301:dimensions(2),:) = []; %Only copes with 300 particles (!)

frameLength = dimensions(1);

startFrame = 1;
endFrame = frameLength-1;

%Storage array to hold position data
%1:3 are x,y,z; 4 is for debugging showing which detected particle was
%closest to previous (x,y,z)
posnArray = zeros(frameLength,4);

initPosn(1:3) = data(startFrame,startParticle,1:3);
posnArray(1,1:3) = initPosn(1:3);

%% LOOP TO CHECK EACH AVAILABLE PARTICLE WITHIN X,Y,Z THRESHOLD
% Note - does not take smallest value if more than one are within threshold

for iFrame = startFrame:endFrame
    iFrame;
    %% Initial
    initPosn;
```

```
    %% Particle option 1
    nextPosn1(1:3) = data(iFrame+1,1,1:3);
    R1=sqrt((nextPosn1(1)-initPosn(1))^2 + (nextPosn1(2)-initPosn(2))^2 +...
        (nextPosn1(3)-initPosn(3))^2);
    %% Particle option 2
    nextPosn2(1:3) = data(iFrame+1,2,1:3);
    R2=sqrt((nextPosn2(1)-initPosn(1))^2 + (nextPosn2(2)-initPosn(2))^2 +...
        (nextPosn2(3)-initPosn(3))^2);
    % . . .
    %% Particle option 299
    nextPosn299(1:3) = data(iFrame+1,299,1:3);
    R299=sqrt((nextPosn299(1)-initPosn(1))^2 + (nextPosn299(2)-initPosn(2))^2↙
+...
        (nextPosn299(3)-initPosn(3))^2);
    %% Particle option 300
    nextPosn300(1:3) = data(iFrame+1,300,1:3);
    R300=sqrt((nextPosn300(1)-initPosn(1))^2 + (nextPosn300(2)-initPosn(2))^2↙
+...
        (nextPosn300(3)-initPosn(3))^2);


%% Checking against threshold
    if R1 <= distThreshold
        posnArray(iFrame+1,1:3) = nextPosn1;
        posnArray(iFrame+1,4)=1;
        initPosn = nextPosn1;
    elseif R2 <= distThreshold
        posnArray(iFrame+1,1:3) = nextPosn2;
        posnArray(iFrame+1,4)=2;
        initPosn = nextPosn2;
    % . . .
    elseif R299 <= distThreshold
        posnArray(iFrame+1,1:3) = nextPosn299;
        posnArray(iFrame+1,4)=299;
        initPosn = nextPosn299;
    elseif R300 <= distThreshold
        posnArray(iFrame+1,1:3) = nextPosn300;
        posnArray(iFrame+1,4)=300;
        initPosn = nextPosn300;
    end
end
%% Output
posnArray;
```

Bibliography

[1] C. Dobell (editor) and A. van Leeuwenhoek, *Anthony van Leeuwenhoek and his "Little Animals"*. New York, NY: Harcourt, Brace and Company, 1932.

[2] M. G. L. Gustafsson, "Surpassing the lateral resolution limit by a factor of two using structured illumination microscopy," *Journal of Microscopy*, vol. 198, no. 2, pp. 82–87, 2000.

[3] S. W. Hell and J. Wichmann, "Breaking the diffraction resolution limit by stimulated emission: Stimulated-emission-depletion fluorescence microscopy," *Optics Letters*, vol. 19, no. 11, p. 780, 1994.

[4] E. Betzig, G. H. Patterson, R. Sougrat, O. W. Lindwasser, S. Olenych, J. S. Bonifacino, M. W. Davidson, J. Lippincott-Schwartz, and H. F. Hess, "Imaging intracellular fluorescent proteins at nanometer resolution," *Science*, vol. 313, no. 5793, pp. 1642–1645, 2006.

[5] M. J. Rust, M. Bates, and X. Zhuang, "Sub-diffraction-limit imaging by stochastic optical reconstruction microscopy (STORM)," *Nature Methods*, vol. 3, no. 10, pp. 793–796, 2006.

[6] R. Lima, S. Wada, K.-i. Tsubota, and T. Yamaguchi, "Confocal micro-PIV measurements of three-dimensional profiles of cell suspension flow in a square microchannel," *Measurement Science and Technology*, vol. 17, no. 4, pp. 797–808, 2006.

[7] W. Hua, D. Sheff, D. Toomre, and I. Mellman, "Vectorial insertion of apical and basolateral membrane proteins in polarized epithelial cells revealed by quantitative 3D live cell imaging," *The Journal of Cell Biology*, vol. 172, no. 7, pp. 1035–1044, 2006.

[8] K. Drescher, K. Leptos, and R. Goldstein, "How to track protists in three dimensions," *Review of Scientific Instruments*, vol. 80, Jan 2009.

[9] D. J. Müller and Y. F. Dufrêne, "Atomic force microscopy: A nanoscopic window on the cell surface," *Trends in Cell Biology*, vol. 21, no. 8, pp. 461–469, 2011.

[10] H. C. Berg and R. A. Anderson, "Bacteria swim by rotating their flagellar filaments," *Nature*, vol. 245, pp. 380 – 382, Oct 1973.

[11] M. Silverman and M. Simon, "Flagellar rotation and the mechanism of bacterial motility," *Nature*, vol. 249, no. 452, p. 73, 1974.

[12] H. C. Berg, "The rotary motor of bacterial flagella," *Biochemistry*, vol. 72, no. 1, p. 19, 2003.

[13] Y. Sowa and R. M. Berry, "Bacterial flagellar motor," *Quarterly Reviews of Biophysics*, vol. 41, no. 2, pp. 103–132, 2008.

[14] D. F. Blair, "How bacteria sense and swim," *Annual Reviews in Microbiology*, vol. 49, no. 1, pp. 489–520, 1995.

[15] H. Flores, E. Lobaton, S. Mendez-Diez, S. Tlupova, and R. Cortez, "A study of bacterial flagellar bundling," *Bulletin of Mathematical Biology*, vol. 67, pp. 137–168, Jan 2005.

[16] M. Kim, J. Bird, P. A. Van, K. Breuer, and T. Powers, "A macroscopic scale model of bacterial flagellar bundling," *Proceedings of the National Academy of*

Sciences of the United States of America, vol. 100, no. 26, pp. 15481–15485, 2003.

[17] M. Kim and T. R. Powers, "Hydrodynamic interactions between rotating helices," *Physical Review E*, vol. 69, Jun 2004.

[18] Y. Gebremichael, G. S. Ayton, and G. A. Voth, "Mesoscopic modeling of bacterial flagellar microhydrodynamics," *Biophysical Journal*, vol. 91, pp. 3640–3652, Nov 2006.

[19] F. Bai, R. W. Branch, D. V. Nicolau, T. Pilizota, B. C. Steel, P. K. Maini, and R. M. Berry, "Conformational spread as a mechanism for cooperativity in the bacterial flagellar switch," *Science*, vol. 327, no. 5966, p. 685, 2010.

[20] H. C. Berg, "Chemotaxis in bacteria," *Annual Review of Biophysics and Bioengineering*, vol. 4, no. 1, pp. 119–136, 1975.

[21] G. H. Wadhams and J. P. Armitage, "Making sense of it all: Bacterial chemotaxis," *Nature Reviews Molecular Cell Biology*, vol. 5, no. 12, pp. 1024–1037, 2004.

[22] S. Porter, G. Wadhams, and J. Armitage, "Signal processing in complex chemotaxis pathways," *Nature Reviews Microbiology*, vol. 9, pp. 153–165, Mar 2011.

[23] W. R. DiLuzio, L. Turner, M. Mayer, P. Garstecki, D. B. Weibel, H. C. Berg, and G. M. Whitesides, "*Escherichia coli* swim on the right-hand side," *Nature*, vol. 435, no. 7046, pp. 1271–1274, 2005.

[24] Y. Magariyama, S. Sugiyama, K. Muramoto, I. Kawagishi, Y. Imae, and S. Kudo, "Simultaneous measurement of bacterial flagellar rotation rate and swimming speed," *Biophysical Journal*, vol. 69, no. 5, pp. 2154–2162, 1995.

[25] E. M. Purcell, "Life at low Reynolds number," *American Journal of Physics*, vol. 45, no. 1, pp. 3–11, 1977.

[26] J. Happel and H. Brenner, *Low Reynolds Number Hydrodynamics: With Special Applications to Particulate Media*. The Hague, The Netherlands: Martinus Nijhoff Publishers, 1983.

[27] K. F. Jarrell and M. J. McBride, "The surprisingly diverse ways that prokaryotes move," *Nature Reviews Microbiology*, vol. 6, no. 6, pp. 466–476, 2008.

[28] J. P. Armitage and R. Schmitt, "Bacterial chemotaxis: *Rhodobacter sphaeroides* and *Sinorhizobium meliloti* − variations on a theme?," *Microbiology (SGM)*, vol. 143, no. 12, pp. 3671–3682, 1997.

[29] G. E. Murphy, J. R. Leadbetter, and G. J. Jensen, "*In situ* structure of the complete *Treponema primitia* flagellar motor," *Nature*, vol. 442, no. 7106, pp. 1062–1064, 2006.

[30] G. Li and J. X. Tang, "Low flagellar motor torque and high swimming efficiency of *Caulobacter crescentus* swarmer cells," *Biophysical Journal*, vol. 91, pp. 2726–2734, Oct 2006.

[31] J. P. Armitage, "Bacterial tactic responses," *Advances in Microbial Physiology*, vol. 41, pp. 229–289, 1999.

[32] S. Romagnoli, H. L. Packer, and J. P. Armitage, "Tactic responses to oxygen in the phototrophic bacterium *Rhodobacter sphaeroides* WS8N," *Journal of Bacteriology*, vol. 184, no. 20, pp. 5590–5598, 2002.

[33] J. P. Armitage and K. J. Hellingwerf, "Light-induced behavioral responses ('phototaxis') in prokaryotes," *Photosynthesis Research*, vol. 76, no. 1-3, pp. 145–155, 2003.

[34] H. C. Berg, "How to track bacteria," *Review of Scientific Instruments*, vol. 42, no. 6, pp. 868–871, 1971.

[35] P. D. Frymier, R. M. Ford, H. C. Berg, and P. T. Cummings, "Three-dimensional tracking of motile bacteria near a solid planar surface," *Proceedings of the National Academy of Sciences*, vol. 92, no. 13, pp. 6195–6199, 1995.

[36] N. Verstraeten, K. Braeken, B. Debkumari, M. Fauvart, J. Fransaer, J. Vermant, and J. Michiels, "Living on a surface: Swarming and biofilm formation," *Trends in Microbiology*, vol. 16, no. 10, pp. 496–506, 2008.

[37] J. W. Costerton, P. S. Stewart, and E. P. Greenberg, "Bacterial biofilms: A common cause of persistent infections," *Science*, vol. 284, no. 5418, pp. 1318–1322, 1999.

[38] J. C. Conrad, M. L. Gibiansky, F. Jin, V. D. Gordon, D. A. Motto, M. A. Mathewson, W. G. Stopka, D. C. Zelasko, J. D. Shrout, and G. C. L. Wong, "Flagella and pili-mediated near-surface single-cell motility mechanisms in *P. aeruginosa*," *Biophysical Journal*, vol. 100, no. 7, pp. 1608–1616, 2011.

[39] E. Lauga and T. R. Powers, "The hydrodynamics of swimming microorganisms," *Reports on Progress in Physics*, vol. 72, p. 096601, 2009.

[40] G. Subramanian and P. R. Nott, "The fluid dynamics of swimming microorganisms and cells," *Journal of the Indian Institute of Science*, vol. 93, Sep 2011.

[41] T. Ishikawa, G. Sekiya, Y. Imai, and T. Yamaguchi, "Hydrodynamic interactions between two swimming bacteria," *Biophysical Journal*, vol. 93, pp. 2217–2225, Sep 2007.

[42] C. M. Pooley, G. P. Alexander, and J. M. Yeomans, "Hydrodynamic interaction between two swimmers at low Reynolds number," *Physical Review Letters*, vol. 99, no. 22, p. 228103, 2007.

[43] G. Corkidi, B. Taboada, C. D. Wood, A. Guerrero, and A. Darszon, "Tracking sperm in three-dimensions," *Biochemical and Biophysical Research Communications*, vol. 373, no. 1, pp. 125–129, 2008.

[44] T. W. Su, L. Xue, and A. Ozcan, "High-throughput lensfree 3D tracking of human sperms reveals rare statistics of helical trajectories," *Proceedings of the National Academy of Sciences of the United States of America*, 2012.

[45] M. Polin, I. Tuval, K. Drescher, J. P. Gollub, and R. Goldstein, "*Chlamydomonas* swims with two 'gears' in a eukaryotic version of run-and-tumble locomotion," *Science*, vol. 325, no. 5939, pp. 487–490, 2009.

[46] K. Drescher, K. Leptos, I. Tuval, T. Ishikawa, T. Pedley, and R. Goldstein, "Dancing *Volvox*: Hydrodynamic bound states of swimming algae," *Physical Review Letters*, vol. 102, no. 16, 2009.

[47] J. S. Guasto, K. A. Johnson, and J. P. Gollub, "Oscillatory flows induced by microorganisms swimming in two dimensions," *Physical Review Letters*, vol. 105, no. 16, p. 168102, 2010.

[48] E. Malkiel, J. Sheng, J. Katz, and J. R. Strickler, "The three-dimensional flow field generated by a feeding calanoid copepod measured using digital holography," *Journal of Experimental Biology*, vol. 206, no. 20, p. 3657, 2003.

[49] J. S. Guasto, R. Rusconi, and R. Stocker, "Fluid mechanics of planktonic microorganisms," *Annual Review of Fluid Mechanics*, vol. 44, pp. 373–400, 2012.

[50] R. Dreyfus, J. Baudry, M. L. Roper, M. Fermigier, H. A. Stone, and J. Bibette, "Microscopic artificial swimmers," *Nature*, vol. 437, no. 7060, pp. 862–865, 2005.

[51] A. M. Leshansky, O. Kenneth, O. Gat, and J. E. Avron, "A frictionless microswimmer," *New Journal of Physics*, vol. 9, p. 145, 2007.

[52] B. Kaehr and J. B. Shear, "High-throughput design of microfluidics based on directed bacterial motility," *Lab on a Chip*, vol. 9, no. 18, pp. 2632–2637, 2009.

[53] R. Di Leonardo, J. Leach, H. Mushfique, J. M. Cooper, G. Ruocco, and M. J. Padgett, "Multipoint holographic optical velocimetry in microfluidic systems," *Physical Review Letters*, vol. 96, no. 13, p. 134502, 2006.

[54] M. Al-Fandi, J.-W. Kim, A. P. Malshe, S. Tung, J. Jenkins, and R. Pooran, "Chemo-sensitivity and reliability of flagellar rotary motor in a MEMS microfluidic actuation system," *Sensors and Actuators B: Chemical*, vol. 114, pp. 229–238, Mar 2006.

[55] N. Darnton, L. Turner, K. Breuer, and H. C. Berg, "Moving fluid with bacterial carpets," *Biophysical Journal*, vol. 86, pp. 1863–1870, Mar 2004.

[56] I. M. Zaid, J. Dunkel, and J. M. Yeomans, "Lévy fluctuations and mixing in dilute suspensions of algae and bacteria," *Journal of The Royal Society Interface*, vol. 8, no. 62, pp. 1314–1331, 2011.

[57] R. Metzler and J. Klafter, "The random walk's guide to anomalous diffusion: A fractional dynamics approach," *Physics Reports*, vol. 339, no. 1, pp. 1–77, 2000.

[58] P. Wang, C. Wen, W. Li, and Y. Chen, "Motile microorganism tracking system using micro-visual servo control," Nano/Micro Engineered and Molecular Sys-

tems, 2008. NEMS 2008. 3rd IEEE International Conference on, pp. 178–182, January 2008.

[59] H. Oku, N. Ogawa, M. Ishikawa, and K. Hashimoto, "Two-dimensional tracking of a motile micro-organism allowing high-resolution observation with various imaging techniques," *Review of Scientific Instruments*, vol. 76, no. 3, pp. 034301–034301, 2005.

[60] J. G. Santiago, S. T. Wereley, C. D. Meinhart, D. J. Beebe, and R. J. Adrian, "A particle image velocimetry system for microfluidics," *Experiments in Fluids*, vol. 25, no. 4, pp. 316–319, 1998.

[61] K. V. Sharp and R. J. Adrian, "On flow-blocking particle structures in microtubes," *Microfluidics and Nanofluidics*, vol. 1, no. 4, pp. 376–380, 2005.

[62] S. T. Wereley and C. D. Meinhart, "Recent advances in micro-particle image velocimetry," *Annual Review of Fluid Mechanics*, vol. 42, pp. 557–576, 2010.

[63] M. Raffel, C. E. Willert, S. T. Wereley, and J. Kompenhans, *Particle Image Velocimetry: A Practical Guide*. Berlin - Heidelburg: Springer Verlag, second ed., 2007.

[64] M. Arroyo and K. Hinsch, "Recent developments of PIV towards 3D measurements," *Particle Image Velocimetry*, pp. 127–154, 2008.

[65] R. J. Adrian, "Twenty years of particle image velocimetry," *Experiments in Fluids*, vol. 39, no. 2, pp. 159–169, 2005.

[66] S. A. Klein, J. L. Moran, D. H. Frakes, and J. D. Posner, "Three-dimensional three-component particle velocimetry for microscale flows using volumetric scanning," *Measurement Science and Technology*, vol. 23, no. 8, p. 085304, 2012.

[67] E. Toprak, H. Balci, B. H. Blehm, and P. R. Selvin, "Three-dimensional particle tracking via bifocal imaging," *Nano Letters*, vol. 7, no. 7, pp. 2043–2045, 2007.

[68] F. Pereira, J. Lu, E. Castaño-Graff, and M. Gharib, "Microscale 3D flow mapping with μDDPIV," *Experiments in Fluids*, vol. 42, pp. 589–599, Apr 2007.

[69] W.-H. Tien, P. Kartes, T. Yamasaki, and D. Dabiri, "A color-coded backlighted defocusing digital particle image velocimetry system," *Experiments in Fluids*, vol. 44, no. 6, pp. 1015–1026, 2008.

[70] S. Chen, N. Angarita-Jaimes, D. Angarita-Jaimes, B. Pelc, A. H. Greenaway, C. E. Towers, D. Lin, and D. P. Towers, "Wavefront sensing for three-component three-dimensional flow velocimetry in microfluidics," *Experiments in Fluids*, vol. 47, no. 4, pp. 849–863, 2009.

[71] R. Bowman, G. Gibson, and M. Padgett, "Particle tracking stereomicroscopy in optical tweezers: Control of trap shape," *Optics Express*, vol. 18, no. 11, pp. 11785–11790, 2010.

[72] B. Ovryn and S. H. Izen, "Imaging of transparent spheres through a planar interface using a high-numerical-aperture optical microscope," *JOSA A*, vol. 17, pp. 1202–1213, Jan 2000.

[73] J. Sheng, E. Malkiel, and J. Katz, "Digital holographic microscope for measuring three-dimensional particle distributions and motions," *Applied Optics*, vol. 45, no. 16, pp. 3893–3901, 2006.

[74] T. Mochizuki, H. Sato, and Y. Mori, "Multi-angle observation scheme for bubbles and droplets," vol. 15, no. 2, pp. 125–137, 2012.

[75] R. Bowman, D. Preece, G. Gibson, and M. Padgett, "Stereoscopic particle tracking for 3D touch, vision and closed-loop control in optical tweezers," *Journal of Optics*, vol. 13, Apr 2011.

[76] A. P. Berke, L. Turner, H. C. Berg, and E. Lauga, "Hydrodynamic attraction of swimming microorganisms by surfaces," *Physical Review Letters*, vol. 101, no. 3, p. 38102, 2008.

[77] E. Lauga, W. R. DiLuzio, G. M. Whitesides, and H. A. Stone, "Swimming in circles: Motion of bacteria near solid boundaries," *Biophysical Journal*, vol. 90, pp. 400–412, Jan 2006.

[78] G. Li, L. K. Tam, and J. X. Tang, "Amplified effect of Brownian motion in bacterial near-surface swimming," *Proceedings of the National Academy of Sciences of the United States of America*, vol. 105, no. 47, p. 18355, 2008.

[79] A. Ashkin, "Optical trapping and manipulation of neutral particles using lasers," *Proceedings of the National Academy of Sciences of the United States of America*, vol. 94, pp. 4853–4860, May 1997.

[80] P. Marquet, B. Rappaz, P. J. Magistretti, E. Cuche, Y. Emery, T. Colomb, and C. Depeursinge, "Digital holographic microscopy: A noninvasive contrast imaging technique allowing quantitative visualization of living cells with subwavelength axial accuracy," *Optics Letters*, vol. 30, no. 5, pp. 468–470, 2005.

[81] Z. Frentz, S. Kuehn, D. Hekstra, and S. Leibler, "Microbial population dynamics by digital in-line holographic microscopy," *Review of Scientific Instruments*, vol. 8, Aug 2010.

[82] M. K. Kim, "Principles and techniques of digital holographic microscopy," *SPIE Reviews*, vol. 1, pp. 1–50, May 2010.

[83] O. Mudanyali, D. Tseng, C. Oh, S. Isikman, I. Sencan, W. Bishara, C. Oztoprak, S. Seo, B. Khademhosseini, and A. Ozcan, "Compact, light-weight and cost-effective microscope based on lensless incoherent holography for telemedicine applications," *Lab on a Chip*, vol. 10, no. 11, pp. 1417–1428, 2010.

[84] T. Tahara, K. Ito, T. Kakue, M. Fujii, Y. Shimozato, Y. Awatsuji, K. Nishio, S. Ura, T. Kubota, and O. Matoba, "Parallel phase-shifting digital holographic microscopy," *Biomedical Optics Express*, vol. 1, no. 2, pp. 610–616, 2010.

[85] J. Katz and J. Sheng, "Applications of holography in fluid mechanics and particle dynamics," *Annual Review of Fluid Mechanics*, vol. 42, pp. 531–555, 2010.

[86] N. Warnasooriya, F. Joud, P. Bun, G. Tessier, M. Coppey-Moisan, P. Desbiolles, M. Atlan, M. Abboud, and M. Gross, "Imaging gold nanoparticles in living cell environments using heterodyne digital holographic microscopy," *Optics Express*, vol. 18, no. 4, pp. 3264–3273, 2010.

[87] F. Verpillat, F. Joud, P. Desbiolles, and M. Gross, "Dark-field digital holographic microscopy for 3D-tracking of gold nanoparticles," *Optics Express*, vol. 19, pp. 26044–55, Dec 2011.

[88] C. S. Seelamantula, N. Pavillon, C. Depeursinge, and M. Unser, "Exact complex-wave reconstruction in digital holography," *Journal of the Optical Society of America A*, vol. 28, no. 6, pp. 983–992, 2011.

[89] P. Jourdain, N. Pavillon, C. Moratal, D. Boss, B. Rappaz, C. Depeursinge, P. Marquet, and P. J. Magistretti, "Determination of transmembrane water fluxes in neurons elicited by glutamate ionotropic receptors and by the co-transporters KCC2 and NKCC1: A digital holographic microscopy study," *The Journal of Neuroscience*, vol. 31, no. 33, p. 11846, 2011.

[90] L. Wilson and R. Zhang, "3D localization of weak scatterers in digital holographic microscopy using Rayleigh-Sommerfeld back-propagation," *Optics Express*, vol. 20, no. 15, p. 16735, 2012.

[91] D. Gabor, "A new microscopic principle," *Nature*, vol. 161, no. 4098, pp. 777–778, 1948.

[92] J. W. Goodman, *Introduction To Fourier Optics*. Greenwood Village, CO: Roberts & Company Publishers, third ed., 2005.

[93] J. Mertz, *Introduction to Optical Microscopy*. Greenwood Village, CO: Roberts & Company Publishers, 2009.

[94] V. Toal, *Introduction to Holography*. Boca Raton, FL: CRC Press, Taylor & Francis Group, LLC, 2011.

[95] U. Schnars and W. Jüptner, *Digital Holography: Digital Hologram Recording, Numerical Reconstruction, and Related Techniques*. Berlin - Heidelberg: Springer-Verlag, 2005.

[96] J. W. Goodman and R. W. Lawrence, "Digital image formation from electronically detected holograms," *Applied Physics Letters*, vol. 11, no. 3, p. 77, 1967.

[97] H. Meng, G. Pan, Y. Pu, and S. H. Woodward, "Holographic particle image velocimetry: From film to digital recording," *Measurement Science and Technology*, vol. 15, p. 673, 2004.

[98] J. Kühn, F. Charrière, T. Colomb, E. Cuche, F. Montfort, Y. Emery, P. Marquet, and C. Depeursinge, "Axial sub-nanometer accuracy in digital holographic microscopy," *Measurement Science and Technology*, vol. 19, p. 074007, 2008.

[99] G. Coppola, P. Ferraro, M. Iodice, S. De Nicola, A. Finizio, and S. Grilli, "A digital holographic microscope for complete characterization of microelectromech-

anical systems," *Measurement Science and Technology*, vol. 15, pp. 529–539, Mar 2004.

[100] T. Colomb, F. Dürr, E. Cuche, P. Marquet, H. G. Limberger, R. P. Salathé, and C. Depeursinge, "Polarization microscopy by use of digital holography: Application to optical-fiber birefringence measurements," *Applied Optics*, vol. 44, no. 21, pp. 4461–4469, 2005.

[101] S. Kim and S. J. Lee, "Measurement of Dean flow in a curved micro-tube using micro digital holographic particle tracking velocimetry," *Experiments in Fluids*, vol. 46, no. 2, pp. 255–264, 2009.

[102] F. C. Cheong, B. Sun, R. Dreyfus, J. Amato-Grill, K. Xiao, L. Dixon, and D. G. Grier, "Flow visualization and flow cytometry with holographic video microscopy," *Optics Express*, vol. 17, no. 15, pp. 13071–13079, 2009.

[103] W. Xu, M. H. Jericho, H. J. Kreuzer, and I. A. Meinertzhagen, "Tracking particles in four dimensions with in-line holographic microscopy," *Optics Letters*, vol. 28, no. 3, pp. 164–166, 2003.

[104] S.-H. Lee, Y. Roichman, G.-R. Yi, S.-H. Kim, S.-M. Yang, A. van Blaaderen, P. van Oostrum, and D. G. Grier, "Characterizing and tracking single colloidal particles with video holographic microscopy," *Optics Express*, vol. 15, no. 26, p. 18275, 2007.

[105] W. Xu, M. H. Jericho, I. A. Meinertzhagen, and H. J. Kreuzer, "Digital in-line holography for biological applications," *Proceedings of the National Academy of Sciences of the United States of America*, vol. 98, no. 20, p. 11301, 2001.

[106] J. Sheng, E. Malkiel, J. Katz, J. Adolf, and R. Belas, "Digital holographic microscopy reveals prey-induced changes in swimming behavior of predatory

dinoflagellates," *Proceedings of the National Academy of Sciences of the United States of America*, vol. 104, no. 44, p. 17512, 2007.

[107] M. Toy, C. Pache, J. Parent, J. Kühn, M. Egli, and C. Depeursinge, "Dual-mode digital holographic and fluorescence microscopy for the study of morphological changes in cells under simulated microgravity," vol. 7570 of *Proceedings of the SPIE Conference on Three-Dimensional and Multidimensional Microscopy: Image Acquisition and Processing XVII*, Feb 2010.

[108] S.-H. Lee and D. G. Grier, "Holographic microscopy of holographically trapped three-dimensional structures," *Optics Express*, vol. 15, no. 4, p. 1505, 2007.

[109] P. A. Blanche, A. Bablumian, R. Voorakaranam, C. Christenson, W. Lin, T. Gu, D. Flores, P. Wang, W. Y. Hsieh, and M. Kathaperumal, "Holographic three-dimensional telepresence using large-area photorefractive polymer," *Nature*, vol. 468, no. 7320, pp. 80–83, 2010.

[110] J. C. Maxwell, "XXV. On physical lines of force," *Philosophical Magazine Series 4*, vol. 21, pp. 161–175, Mar 1861.

[111] C. Huygens, *Traité de la Lumière*. Leiden, The Netherlands: Pieter van der Aa, 1690.

[112] T. M. Pritchett and A. D. Trubatch, "A differential formulation of diffraction theory for the undergraduate optics course," *American Journal of Physics*, vol. 72, pp. 1026–34, Aug 2004.

[113] S. Silver, "Microwave aperture antennas and diffraction theory," *JOSA*, vol. 52, pp. 131–139, Jan 1962.

[114] S. Chi and Q. Guo, "Vector theory of self-focusing of an optical beam in Kerr media," *Optics letters*, vol. 20, no. 15, pp. 1598–1600, 1995.

[115] G. B. Arfken, H. J. Weber, and F. E. Harris, *Mathematical Methods for Physicists*. Waltham, MA: Elsevier Academic Press, seventh ed., 2013.

[116] G. Kirchhoff, "Zur theorie der lichtstrahlen," *Annalen der Physik*, vol. 18, pp. 663–695, 1883.

[117] E. Cuche, P. Marquet, and C. Depeursinge, "Simultaneous amplitude-contrast and quantitative phase-contrast microscopy by numerical reconstruction of Fresnel off-axis holograms," *Applied Optics*, vol. 38, no. 34, pp. 6994–7001, 1999.

[118] F. C. Cheong, B. J. Krishnatreya, and D. G. Grier, "Strategies for three-dimensional particle tracking with holographic video microscopy," *Optics Express*, vol. 18, no. 13, p. 13563, 2010.

[119] M. Born and E. Wolf, *Principles of Optics: Electromagnetic Theory of Propagation, Interference and Diffraction of Light*. Cambridge, UK: Cambridge University Press, seventh (expanded) ed., 1999.

[120] A. S. Marathay and J. F. McCalmont, "On the usual approximation used in the Rayleigh-Sommerfeld diffraction theory," *JOSA A*, vol. 21, no. 4, pp. 510–516, 2004.

[121] A. D. Tichenor and J. W. Goodman, "Coherent transfer function," *JOSA*, vol. 62, pp. 293–295, Jan 1972.

[122] C. E. Shannon, "Communication in the presence of noise (1949 classic paper reprint)," *Proceedings of the IEEE*, vol. 86, Feb 1998.

[123] E. N. Leith and J. Upatnieks, "Reconstructed wavefronts and communication theory," *Journal of the Optical Society of America*, vol. 52, no. 10, pp. 1123–1128, 1962.

[124] M. Liebling, T. Blu, and M. Unser, "Complex-wave retrieval from a single off-axis hologram," *Journal of the Optical Society of America A*, vol. 21, no. 3, pp. 367–377, 2004.

[125] E. Cuche, P. Marquet, and C. Depeursinge, "Spatial filtering for zero-order and twin-image elimination in digital off-axis holography," *Applied Optics*, vol. 39, no. 23, pp. 4070–4075, 2000.

[126] S. Lai, B. Kemper, and G. von Bally, "Off-axis reconstruction of in-line holograms for twin-image elimination," *Optics Communications*, vol. 169, no. 1, pp. 37–43, 1999.

[127] H. Meng, W. L. Anderson, F. Hussain, and D. D. Liu, "Intrinsic speckle noise in in-line particle holography," *Journal of the Optical Society of America A*, vol. 10, no. 9, p. 2046, 1993.

[128] Y. Pu and H. Meng, "Intrinsic speckle noise in off-axis particle holography," *Journal of the Optical Society of America A*, vol. 21, no. 7, p. 1221, 2004.

[129] T. Zhang and I. Yamaguchi, "Three-dimensional microscopy with phase-shifting digital holography," *Optics Letters*, vol. 23, no. 15, pp. 1221–1223, 1998.

[130] J. Rosen and G. Brooker, "Non-scanning motionless fluorescence three-dimensional holographic microscopy," *Nature Photonics*, vol. 2, pp. 190–195, Mar 2008.

[131] W. Xu, M. H. Jericho, I. A. Meinertzhagen, and H. J. Kreuzer, "Digital in-line holography of microspheres," *Applied Optics*, vol. 41, no. 25, pp. 5367–5375, 2002.

[132] D. Gabor, *Nobel Lectures, Physics 1971-1980*, ch. Holography, 1948-1971. Singapore: World Scientific Publishing Co., 1992.

[133] D. Garber, "Digital holography using a laser pointer and consumer digital camera," Undergraduate Report, John Hopkins University, Jun 2004.

[134] S. K. Jericho, J. Garcia-Sucerquia, W. Xu, M. H. Jericho, and H. J. Kreuzer, "Submersible digital in-line holographic microscope," *Review of Scientific Instruments*, vol. 77, no. 4, p. 043706, 2006.

[135] P. Guo and A. Devaney, "Digital microscopy using phase-shifting digital holography with two reference waves," *Optics Letters*, vol. 29, no. 8, pp. 857–859, 2004.

[136] Y. Pu and H. Meng, "An advanced off-axis holographic particle image velocimetry (HPIV) system," *Experiments in Fluids*, vol. 29, pp. 184–197, Aug 2000.

[137] J. Sheng, E. Malkiel, and J. Katz, "Single beam two-views holographic particle image velocimetry," *Applied Optics*, vol. 42, no. 2, p. 235, 2003.

[138] J. Zhang, B. Tao, and J. Katz, "Turbulent flow measurement in a square duct with hybrid holographic PIV," *Experiments in Fluids*, vol. 23, no. 5, pp. 373–381, 1997.

[139] N. Pavillon, C. S. Seelamantula, J. Kühn, M. Unser, and C. Depeursinge, "Suppression of the zero-order term in off-axis digital holography through nonlinear filtering," *Applied Optics*, vol. 48, no. 34, p. 186, 2009.

[140] L. Xu, J. Miao, and A. Asundi, "Properties of digital holography based on in-line configuration," *Optical Engineering*, vol. 39, pp. 3214–3219, Dec 2000.

[141] M. Liebling and M. Unser, "Comparing algorithms for reconstructing digital off-axis fresnel holograms," vol. 6016 of *Proceedings of the SPIE Conference on Three-Dimensional TV, Video, and Display IV*, pp. 213 – 222, Oct 2005.

[142] N. Pavillon, C. S. Seelamantula, M. Unser, and C. Depeursinge, "Artifact-free reconstruction from off-axis digital holograms through nonlinear filtering," vol. 7723 of *Proceedings of the SPIE Conference on Optics, Photonics and Digital Technologies for Multimedia Applications*, May 2010.

[143] Y. Sowa, B. Steel, and R. Berry, "A simple backscattering microscope for fast tracking of biological molecules," *Review of Scientific Instruments*, vol. 81, Nov 2010.

[144] W. Hergert and T. Wriedt, eds., *The Mie Theory: Basics and Applications*. Berlin - Heidelberg: Springer-Verlag, 2012.

[145] P. Jain, K. Lee, I. El-Sayed, and M. El-Sayed, "Calculated absorption and scattering properties of gold nanoparticles of different size, shape, and composition: Applications in biological imaging and biomedicine," *Journal of Physical Chemistry B*, vol. 110, pp. 7238–7248, Apr 2006.

[146] M. Daniel and D. Astruc, "Gold nanoparticles: Assembly, supramolecular chemistry, quantum-size-related properties, and applications toward biology, catalysis, and nanotechnology," *Chemical Reviews*, vol. 104, pp. 293–346, Jan 2004.

[147] A. Klöckner, N. Pinto, Y. Lee, B. Catanzaro, P. Ivanov, and A. Fasih, "PyCUDA and PyOpenCL: A scripting-based approach to GPU run-time code generation," *Parallel Computing*, vol. 38, no. 3, pp. 157–174, 2012.

[148] *NVIDIA CUDA C Programming Guide Version 4.2*. Apr 2012.

[149] B. Ovryn, "Three-dimensional forward scattering particle image velocimetry applied to a microscopic field-of-view," *Experiments in Fluids*, vol. 29, pp. 175–184, Dec 2000.

[150] A. Einstein, "Über die von der molekularkinetischen theorie der wärme geforderte bewegung von in ruhenden flüssigkeiten suspendierten teilchen," *Annalen der Physik*, vol. 322, no. 8, pp. 549–560, 1905.

[151] D. D. Nolte, *Optical Interferometry for Biology and Medicine*. New York, NY: Springer, 2012.

[152] H. C. Berg and D. A. Brown, "Chemotaxis in *Escherichia coli* analysed by three-dimensional tracking," *Nature*, vol. 239, no. 5374, pp. 500–504, 1972.

[153] J. Adler and M. M. Dahl, "A method for measuring the motility of bacteria and for comparing random and non-random motility," *Journal of General Microbiology*, vol. 46, pp. 161–173, Jan 1967.

[154] M. Egmont-Petersen, D. de Ridder, and H. Handels, "Image processing with neural networks – a review," *Pattern Recognition*, vol. 35, no. 10, pp. 2279–2301, 2002.

[155] J. Jiang, P. Trundle, and J. Ren, "Medical image analysis with artificial neural networks," *Computerized Medical Imaging and Graphics*, vol. 34, no. 8, pp. 617–631, 2010.